X-Ray Dark-Field Tensor Tomography

– a Hitchhiker's Guide to Tomographic Reconstruction and Talbot Imaging –

Dissertation zur Erlangung des
naturwissenschaftlichen Doktorgrades
der Julius-Maximilians-Universität Würzburg

vorgelegt von

Jonas Graetz
(geb. Dittmann)

aus Kitzingen

Würzburg 2021

Eingereicht am: 28. Juni 2021

bei der Fakultät für Physik und Astronomie

1. Gutachter: Prof. Dr. Randolf Hanke
2. Gutachter: Prof. Dr. Peter Jakob
3. Gutachter: Prof. Dr. Thorsten M. Buzug

der Dissertation

Vorsitzender: Prof. Dr. Karl Mannheim

1. Prüfer: Prof. Dr. Randolf Hanke
2. Prüfer: Prof. Dr. Peter Jakob
3. Prüfer: Prof. Dr. Haye Hinrichsen

im Promotionskolloqium

Tag des Promotionskolloquiums: 8. April 2022

Doktorurkunde ausgehändigt am:

Preface

Computed tomography now approaches its 50th anniversary, and an overwhelmingly large body of literature has been created throughout the past decades. The countless variants of tomographic imaging devices in a growing number of application fields have given rise to uncountable contributions on many aspects of tomographic reconstruction beyond the mathematical foundations typically covered by textbooks. The fragmentation of literature over many areas of application on the one hand, and overlaps with other fields of computational imaging, computer science, mathematics, physics and engineering on the other hand, have made it increasingly complex for new researchers entering the field to identify the present state of the art or best practice with respect to any given problem. A central concern of the present dissertation therefore is, besides obviously adding a further piece of literature, to reduce the apparent complexity by providing brief reviews, practical formulas and explicit algorithms especially also for the fundamental tasks in tomographic reconstruction.

I am indebted to Prof. Dr. Randolf Hanke for giving me the opportunity to explore the field autodidactively, and to Dr. habil. Simon Zabler for proposing and supporting the topic of dark-field tensor tomography and his essential initiatives towards actual experiments. I am especially grateful for the inspiring experimental environment created by the fellow PhD students and colleagues at the chair of X-ray microscopy, which motivated the involvement with image reconstruction problems. The variety of projects, problems and tasks also at the associated groups of the Fraunhofer IIS that I have meanwhile become part of has always been an unlimited source of interesting and richly diverse challenges, and I therefore also appreciate the due patience and respect shown while focusing to finalize this dissertation and related publications. Special thanks further go in particular to the many researchers I had the chance to meet at conferences and various other occasions, who have been an essential source of motivation and feedback.

Finally, I deeply thank my wife Teresa for her invaluable patience and support throughout the sometimes demanding times while writing this dissertation.

Zusammenfassung

Die Röntgen-Dunkelfeld-Bildgung vermag den Widerspruch zwischen dem Bedarf nach großen Sichtfeldern im Zentimeterbereich und der nötigen Bildauflösung zur Charakterisierung von Fasermaterialien mit Strukturgrößen im Mikrometerbereich aufzulösen. Sie bedient sich dafür der Eigenschaft von Röntgen-Talbot-Interferometern, Ultrakleinwinkelstreueigenschaften einer Probe vollflächig abzubilden, womit eine Lücke von mehreren Größenordnung zwischen der Bildauflösung und der konstrastgebenden Strukturgröße überbrückt werden kann. Der Zusammenhang zwischen Strukturanisotropie und gerichteter Streuung ermöglicht dabei Rückschlüsse auf die Orientierung der Mikrostruktur einer Probe unterhalb der Bildauflösung. Erste Demonstrationen haben, basiered auf verschiedenen heuristischen Signalmodellen und Rekonstruktrionsansätzen, die grundsätzliche Erweiterbarkeit auf die Volumen-Bildgebung gezeigt. In der vorliegenden Arbeit wird, aufbauend auf einer umfassenden Analyse der Dunkelfeld-Bildgebung und tomographischer Rekonstruktionsmethoden, sowohl ein verifiziertes Modell der Signalanisotropie als auch eine Rekonstruktionstechnik entwickelt, die für große tensorwertige Volumina und allgemeine Abbildungsgeometrien praktikabel ist.

In diesem Sinne wird ein weites interdisziplinäres Feld von Bildgebungs- und Rekonstruktionsmethoden aufgearbeitet. Zunächst werden anhand einer neuen Einführung in die mathematische Beschreibung perspektivischer Projektionen essenzielle Einsichten in die Zusammenhänge zwischen der greifbaren Realraum-Darstellung der Kegelstrahl-Geometrie und ihrer technisch relevanten Beschreibung mittels homogener Koordinaten und Projektionsmatrizen gegeben. Aufbauend auf diesen Grundlagen wird eine neue Methode zur Auto-Kalibration entwickelt, die die praktische Bestimmung von perspektivischen Abbildungsgeometrien unter minimalen Anforderungen an die experimentelle Ausführung ermöglicht. Passend dazu wird eine verallgemeinerte Formulierung des weit verbreiteten Feldkamp-Algorithmus gegeben, um eine schnelle und flexible Volumenrekonstruktion aus beliebigen tomographischen Bildgebungsgeometrien zu ermöglichen. Iterative Rekonstruktionsverfahren werden ebenfalls für allgemeine Aufnahmegeometrien eingeführt, wobei ein Schwerpunkt auf der effizienten Berechnung des mit der tomographischen Bildgebung assoziierten Vorwärtsproblems liegt. Zu diesem Zweck wird eine hochperformante 3D-Erweiterung des klassischen, linear interpolierenden Linienintegrationsalgorithmus von Joseph entwickelt und mit typischen Alternativen verglichen. In Bezug auf die anisotrope Bildmodalität, die die Grundlage der Tensortomographie bildet, wird der Röntgen-Dunkelfeld-Kontrast umfassend besprochen. Die vorhandende Literatur wird dazu in einen gemeinsamen Kontext und eine gemeinsame Nomenklatur gebracht und mit neuen Überlegungen zu einer konsistenten Darstellung der Theorie zur Dunkelfeldsignalentstehung vervollständigt. Zentrale Ergebnisse werden dabei explizit anhand experimenteller Daten verifiziert, wobei besonders die Tomographie und die Eigenschaften anisotroper, faseriger Streuer im Vordergrund stehen. Um die ausgeprägte Empfindlichkeit interferometrischer Bilder auf feinste mechanische Instabilitäten zu kompensieren, wird ein effizientes Optimierungsverfahren zur Auswertung der Rohdaten aus Talbot-Interferometern entwickelt. Schließlich wird die Anwendbarkeit von linearen Tensor-Modellen in Bezug auf die hergeleiteten Anisotropie-Eigenschaften des Dunkelfeld-Kontrastes diskutiert, und ein iteratives Verfahren für die Rekonstruktion tensorwertiger Volumen aus Projektionsbildern vorgeschlagen. Die entwickelten Methoden werden effizient implementiert und auf Proben aus faserverstärktem Kunstoff angewandt, die dafür an der Bildgebungs-Strahllinie ID19 des Europäischen Synchrotrons ESRF abgebildet wurden. Die Ergebnisse stellen eine bisher einmalige Demonstration von Röntgen-Dunkelfeld-Tensor-Tomographie mit einem Sichtfeld von 3-4cm dar, wobei lokale Faserorientierung sowohl für komplex geformte als auch kontrastarme Objekte mit einer räumlichen Auflösung von 0.1mm in 3D dargestellt werden kann. Ein unabhängiger Vergleich mit Mikro-CT basierter Faser-Analyse bestätigt die Ergebnisse.

Abstract

X-ray dark-field imaging allows to resolve the conflict between the demand for centimeter scaled fields of view and the spatial resolution required for the characterization of fibrous materials structured on the micrometer scale. It draws on the ability of X-ray Talbot interferometers to provide full field images of a sample's ultra small angle scattering properties, bridging a gap of multiple orders of magnitude between the imaging resolution and the contrasted structure scale. The correspondence between shape anisotropy and oriented scattering thereby allows to infer orientations within a sample's microstructure below the imaging resolution. First demonstrations have shown the general feasibility of doing so in a tomographic fashion, based on various heuristic signal models and reconstruction approaches. Here, both a verified model of the signal anisotropy and a reconstruction technique practicable for general imaging geometries and large tensor valued volumes is developed based on in-depth reviews of dark-field imaging and tomographic reconstruction techniques.

To this end, a wide interdisciplinary field of imaging and reconstruction methodologies is revisited. To begin with, a novel introduction to the mathematical description of perspective projections provides essential insights into the relations between the tangible real space properties of cone beam imaging geometries and their technically relevant description in terms of homogeneous coordinates and projection matrices. Based on these fundamentals, a novel auto-calibration approach is developed, facilitating the practical determination of perspective imaging geometries with minimal experimental constraints. A corresponding generalized formulation of the widely employed Feldkamp algorithm is given, allowing fast and flexible volume reconstructions from arbitrary tomographic imaging geometries. Iterative reconstruction techniques are likewise introduced for general projection geometries, with a particular focus on the efficient evaluation of the forward problem associated with tomographic imaging. A highly performant 3D generalization of Joseph's classic linearly interpolating ray casting algorithm is developed to this end and compared to typical alternatives. With regard to the anisotropic imaging modality required for tensor tomography, X-ray dark-field contrast is extensively reviewed. Previous literature is brought into a joint context and nomenclature and supplemented by original work completing a consistent picture of the theory of dark-field origination. Key results are explicitly validated by experimental data with a special focus on tomography as well as the properties of anisotropic fibrous scatterers. In order to address the pronounced susceptibility of interferometric images to subtle mechanical imprecisions, an efficient optimization based evaluation strategy for the raw data provided by Talbot interferometers is developed. Finally, the fitness of linear tensor models with respect to the derived anisotropy properties of dark-field contrast is evaluated, and an iterative scheme for the reconstruction of tensor valued volumes from projection images is proposed. The derived methods are efficiently implemented and applied to fiber reinforced plastic samples, imaged at the ID19 imaging beamline of the European Synchrotron Radiation Facility. The results represent unprecedented demonstrations of X-ray dark-field tensor tomography at a field of view of 3-4cm, revealing local fiber orientations of both complex shaped and low-contrast samples at a spatial resolution of 0.1mm in 3D. The results are confirmed by an independent micro CT based fiber analysis.

Contents

List of Figures . . . vi
List of Algorithms . . . vii

Introduction **1**

1 Fundamentals of Volume Reconstruction in Cone Beam Computed Tomography **3**
1.1 Perspective projections and their parametrization . . . 3
1.1.1 Vector algebra representation . . . 3
1.1.2 Projection matrices and homogeneous coordinates . . . 5
1.1.3 Relation to the classic understanding of projection matrices . . . 5
1.1.4 Example: Ideal cone-beam geometry in classic parametrization . . . 7
1.1.5 Special cases: parallel beam and fan beam projection geometries . . . 7
1.1.6 Conversion of projection matrices to real space geometries . . . 9
1.1.7 Homographies . . . 10
1.1.7.1 Transformation of the detection plane (Rectification) . . . 11
1.1.7.2 Object motion estimation . . . 12
1.2 Volume Reconstruction . . . 13
1.2.1 Analytic reconstruction: Filtered Backprojection and FDK . . . 13
1.2.2 Generalized formulation of the Wang-FDK algorithm . . . 15
1.2.3 Iterative Volume Reconstruction . . . 17
1.2.3.1 Algebraic and Simultaneous Algebraic Reconstruction Techniques 17
1.2.3.2 Practical formulation of SART . . . 19
1.2.3.3 Other approaches and general considerations . . . 19

2 Perspective Volume Projection **21**
2.1 Literature Review . . . 22
2.2 Branchless generalized Joseph projector . . . 24
2.2.1 Driving axis aligned grid traversal . . . 24
2.2.2 Interpolated sampling . . . 24
2.3 Benchmarks . . . 28
2.3.1 Quality of projection images . . . 28
2.3.2 Quality of iterative tomographic reconstructions . . . 29
2.3.3 Projection speed . . . 30
2.4 Discussion and Conclusion . . . 31

3 Auto-Calibration of Cone Beam Projection Geometries **33**
3.1 Classification of approaches based on fiducial markers . . . 33
3.2 Review of previous auto-calibration techniques . . . 34
3.3 Formalization of the calibration task . . . 36
3.4 Projective ambiguities . . . 38
3.4.1 Detector pixel aspect ratio . . . 40
3.4.2 Detector tilt and shear . . . 41
3.5 Simulation Study . . . 42
3.6 Discussion . . . 44
3.7 Appendix: Implementation . . . 46
3.7.1 Iterative projection matrix reconstruction . . . 46
3.7.2 Extraction of the trajectories' sinusoid parameters . . . 48

4 Talbot-Lau Imaging **53**
4.1 Grating Interferometer . . . 53
4.2 Image Extraction from Phase Stepping Series . . . 55
4.2.1 Sinusoid Fitting and Fourier Analysis . . . 55
4.2.2 Phase stepping analysis in the presence of motion imprecisions . . . 58
4.3 Noise properties of grating interferometric images . . . 60
4.3.1 Noise variance of the stepping curve's sinusoid parameters . . . 60
4.3.2 Noise variance of the dark-field image . . . 61
4.3.3 Asymptotic properties of dark-field noise variance . . . 62
4.3.4 Systematic errors in phase stepping analysis . . . 63
4.4 Dark-field Contrast Interpretation . . . 64
4.4.1 Visibility reduction by Gaussian point spread . . . 64
4.4.2 Linear diffusion interpretation . . . 65
4.4.3 Ab initio derivation of visibility reduction . . . 65
4.4.4 Relation to the linear diffusion interpretation . . . 66
4.4.5 Magnification and Fresnel scaling in cone beam geometry . . . 67
4.4.6 Relation to Small Angle Scattering . . . 69
4.4.7 Superposition of dark-field signals . . . 70
4.5 Dark-field tomography . . . 71
4.5.1 Experimental verification of distance and structure size effects . . . 71
4.5.2 Quantitative dark-field tomography despite distance dependence . . . 74
4.6 Anisotropic Dark-field Contrast . . . 77
4.6.1 Literature review . . . 77
4.6.2 Gaussian ellipsoid model of anisotropic scatterers . . . 77
4.6.2.1 Scattering cross section . . . 78
4.6.2.2 Autocorrelation function . . . 79
4.6.3 Model of dark-field contrast anisotropy . . . 80
4.6.4 Experimental confirmation . . . 81

5 X-Ray Dark-Field Tensor Tomography **85**
5.1 Literature reviewr . . . 85
5.2 Nested iterative tomographic reconstruction . . . 86
5.3 Tensor as linear anisotropy model . . . 87
5.4 Experiment . . . 92
5.5 Discussion of Results . . . 93

Conclusion **101**

Publications **102**

Acknowledgemends **104**

Bibliography **105**

List of Figures

1.1 Sketch of the cone beam projection geometry. 4
1.2 Illustrations of parallel beam and stacked fan beam projection geometries. 8
1.3 Rectification of projection images. 11
1.4 Illustration of reconstruction processes using the Shepp-Logan head phantom. . . . 13
1.5 Sketches of ideal and slanted fan-beam acquisition geometries with a flat detector. 14

2.1 Ray casting through a volume along a line defined by two points. 25
2.2 One dimensional examples of linear and spline interpolation kernels. 25
2.3 Illustration of rays piercing 4-voxel planes perpendicular to different driving axes and corresponding interpolation scheme. 25
2.4 Approximation errors of different projection algorithms for a 10° conebeam geometry. 28
2.5 Axial and sagittal central slices of iterative SART reconstructions from analytic projections of the modified Shepp Logan phantom using different numeric projection methods within the iterative process. 29

3.1 Projections of fiducial markers moving along circular trajectories about the rotational axis (center) of a cone beam computed tomography setup, projected by a point source onto a planar detector. 36
3.2 Depiction of the real space geometry description used here. 37
3.3 Examples of projective ambiguity. 39
3.4 Examples of simulated projections of rotating fiducial markers as used to quantify the auto calibration precision. 42
3.5 Normalized histograms (probability densities) showing calibration variances in terms of classic geometry parameters found for projection geometries reconstructed from noisy projections of circular trajectories. 43
3.6 Sketches depicting the employed geometry parametrization. 43

4.1 Sketch of a Talbot-interferometer and phase stepping curve. 54
4.2 Example experimental data from a Talbot-Lau interferometer 57
4.3 Example material thickness dependent signal-to-noise ratio for attenuation and dark-field contrast. 62
4.4 Comparison of experimental data acquired in cone beam geometry by M. Chabior with the Yashiro-Lynch model under consideration of Fresnel scaling and a generic exponential autocorrelation model. 67
4.5 Experimental data on the dependence of dark-field contrast both on the distance between sample and analyzer grating G_2 and on the structure size. 72
4.6 Tomographic reconstructions of a cylindrical sample container comprising nine capillaries filled with spherules of varying diameter between 0.25µm and 80µm from absorption and dark-field projections acquired in parallel beam geometry. 75
4.7 Evaluation of the dark-field contrast after tomographic reconstruction. 75
4.8 Illustration of the projection of a Gaussian mass density distribution along the optical axis and effect of reduced pixel size. 78
4.9 Two dark-field image series of a pack of three carbon fiber reinforced rods rotating about the vertical image axis over a range of 180° at different inclinations. 81

4.10 Dark-field signals (negative logarithm of visibility) for different fiber orientations in the large pixel and small pixel cases. 83
4.11 Comparison of model and data for the classic case of fibers perpendicular to the optical axis. 83

5.1 Illustration of nesting additional projection and backprojection operations at the voxel level. 88
5.2 Spatial representation of the anisotropic dark-field signal of a fiber object and a respective tensor model fit. The experimental data is here represented on a unit sphere defined by the optical paths or grating normals. 90
5.3 Spatial representation of the anisotropic dark-field signal of a fiber object and a respective tensor model fit analog to Fig. 5.2. The data is here represented on a unit sphere defined by the grating sensitivity orientations. 90
5.4 Systematic comparison of approximative dark-field models $\hat{\boldsymbol{n}}\boldsymbol{T}_{(\boldsymbol{n})}\hat{\boldsymbol{n}}$ and $\hat{\boldsymbol{e}}\boldsymbol{T}_{(\boldsymbol{e})}\hat{\boldsymbol{e}}$ to the physical model $\mu_{\mathrm{DF}}(\boldsymbol{T}, \hat{\boldsymbol{n}}, \hat{\boldsymbol{e}})$ (Eq. 4.52) and its Gaussian mass distribution tensor $\boldsymbol{T}$ (Eq. 4.41) in analogy to the selective experiments shown in Figs. 5.2–5.3 91
5.5 Illustration of a 13-faced polyhedral sample cage for anisotropic X-ray dark-field tensor tomography with an example cubic sample and the resulting feasible scanning trajectories about the sample. 91
5.6 Diagrammatic representation of the acquisition and processing workflow for the generation of tensor valued volume reconstructions of anisotropic dark-field signals. 93
5.7 Example projection images for both considered samples. 94
5.8 Injection molded fiber reinforced plastic samples considered here for X-ray dark-field tensor tomography. 95
5.9 Depiction of the reconstructed tensor components for a single slice. 95
5.10 Tensor tomography of an injection molded cellulose fiber reinforced sample. 95
5.11 Illustrations of dominant fiber orientation, tensor anisotropy and mean eigenvalue for two different tensor tomographic reconstructions of a glass fiber reinforced sample. 97
5.12 Results from classic fiber orientation tensor analysis based on micro CT images resolving the actual fibers. 97
5.13 Angular deviations between tensor tomography ($\boldsymbol{T}_{(\boldsymbol{n})}$) and micro CT reference. . . 98
5.14 Angular deviations between tensor tomography ($\boldsymbol{T}_{(\boldsymbol{e})}$) and micro CT reference. . . 98

List of Algorithms

1.1 Deduction of real space geometry descriptions from projection matrices. 9
1.2 Generalized formulation of the Wang-Feldkamp-Davies-Kress algorithm for tomographic reconstruction from cone beam geometries. 16
1.3 Practical formulation of the simultaneous algebraic reconstruction technique. . . . 20
2.1 Branchless ray casting through a voxel volume with axis aligned sampling and first order interpolation among four nearest neighbors. 27
3.1 Self-consistent reconstruction of projection matrix and marker coordinates from projections of circular marker trajectories. 47
3.2 Extraction of circular trajectories' sinusoid parameters as required for Algorithm 3.1 from perspective projections. 51
4.1 Iterative reconstruction of phase stepping curves' parameters and the actual phase steps. 59
5.1 Tensor-SART for the iterative reconstruction of tensor valued volumes from scalar projections. 88

Introduction

Tensor tomography describes the volume reconstruction of tensor fields from a large number of projections thereof. Its practical realization for X-rays draws on an extensive set of techniques from the field of volume reconstruction, plus a number of specific ones. Computed tomography has become an established, yet evolving instrument in both life and material sciences throughout the past 50 years, and a mathematician might be inclined to loose interest once learning that it can be, at its core, reduced to Fourier transformation. When turning from the blackboard to the experimental bench though, multiple practical challenges arise that eventually define the actual problem set beyond the fundamental question of solvability: foremost, it is the sheer amount of data that needs to be processed. With gigabytes commonly being the smallest unit, and hundreds of gigabytes not being untypical for advanced applications, a significant amount of time needs to be devoted to the design of efficient algorithms and processing strategies. The respective constraints thereby constantly evolve together with computing hardware. A further class of problems arises from the practical implementation of mathematical assumptions and the unavoidable deviations thereof, typically in the form of imperfect acquisition geometries and signal nonlinearities. The last class of problems is finally spanned by the specifics of tensor tomography and the required anisotropic contrast modality. Adding to this are, last but not least, the practical needs for hardware-optimized software engineering and development, experimental realization, and visual processing.

The central ingredient to X-ray tensor tomography beyond the algorithmic preliminaries is provided by the dark-field contrast obtained with Talbot or Talbot-Lau interferometers, which have seen considerable research interest over the past decade for their sensitivity to ultra small angle scattering originating from structures on the $10^{-6}\,\mathrm{m}$ to $10^{-4}\,\mathrm{m}$ scale at fields of view in the order of magnitude of $10^{-1}\,\mathrm{m}$. Due to its origin in scattering, X-ray dark-field contrast is in particular sensitive to variations in structure size, reflecting shape anisotropies and thus providing the anisotropic contrast modality required for tensor tomography. The processing of interferometric data and the properties and physical interpretation of the resulting image contrast thereby represent research topics in their own right that need to be addressed as well.

The present dissertation aims to provide concise yet thorough presentations of all aspects of tomographic reconstruction, dark-field imaging and experimental design developed and required towards the final objective of creating and interpreting tensor valued volume reconstructions of a sample's anisotropic ultra small angle scattering properties. Particular focus is thereby put on the identification of best practices based on in-depth literature reviews and validating experiments in order to provide a sound basis for the final applications that ultimately form the recognizable tip of a large iceberg of involved methodologies. Many aspects have also been motivated by related reconstruction problems in X-ray nano tomography, which has been a parallel focus throughout this work. A number of original solutions and insights have emerged in the course of this research, both with respect to the wider field of computed tomography and the emerging field of X-ray dark-field tensor tomography. The following text intends to provide a convenient handbook motivating, documenting and validating all central methods to the necessary level of detail as required for practical realizations of (tensor-) tomographic reconstructions, excluding only the technical topic of actual programming for and on dedicated graphics processors.

Chapter 1

Fundamentals of Volume Reconstruction in Cone Beam Computed Tomography

1.1 Perspective projections and their parametrization

Tomographic imaging has historically been discussed in terms of the Radon transform describing coplanar line integrals parametrized by a distance from the origin r and an orientation angle ω. Although this mathematically motivated formulation of (X-ray) projections is essential with regard to the derivation of image reconstruction formulas, it is however subsequently desirable to generalize the mathematical representation to typical imaging systems rather than to actually build systems according to a constrained mathematical model. It will turn out in the following Chapters that this is indeed both reasonable and beneficial in a wide range of scenarios and use cases.

Technically relevant X-ray imaging systems acquire line integrals along divergent paths (fan- and cone-beam geometries) intersecting at a common focal point (the X-ray source). A most general description of such perspective imaging geometries can be achieved by means of vectors characterizing the positions and orientation of focal point and projection plane (X-ray detector) relative to the considered field of view. Such a description can equivalently be formulated in terms of projection matrices mapping between homogeneous coordinates of projective spaces, which has a long history in the fields of computer graphics and computer vision, and has been partially adopted in cone beam tomography for the related calibration techniques known in the field of computer vision.

The following subsections will derive fundamental relations between vector geometry, perspective projections, and projection matrices. These relations will provide the basis for a very general formulation of tomographic reconstruction algorithms for arbitrary imaging geometries (Section 1.2 and later Chapters) as well as for the auto-calibration of respective geometries from projection images (Chapter 3). In contrast to the established discussion of projection matrices in terms of affine transformations from object space to a canonical camera space (cf. the textbook by Hartley and Zisserman [63]), they will here be derived from an explicit vectorial description of the camera within object space, providing important relations between both representations particularly with regard to motion estimation and geometry calibration. Parts of the following subsections are published together with Chapter 3 as [45].

1.1.1 Vector algebra representation

Let $\vec{s}$, $\vec{d}$, $\vec{H}$, $\vec{V}$ be vectors in a three dimensional euclidean space describing the positions of X-ray source ($\vec{s}$) and detector ($\vec{d}$) as well as the orientations and pitches of the detector's columns ($\vec{V}$) and rows ($\vec{H}$). The latter are not strictly required to be orthogonal, although they typically are in practice. The integration paths between focal point $\vec{s}$ and detector pixels (h, v) describing X-ray image formation (cf. Figure 1.1) can then be represented in the following way:

Sections 1.1.1–1.1.2 are published in adapted form as part of Graetz, Phys. Med. Biol. 2021 [45]

$$\vec{p}(h,v,w) = \vec{s} + w \underbrace{\left(\overbrace{(\vec{d} + h\vec{H} + v\vec{V})}^{\text{position of pixel } (h,v) \text{ in 3D space}} - \vec{s} \right)}_{\text{line orientation}}, \tag{1.1}$$

straight forwardly allowing to sample values of a given volume image at locations $\vec{p}(h,v,w)$ and integrate them with respect to the path coordinate w, yielding a two dimensional projection image indexed by h and v (cf. Chapter 2).

The backprojection operation within any tomographic reconstruction algorithm (cf. Section 1.2) requires the inverse relation, which is mapping a given point $\vec{p}$ (the location of a voxel) to coordinates (h,v) on the projection plane based on known vectors $\vec{s}$, $\vec{d}$, $\vec{H}$, $\vec{V}$ (i.e., $\vec{p}$ is projected onto the image plane). By choice of a more convenient representation of Eq. 1.1 introducing the auxiliary variables h' and v', the inversion becomes apparent:

$$\vec{p} = \vec{s} + \overbrace{w\,h}^{h'}\,\vec{H} + \overbrace{w\,v}^{v'}\,\vec{V} + w\,(\vec{d} - \vec{s}) \tag{1.2}$$

$$\vec{p} - \vec{s} = \left[\; \vec{H} \;\middle|\; \vec{V} \;\middle|\; \vec{d} - \vec{s} \;\right] \begin{bmatrix} h' \\ v' \\ w \end{bmatrix}$$

$$\begin{bmatrix} h' \\ v' \\ w \end{bmatrix} = \left[\; \vec{H} \;\middle|\; \vec{V} \;\middle|\; \vec{d} - \vec{s} \;\right]^{-1} \left[\vec{p} - \vec{s}\right] \tag{1.3}$$

$$\begin{bmatrix} h \\ v \end{bmatrix} = \frac{1}{w} \begin{bmatrix} h' \\ v' \end{bmatrix}. \tag{1.4}$$

By application of Cramer's rule, the explicit relations

$$h = \frac{\left[\vec{V} \times (\vec{d} - \vec{s})\right] \cdot (\vec{p} - \vec{s})}{\left[\vec{H} \times \vec{V}\right] \cdot (\vec{p} - \vec{s})} \qquad v = -\frac{\left[\vec{H} \times (\vec{d} - \vec{s})\right] \cdot (\vec{p} - \vec{s})}{\left[\vec{H} \times \vec{V}\right] \cdot (\vec{p} - \vec{s})} \tag{1.5}$$

are obtained, with the bracketed terms being constants of the imaging configuration (i.e. independent of $\vec{p}$), and $(\vec{p} - \vec{s})$ characterizing the orientation of the path through source $\vec{s}$ and a given point $\vec{p}$.

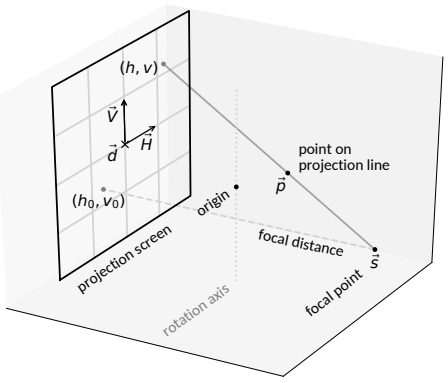

Figure 1.1: Sketch of the cone beam projection geometry. The locations of focal point and detection plane are given by $\vec{s}$ and $\vec{d}$. The row and column vectors $\vec{H}$ and $\vec{V}$ describe both the orientation of the detection plane and its 2D coordinate system (h,v). The orthogonal line between source and projection plane intersects at (h_0, v_0). Depending on the task, either $\vec{p}(h,v,w)$ or $h(\vec{p}), v(\vec{p})$ is to be calculated given a set of vectors $\vec{s}, \vec{d}, \vec{H}, \vec{V}$. For tomography applications, the projection system will be further rotated about a rotation axis, that will typically be aligned (approximately) parallel to $\vec{V}$.

Sections 1.1.1–1.1.2 are published in adapted form as part of Graetz, Phys. Med. Biol. 2021 [45]

1.1.2 Projection matrices and homogeneous coordinates

The solution to the mapping $\vec{p} \to (h, v)$ just given in Eqs. 1.3–1.5 can be further reformulated to reproduce the projection matrix formalism commonly used in the field of computer graphics:

$$\overbrace{\begin{bmatrix} h' \\ v' \\ w \end{bmatrix}}^{\text{2D+1 homogeneous coordinate}} = \Big[\overbrace{\underbrace{\Big[\, \vec{H} \,\Big|\, \vec{V} \,\Big|\, \vec{d} - \vec{s} \,\Big]^{-1}}_{\boldsymbol{P}_{3\times3}} \Big| \underbrace{\Big[\, \vec{H} \,\Big|\, \vec{V} \,\Big|\, \vec{d} - \vec{s} \,\Big]^{-1} \big[-\vec{s}\big]}_{\boldsymbol{P}_4}}^{3\times4 \text{ projection matrix } \boldsymbol{P}} \Big] \overbrace{\begin{bmatrix} \vec{p} \\ 1 \end{bmatrix}}^{\text{3D+1 homogeneous coordinate}}, \tag{1.6}$$

where the remaining constant ($\vec{s}$) of the projection geometry has been included within the fourth column ($\boldsymbol{P}_4$) of the projection matrix $\boldsymbol{P}$. By means of the corresponding fourth component added to the to-be-projected point $\vec{p}$, the projection matrix formalism exactly reproduces Eq. 1.3 while absorbing all constants of the projection geometry within $\boldsymbol{P}$.

Eq. 1.6 is understood, in the fields of computer graphics and projective geometry, as a linear mapping between projective spaces, formalizing the necessity to divide h' and v' by the last component w (which here emerged from the particular relation defined by Eqs. 1.1 and 1.2) to the general concept of "homogeneous coordinates" holding an additional scaling component. Corresponding euclidean coordinates are, by definition, obtained from the remaining components divided by the scaling component. Obviously, the constructed vector $(\vec{p}, 1)$ can be understood in these terms. Homogeneous coordinates are thus invariant with respect to arbitrary non-zero scalings, i.e., $(p_1, p_2, p_3, 1)$ and $(\alpha p_1, \alpha p_2, \alpha p_3, \alpha)$ describe (for $\alpha \neq 0$) identical points yielding identical projections (h, v). Analogously, the projection results are invariant with respect to the absolute scale of $\boldsymbol{P}$.

By applying Cramer's rule to Eq. 1.6, an explicit expression of $\boldsymbol{P}$ in terms of the vectors $\vec{s}$, $\vec{d}$, $\vec{V}$, $\vec{H}$ can be given:

$$\begin{aligned} \boldsymbol{P} &= \alpha \left[\begin{array}{c|c} (\vec{V} \times (\vec{d} - \vec{s}))^T & -(\vec{V} \times \vec{d}) \cdot \vec{s} \\ -(\vec{H} \times (\vec{d} - \vec{s}))^T & (\vec{H} \times \vec{d}) \cdot \vec{s} \\ (\vec{H} \times \vec{V} \quad)^T & -(\vec{H} \times \vec{V}) \cdot \vec{s} \end{array}\right] \\ \text{with} \quad \alpha &= \det\Big(\Big[\, \vec{H} \,\Big|\, \vec{V} \,\Big|\, \vec{d} - \vec{s} \,\Big]\Big)^{-1} = \Big((\vec{H} \times \vec{V}) \cdot (\vec{d} - \vec{s})\Big)^{-1}, \end{aligned} \tag{1.7}$$

where the determinant α can, due to the invariance of projections with respect to the absolute scale of $\boldsymbol{P}$, be dropped for all practical purposes. It is here explicitly included for completeness and consistency with Eq. 1.6. The above representation, when applied to $(\vec{p}, 1)$, will reproduce Eq. 1.5. Most obviously, Eq. 1.7 reveals that the third row of $\boldsymbol{P}$ provides direct information on the detector normal and the distance of the focal point from the origin. The inverse relation $\boldsymbol{P} \to \vec{s}, \vec{d}, \vec{H}, \vec{V}$ will be derived in Section 1.1.6.

1.1.3 Relation to the classic understanding of projection matrices

Usually, the projection matrix is represented in completely different terms, which shall be briefly outlined here due to their wide adoption. The classic derivation employed in the field of computer graphics (cf. the book by Hartley and Zissermann [63]) begins, instead of a system of equations, with a canonical camera coordinate system with the focal point at the origin, the optical axis along z and an orthonormal projection plane $(x, y, z = 1)$ at $z = 1$. Based on the intercept theorem, the perspective projection of any point (p_x, p_y, p_z) onto this plane is then directly given by $(\frac{p_x}{p_z}, \frac{p_y}{p_z})$. As previously, the point can as well be generalized as homogeneous vector (wp_x, wp_y, wp_z, w), resulting in identical projections $(\frac{wp_x}{wp_z}, \frac{wp_y}{wp_z}) = (\frac{p_x}{p_z}, \frac{p_y}{p_z})$. In order to define an independent planar coordinate system on the detection screen as well as to change the relative scale, orientation and position of the projected objects, an upper triangular 3×3 camera calibration matrix $\boldsymbol{C}$, a unitary 3D rotation matrix $\boldsymbol{R}$ and the 3D translation vector $\vec{t}$ are introduced, such that

$$\boldsymbol{P} = \big[\underbrace{\boldsymbol{C}\boldsymbol{R}}_{\boldsymbol{P}_{3\times3}} \big| \underbrace{\boldsymbol{C}\vec{t}}_{\boldsymbol{P}_4} \big]. \tag{1.8}$$

Sections 1.1.1–1.1.2 are published in adapted form as part of Graetz, Phys. Med. Biol. 2021 [45]

By application of $\boldsymbol{P}$ to a homogeneous vector (wp_x, wp_y, wp_z, w), an euclidean point (p_x, p_y, p_z) is first rotated by $\boldsymbol{R}$ about the origin (which coincides with the focal point), then translated by $\vec{t}$ to its relative position with respect to the focal point, and then scaled and sheared by $\boldsymbol{C}$ prior to actual projection by means of the intercept theorem (i.e, by means of division by the last component). $\boldsymbol{C}$ further effects a final translation on the projection screen, corresponding to the freedom of choice of the origin of its 2D coordinate system.

I.e., projection matrices are generally understood in terms of operations transforming points of the field of view into a canonical camera coordinate system as opposed to vectors describing the camera relative to the field of view.

$\boldsymbol{R}$ and $\vec{t}$ are referred to as "extrinsic" parameters defining the camera position relative to the coordinate system of an object, while $\boldsymbol{C}$ characterizes the "intrinsic" camera parameters: focal distance, origin and shear of the projection grid.

A formal decomposition of $\boldsymbol{P}$ will show the relations among both parametrizations. To this end, QR decomposition is commonly applied to $\boldsymbol{P}_{3\times3} = \boldsymbol{C}\boldsymbol{R}$, which by definition decomposes quadratic matrices into the product of a triangular and a unitary matrix. Once $\boldsymbol{C}$ and $\boldsymbol{R}$ have been determined, the remaining parameter $\vec{t}$ is given by $\vec{t} = \boldsymbol{C}^{-1}\boldsymbol{P}_4$, as a direct consequence of Eq. 1.8.

The parameters $\boldsymbol{C}$ and $\vec{t}$ are then, considering Eq. 1.6, given by

$$\begin{aligned} \boldsymbol{C} = \boldsymbol{P}_{3\times3}\boldsymbol{R}^{-1} &= \left[\ \boldsymbol{R}\vec{H}\ \middle|\ \boldsymbol{R}\vec{V}\ \middle|\ \boldsymbol{R}(\vec{d}-\vec{s})\ \right]^{-1} \\ \vec{t} = \boldsymbol{C}^{-1}\boldsymbol{P}_4 \quad &= -\boldsymbol{R}\vec{s}\,. \end{aligned} \tag{1.9}$$

$\boldsymbol{C}$ generally is of the upper triangular form

$$\boldsymbol{C} = \alpha \begin{bmatrix} f_\mathrm{h} & s & h_0 \\ 0 & f_\mathrm{v} & v_0 \\ 0 & 0 & 1 \end{bmatrix} \tag{1.10}$$

with some arbitrary absolute scale α. The individual components can be interpreted (cf. [63]) as focal lengths (distance between focal point and projection screen) f_h and f_v in units of pixel width and height, shear s and the intersection of the orthogonal line between source and detector with the detector coordinate system at $(h = h_0, v = v_0)$. s is non-zero only for non-orthogonal detector grids (i.e., when $\vec{H}\cdot\vec{V} \neq 0$), and the focal lengths f_h and f_v are analogously of equal magnitude in the case of square pixels.

Given the vectorial geometry description introduced previously, the rotation matrix $\boldsymbol{R}$ may be explicitly constructed based on the known properties of the canonical camera system, i.e., that the canonical projection screen's normal is oriented along z, and its rows along x. With the normal orientation being given by $\vec{H}\times\vec{V}$ and the row's direction by $\vec{H}$, the rotation matrix can be straight forwardly constructed:

$$\vec{R_3} = \frac{\vec{H}\times\vec{V}}{\left\|\vec{H}\times\vec{V}\right\|};\quad \vec{R_1} = \frac{\vec{H}}{\left\|\vec{H}\right\|};\quad \vec{R_2} = \frac{\vec{R_3}\times\vec{R_1}}{\left\|\vec{R_3}\times\vec{R_1}\right\|};\quad \boldsymbol{R} = \begin{bmatrix} \vec{R_1}^{\,T} \\ \vec{R_2}^{\,T} \\ \vec{R_3}^{\,T} \end{bmatrix}. \tag{1.11}$$

The remaining row $\vec{R_2}$ is constructed orthogonal to $\vec{R_1}$ and $\vec{R_3}$ in order to obtain a valid rotation matrix (i.e., a unitary matrix).

For the common case of rectangular or square pixels (i.e., $\vec{H}\cdot\vec{V} = 0$ and thus $s = 0$), the above results will then reduce to:

$$\begin{aligned} f_\mathrm{h} &= \frac{(\vec{H}\times\vec{V})\cdot(\vec{d}-\vec{s})}{\left\|\vec{H}\right\|^2\left\|\vec{V}\right\|} & h_0 &= -\vec{H}\cdot(\vec{d}-\vec{s})/\left\|\vec{H}\right\|^2 \\ & & & \qquad \text{for } \vec{H}\cdot\vec{V} = 0 \\ f_\mathrm{v} &= \frac{(\vec{H}\times\vec{V})\cdot(\vec{d}-\vec{s})}{\left\|\vec{H}\right\|\ \left\|\vec{V}\right\|^2} & v_0 &= -\vec{V}\cdot(\vec{d}-\vec{s})/\left\|\vec{V}\right\|^2. \end{aligned} \tag{1.12}$$

1.1.4 Example: Ideal cone-beam geometry in classic parametrization

In order to illustrate the relation of the general results given by Eqs. 1.5–1.7 to typical explicit formulas in terms of focal distance and projection angle found in literature, an ideal cone-beam geometry shall be explicitly constructed from a rotation angle ω, the focus–object distance FOD, the focus–detector distance FDD and the detector pixel size Δp:

$$\vec{s} = -\mathrm{FOD}\begin{bmatrix}-\sin(\omega)\\ \cos(\omega)\\ 0\end{bmatrix}, \quad \vec{d} = (\mathrm{FDD}-\mathrm{FOD})\begin{bmatrix}-\sin(\omega)\\ \cos(\omega)\\ 0\end{bmatrix}, \quad \vec{H} = \Delta p\begin{bmatrix}\cos(\omega)\\ \sin(\omega)\\ 0\end{bmatrix}, \quad \vec{V} = \Delta p\begin{bmatrix}0\\ 0\\ 1\end{bmatrix}.$$

The projection coordinates (h, v) of a point $\vec{p} = (x, y, z)$ on the detection plane in units of detector pixels are then found, by means of Eqs. 1.5–1.6, to be:

$$\begin{bmatrix} h' \\ v' \\ w \end{bmatrix} = \underbrace{-\Delta p \begin{bmatrix} \mathrm{FDD}\cos(\omega) & \mathrm{FDD}\sin(\omega) & 0 & 0 \\ 0 & 0 & \Delta p\,\mathrm{FDD} & 0 \\ -\Delta p\sin(\omega) & \Delta p\cos(\omega) & 0 & \Delta p\,\mathrm{FOD} \end{bmatrix}}_{=\boldsymbol{P}} \begin{bmatrix} x \\ y \\ z \\ 1 \end{bmatrix}$$

$$h = \frac{h'}{w} = \frac{\mathrm{FDD}}{\Delta p}\frac{x\cos(\omega) + y\sin(\omega)}{\mathrm{FOD} - x\sin(\omega) + y\cos(\omega)}$$
$$v = \frac{v'}{w} = \frac{\mathrm{FDD}}{\Delta p}\frac{z}{\mathrm{FOD} - x\sin(\omega) + y\cos(\omega)},$$

corresponding to the typical expressions found e.g. in the textbook by Buzug [15].

1.1.5 Special cases: parallel beam and fan beam projection geometries

For completeness, also the cases of parallel and stacked fan beam projections as depicted in Figure 1.2 shall be briefly discussed. Parallel beam geometries typically occur at synchrotron imaging beamlines exhibiting extremely large focal distances, while stacked fanbeam geometries typically arise in line scanning configurations. They are, in different contexts, also referred to as orthographic projection and pushbroom geometry respectively. In contrast to regular perspective projections, these geometries do not exhibit a single focal point. The projection paths $\vec{p}(h, v, w)$ are rather characterized by a source point moving along with one or both of the detector rows and columns:

$$\text{fan beam:}\quad \vec{p}_{\mathrm{fb}}(h,v,w) = \overbrace{\vec{s}+v\vec{V}}^{\substack{\text{focal points}\\ \text{(fan beam)}}} + w\Big(\overbrace{(\vec{d}+v\vec{V}+h\vec{H})}^{\substack{\text{position of detector-}\\ \text{pixel } (h,v) \text{ in 3D space}}} - (\vec{s}+v\vec{V})\Big) = \vec{s}+v\vec{V}+\overbrace{w\,h}^{h'}\vec{H}+w\,(\vec{d}-\vec{s})$$

$$\text{parallel beam:}\quad \vec{p}_{\mathrm{pb}}(h,v,w) = \underbrace{\vec{s}+v\vec{V}+h\vec{H}}_{\substack{\text{"focal points"}\\ \text{(parallel beam)}}} + w\Big(\overbrace{(\vec{d}+v\vec{V}+h\vec{H}) - (\vec{s}+v\vec{V}+h\vec{H})}^{\text{line orientation}}\Big) = \vec{s}+v\vec{V}+\quad h\,\vec{H}+w(\vec{d}-\vec{s}).$$

Analog to Eqs. 1.1–1.4, the inverses are found to be

$$\begin{array}{ll} \text{fan beam:} & \text{parallel beam:} \\ \begin{bmatrix} h' \\ v \\ w \end{bmatrix} = \boldsymbol{P}\begin{bmatrix} \vec{p} \\ 1 \end{bmatrix} & \begin{bmatrix} h \\ v \\ w \end{bmatrix} = \boldsymbol{P}\begin{bmatrix} \vec{p} \\ 1 \end{bmatrix}, \\ \begin{bmatrix} h \\ v \end{bmatrix} = \begin{bmatrix} \frac{h'}{w} \\ v \end{bmatrix} & \end{array} \tag{1.13}$$

with $\boldsymbol{P}$ according to Eqs. 1.6 and 1.7. They differ from the cone beam solution only in perspective scaling w on h and v, which expectedly is completely absent in the parallel beam case and only applies to the detector rows in the fan beam case. The absence of scaling with respect to one or both

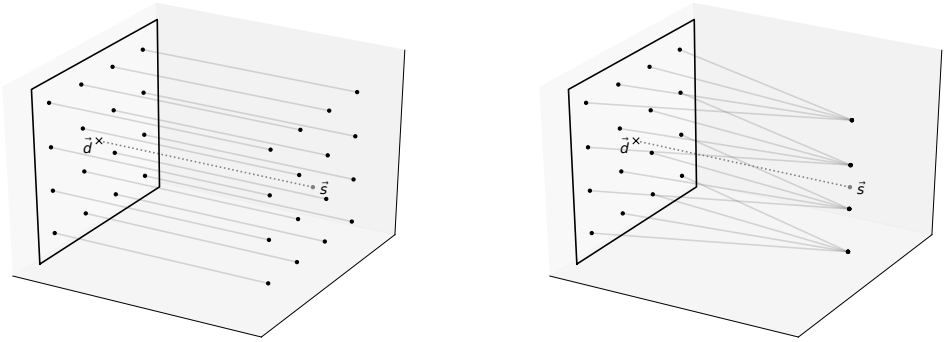

Figure 1.2: Illustrations of parallel beam (left) and stacked fan beam (right) projection geometries. While the former commonly arises as a limiting case of cone beam geometries with large focal lengths, the latter typically arises in the context of successive tomographic scans using a line detector.

detector dimensions implies that the homogeneous coordinate formalism isn't directly applicable. For the same reason, scaling invariance is broken for the projection matrix, as well as the vectors on the left and right hand side of the equation.

While the fan beam case indeed generally needs to be considered a special case with regard to the projection matrix formalism, a modified projection matrix can be formulated for the parallel beam case, embedding it into the homogeneous coordinate formalism again and restoring scaling invariance. As the w component in Eq. 1.13 (parallel case) is, in contrast to perspective projections, not used for the computation of (h, v), it may as well be exchanged with the determinant $(\vec{H} \times \vec{V}) \cdot (\vec{d} - \vec{s})$ (cf. Eq. 1.7) by means of the following modified projection matrix:

$$\boldsymbol{P}_{\mathrm{pb}} = \left[\begin{array}{ccc|c} \overbrace{\begin{array}{ccc} & & \\ (\vec{V} \times (\vec{d} - \vec{s}))^T & & \\ -(\vec{H} \times (\vec{d} - \vec{s}))^T & & \\ 0 & 0 & 0 \end{array}}^{\boldsymbol{P}_{\mathrm{pb}\,3\times3}} & \begin{array}{c} (\vec{V} \times \vec{d}\,) \cdot (\vec{d} - \vec{s}) \\ -(\vec{H} \times \vec{d}\,) \cdot (\vec{d} - \vec{s}) \\ (\vec{H} \times \vec{V}) \cdot (\vec{d} - \vec{s}) \end{array} \end{array}\right] \left[\begin{array}{c} p_x \\ p_y \\ p_z \\ 1 \end{array}\right], \tag{1.14}$$

such that

$$\left[\begin{array}{c} h'_{\mathrm{pb}} \\ v'_{\mathrm{pb}} \\ w_{\mathrm{pb}} \end{array}\right] = \boldsymbol{P}_{\mathrm{pb}} \left[\begin{array}{c} \vec{p} \\ 1 \end{array}\right]$$
$$\left[\begin{array}{c} h_{\mathrm{pb}} \\ v_{\mathrm{pb}} \end{array}\right] = \frac{1}{w_{\mathrm{pb}}} \left[\begin{array}{c} h_{\mathrm{pb}} \\ v_{\mathrm{pb}} \end{array}\right].$$

The correct scaling of (h, v) is now, as for perspective projections, achieved by division of the projected vector by its last component, which is here, in contrast to perspective projections, invariant with respect to the projected point $\vec{p}$.

Other properties of perspective projection matrices are broken though for $\boldsymbol{P}_{\mathrm{pb}}$. Most obviously, $\boldsymbol{P}^{-1}_{\mathrm{pb}\,3\times3}$ is undefined. As the actual focal point for the orthographic projection lies at infinity, the "source point" $\vec{s}$ rather serves the purpose of defining the projection direction $\vec{d} - \vec{s}$ (cf. Fig. 1.2). This has been consequently transferred into the explicit representation of $\boldsymbol{P}_{\mathrm{pb}}$ by means of the vector algebra identity $(\vec{a} \times \vec{b}) \cdot \vec{b} = 0$.

1.1.6 Conversion of projection matrices to real space geometries

Both with respect to calculating volume projection images based on the forward problem defined in Eq. 1.1 (cf. Chapter 2), as well as with respect to real space interpretations of the geometry encoded within a projection matrix (cf. Chapter 3 on projection geometry calibration), the conversion of projection matrices to real space vectors is of interest and shall therefore be derived here.

Based on the representations given in Eqs. 1.6 and 1.8, the relations

$$\vec{s} = -\boldsymbol{P}_{3\times3}^{-1}\boldsymbol{P}_4 \quad (= -\boldsymbol{R}^T\vec{t}) \tag{1.15}$$

can be directly inferred, with $\vec{s}$ being the focal point of the projection. As can be easily verified, Eq. 1.15 is invariant with respect to the absolute scale of $\boldsymbol{P}$ (equivalently, it is invariant with respect to the absolute scale of $\boldsymbol{C}$ within $\boldsymbol{P}$, cf. Eq. 1.8).

The remaining vectors $\vec{H}$, $\vec{V}$ and $\vec{d}$ are, in contrast, related to the absolute scale of $\boldsymbol{P}$. The ambiguity corresponds to the fact that projections in the coordinate system of the detection screen are invariant under a proportional change of scale and distance of that screen, as well as under reflection through the focal point. In order to recover the screen's actual scale from an arbitrarily normalized matrix $\boldsymbol{P}$, prior knowledge such as the true pixel pitch $\left\|\vec{H}\right\|$ or $\left\|\vec{V}\right\|$ and the screen's orientation with respect to $\vec{s}$ needs to be incorporated. Nevertheless, a valid preliminary set of equivalent vectors $\vec{H}'$, $\vec{V}'$ and $\vec{d}'$ reproducing a given projection matrix $\boldsymbol{P}$ can generally be obtained irrespective of the original system dimensions based on Eqs. 1.6 and 1.15:

$$\left[\ \vec{H}' \ \middle|\ \vec{V}' \ \middle|\ \vec{d}' - \vec{s}\ \right] = \boldsymbol{P}_{3\times3}^{-1} \tag{1.16}$$

Based on the assumption typical to X-ray imaging that $(\vec{d} - \vec{s}) \cdot \vec{s} < 0$, i.e., that the focal point never lies between the projected field of view and the projection screen, and further assuming the pixel pitches $\left\|\vec{H}\right\|$ and $\left\|\vec{V}\right\|$ to be known, Equations 1.15 and 1.16 may be completed to Alg. 1.1:

Algorithm 1.1 Deduction of real space geometry descriptions from projection matrices. The factor $\mathrm{sign}((\vec{d}' - \vec{s}) \cdot \vec{s})$ resolves the point symmetry of perspective projections, while knowledge of the true pixel pitches $\left\|\vec{H}\right\|$ and $\left\|\vec{V}\right\|$ allows to resolve the arbitrary scale of $\boldsymbol{P}$. The geometric mean over both pixel pitches is meaningful in the presence of noise on $\vec{H}'$ and $\vec{V}'$, as will be the case when $\boldsymbol{P}$ is actually determined from experimental data instead of being explicitly constructed (cf. Chapter 3).

$$\begin{aligned}
\vec{s} &= -\boldsymbol{P}_{3\times3}^{-1}\boldsymbol{P}_4 \\
\left[\ \vec{H}' \ \middle|\ \vec{V}' \ \middle|\ \vec{d}' - \vec{s}\ \right] &= \ \ \boldsymbol{P}_{3\times3}^{-1} \\
\left[\ \vec{H} \ \middle|\ \vec{V} \ \middle|\ \vec{d} - \vec{s}\ \right] &= -\mathrm{sign}((\vec{d}' - \vec{s}) \cdot \vec{s}) \sqrt{\frac{\left\|\vec{H}\right\|}{\left\|\vec{H}'\right\|}\frac{\left\|\vec{V}\right\|}{\left\|\vec{V}'\right\|}} \left[\ \vec{H}' \ \middle|\ \vec{V}' \ \middle|\ \vec{d}' - \vec{s}\ \right] \\
\vec{d} &= (\vec{d} - \vec{s}) + \vec{s}\,,
\end{aligned}$$

With respect to applications in auto-calibration (Chapter 3), it will be insightful to explicitly state the inverse $\boldsymbol{P}_{3\times3}^{-1}$ using Cramer's rule:

$$\begin{aligned}
\vec{H} \propto \quad & \vec{H}' = \ \ \alpha^{-1}\,(P_{21}, P_{22}, P_{23}) \times (P_{31}, P_{32}, P_{33}) \\
\vec{V} \propto \quad & \vec{V}' = -\alpha^{-1}\,(P_{11}, P_{12}, P_{13}) \times (P_{31}, P_{32}, P_{33}) \\
(\vec{d} - \vec{s}) \propto \quad & (\vec{d}' - \vec{s}) = \ \ \alpha^{-1}\,(P_{11}, P_{12}, P_{13}) \times (P_{21}, P_{22}, P_{23}) \\
& \alpha = \det \boldsymbol{P}_{3\times3} = [(P_{11}, P_{12}, P_{13}) \times (P_{21}, P_{22}, P_{23})] \cdot (P_{31}, P_{32}, P_{33}) \\
& \alpha^{-1} = \det \boldsymbol{P}_{3\times3}^{-1} = (\vec{H}' \times \vec{V}') \cdot (\vec{d}' - \vec{s}) \quad \text{(cf. also Eq. 1.7)}
\end{aligned} \tag{1.17}$$

Section 1.1.6 is published in adapted form as part of Graetz, Phys. Med. Biol. 2021 [45]

1.1.7 Homographies

Homography transformations are invertible transformations between projective spaces. Two kinds are of particular practical relevance here: 4×4 homography matrices transforming between two projective 3D spaces, and 3×3 homographies transforming between projective 2D planes. Given that, for the present purposes, 3D space generally refers to the object space before projection and 2D space to the image space after projection, 4×4 homographies are commonly required for object or camera manipulation (e.g. for the purpose of rotating a given projection geometry about a rotational axis in order to reproduce tomographic acquisition trajectories), and 3×3 homographies are required for image transformations, i.e., to retrospectively manipulate position and orientation of the projection screen (in some cases also referred to as "rectification", cf. Section 1.1.7.1).

With $\boldsymbol{x}$ and $\boldsymbol{y}$ denoting points in object space and screen space respectively, and $\boldsymbol{P}$ and $\boldsymbol{H}$ denoting projections and homographies respectively, the following typical situations can be identified:

$$\boldsymbol{y}_3 = \underbrace{\boldsymbol{P}_{3\times4}\overbrace{\boldsymbol{H}_{4\times4}\boldsymbol{x}_4}^{\boldsymbol{x}'_4}}_{\boldsymbol{P}'_{3\times4}} \tag{1.18}$$

$$\boldsymbol{y}_3 = \overbrace{\boldsymbol{P}_{3\times4}\underbrace{\boldsymbol{H}^{-1}_{4\times4}}_{=\boldsymbol{I}}\boldsymbol{H}_{4\times4}}^{\boldsymbol{P}'_{3\times4}}\overbrace{\boldsymbol{x}_4}^{\boldsymbol{x}'_4} \tag{1.19}$$

$$\boldsymbol{y}_3 = \underbrace{\boldsymbol{H}_{3\times3}\overbrace{\boldsymbol{P}_{3\times4}\boldsymbol{x}_4}^{\boldsymbol{x}_3}}_{=\boldsymbol{P}'_{3\times4}} \tag{1.20}$$

$$\boldsymbol{y}_3 = \underbrace{\boldsymbol{P}_{3\times4}\overbrace{\boldsymbol{D}_{4\times3}\boldsymbol{x}_3}^{\boldsymbol{x}_4}}_{=\boldsymbol{H}_{3\times3}} \,. \tag{1.21}$$

For clarity, the dimensions of all vectors and matrices are explicitly indicated. According to the homogeneous coordinate formalism (cf. Section 1.1.2), points in 3D object space comprise $3+1$ components (right hand side), and their 2D projections $2+1$ (left hand side). Eq. 1.18 describes the case of modifying (e.g. translating, scaling, rotating, or even shearing or warping) either the camera or the object using a 4×4 homography, depending on whether it is applied to $\boldsymbol{P}_{3\times4}$ or $\boldsymbol{x}_4$. Eq. 1.19 in contrast describes the case of simultaneous transformation of both camera and object while leaving the actual projections unchanged (cf. projective ambiguities, Chapter 3, Section 3.4). Eq. 1.20 describes a transformation after projection, which may be interpreted in multiple ways that will be discussed in the following Sections 1.1.7.1–1.1.7.2. Generally, it corresponds to a transformation of the projection plane, a case that is further explicitly considered in Eq. 1.21, with a matrix $\boldsymbol{D}_{4\times3}$ describing a plane in 3D space, and the product $\boldsymbol{D}_{4\times3}\,\boldsymbol{x}_3$ describing the 3D coordinates of 2D points $\boldsymbol{x}_3$ on that plane. By regrouping of the matrices, the transformation between both planes can be directly expressed by a 3×3 homography transforming between two projective 2D spaces. This case will be discussed in more detail in the following Section 1.1.7.1.

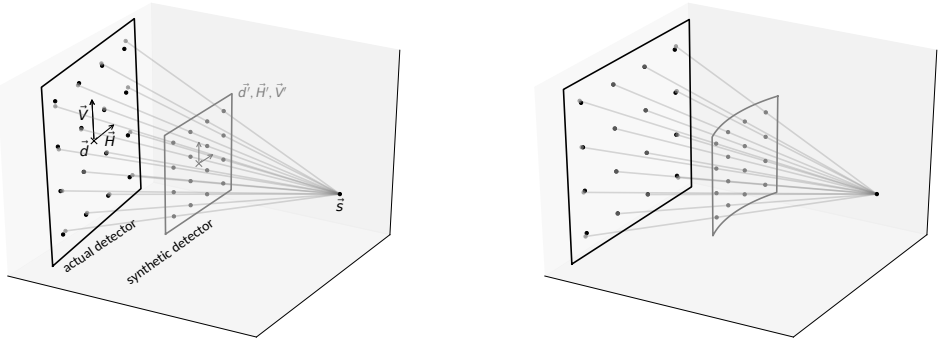

Figure 1.3: Rectification of projection images by means of projecting a synthetic sampling plane onto the original one (left). An image on the synthetic grid is obtained by interpolated sampling from the original grid at the projected coordinates. The concept may be extended to non-planar grids (right), although the corresponding coordinate transformations become non-linear, complicating in particular the inverse mapping (which is otherwise given by the inverse of the respective homography matrix)

1.1.7.1 Transformation of the detection plane (Rectification)

Rectification refers to the transformation of projection images to a different image plane that is more adequate in a given context. The image transformation involves both a homography mapping between two projective planes as well as resampling of discrete image data onto the desired synthetic grid. Given a known projection matrix $\boldsymbol{P}$ as well as a set of vectors $\vec{H}^{\mathrm{r}}$, $\vec{V}^{\mathrm{r}}$, $\vec{d}^{\mathrm{r}}$ characterizing the rows, columns and origin of the rectified image plane in euclidean space, the homography transform is found by formal projection of the synthetic grid (indexed by $h^{\mathrm{r}}, v^{\mathrm{r}}$) onto the original one (indexed by h, v) encoded in $\boldsymbol{P}$ (cf. Figure 1.3):

$$\begin{bmatrix} h'(h^{\mathrm{r}},v^{\mathrm{r}}) \\ v'(h^{\mathrm{r}},v^{\mathrm{r}}) \\ w(h^{\mathrm{r}},v^{\mathrm{r}}) \end{bmatrix} = \underbrace{\begin{bmatrix} P_{11} & P_{12} & P_{13} & P_{14} \\ P_{21} & P_{22} & P_{23} & P_{24} \\ P_{31} & P_{32} & P_{33} & P_{34} \end{bmatrix} \overbrace{\begin{bmatrix} H_1^r & V_1^r & d_1^{\mathrm{r}} \\ H_2^r & V_2^r & d_2^{\mathrm{r}} \\ H_3^r & V_3^r & d_3^{\mathrm{r}} \\ 0 & 0 & 1 \end{bmatrix}}^{\text{grid points on the synthetic image plane}}}_{\boldsymbol{H}^{\mathrm{r}}} \underbrace{\begin{bmatrix} h^{\mathrm{r}} \\ v^{\mathrm{r}} \\ 1 \end{bmatrix}}_{\text{indices on the synthetic grid}} \tag{1.22}$$

i.e.

$$\boldsymbol{H}^{\mathrm{r}} = \boldsymbol{P} \left[\begin{array}{c|c|c} \vec{H}^{\mathrm{r}} & \vec{V}^{\mathrm{r}} & \vec{d}^{\mathrm{r}} \\ 0 & 0 & 1 \end{array}\right] \tag{1.23}$$

and

$$\begin{bmatrix} h'(h^{\mathrm{r}},v^{\mathrm{r}}) \\ v'(h^{\mathrm{r}},v^{\mathrm{r}}) \\ w(h^{\mathrm{r}},v^{\mathrm{r}}) \end{bmatrix} = \boldsymbol{H}^{\mathrm{r}} \begin{bmatrix} h^{\mathrm{r}} \\ v^{\mathrm{r}} \\ 1 \end{bmatrix} \quad \text{with} \quad \begin{bmatrix} h \\ v \end{bmatrix} = \frac{1}{w} \begin{bmatrix} h' \\ v' \end{bmatrix} . \tag{1.24}$$

Using the relations $\boldsymbol{P} = [\, \boldsymbol{P}_{3\times3} \,|\, -\boldsymbol{P}_{3\times3}\, \vec{s}\,]$ and $\boldsymbol{P}_{3\times3} \propto [\vec{H}|\vec{V}|\vec{d}-\vec{s}\,]^{-1}$ (cf. Eq. 1.6), Eq. 1.23 can also be formulated as

$$\boldsymbol{H}^{\mathrm{r}} = \left[\begin{array}{c|c|c} \vec{H} & \vec{V} & \vec{d}-\vec{s} \end{array}\right]^{-1} \left[\begin{array}{c|c|c} \vec{H}^{\mathrm{r}} & \vec{V}^{\mathrm{r}} & \vec{d}^{\mathrm{r}}-\vec{s} \end{array}\right], \tag{1.25}$$

more explicitly revealing the exchange of projection planes.

In the context of cone beam computed tomography, one typical use case for image rectification is the resampling of projection data to a standard acquisition geometry expected by a given reconstruction algorithm. In particular non-iterative methods are often based on highly symmetric geometries describable by a minimal number of parameters. Similarly, motion compensation is a typical application.

1.1.7.2 Object motion estimation

In contrast to explicit construction, homography matrices may also be determined by comparison of pairs of different projection images of the same object. Multiple interpretations on the origin of the respective transformations can then be given. While, in analogy to the previous Section 1.1.7.1, a change of intrinsic camera properties may be assumed to be the cause of differences between two images, a change of extrinsic position parameters equivalently gives rise to observable image transformations. This relation thus allows to extract quantitative information on general object or camera displacements from image comparisons, allowing for a generalization of common motion correction algorithms applied in micro tomography from a transformation of the image plane to actual corrections of the camera pose.

Here, the restricted case of 3D translatory motions shall be considered. When further approximating the imaged object as planar and parallel to the projection screen, the expected transformations are restricted to translations t_h, t_v and isotropic scaling α. The corresponding homography matrix is then given by

$$\boldsymbol{H} = \begin{bmatrix} 1 & 0 & t_\mathrm{h} \\ 0 & 1 & t_\mathrm{v} \\ 0 & 0 & \alpha \end{bmatrix} . \tag{1.26}$$

Given a homogeneous vector $\boldsymbol{x} = \begin{bmatrix} \vec{p} \\ 1 \end{bmatrix}$ and a projection matrix $\boldsymbol{P} = [\boldsymbol{P}_{3\times3}|\boldsymbol{P}_4]$ with

$$\begin{bmatrix} h'_p \\ v'_p \\ w_p \end{bmatrix} = \boldsymbol{P}\boldsymbol{x} = \boldsymbol{P}_{3\times3}\,\vec{p} + \boldsymbol{P}_4 \,, \tag{1.27}$$

the transformation $\boldsymbol{H}\boldsymbol{P}\boldsymbol{x}$ can be explicitly stated:

$$\boldsymbol{H}\boldsymbol{P}\boldsymbol{x} = \begin{bmatrix} 1 & 0 & t_\mathrm{h} \\ 0 & 1 & t_\mathrm{v} \\ 0 & 0 & \alpha \end{bmatrix} \begin{bmatrix} h'_p \\ v'_p \\ w_p \end{bmatrix} = \begin{bmatrix} h'_p \\ v'_p \\ w_p \end{bmatrix} + w_p \begin{bmatrix} t_\mathrm{h} \\ t_\mathrm{v} \\ \alpha - 1 \end{bmatrix} . \tag{1.28}$$

It can be, considering Eq. 1.27, brought into the form

$$\boldsymbol{H}\boldsymbol{P}\boldsymbol{x} = \boldsymbol{P}\tilde{\boldsymbol{x}} = \boldsymbol{P} \begin{bmatrix} \vec{p} + \Delta\vec{p} \\ 1 \end{bmatrix} \qquad \text{with} \quad \Delta\vec{p} = \boldsymbol{P}_{3\times3}^{-1}\, w_p \begin{bmatrix} t_\mathrm{h} \\ t_\mathrm{v} \\ \alpha - 1 \end{bmatrix} . \tag{1.29}$$

I.e., the observed image transformation $\boldsymbol{H}$ can be reduced to a translation $\Delta\vec{p}$ of the object plane at $\vec{p}$ relative to the camera.

The translation vector $\Delta\vec{p}$ as stated in Eq. 1.29 can be, using Eqs. 1.6, 1.7 and 1.27, specified to

$$\Delta\vec{p} = \frac{(\vec{H}\times\vec{V})\cdot(\vec{p}-\vec{s})}{(\vec{H}\times\vec{V})\cdot(\vec{d}-\vec{s})} \left[\; \vec{H} \;\middle|\; \vec{V} \;\middle|\; \vec{d}-\vec{s} \;\right] \begin{bmatrix} t_\mathrm{h} \\ t_\mathrm{v} \\ \alpha - 1 \end{bmatrix} , \tag{1.30}$$

using the vectors $\vec{s}$, $\vec{d}$, $\vec{H}$, $\vec{V}$ describing the position of the focal spot, the origin of the projection plane and the orientation and pitches of its rows and columns. The relation between $\Delta\vec{p}$ and the corresponding homography transform is dependent on the original position $\vec{p}$ of the moved plane. This dependence relates to the position dependent geometric magnification of both the object and its motions. A reasonable choice for $\vec{p}$ is the center of mass of the considered object, which may, in the absence of more precise data, be approximated by the center of the field of view, which is typically characterized by $\vec{p} = (0, 0, 0)$. Such motion information is typically relevant to realize object or camera motion corrections within reconstruction algorithms based either on a set of reference images or as part of iterative reconstruction techniques.

1.2 Volume Reconstruction

Reconstruction of volume images from projections thereof represents the core aspect and achievement of tomographic imaging. The general feasibility is provided by the relation between the Radon transform (the formalized definition of projection imaging as line integrals over a multidimensional space, continuously parametrized by orientation and distance from a center point) and the Fourier transform. These mathematical foundations of tomography, as well as the derived basic reconstruction formulas, are widely covered in literature. The most widely adopted methods, i.e., the FDK ("Feldkamp") formula as well as the iterative algebraic techniques ART and SART will be briefly recapitulated and presented in a clear algorithmic form facilitating straight forward implementation. The Feldkamp approach will be generalized to generic geometry parametrizations based on the concepts introduced in Section 1.1, allowing to directly handle a wide variety also of non-circular acquisition geometries at arbitrary orientations relative to the sample coordinate system.

1.2.1 Analytic reconstruction: Filtered Backprojection and FDK

Filtered Backprojection derives from the Fourier slice theorem, which provides a straight forward relation between the Radon transform and the Fourier transform of a tomographic slice. It applies to parallel beam geometries and can be straight forwardly extended to fanbeam geometries based on coordinate transformation (cf. [84, 180, 15], and Fig. 1.2 for an illustration of parallel beam and fan beam geometries).

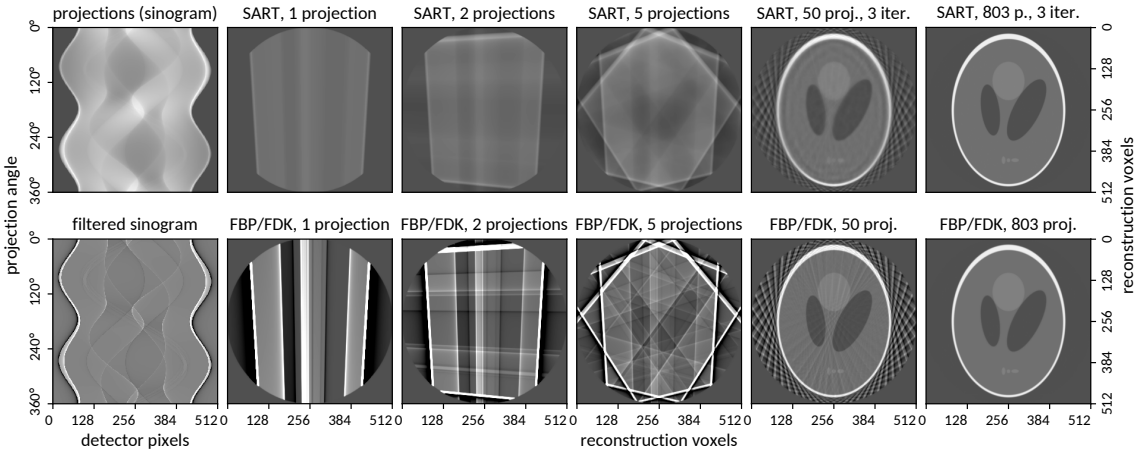

Figure 1.4: Illustration of reconstruction processes using the Shepp-Logan head phantom, whose projections can be analytically calculated.

The top row demonstrates iterative SART reconstruction (cf. Section 1.2.3) of a tomographic slice from fanbeam projection data (shown on the left). The iterative process starts by backprojecting the first projection into the empty reconstruction space (along the known projection paths). In the subsequent steps, individual projections of that image are simulated based on a discrete imaging model, and just the difference to the respective acquired projections is backprojected and added. On the right, SART reconstructions with three iterations over 50 and 803 ($\approx 512\,\pi/2$) projections respectively are shown.

The bottom row shows the corresponding reconstruction steps using (non-iterative) filtered backprojection (or FDK, cf. Section 1.2.1). The projection data is first weighted and filtered. Filtered projection lines of the sinogram are then backprojected, weighted and accumulated. On the right, reconstructions from 50 and 803 projections are shown.

While iterative reconstruction techniques ensure the validity of a solution by repeated re-projection and comparison with the available data, filtered backprojection approaches rely on prior mathematical analysis of the problem. Although the latter are typically faster, the former are more flexible, as no explicit assumptions on the imaging geometry are made. When reconstructing from too few projections, tangential lines along high contrast edges remain visible, which are further enhanced by the filtering process in the case of FBP reconstruction. In terms of algebraic reconstruction, they lie within the null space of an underdetermined system of equations, and may be suppressed by adequate regularization. In terms of filtered backprojection, they correspond to an insufficient angular sampling of the continuous radon transform.

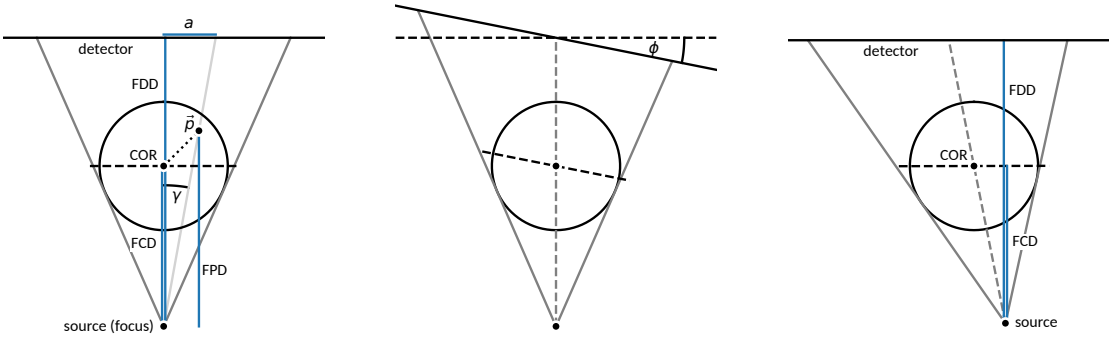

Figure 1.5: Sketches of ideal (left) and slanted (center and right) fan-beam acquisition geometries with a flat detector. The slanted detector geometry (center) is equivalent to a geometry with source and detector shifted horizontally in opposing directions (right). COR: center of rotation (and coordinate origin of the field of view), FCD: focus center distance, FDD: focus detector distance, a: linear detector coordinate, $\vec{p}$: point in the reconstruction field of view, γ: angle between $\vec{p}$ and the detector normal with respect to the focus point, FPD: focus point distance parallel to the detector normal. Different projection views of the circular field of view are generated by rotating source and detector equally about the COR by a rotation angle $\omega \in [0, 2\pi[$ (in the depicted case, $\omega = 0$ and therefore not shown). Note that the FPD for a given point $\vec{p}$ is ω-dependent (as is its projection on the detector).

Cone beam geometries (cf. e.g. Fig. 1.1 or Fig. 1.3) take a special role, as the divergence of line integrals also with respect to the central plane violates, for typical planar acquisition trajectories, the mathematical prerequisites of tomographic reconstruction. The technical advantages of this geometry and the fact that the resulting reconstruction artifacts are, with respect to many applications, tolerable, make it highly relevant in practice nevertheless. Feldkamp, Davies and Kress [38] proposed a widely adopted algorithm (referred to as FDK or Feldkamp algorithm) for circular cone-beam geometries, which heuristically extends the exact Filtered Backprojection (FBP) method for circular fan-beam geometries to the third dimension. Wang et al. [186] further showed that the FDK algorithm is also applicable to symmetric non-circular (e.g., polygonal or elliptical) scanning trajectories. With the aim of further extending the Wang-FDK algorithm to a general geometry parametrization using vectors or (equivalently) projection matrices, first the classic formulations of fan- and cone-beam reconstruction formulas as found in literature shall be briefly revisited.

Commonly, a perfect fan- or cone-beam geometry is assumed with the center of rotation (COR) lying on the perpendicular connecting line between source and detector as shown Fig. 1.5 (left). The fan-beam reconstruction algorithm can be partitioned into three steps: cosine weighting of the projection images, convolution filtering of the weighted projections (equivalent to parallel-beam reconstruction), and distance-weighted backprojection of the weighted and filtered projections into the reconstruction field of view along their respective projection paths. The central results, including the cone beam extensions by Feldkamp et al. and the generalization by Wang et al. (cf. also [38, 186, 84, 180, 15]), are:

$$\text{2D cosine weighting} \qquad \tilde{g}(\omega, v, h) = \frac{\overbrace{\cos(\gamma)}^{}}{\dfrac{\mathrm{FDD}(\omega)}{\sqrt{\mathrm{FDD}^2(\omega) + a_\mathrm{h}^2(h) + a_\mathrm{v}^2(v)}}} \overbrace{g(\omega, v, h)}^{\text{projection images}} \tag{1.31}$$

$$\text{1D convolution filtering over } h \qquad \tilde{g}'(\omega, v, h) = \int_{-\infty}^{+\infty} u(\tau)\, g(\omega, v, h - \tau)\, \mathrm{d}\tau \tag{1.32}$$

$$\text{3D weighted backprojection} \qquad f(\vec{p}) = \frac{1}{2} \int_0^{2\pi} \underbrace{\left(\frac{\mathrm{FCD}(\omega)}{\mathrm{FPD}(\vec{p}, \omega)} \right)^2}_{\text{distance weight}} \tilde{g}'(\omega, \underbrace{v(\vec{p}, \omega), h(\vec{p}, \omega)}_{\text{projection of } \vec{p} \text{ onto the detector}}) \, \mathrm{d}\omega \tag{1.33}$$

where $g(\omega, v, h)$ is the projection (line integral) data at projection angle ω and detector coordinate (v, h), u denotes the convolution filter to be detailed later (cf. Eq. 1.34, typically effecting a linear frequency weighting) and f is the reconstructed three dimensional image. γ is the angle of an

individual ray from source to detector with respect to the optical axis, and $\vec{p}$ is a point within the reconstruction field of view. FDD, FCD and FPD$(\vec{p},\omega)$ are distances (along the optical axis) between the focal spot and the detector, the center of rotation and the point $\vec{p}$ respectively, as sketched in Fig. 1.5. The optical axis is defined by the focal point and detector normal, and further assumed to both intersect and be orthogonal to the axis of rotation. The parametrized coordinates $(h(\vec{p},\omega), v(\vec{p},\omega))$ describe the projection of $\vec{p}$ onto the planar detector matrix at projection angle ω.

The distances FDD(ω), FCD(ω) and FPD$(\vec{p},\omega)$ as well as the intersections with the detector $h(\vec{p},\omega)$ and $v(\vec{p},\omega)$ are commonly expressed directly in terms of basic parameters of an ideal fan- or cone-beam geometry, i.e. in terms of scalar distances, pixel sizes and the rotation angle ω (cf. the example given in Section 1.1.4). $a_\mathrm{h}(h)$ and $a_\mathrm{v}(v)$ denote the horizontal and vertical distances of a detector pixel (h,v) from the optical axis, and are classically assumed to be directly proportional to h and v respectively.

With regard to quantitative reconstructions of $\vec{f}(\vec{p})$, it is important to note that distances on the detection plane are, in the context of the derivation of the convolution filter, generally understood with respect to a virtual detector at the location of the rotational axis. While Eqs. 1.31 and 1.33 are invariant with respect to similarity transforms of the detection plane (i.e., simultaneous scaling of its pixel spacing and focal distance), correct ω-dependent normalization of the convolution filter is based on the projected pixel spacing at the location of the rotational axis. This becomes especially important in the context of non-circular trajectories with varying distances FCD(ω) and/or FDD(ω) (cf. [186]), which imply varying pixel spacings with respect to the canonical detection plane at the rotational axis.

1.2.2 Generalized formulation of the Wang-FDK algorithm

While a minimal sufficient parametrization is essential with respect to mathematical discussions of the volume reconstruction problem, a more flexible parametrization is generally desired with regard to practical algorithmic implementations. While resampling of experimental data (cf. Section 1.1.7.1) is one common way to comply with some given parametrization, the respective transformations may rather be directly incorporated into the design of the reconstruction algorithm.

To this end, all distances, weights and intersections shall be expressed in terms of the general vectorial description of the projection geometry introduced in Section 1.1. Arbitrarily oriented detector planes can be characterized by a position $\vec{d}$ and row and column pitches $\vec{V}$ and $\vec{H}$, which in combination with grid indices (h,v) characterize the actual spatial locations $\vec{d}+h\vec{H}+v\vec{V}$ of the detector pixels addressed by h and v. Likewise, the position of the focal spot (or X-ray source) $\vec{s}$ shall be defined within 3D space. Using basic principles of vector geometry, the following relations can be defined (for each projection angle ω, which is not explicitly stated here for improved readability):

$$\mathrm{FDD} = \left|\vec{n}\cdot(\vec{s}-\vec{d})\right| \qquad \mathrm{FCD} = \left|\vec{n}\cdot(\vec{s}-\vec{o})\right| \qquad \mathrm{FPD} = \left|\vec{n}\cdot(\vec{s}-\vec{p})\right|$$

$$\vec{n} = \frac{\vec{H}\times\vec{V}}{\left\|\vec{H}\times\vec{V}\right\|} \qquad \cos(\gamma) = \frac{\left|\vec{n}\cdot(\vec{s}-\vec{d})\right|}{\left\|\vec{s}-(\vec{d}+h\vec{H}+v\vec{V})\right\|}$$

with $\vec{n}$ being the detector normal and $\vec{o}$ characterizing a point on the axis of rotation, which typically coincides with the center of the field of view and which in turn may just be the origin of the coordinate system, such that $\vec{o}=(0,0,0)$. In the case of an ideal cone-beam geometry, i.e. source and detector moving on a circular trajectory about the center of rotation and the detector normal being parallel to the connecting line between source and axis of rotation, these definitions are exactly equivalent to the usual fan-beam or FDK formulas. In addition though, this formulation flexibly allows to account for deviations from the ideal geometry even for individual projection views. Apart from imprecise rotary motions, relevant examples are a slanted or offset detector as sketched in Figure 1.5 as well as non-circular trajectories (as were considered e.g. by Wang et al. [186]). The generality of this parametrization further allows to freely chose the reconstruction coordinate system, i.e., allows to directly integrate rigid volume transformations into the reconstruction process and thus to register multiple tomographic scan trajectories within a shared reconstruction grid.

Algorithm 1.2 Generalized formulation of the Wang-Feldkamp-Davies-Kress algorithm (Eqs. 1.31–1.33) for tomographic reconstruction from cone beam geometries. The employed geometry model allows to process reconstructions from arbitrary acquisition geometries loosely compliant with the concept of a common axis of rotation parallel to the detector columns and projection orientations ω covering a full circle. Arbitrary rotations of the coordinate system, variable angular sampling densities and variable geometric magnification factors are explicitly covered. Typical deviations such as imperfectly aligned detectors or imperfect rotary motions are tolerated (when described by the provided geometry information) with minimal low-frequency artifacts arising from gradual inconsistencies with the prerequisites of the convolution filter and associated weightings. General deficiencies of cone beam tomography in the off-center planes ("Feldkamp artifacts") apply likewise.

common reference point on the rotational axis
$$\vec{o}$$

cone beam projection data
$$g(\omega, v, h): \text{ line integrals at angle } \omega \text{ and detector pixel } (h, v)$$

detector normal
$$\vec{n}_\omega = \frac{\vec{H}_\omega \times \vec{V}_\omega}{\left\|\vec{H}_\omega \times \vec{V}_\omega\right\|}$$

canonical pixel size
$$\Delta a'_{\mathrm{h}}(\omega) = \left\|\vec{H}_\omega\right\| \frac{\mathrm{FCD}(\omega)}{\mathrm{FDD}(\omega)} = \left\|\vec{H}_\omega\right\| \left| \frac{\vec{n}_\omega \cdot (\vec{s}_\omega - \vec{d}_\omega)}{\vec{n}_\omega \cdot (\vec{s}_\omega - \vec{o})} \right|$$

cosine weighting
$$\tilde{g}(\omega, v, h) = \frac{\left|\vec{n}_\omega \cdot (\vec{s}_\omega - \vec{d}_\omega)\right|}{\left\|\vec{s}_\omega - (\vec{d}_\omega + h\vec{H}_\omega + v\vec{V}_\omega)\right\|} \, g(\omega, v, h)$$

convolution filtering (cf. Eq. 1.34)
$$\tilde{g}'(\omega, v, h) = \Delta a'_{\mathrm{h}}(\omega) \sum_{n=-\infty}^{\infty} \tilde{g}(\omega, v, h-n) \, u(n, \Delta a'_{\mathrm{h}}(\omega))$$

grid projection onto detector (Eq. 1.5)
$$\begin{aligned} v(\vec{p}, \omega) &= -[\vec{H}_\omega \times (\vec{d}_\omega - \vec{s}_\omega)] \cdot (\vec{p} - \vec{s}_\omega) \,/\, [\vec{H}_\omega \times \vec{V}_\omega] \cdot (\vec{p} - \vec{s}_\omega) \\ h(\vec{p}, \omega) &= [\vec{V}_\omega \times (\vec{d}_\omega - \vec{s}_\omega)] \cdot (\vec{p} - \vec{s}_\omega) \,/\, [\vec{H}_\omega \times \vec{V}_\omega] \cdot (\vec{p} - \vec{s}_\omega) \end{aligned}$$

weighted backprojection
$$f(\vec{p}) = \frac{1}{2} \sum_\omega \Delta\omega(\omega) \left(\frac{\vec{n}_\omega \cdot (\vec{s}_\omega - \vec{o})}{\vec{n}_\omega \cdot (\vec{s}_\omega - \vec{p})} \right)^2 \tilde{g}'\Big(\omega, v(\vec{p}, \omega), h(\vec{p}, \omega)\Big)$$

$$\text{with } \sum_\omega \Delta\omega(\omega) = 2\pi$$

Algorithm 1.2 summarizes the generalized formulation of the Wang-FDK algorithm for discretely sampled projections, further using Eq. 1.5 (Section 1.1) for the point projections $v(\vec{p}, \omega), h(\vec{p}, \omega)$. $\sum_\omega$ therein denotes the sum over all discrete projection angles ω (assumed to cover 360°) and $\Delta\omega(\omega)$ characterizes the respective angular increment in radians. For standard scanning trajectories with equidistant angular sampling over a full circle, $\Delta\omega$ reduces to $\Delta\omega = 2\pi/N$, with N denoting the total number of projections. The set of angles ω is assumed to cover the domain $[0, 2\pi[$ with sufficient density in relation to the detector resolution and anticipated resolution of the discrete volume grid $f(\vec{p})$. The projections $v(\vec{p}, \omega), h(\vec{p}, \omega)$ of grid points $\vec{p}$ onto the detection plane required for (interpolated) sampling from $\tilde{g}'(\omega, v, h)$ may alternatively be formulated in terms of projection matrices (cf. Section 1.1.2). An example reconstruction procedure is shown in Figure 1.4 .

The convolution filter u effects a linear weighting of the frequency components to compensate for the inherent overrepresentation of low frequencies in the projection data $\tilde{g}(\omega, v, h)$. Technically, it emerges from coordinate transformations in the derivation of filtered backprojection algorithms (cf. Buzug [15]). It may be combined with additional spectral windowing functions or other frequency filters to be applied to the reconstructed image f, e.g., for noise suppression or integration of differential signals. While the reader shall be referred to literature for more information and detailed derivations, the three most relevant filters in context of the present work shall be explicitly stated here in their discrete form for completeness. Namely, these are the linear ramp (in Fourier

space) filter, also referred to as the "Ram-Lak" filter (after Ramachandran and Lakshminarayanan [146]), the sinc-windowed ramp filter proposed by Shepp and Logan, and the Hilbert filter, which transforms between gradient- and ramp-filtered images. The latter is relevant in the context of differential phase contrast imaging, which inherently produces gradient images. Their explicit discrete bandlimited real space form as required for the processing of projection data from pixelated detectors is (cf. e.g. [15, 122]), with $n \in \mathbb{N}$ describing a distance in units of detector pixels:

$$\begin{aligned} u_{\mathrm{Ram-Lak}}(n, \Delta a'_{\mathrm{h}}) &= \frac{1}{\Delta a'^{2}_{\mathrm{h}}} \begin{cases} \frac{1}{4} & n = 0 \\ -\frac{1}{(\pi n)^2} & n \,\text{odd} \\ 0 & n \,\text{even} \end{cases} \\ u_{\mathrm{Shepp-Logan}}(n, \Delta a'_{\mathrm{h}}) &= -\frac{1}{\Delta a'^{2}_{\mathrm{h}}} \frac{2}{\pi^2} \frac{1}{4n^2 - 1} \\ u_{\mathrm{Hilbert}}(n, \Delta a'_{\mathrm{h}}) &= \frac{1}{\Delta a'_{\mathrm{h}}} \begin{cases} -\frac{1}{\pi^2 n} & n \,\text{odd} \\ 0 & n \,\text{even} \end{cases} \end{aligned} \tag{1.34}$$

1.2.3 Iterative Volume Reconstruction

While filtered backprojection and related approaches derive from the continuous radon transform model of tomographic imaging, iterative algebraic reconstruction techniques result from a discrete model of the imaging process. Such models take the form of equation systems that are to be solved using algebraic methods. Typically, this will be a linear system of equations of the form

$$\sum_j A_{ij} f_j = g_i \,,$$

that may be formulated as a matrix–vector product

$$\boldsymbol{A}\boldsymbol{f} = \boldsymbol{g} \,. \tag{1.35}$$

The vector $\boldsymbol{f}$ holds discrete information (enumerated by j) about the field of view, the system model $\boldsymbol{A}$ describes the intersections of each volume element j with different integration paths enumerated by i, and $\boldsymbol{g}$ describes the resulting projections. In tomographic imaging, $\boldsymbol{g}$ is the observable quantity, $\boldsymbol{f}$ is to be reconstructed, and $\boldsymbol{A}$ is modeled based on knowledge of the imaging geometry and the chosen discretization scheme or basis. Most commonly, a Cartesian grid of voxels (volume elements) is used, although a large variety is found in the particular definitions of voxel basis functions and their intersections with the integration paths (see also Chapter 2).

The unique advantage of iterative reconstruction based on definitions of the forward problem (as opposed to explicit expressions for the solution of that problem) lies in the flexibility to easily extend the forward model beyond classic X-ray imaging. This will lay the foundation for the reconstruction of tensor fields addressed in Sections 5.2–5.3.

The central challenge lies in the size of $\boldsymbol{A}$: with typical discretization grid sizes of 500^3 to 2000^3, the dimension of $\boldsymbol{f}$ ranges on the order of magnitude of 10^8 to 10^{10} components, with $\boldsymbol{A}$ being about that size squared. Already when considering only small, two dimensional slices of 10^5 voxels, storage of the full system matrix requires tens of gigabytes of memory. Even when accounting for the fact that the matrix is generally very sparse – as each ray (enumerated by the row index) will actually intersect only a very small fraction of voxels (enumerated by the column index) – explicit storage of $\boldsymbol{A}$ is rarely feasible in practice, let alone explicit algebraic inversion. However, components of $\boldsymbol{A}$ and thus projections $\boldsymbol{A}_i\boldsymbol{f}$ can be computed on the fly (cf. Chapter 2), based on the relative positions of source, detector pixels and volume elements, allowing to handle the system of equations as an inverse problem.

1.2.3.1 Algebraic and Simultaneous Algebraic Reconstruction Techniques

One of the earliest approaches to tomographic reconstruction was the "Algebraic Reconstruction Technique" ART [44, 71], that has later been identified as a solution strategy otherwise known as "Kaczmarz method" in linear algebra (cf. e.g. [84]). The latter iteratively enforces consistency of $\boldsymbol{f}$

with individual components g_i of $\boldsymbol{g}$ and the corresponding rows $\boldsymbol{A}_i$ of the imaging model by means of the following assignment:

$$\boldsymbol{f}^{(k+1)} = \boldsymbol{f}^{(k)} + \lambda_k \underbrace{\frac{\boldsymbol{A}_{i(k)}}{\left\|\boldsymbol{A}_{i(k)}\right\|} \frac{g_{i(k)} - \overbrace{\boldsymbol{A}_{i(k)}\boldsymbol{f}^{(k)}}^{\text{forward projection}}}{\left\|\boldsymbol{A}_{i(k)}\right\|}}_{\text{backprojection}}$$

where k is an iteration index, $i(k)$ represents the particular row addressed at iteration k, and $\lambda_k \in]0, 1]$ is a relaxation or damping parameter. The original ART approaches assumed binary A_{ij} for computational simplicity, with $\left\|\boldsymbol{A}_{i(k)}\right\|^2$ then corresponding to the number of voxels intersected by ray i. The iteration typically starts with $f_j^{(0)} = 0 \,\forall\, j$. It can be easily confirmed that if all rows of $\boldsymbol{A}$ were mutually orthogonal, and $\lambda_k = 1$, the scheme would immediately converge after each row has been considered once. Yet in general, subsequent updates to $\boldsymbol{f}$ reintroduce inconsistencies with previously considered rows. These inconsistencies are progressively minimized by iterating over all rows multiple times, and in order to damp the (potentially oscillatory) effects of individual updates, λ_k may be chosen smaller than 1. Eventually, the difference $\boldsymbol{g} - \boldsymbol{A}\boldsymbol{f}^{(k)}$, and thus also the backprojected values, will converge to 0 or a small residual. Although the row wise ART is now seldomly used for X-ray CT in practice for several reasons, it is instructive for its simplicity and has been the origin for many other iterative approaches.

Based on the observation that non-intersecting rays may be handled in parallel, the "Simultaneous ART" (SART) has been proposed [2, 84], which groups the rows of $\boldsymbol{A}$ into blocks of non-intersecting rays belonging to individual, one or two dimensional projection images. As adjacent rays will nevertheless, due to the discrete nature of the imaging model, partially intersect common voxels, SART features a modified backprojection weight accounting for such overlaps by means of weighted averages:

$$f_j^{(k+1)} = f_j^{(k)} + \lambda_k \sum_{i \in P_k} \frac{A_{ij}}{\sum_{i \in P_k} A_{ij}} \frac{g_i - \boldsymbol{A}_i \boldsymbol{f}^{(k)}}{\left\|\boldsymbol{A}_i\right\|_1} \qquad \forall\, j \text{ with } \sum_{i \in P_k} A_{ij} \neq 0\,, \tag{1.36}$$

where P_k is the set of rays (or rows of $\boldsymbol{A}$) belonging to a projection image that is to be considered in iteration k. Although the weighting scheme has originally been motivated as an heuristic adaption of ART, a quite intuitive interpretation can be given: The row norm $\left\|\boldsymbol{A}_i\right\|_1$ represents the total intersection of ray i with the reconstruction volume, and the normalized weights $A_{ij} / \sum_{i \in P_k} A_{ij}$ effect an interpolation of backprojection values among all rays intersecting a particular voxel j. Following the idea of ART, the backprojection approximates a pseudo-inverse with respect to the considered subset of rows, such that

$$\boldsymbol{A}_i \left(\sum_{i \in P_k} \frac{A_{ij}}{\sum_{i \in P_k} A_{ij}} \frac{g_i}{\left\|\boldsymbol{A}_i\right\|_1} \right) \approx g_i \quad \forall\, i \in P_k$$

and thus

$$\boldsymbol{A}_i \left(f_j^{(k)} + \sum_{i \in P_k} \frac{A_{ij}}{\sum_{i \in P_k} A_{ij}} \frac{g_i - \boldsymbol{A}_i \boldsymbol{f}^{(k)}}{\left\|\boldsymbol{A}_i\right\|_1} \right) \approx g_i \quad \forall\, i \in P_k\,.$$

The scheme converges as $\boldsymbol{f}^{(k)}$ becomes consistent with $\boldsymbol{A}$ and $\boldsymbol{g}$.[1] Convergence – in a practical sense – is typically reached within less than 10 iterations over all projection images.

[1] Along with the proposition of the SART update scheme, the authors also suggested to apply a hamming-like weighting along the backprojection paths (i.e., a spatially variant $\lambda_k(j)$) in order to account for the fact that most image content is typically expected in the central region. This idea may also be interpreted as a heuristic approximation to modern approaches in the field of compressed sensing, which aim to precisely identify the support of image data within the voxel grid $\boldsymbol{f}$ as part of a regularized reconstruction scheme.

1.2.3.2 Practical formulation of SART

As explicit calculations on $\boldsymbol{A}$, as has been pointed out earlier, are generally cumbersome, a technically more practical way to reproduce the outlined idea of SART backprojection consists in voxel driven backprojection. Instead of explicitly iterating over rows of $\boldsymbol{A}$ (i.e., over rays between source and detector pixels) in order to identify and weight those that intersect a given voxel, new rays are rather cast from the focal point through each voxel's center in order to determine the respective intersections on the detector plane (e.g. by means of Eqs. 1.5 or 1.6, cf. Section 1.1). The contributions of individual detector pixels to a particular voxel (that is, the equivalent to $A_{ij}/\sum_{i\in P_k} A_{ij}$ within Eq. 1.36) can then be determined based on the distance between those intersections and the adjacent detector pixels, i.e., by classic interpolated sampling. This is also the general backprojection approach within analytic reconstruction techniques, which inherently do not define a discrete transformation $\boldsymbol{A}$ (cf. Section 1.2.2). The required normalization factors $\left\|\boldsymbol{A}_i\right\|_1 = \sum_j A_{ij}$ are easily computed within the forward projection procedure (required to determine the residuals $g_i - \boldsymbol{A}_i\boldsymbol{f}^{(k)}$), during which the contributing, non-zero components A_{ij} are computed anyway. Algorithm 1.3 summarizes the outlined approach. An example SART reconstruction procedure is shown Figure 1.4.

1.2.3.3 Other approaches and general considerations

Although there exists a multitude of alternative iterative reconstruction schemes, the general concept remains unchanged. Differences can be found in the particular ways updates to $\boldsymbol{f}$ (based on the residuals $\boldsymbol{g}-\boldsymbol{A}\boldsymbol{f}^{(k)}$) are backprojected, weighted and grouped. Without going into further detail, the reader shall be made aware of the concepts of "multiplicative ART" (MART), maximum likelihood expectation maximization (ML-EM, sometimes also "statistical iterative reconstruction"), the "simultaneous iterative reconstruction technique" SIRT and the projection grouping concepts used in "block iterative" or "ordered subset" approaches. The main drivers motivating different algorithms or discretization schemes are image quality with respect to some specific field of application and its particular requirements on the one hand, and computational efficiency with respect to some given problem size and hardware on the other hand. All iterative techniques however share the necessity to define a discrete imaging model, for which a large variety of ray–volume intersection models has been proposed as discussed in Chapter 2. In the present work, SART based on parallelized ray-casting on general purpose graphics processors (cf. Section 2.2) and voxel driven backprojection will be the method of choice.

A unique advantage of iterative reconstruction techniques is the general possibility to consider more complex and even non-linear forward models. However, as linearity is an important property with respect to the stability of the iterative process as well as with respect to the uniqueness of the solution, practical applications are restricted to moderate nonlinearities. Physical beam hardening models are one typical example, and further applications include explicit incorporation of source- or detector point spread functions or scattering models as considered e.g. in [34]. Iterative reconstruction techniques incorporating advanced physical modeling within the forward problem are also termed "Model Based Iterative Reconstruction". A review was given by Nuyts et al. [131].

Another important application of iterative techniques is the reconstruction from few projections, i.e., from an underdetermined system of equations. Regularization techniques such as total variation minimization are applied to suppress erroneous signal oscillations in the null space of the respective system matrix $\boldsymbol{A}$. The theory of Compressed Sensing, being closely related to concepts of data compression in general, thereby ensures that the resulting reconstruction is, with high probability, a correct representation of the true signal, provided that the signal can be sparsely represented in some basis (here: spatial representation) that is sufficiently different to the measurement basis (here: X-ray projections or Fourier space), and the amount of available data (X-ray projections) stands in a reasonable relation to the signal's support in its sparse basis (as opposed to the – generally much larger – number of feasible grid points in that basis). Compressed Sensing based CT reconstruction has been considered in the preceding Master's thesis [28].

Algorithm 1.3 Practical formulation of the simultaneous algebraic reconstruction technique (SART, originally defined by Eq. 1.36) with implicit evaluations of the system matrix $\boldsymbol{A}$ both in the forward projection steps (using ray casting as detailed in Chapter 2) and in the backprojection steps (using "voxel driven backprojection" analog to Section 1.2.2, Alg. 1.2 based on the relations between image space and projection space derived in Section 1.1). $\vec{p}_j$ characterizes the spatial location of the volume element f_j. The sets P_k of row indices specify blocks of $\boldsymbol{A}$ describing individual 2D projection images. They should be chosen such that all 2D projection views are considered adequately often throughout the iterative process. In order to improve convergence, the order of projection angles ω_k should be non-sequential (random order is a common choice, yet a number of deterministic ordering schemes have been discussed in [2, 67, 54, 125, 89]). The combination of first order interpolation among nearest neighbors both in the forward projection and backprojection step implicitly requires the volume grid sampling density to be sufficiently similar to the density of rays (integration paths) traversing the volume from the focal point to each detector pixel.

cone beam projection data: $g(\omega, v, h)$: line integrals at angle ω and detector pixel (h, v)

projection geometries defining $\boldsymbol{A}$: $\vec{s}_\omega, \vec{d}_\omega, \vec{H}_\omega, \vec{V}_\omega$

indices of the discrete imaging model $g_i = \sum_j A_{ij} f_j$: i : enumerates line integrals / detector pixels for all ω; j : enumerates discrete volume elements

sets of row indices i to be considered in iteration k: P_k : each set comprises a 2D image at projection angle ω_k

initial volume: $f_j^{(0)} = 0$

relaxation factor(s) weighting individual update steps: $\lambda_k \in]0, 1]$; typically $\lambda_k = \lambda \leq 0.5$

for $k = 0..N_{\text{iter}} - 1$ **do** :

forward projection using Algorithm 2.1: $\tilde{g}_i^{(k)} = \boldsymbol{A}_i \boldsymbol{f}^{(k)} \qquad \forall\, i \in P_k$

corresponding ray lengths at $\omega_k = \omega_i \;\forall\, i \in P_k$: $l(\omega_k, v_i, h_i) = \left\| \boldsymbol{A}_i \right\|_1 \qquad \forall\, i \in P_k$

2D residual projection image at $\omega_k = \omega_i \;\forall\, i \in P_k$: $\Delta g^{(k)}(\omega_k, v_i, h_i) = g(\omega_k, v_i, h_i) - \tilde{g}_i^{(k)} \quad \forall\, i \in P_k$

grid projection onto detector (Eq. 1.5):

$$v(\vec{p}_j, \omega) = -[\vec{H}_\omega \times (\vec{d}_\omega - \vec{s}_\omega)] \cdot (\vec{p}_j - \vec{s}_\omega) \,/\, [\vec{H}_\omega \times \vec{V}_\omega] \cdot (\vec{p} - \vec{s}_\omega)$$
$$h(\vec{p}_j, \omega) = \;\; [\vec{V}_\omega \times (\vec{d}_\omega - \vec{s}_\omega)] \cdot (\vec{p}_j - \vec{s}_\omega) \,/\, [\vec{H}_\omega \times \vec{V}_\omega] \cdot (\vec{p} - \vec{s}_\omega)$$

backprojection of residuals into image space with interpolated sampling from $\Delta g^{(k)}$ and l:

$$f_j^{(k+1)} = f_j^{(k)} + \lambda_k \frac{\Delta g^{(k)}\Big(\omega_k, v(\vec{p}_j, \omega_k), h(\vec{p}_j, \omega_k)\Big)}{l\Big(\omega_k, v(\vec{p}_j, \omega_k), h(\vec{p}_j, \omega_k)\Big)}$$

end for.

Chapter 2

Perspective Volume Projection

The simulation of X-ray images by numeric projection of gridded volume images represents, in the context of computed tomography, the calculation of the forward problem within iterative solutions of the inverse problem, i.e., the reconstruction problem. It is thus also referred to as "forward projection" (as opposed to the "backprojection" step) and is both one of the most essential and time consuming aspects of iterative reconstruction techniques (cf. Section 1.2.3). Forward or volume projection therefore takes a central role with respect to both efficiency and quality of these algorithms, wherefore the topic shall be addressed quite detailed.

Foremost, simulated X-ray projection involves casting rays through volumes (cf. Fig. 2.1, left) based on given projection geometries (cf. Section 1.1) and integration of image data along these ray paths. Irrespective of additional features (such as tensor valued voxels as used for tensor tomography, or non-linear transformations simulating e.g. beam-hardening), the fundamental component of any X-ray imaging model therefore is an adequate sampling and accumulation strategy for the evaluation and integration of values from three dimensional voxel grids. As many samples – between 10^8 and 10^{10} for typical volume sizes of 500^3 to 2000^3 voxels – are required to compute 2D X-ray projections, and thousands of such projections are required within iterative tomographic reconstruction, efficiency of the sampling and integration process is of outmost importance. The sampling strategy further affects the outcome of iterative reconstruction algorithms, which are fundamentally based on optimizing the similarity between simulated and actual X-ray projections. Both aspects – efficiency and physical modeling – have given rise to a large number of publications in various fields including tomographic reconstruction, radiation therapy planning and computer graphics. As the constraints and capabilities of computing hardware are constantly evolving, the quest for most efficient solutions (with respect to some definition) remains a timeless task.

In the following, a 3D generalization of Joseph's classic interpolating projection method optimized for general purpose graphics processing units is given and discussed. It is shown to feature excellent memory access efficiency without explicitly restricting the projection geometry nor making use of sophisticated memory layout schemes or read-only texture memory. The contribution is twofold: On the one hand, a concise algorithm is derived, benchmarked and provided in an easily implementable form, ensuring its practical availability. Likewise importantly, its qualitative eligibility with respect to volume projection and iterative tomographic reconstruction as compared to more complex approaches is assessed in order to establish it as not only extremely fast, but also competitive despite its intriguing simplicity. As no unique benchmark exists in this respect, a survey of previous literature is given on the one hand, and selected experiments demonstrating and comparing discretization artifacts of multiple algorithms are shown on the other hand. First results have been published in [30].

Chapter 2 extends on the presentations in Dittmann/Graetz 2016/2021 [32] and Dittmann, Hanke 2017 [30]

2.1 Literature Review

Two general classes of volume projection approaches may be distinguished upfront: those following integration paths and performing some kind of sampling on the volume image grid, and those iterating over volume elements (voxels) and accumulating renderings of each voxel's projection onto the detection screen. The first approaches are referred to as "ray driven", "ray casting" or "ray tracing" methods, while the latter methods are usually termed "voxel driven" or "splatting". The methods first of all differ in their memory access pattern: while ray driven methods iterate over camera pixels and typically require less efficient random read access to the volume image data, splatting methods can sequentially iterate over the volume elements, yet instead require a large amount of non-sequential read and write accesses to the projection image. Intermediate approaches are resampling strategies (e.g., the shear-warp approach [91]) and the more recent "distance driven" method [24, 98]. The former transform the volume image such that the subsequent projection reduces to a summation over one coordinate axis and are most similar to ray driven methods. The latter approach aims to combine the sequential memory access pattern of voxel driven methods with sequential write accesses to the projection image.

Ray driven projection has two important advantages, wherefore it will be the method of choice here: first, it is trivially parallelizable, as by design no concurrent write accesses to the projection screen need to be managed. Secondly, the correct normalization of ray integrals with respect to the associated run lengths through the volume is considerably simpler as compared to splatting approaches. Simplicitly is a key to efficiency, and it will be shown that highly efficient memory access patterns are indeed possible also with ray driven approaches. Tracing of linear paths through grids has been studied since the advent of raster graphics, and the following review shall provide a reasonable overview of the essential ideas that have come up in the past, with a particular focus on the tomography context.

A central concept in the majority of fast ray casting algorithms on regular grids is the notion of a "driving axis" [79, 100, 41, 35, 99] as already introduced in the 1960s by Bresenham in the context of rasterized line drawing. Instead of just arbitrarily defining a number of sampling points along the linear coordinate of an integration path, the path will rather be traversed in unit steps of the designated driving axis of the algorithm. The driving axis is chosen to be the dimension along which the considered path progresses fastest, such that the resulting non-integer step sizes along the remaining coordinate axes are always guaranteed to not exceed the grid spacing, thereby ensuring that no intersected pixels or voxels will be skipped in the tracing procedure. Figure 2.1 gives an illustration.

This concept of grid-aligned sampling is explicitly or implicitly used e.g. by Josephs' algorithm [79] (one of the early methods proposed for 2D iterative tomographic reconstruction), by shear-warp resampling techniques [16, 91] (proposed for volume visualization) or ray-driven formulations of splatting algorithms [111, 124, 12] as well as by the recent "Distance Driven Method" [24, 98]. It emerges naturally from practical sampling considerations, as interpolation can thereby be avoided along the driving axis. Prominent alternative techniques are the much-cited algorithm by Siddon [169] and variants thereof [1, 73, 215, 23, 200] (known as digital differential analyzer or DDA algorithm in the field of computer graphics), which trace lines in irregular steps from intersection to intersection with any of the raster planes perpendicular to the coordinate axes. The final objective of calculating exact ray-box intersections though can as well be achieved with driving-axis based algorithms [100, 42], although the complexity increases in the 3D case.

In addition to basic algorithmic concepts, the assumed underlying system model is a central aspect. Particularly prevalent is the assumption that imaged objects can be exactly modeled by cubic voxels of homogeneous density, and incident radiation by rectangular beam profiles of finite extent (as opposed to the also common assumption of pencil beams, cf. Siddon [169]). Much effort has been put into the development of exact projection algorithms in this respect [100, 42, 207, 101, 199, 128, 214, 57, 58, 155], using both ray driven and splatting approaches. When arguing that there is no outstanding reason to assume homogeneous cubic voxels, the complexity for an "exact" volume projector can be reduced by using algorithmically more convenient voxel basis functions as compared to the box profile. Modeling of both voxel and beam profiles can then be merged into diffused, overlapping interpolation kernels or projection footprints parametrized by ray-voxel distances [124, 61, 93, 217, 119]. Other methods replace the latter distance by even

more efficient approximations [79, 24, 178]. The modeled beam width is directly related to the extent of the employed interpolation or sampling kernel, and an approximate modeling of the beam width (neglecting e.g. divergence) has been found to be sufficient in practice [68]. Joseph's 2D projector in particular straight forwardly performs linear interpolation among the nearest neighbors of each sampling point, which may as well be interpreted as an approximation to normalized radial basis function interpolation within a tightly limited radius. The modeled beam width thus approximately corresponds to the voxel raster spacing. It has been extended to 3D in the past by several authors to e.g. trace X-rays through parallel stacks of textured planes [201, 202] or for list mode reconstructions in positron emission tomography [163], and is also found in recent reconstruction toolkits [151, 181]. More elaborate calculations of line integrals over multilinearily interpolated grids [90] have not been found to provide practical benefits [180], and neither has the distance driven method [59]. In their reviews on iterative tomographic reconstruction, Pan et al. and Nuyts et al. similarly conclude that sophisticated sampling methods are usually secondary as compared to an adequate resolution of the voxel grid with respect to the features it is supposed to represent [136, 131]. I.e., an increasing support for the general eligibility and sufficiency of basic interpolation approaches can be identified.

Considering computational efficiency again, it is preferable to keep both the interpolation kernel size and the grid resolution to a necessary minimum. Various strategies have been used to push that optimum beyond localized kernels by using grids with adaptive resolution [72, 182] and non-cartesian layout [170, 162] or even unstructured point clouds [49]. With regard to cache efficiency of the given hardware, the layout of the volume image data in memory may be better arranged with regard to expected access patterns using e.g. techniques such as Z-ordering or blocking [11]. Similarly, the algorithm design may be explicitly taylored or restricted with respect to a given memory layout [24, 179]. A central drawback of these more elaborate approaches to the reduction and optimization of memory accesses is the increased algorithmic complexity, limiting the net performance gain. In the present work, efficiency shall rather be drawn from algorithmic simplicity and efficient parallel memory accesses. In the case of very small grids (typically less than 10^6 voxels) and particularly when high degrees of symmetry can be exploited, precalculation and explicit storage of the sparse system matrix describing the projection process can be an option as well, as addressed e.g. by [162]. Finally, when simultaneously calculating large amounts of X-ray projections of the same volume, divide and conquer approaches allow to systematically reduce the amount of total memory accesses by exploiting spatial overlaps of rays from close by viewing angles [13]. For parallel beam geometries, this can also be achieved by evaluating projections in Fourier space [110], based on the Fourier slice theorem. In the present context of efficient calculation of individual projections within read-and-write memory (as required for block-iterative reconstruction techniques), these strategies are however not applicable.

Starting with SGI graphics workstations in the 1990s, researchers have further been utilizing the processing power of dedicated graphics processors (GPUs) in order to speed up CT reconstruction. Reviews on the previous usage of GPUs in tomography have been given e.g. by Mueller, Pratx, Després and co-authors [123, 144, 27]. The aim of the following work is to demonstrate a ray driven projection algorithm to be applied on read-and-write memory, whose memory efficiency is implicit in its coherent sampling pattern among parallel threads (as opposed to relying on specialized read-only texture memory), and which is further formulated in a computationally lean way. It thereby allows to perfectly utilize the specific capabilities of modern general purpose GPUs, eventually resolving the common conflict between sampling quality and processing speed.

2.2 Branchless generalized Joseph projector

2.2.1 Driving axis aligned grid traversal

The basic sampling concept is illustrated in Figures 2.1 and 2.3. A ray emanating from a source at $\vec{s}$ traverses a voxel volume and hits a detector pixel at $\vec{d}$. Along its intersection with the volume, the latter will be sampled in steps of $\tilde{r}$, which will be concretized in the following. While the resulting scheme is equivalent to general driving axis based methods, the present vector representation allows for a unified treatment of all cases, such that the "driving axis", which normally distinguishes different code branches, now only implicitly determines the orientation of sampling planes within a branchless sampling loop.

Given the positions of source $\vec{s}$ and detector pixel $\vec{d}$ relative to the volume origin, the integration path is characterized by the set of points $\vec{p}$

$$\vec{p} = \vec{s} + l\vec{r}$$

with

$$\vec{r} = \vec{d} - \vec{s}$$

and $l \in \mathbb{R}$ being the free parameter. The driving axis m is then identified by the largest component of $\vec{r}$:

$$m = \underset{i}{\operatorname{argmax}}(|r_i|) \,.$$

The increment vector $\tilde{r}$ between successive sampling points will be chosen such that the resulting sampling points remain aligned with the driving axis, which holds for

$$\tilde{r} = \frac{\vec{r}}{r_m} \,.$$

Assuming that grid coordinates correspond here to non-negative memory indices, the first possible sampling point is defined by the intersection of the ray with a plane through the origin and perpendicular to the driving axis m, i.e.,

$$\begin{aligned} [\vec{s} + o\,\tilde{r}]_m &\overset{!}{=} 0 \\ \Rightarrow o &= -s_m \end{aligned}$$

where o is the distance between source and first sampling plane in units of the sampling increment $\left\|\tilde{r}\right\|$. o will thus be termed "sampling offset". The volume can now be sampled at points $\vec{p}^{(i)}$ along the defined path in unit steps of axis m by evaluating

$$\vec{p}^{(i)} = (\vec{s} + o\,\tilde{r}) + i\,\tilde{r}$$

for integer $i \in [0, i_{\max}]$, where $i_{\max}$ is defined by the extent of the voxel grid along axis m.

2.2.2 Interpolated sampling

When sampling from (GPU) main memory, the 4-neighborhood $\{\vec{v}^{(i,1)}, \vec{v}^{(i,2)}, \vec{v}^{(i,3)}, \vec{v}^{(i,4)}\}$ of integer valued grid coordinates around each sampling point $\vec{p}^{(i)}$ needs to be explicitly enumerated. The driving axis component $p_m^{(i)}$ is, by construction of the sampling increment $\tilde{r}$ and offset o, guaranteed to be integer for all integer i. The remaining non-integer components necessarily lie between two integer ones along their respective coordinate axes. For each sampling point $\vec{p}^{(i)}$, the set of four neighboring voxels can thus be determined by regarding all combinations of floor and ceiling values of these non-integer components (with $\lfloor\,\rfloor$ and $\lceil\,\rceil$ being the floor and ceiling operators respectively):

$$\begin{aligned} \vec{v}^{(i,1)} &= \lfloor p_1^{(i)} \rfloor, \lfloor p_2^{(i)} \rfloor, \lfloor p_3^{(i)} \rfloor \\ \vec{v}^{(i,2)} &= \lfloor p_1^{(i)} \rfloor, \lceil p_2^{(i)} \rceil, \lceil p_3^{(i)} \rceil \\ \vec{v}^{(i,3)} &= \lceil p_1^{(i)} \rceil, \lfloor p_2^{(i)} \rfloor, \lceil p_3^{(i)} \rceil \\ \vec{v}^{(i,4)} &= \lceil p_1^{(i)} \rceil, \lceil p_2^{(i)} \rceil, \lfloor p_3^{(i)} \rfloor \,, \end{aligned} \tag{2.1}$$

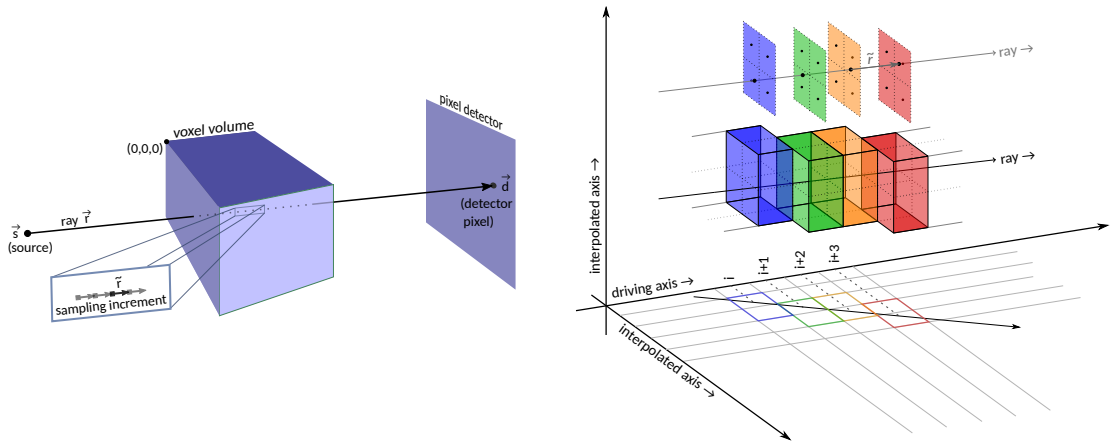

Figure 2.1: Ray casting through a volume along a line defined by two points $\vec{s}$ and $\vec{d}$. On the right, driving-axis aligned sampling is illustrated on the grid scale. Integer steps along the driving axis imply increments of $\tilde{r} = \vec{r}/r_m$ along the actual path, with $1 \leq \left\|\tilde{r}\right\| \leq \sqrt{3}$. Due to the alignment with one designated axis, interpolation is required only within 4-voxel blocks – marked in varying colors – extending along the remaining axes. Above, the respective sampling points $\vec{p}^{(i)}$ are illustrated within their sampling planes described by the respective nearest neighbour locations $\vec{v}^{(i,1-4)}$.

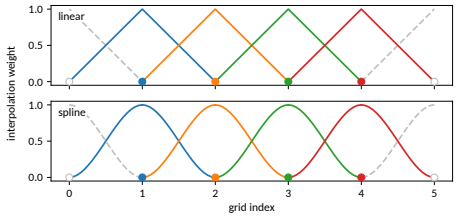

Figure 2.2: One dimensional examples of linear and spline interpolation kernels as defined by Equations 2.4 and 2.5. Each marker represents a data point on the grid. The respective interpolation weights as a function of fractional position between grid points (i.e., the interpolation kernels) are shown in matching color. The resulting two dimensional image interpolation is demonstrated in Figure 2.3 (right).

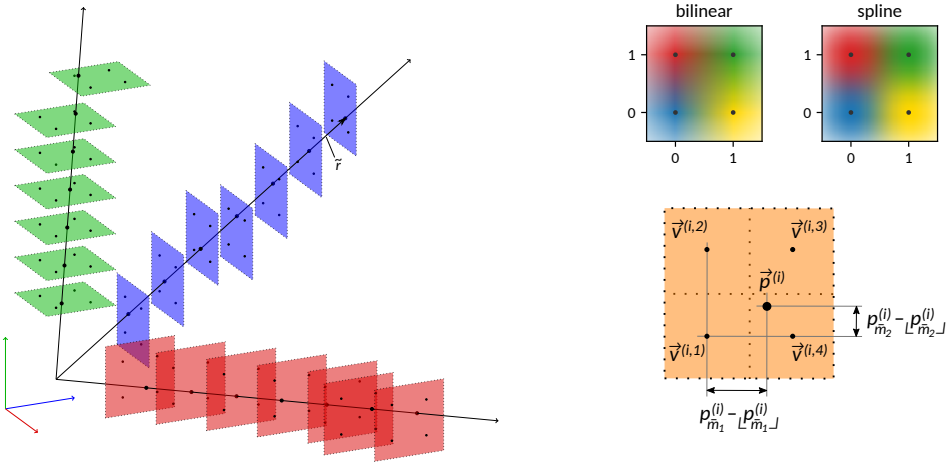

Figure 2.3: Illustration of rays piercing 4-voxel planes perpendicular to different driving axes. On the right hand side, the interpolation within each plane is detailed, with $\lfloor\ \rfloor$ designating the floor operation, and $\bar{m}_1$ and $\bar{m}_2$ the indices of the two non-driving axes. On the upper right, bilinear interpolation is compared to spline interpolation. Both interpolation kernels are explicitly shown in Figure 2.2.

exploiting that

$$\lfloor p_m^{(i)} \rfloor = \lceil p_m^{(i)} \rceil = p_m^{(i)} \, .$$

Independent of $m \in \{1, 2, 3\}$, the vectors $\vec{v}^{(i,1-4)}$ define a group of four voxels in a plane perpendicular to the driving axis. Illustrations of the planes spanned by these nearest neighbor voxels around sampling points $\vec{p}^{(i)}$ are given in Figures 2.1 and 2.3. Special cases arise when either of the non-m components of $\vec{p}^{(i)}$ happen to be also integer, which leads to redundant vectors among $\vec{v}^{(i,1-4)}$. Given the final objective of interpolation, these cases will be accounted for by adequate choice of the respective weights.

Interpolation will be based on scalar distance weights

$$\begin{aligned} & w(d); \quad d \in [0, 1] \\ \text{with} \quad & w(1-d) = 1 - w(d) \end{aligned}$$

with respect to the component wise distances of the contributing grid points next to a sampling point:

$$d_k^{(\mathrm{fl})} = p_k^{(i)} - \lfloor p_k^{(i)} \rfloor \, ; \qquad d_k^{(\mathrm{cl})} = 1 - d_k^{(\mathrm{fl})} \, ,$$

where the superscripts (fl) and (cl) indicate distances to the integer grid indices below and above the components $p_k^{(i)}$ of $\vec{p}^{(i)}$. The definition of $d_k^{(\mathrm{cl})}$ as complement to $d_k^{(\mathrm{fl})}$ guarantees correct interpolation weights also in the special case of integer components $p_k^{(i)}$, where floor and ceiling values coincide. When explicitly defining

$$\begin{aligned} w_{\mathrm{fl},k} &= w(d_k^{(\mathrm{fl})}) \quad \text{for } k \neq m \\ w_{\mathrm{cl},k} &= 1 - w_{\mathrm{fl},k} \quad \text{for } k \neq m \\ w_{\mathrm{fl},m} &= w_{\mathrm{cl},m} = 1 \end{aligned} \tag{2.2}$$

the interpolation weights $w^{(i,1-4)}$ for the respective voxels $\vec{v}^{(i,1-4)}$ can be conveniently represented as:

$$\begin{aligned} w^{(i,1)} &= w_{\mathrm{fl},1}^{(i)} \cdot w_{\mathrm{fl},2}^{(i)} \cdot w_{\mathrm{fl},3}^{(i)} \\ w^{(i,2)} &= w_{\mathrm{fl},1}^{(i)} \cdot w_{\mathrm{cl},2}^{(i)} \cdot w_{\mathrm{cl},3}^{(i)} \\ w^{(i,3)} &= w_{\mathrm{cl},1}^{(i)} \cdot w_{\mathrm{fl},2}^{(i)} \cdot w_{\mathrm{cl},3}^{(i)} \\ w^{(i,4)} &= w_{\mathrm{cl},1}^{(i)} \cdot w_{\mathrm{cl},2}^{(i)} \cdot w_{\mathrm{fl},3}^{(i)} \end{aligned} \tag{2.3}$$

without requiring further explicit consideration of the particular driving axis m.

Two specific weighting functions shall be considered:

$$w_{\mathrm{lin}}(d) = 1 - d \tag{2.4}$$

$$w_{\mathrm{spl}}(d) = 1 - 3d^2 + 2d^3, \tag{2.5}$$

with w_{lin} reproducing classic multilinear interpolation and w_{spl} being a smooth spline function in the style of a smooth cosine window that ensures differentiability also at grid points, i.e., when $d = 0$ or $d = 1$. The resulting interpolation kernels are depicted in Figure 2.2, and Figure 2.3 illustrates two-dimensional interpolation. The practical consequences of the different interpolations schemes are later addressed in Sections 2.3.1–2.3.2 and Figures 2.4–2.5 therein.

Algorithm 2.1 combines the above considerations on volume traversal, implicit identification of sampling planes, and interpolation among the respective nearest neighbors into a single sampling loop. Explicit consideration of the driving axis only occurs in line 16. As can be verified by explicitly assuming different driving axes, the weighted sampling performed in lines 17–20 always correspond to a 2D-interpolation among the nearest neighbors of the respective sampling point within a plane perpendicular to the axis m.

Algorithm 2.1 Branchless ray casting through a voxel volume with axis aligned sampling and first order interpolation among four nearest neighbors. For a linear interpolation kernel, the scheme corresponds to a 3D generalization of Joseph's 2D projector [79] for iterative tomographic reconstructions. The particular formulation of the algorithm handles all possible driving axes in a single code branch. Scaling by $\left\|\tilde{r}\right\|$ accounts for the varying sampling distances depending on the orientation of the ray $\vec{r}$. 2D X-ray projection images of a volume are obtained by parallel evaluation for multiple rays defined by multiple detector pixel locations and one ore more (in the case of stacked fanbeam or parallel beam projections) source locations. See Section 1.1 for details on projection geometry parametrization.

assuming : $\vec{s}, \vec{d}, \vec{H}, \vec{V}$ defined in units of voxel grid indices
$\vec{r} \leftarrow \vec{d} + h\vec{H} + v\vec{V} - \vec{s}$ ▷ (h, v): detector pixel (cf. Fig. 1.1)
$m \leftarrow \text{argmax}_i(|r_i|)$ ▷ m: major (driving) axis
$\tilde{r} \leftarrow \vec{r}/r_m$ ▷ $\tilde{r}$: sampling increment vector
$o \leftarrow -s_m$ ▷ o: sampling offset, $\vec{s}$: ray source point
$i_{\max} \leftarrow \text{volumeDimensions}[m]$ ▷ $i_{\max}$: maximal sampling points
$a \leftarrow 0$ ▷ a: accumulator variable
for $i = 0 \,..\, i_{\max}$ **do** ▷ iterate over sampling points
    $\vec{p} \leftarrow \vec{s} + (o + i) \cdot \tilde{r}$ ▷ $\vec{p}$: current sampling point
    if $\vec{p}$ **is in** volume **then** ▷ alternatively: precise choices for o and $i_{\max}$
        $\vec{p}_{\text{fl}} \leftarrow \text{floor}(\vec{p})$ ▷ find lower voxel grid indices
        $\vec{p}_{\text{cl}} \leftarrow \text{ceil}(\vec{p})$ ▷ find upper voxel grid indices
        assert: $p_{\text{fl},m} = p_{\text{cl},m} = p_m = i$ ▷ by design of o and $\tilde{r}$, $p_m = i$
        $\vec{w}_{\text{fl}} \leftarrow w(\vec{p} - \vec{p}_{\text{fl}})$ ▷ elementwise mapping of distances to interpolation weights (cf. Eqs. 2.4, 2.5, Fig. 2.2)
        $\vec{w}_{\text{cl}} \leftarrow \vec{1} - \vec{w}_{\text{fl}}$ ▷ complementary interpolation weights
        $\text{w}_{\text{cl},m} \leftarrow w_{\text{fl},m} \leftarrow 1$ ▷ special case: driving axis
        $a \leftarrow a + \text{volume}[\, p_{\text{fl},1}\,,\, p_{\text{fl},2}\,,\, p_{\text{fl},3}\,] \cdot \|\tilde{r}\| \cdot w_{\text{fl},1} \cdot w_{\text{fl},2} \cdot w_{\text{fl},3}$ ▷ (cf. Eqs. 2.1–2.3)
        $a \leftarrow a + \text{volume}[\, p_{\text{fl},1}\,,\, p_{\text{cl},2}\,,\, p_{\text{cl},3}\,] \cdot \|\tilde{r}\| \cdot w_{\text{fl},1} \cdot w_{\text{cl},2} \cdot w_{\text{cl},3}$
        $a \leftarrow a + \text{volume}[\, p_{\text{cl},1}\,,\, p_{\text{fl},2}\,,\, p_{\text{cl},3}\,] \cdot \|\tilde{r}\| \cdot w_{\text{cl},1} \cdot w_{\text{fl},2} \cdot w_{\text{cl},3}$
        $a \leftarrow a + \text{volume}[\, p_{\text{cl},1}\,,\, p_{\text{cl},2}\,,\, p_{\text{fl},3}\,] \cdot \|\tilde{r}\| \cdot w_{\text{cl},1} \cdot w_{\text{cl},2} \cdot w_{\text{fl},3}$
    end if
end for.

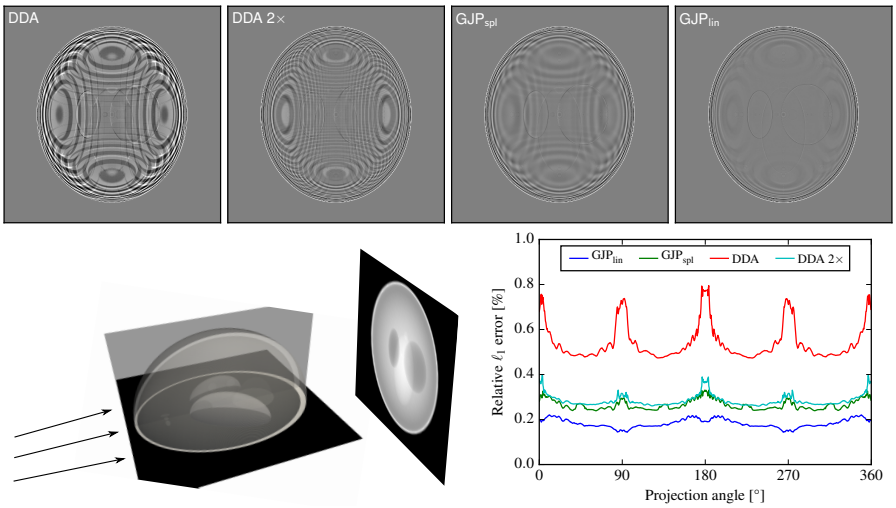

Figure 2.4: Approximation errors of different projection algorithms for a 10° conebeam geometry. Numeric projections of the rasterized Shepp Logan phantom (on a 512^3 grid) onto a 512^2 detector are compared to corresponding reference projections obtained by analytic integration of the ellipsoids defining the phantom. The top row shows example difference images for a frontal view. Below, the ℓ_1 norm of these residuals, normalized to the ℓ_1 norm of the analytic reference projection, is plotted for all projection angles. On the bottom left, an illustration of the Shepp Logan phantom and the applied projection geometry is given.

2.3 Benchmarks

2.3.1 Quality of projection images

The performance with respect to adequate modeling of of ray-volume intersections is demonstrated on cone beam projections of the classic three dimensional Shepp Logan phantom based on the definition reproduced in [159]. The phantom is described by a sum of ellipsoids, which can on the one hand be easily rasterized at any desired resolution and on the other hand allows the direct calculation of projection images by analytical evaluation of line integrals over the defining ellipsoids. A ground truth is thus available for comparison with respective numeric projections calculated from the rasterized version. In order to also adequately account for the extent and integrating nature of detector pixels, the reference projections are evaluated as an average over 64 line integrals between the focal spot and regular arrays of 8×8 points within each detector pixel. Analogously, oversampling is applied also in the rasterization process of the phantom: It is rasterized on a regular grid of 512^3 voxels, whereat each voxel value is determined as an average over $5 \times 5 \times 5$ regularly distributed samples of the function defining the phantom.

Following typical experimental conditions, a cone angle of 10° is modeled (i.e., the focal distance is about 5.7 times the detector width), projecting the volume onto a square detector of 512^2 pixels. In total, 803 ($\approx \frac{\pi}{2}512$) projection images from different orientations covering a full circle are computed, whereat the chosen number of projections corresponds to a common recommendation with regard to analytic tomographic reconstruction (cf. [15]).

Figure 2.4 shows residual projection errors observed for various numeric projection approaches. Although the general occurrence of such residuals is generally expected due to the inherently approximative nature of discrete volume represenations, the adequacy of a projection model may reasonably be measured by its ability to keep such residuals minimal. Siddon's pencil beam projection model, realized using the DDA algorithm, exhibits most artifacts, particularly in cases where rays run roughly parallel to grid axes. In these situations the model of pencil beams intersecting box-shaped voxels is equivalent to nearest neighbor sampling. When oversampling the DDA by a factor of two in each dimension in order to approximate a finite beam extent, i.e. tracing and averaging over four rays per detector pixel, the resulting projection residuals become comparable to those of the non-oversampled $\mathrm{GJP}_{\mathrm{spl}}$ algorithm using spline interpolation, although the latter further shows a considerable reduction of high frequency artifacts. The best results are, despite the kinked interpolation kernel, achieved by the liner interpolating $\mathrm{GJP}_{\mathrm{lin}}$ algorithm.

Chapter 2 extends on the presentations in Dittmann/Graetz 2016/2021 [32] and Dittmann, Hanke 2017 [30]

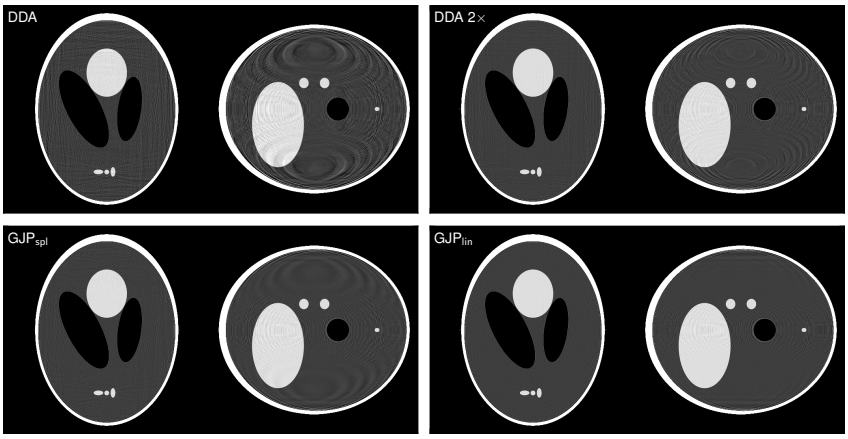

Figure 2.5: Axial and sagittal central slices of iterative SART reconstructions (10 iterations, $\lambda_k = 0.5$, cf. Algorithm 1.3) on a discrete voxel grid from analytic projections of the modified Shepp Logan phantom using different numeric projection methods within the iterative process. The chosen grayscale window shows a range of [0.16,0.32] out of the maximal range of [0,1]. Limitations of the discrete forward models (cf. Fig. 2.4) manifest themselves in the final reconstruction result.

2.3.2 Quality of iterative tomographic reconstructions

As iterative reconstruction techniques such as SART (cf. Section 1.2.3, Algorithm 1.3) subsequently enforce consistency of the reconstructed volume with each experimentally observed projection image based on a given forward model, inaccuracies of the respective discrete forward projectors will directly translate to artifacts in the reconstruction result. In contrast to typical artifacts arising when reconstructing from an under-determined system of equations, e.g., when reconstructing from too few projections (cf. the example given in Figure 1.4), deficiencies of the projection model defining the system matrix $\boldsymbol{A}$ (cf. Section 1.2.3, Eq. 1.35) inherently do not lie in its null space, and can therefore not, without loss of resolution, be compensated by typical regularization approaches that are otherwise used to suppress artifacts emerging *in the null space* of $\boldsymbol{A}$, i.e., in image domains that are *not affected* by $\boldsymbol{A}$ and its defining projection model.

In order to illustrate the practical consequences, multiple SART reconstructions are compared using different projection algorithms. In general, such experiments typically suffer either from unrelated artifacts when working with actual experimental data, or from the "inverse crime" that is often committed when synthesizing experimental data based on the same algorithms that are also used in the subsequent reconstruction procedure. Both issues can however be avoided in the case of the Shepp-Logan phantom due to the possibility to analytically calculate its projections without prior rasterization, as has been done already for the previous benchmark.

Figure 2.5 shows central axial and sagittal slices of respective SART reconstructions on a 512^3 voxel grid of the Shepp-Logan phantom from analytically calculated projections as described previously. As volume rasterization is here only introduced with the discrete imaging model fundamental to iterative reconstruction techniques, the observed reconstruction artifacts can be largely attributed to the employed discrete projection method. While other parameters such as iteration count or the interpolation scheme of the voxel based backprojector can also be argued to affect the reconstruction outcome, it should nevertheless be without doubt that these, in contrast to the forward model, do not actually explicitly define the properties of the solution.

In accordance with the previously found projection errors shown in Fig. 2.4, the reconstruction quality is found to be worst for the non-oversampling DDA, comparable for 2-fold oversampled DDA and $\mathrm{GJP}_{\mathrm{spl}}$ and best for $\mathrm{GJP}_{\mathrm{lin}}$. Although it is out of the scope of the present work to explicitly demonstrate the effect of each SART parameter, the reader shall however be assured that variations in iteration count, relaxation factor and backprojection interpolation scheme have been confirmed to not fundamentally change the relative performance of different forward models. This is in accordance with the preceding reasoning attributing the differing artifact patterns to differing discretization errors among the various methods.

	DDA		DDA 2×		GJP_{lin}		GJP_{hwlin}	
	GTX970	GTX1080	GTX970	GTX1080	GTX970	GTX1080	GTX970	GTX1080
Tex.	4.59 ms	3.46 ms	15.2 ms	6.74 ms	4.97 ms	2.40 ms	3.28 ms	2.23 ms
	118 GB/s	157 GB/s	143 GB/s	323 GB/s	334 GB/s	686 GB/s	502 GB/s	740 GB/s
RAM	4.39 ms	5.20 ms	15.7 ms	7.65 ms	5.69 ms	2.70 ms	—	—
	123 GB/s	104 GB/s	139 GB/s	285 GB/s	292 GB/s	609 GB/s	—	—

Table 2.1: Average projection speed in milliseconds and memory access rates in gigabytes per second for 2D projections of a cylindrical volume within a 512^3 bounding box onto a 512^2 detector in a 10° conebeam setup measured on both an Nvidia GTX 970 GPU and a more recent GTX 1080 model. The voxel data is stored in 32bit floating point format in either main GPU memory ("RAM") or in read-only texture memory ("Tex."). Timings are measured for the Digital Differential Analyzer (DDA, reproducing Siddon's pencil-beam model), 2-fold oversampled DDA (i.e. tracing and averaging 2×2 rays per detector pixel to simulate finite beam widths) and the proposed Generalized Joseph Projector using linear interpolation (GJP_{lin}).

2.3.3 Projection speed

Run time performance is evaluated for projections of a cylindric volume within a cubic bounding box of 512^3 voxels onto a 512^2 pixel detector. The performance of Algorithm 2.1 is benchmarked against the branchless DDA formulation given by [200]. The volume is stored in 32bit floating point format in either main- or texture memory of the graphics processing unit. For the case of texture memory, also hardware provided interpolation is tested. As typical for computed tomography setups, projections are performed for a multitude of source and detector orientations over the full angular range of 360° on a circular trajectory around the volume center. The rotational axis is aligned parallel to the fastest index of the memory layout (i.e., the first dimension in the case of Fortran-style memory order, or the last dimension in the case of C-style memory order). For each individual configuration of source and detector, the run time is optimized over a wide range of possible thread block or work group size parameters (CUDA and OpenCL terminology respectively). This eliminates the potential influence of technicalities introduced by the parallelization schemes of graphics processors. Measured execution times further exhibit a variance of up to 10% when running the same code multiple times due to dynamic performance adaptions related to temperature management. Reported are the fastest measured times for each algorithm.

Table 2.1 lists the so evaluated run times as averages over 360 equidistant projection angles for two GPU models. As a measure for GPU occupancy it further lists average memory access rates based on the total runtime and the amount of accessed voxels by each raytracing algorithm respectively. Although the latter is not strictly known in the case of GJP_{hwlin} due to unknown implementation details within the GPU, it is reasonably assumed to be the same as for GJP_{lin}.

A number of interesting conclusions can be drawn from the observed timings: First of all, the DDA algorithm can only benefit from newer hardware (GTX 1080) in the oversampled case. Oversampling increases the number of duplicate accesses to the same voxels by parallel threads handling neighboring rays, wherefore it can be reasonably assumed that the oversampled DDA better profits from memory caches. The additional computational overhead associated with oversampling appears to be a limiting factor on older hardware in contrast, where the overall runtime increases almost linear with the amount of traced rays. This assessment is consistent with the observation that the DDA algorithm does not profit from optimized accesses to read only texture memory. The GJP algorithm in contrast is able to outperform even the regular DDA algorithm by a factor of up to 2, despite accessing about twice as much memory on average. The driving axis aligned sampling scheme of the GJP ensures that neighboring threads partially access the same voxels in the course of interpolated sampling, thereby apparently exploiting memory caches even better than the oversampled DDA. The additional speedup observed when simplifying the GJP algorithm even further (by using the intrinsic interpolation capabilities of texture memory) indicates that it operates close to the limits both of the computational resources and the available memory bandwidth (including caching benefits).

2.4 Discussion and Conclusion

The calculation of projections from discrete volumes is a core aspect of iterative reconstruction techniques, both with respect to reconstruction speed and quality. Although a remarkable variety of approaches to the advanced modeling of ray-volume intersections has been presented in previous literature, the demand for maximal parallelizability and computational efficiency on modern graphics processors immediately collapses the wide palette of choices to ray driven methods with strongly confined sampling kernels. "Ray driven" thereby implies a sampling loop iteratively traversing the voxel grid along defined paths (rays) between focal point and detector pixels, and "strongly confined" implies the evaluation of only the immediate neighborhood around each sampling point. For the traversal of regular grids, two methods can be named: the digital differential analyzer (DDA) algorithm [1], traversing the grid in unevenly spaced steps from intersection to intersection with any of the orthogonal grid planes, and methods traversing the grid in equidistant steps aligned with a designated driving axis. The former technique allows to precisely determine line-box intersection lengths and corresponds to the much cited pencil-beam X-ray imaging model given by Siddon [169], while the latter technique is typically combined with interpolated sampling and then corresponds to the competing model proposed in the context of tomographic reconstruction by Joseph [79].

A branchless formulation of a Joseph type interpolating volume projection algorithm has been derived here, with the particular benefit of being extremely simple, which is a general prerequisite for maximal computational efficiency. Driving axis aligned sampling ensures an optimal amount of sampling points along each path in the sense that voxels are neither skipped nor oversampled. The resulting synchronous progression of parallel rays through the voxel grid thereby ensures high cache hit rates without explicitly constraining the exact imaging geometry (as opposed to e.g. the cache optimized Siddon's algorithm proposed by [179], or the symmetry exploiting projection model given by [162]). Interpolated sampling among the remaining dimensions has been argued, besides being a practical necessity, to be consistent with ideas on exact modeling of X-ray projections based on normalized radial basis functions or projection footprints. Approximate matching of the voxel grid spacing to the average density of rays between focal point and detector array thereby ensures an adequate modeling of beam width, implicitly reproducing the integrating nature of detector pixels of finite extent without requiring far ranging interpolation kernels or oversampled ray casting. In accordance with assessments given in previous literature, higher order effects such as cone beam related variations in beam extent can be safely neglected in the modeling. (cf. e.g. [131, 68])

The performed benchmarks compared a number of self-suggesting variants of both ray casting algorithms with respect to artifacts and computational efficiency, addressing the recurring questions of adequate beam shape modeling and the role of the chosen interpolation kernel. The results indicate that no tradeoff needs to be made between computational efficiency and fitness for the purpose: the proposed simple and efficient branchless 3D Joseph projector employing linear interpolation is found to clearly perform best both with regard to approximation of the ground truth and with regard to efficiency, operating in the range of the theoretic maximum capabilities of the employed hardware.

A recurring concern with regard to local interpolation exists in situations where a sufficient matching of the voxel grid resolution to the detector resolution is seemingly impossible. Such situations can e.g. arise when attempting to combine isotropic volume sampling with highly asymmetric detector pixels. It is in such cases obviously generally possible to cast an adequate amount of rays per detector bin ensuring sufficient coverage of the voxel grid, i.e., to adequately oversample the detector image. Similarly, the voxel shape may be chosen non-square (in terms of spatial units) to adequately match the detector properties, which in units of grid indices does not alter the discussed algorithms. Finally, although only one particular example sample was considered for the sake of analytic integrability, it is noteworthy that the observed artifacts arise at extended material boundaries of moderate curvature, i.e., a situation that is typical to many CT applications.

The proposed formulation of a linearly interpolating Joseph-type projection algorithm may eventually be considered a favorable choice in many regards (simplicity of implementation, computational efficiency, and fitness for the purpose) for typical CT reconstruction applications, in particular as compared to the competing DDA algorithm, and further considering that oversampling (i.e., increasing the density of traced rays) generally remains an option.

Chapter 2 extends on the presentations in Dittmann/Graetz 2016/2021 [32] and Dittmann, Hanke 2017 [30]

Chapter 3

Auto-Calibration of Cone Beam Projection Geometries

Knowledge of the precise projection geometry is an essential prerequisite to tomographic reconstruction. Although the geometry is, in principle, ought to be determined by the mechanical design of a system, there are numerous reasons why it nevertheless is commonly not specified to the required precision. Typical examples are systems that lack sufficient mechanical rigidity (e.g., due to heavy weight components), as well as highly flexible systems allowing for varying projection geometries and extreme magnification factors. The latter type is common in the field of micro-CT, which is the focus of the present work. Consequently, practical calibration procedures are required in order to determine the respective projection geometry.

The problem of cone beam CT calibration is closely related to the problem of optical camera calibration, which has been extensively studied in the field of computer vision in terms of intrinsic and extrinsic camera parameters (cf. Section 1.1.3). While optical camera calibration is largely based on planar reference objects, X-ray imaging systems can easily make use of three dimensional calibration structures. And whereas classic calibration generally presumes the reference object to be known, auto-calibration addresses the self-consistent reconstruction of both the reference object and the projection geometry by means of exploiting known relations between multiple images of the same object.

Particularly in the context of micro tomography with sub-millimeter fields of view and sub-micrometer resolutions, well defined reference objects are hardly manufacturable. However, such systems offer high precision mechanical actuators, facilitating precisely defined motion trajectories. And indeed, the characteristic magnification effects in projective imaging will be shown to allow extensive inferences on the projection geometry solely based on the assumption of circular motion of otherwise undefined markers about a common rotational axis.

The following sections will give a concise introduction to the problem and previous literature, and deduce based on the foundations derived in Chapter 1 a practical algorithm to gain the necessary information on source and detector placement required for a consistent tomographic reconstruction of cone beam (micro) computed tomography datasets. The present chapter has been published in [45]

3.1 Classification of approaches based on fiducial markers

Two general classes of approaches can be identified: those based on precisely defined or known marker assemblies [154, 152, 26, 126, 173, 20, 177, 206, 69, 108, 78, 153, 112, 96, 40, 204, 213], which allow calibration on a per-view basis, and those working with fiducials of unknown placement yet requiring precise circular motion of these markers throughout a tomographic scan [55, 95, 130, 172, 206, 187, 198, 52, 157, 203, 94] (with some of these assuming the distances between markers known [130, 206, 187, 198, 203]). While the former methods are typically used for macroscopic systems with fields of view in the range of 10 cm and larger, the latter are required for microscopic systems for which the manufacturing of well-defined calibration phantoms is hard to impossible.

Chapter 3 is published in adapted form as Graetz, Phys. Med. Biol. 2021 [45]

[9] assumes both known markers and perfect rotation, and [25] provides a method to account for deviations from expected precise motions, enabling per-view calibration also for methods originally assuming stable circular motions.

An additional distinction can be made from the technical point of view of system parametrization: methods aiming to determine the projective mapping from 3D to 2D space in terms of a projection matrix that is consistent with the available observations irrespective of the question how the particular mapping arises physically [154, 126, 173, 177, 69, 96], and methods aiming to relate projections or properties thereof to real space geometry parameters (relative distances and orientation angles of source and detector) [55, 95, 154, 152, 130, 9, 172, 20, 206, 108, 78, 153, 112, 40, 198, 52, 157, 203, 204, 94]. Differences also exist in the evaluation of the projection data used for calibration: methods directly working on extracted projection samples (2D points) without further data reduction or interpretation [55, 95, 154, 26, 126, 9, 173, 69, 108, 157, 213, 94], as well as methods reducing the observed projections by means of matching them to an expected model (such as e.g. elliptic trajectories) or otherwise exploiting specific geometric features of the utilized calibration structure [152, 130, 172, 20, 177, 206, 78, 153, 112, 40, 198, 52, 203, 204]. Calibration methods may further be characterized based on their core calibration approaches: [154, 126, 173, 177, 69, 96] reduce the calibration problem to the solution of a linear system of equations in a least squares sense e.g. by means of singular value decomposition (requiring the imaged object to be known). [130, 172, 20, 206, 112, 203, 204] derive direct relations between parameters of the observed marker patterns and the underlying projection geometry. [55, 95, 154, 9, 187, 213] use local optimization techniques requiring sufficiently good initial estimates and [108, 52, 157, 94] rely on global optimization techniques for the solution of the inverse problem (also requiring initial estimates). Combinations are used e.g. in [152, 26, 78, 153], and a comparison of a matrix inversion and an optimization based approach is given by [154]. Finally, the cited methods differ in the amount of degrees of freedom that are addressed. While methods based on fully known reference objects are generally able to determine all system parameters with reasonable precision, the situation is more complex when no or only few assumptions can be made on the calibration structure.

3.2 Review of previous auto-calibration techniques

The early methods addressing the problem of calibration from unknown markers with straight forward least squares minimization approaches considered only the focal distance and the most relevant translations of the detector and the rotational axis [55, 95] due to the instability of the full optimization problem. Noo et al. [130] showed that generic optimization can be largely avoided by systematic analysis of the problem. By constraining the detector columns parallel to the rotational axis, they were able to derive relations between the remaining geometric parameters and the ellipse parameters of the observable projections of two opaque markers moving along circular trajectories around the rotational axis. Potential detector in-plane rotations are considered in an independent preprocessing step. They assumed the distance between the markers known in order to determine also the absolute scale. The method was further simplified by Yang et al. [206] for the case of also negligible detector slant about the rotational axis. Johnston et al. [78] use the latter approximate approach for the initialization of a generic local optimization procedure that is then able to recover all parameters using a phantom of ten collinear bearing balls with defined distances. A further adaption of the Noo method was presented by [198]. Bequé et al. [9, 10] and Wang and Tsui [187] fully revert to local optimization again yet analyze the uniqueness of general solutions based on one, two and three rotating markers and conclude that one known distance between two markers is sufficient in the presence of detector slant about the rotational axis, and two known distances (which they relate to distances between three markers) are required for a generally unique solution for all system parameters, which was also conjectured previously by Noo et al. [130] and is also stated by Xu and Tsui [203]. In the related methods addressing all system parameters based on two known parallel rings (of equal radius) of bearing balls by Cho et al. [20] and Robert et al. [153], this condition is fulfilled by knowledge of both the vertical distance of those circles and their (common) radius. Xu and Tsui [203] propose another calibration procedure based on relations between elliptical projections of rotating markers, known marker distances and the system geometry, yet in contrast to [130, 206, 153] identify geometrically meaningful intersection points on the ellipses

Chapter 3 is published in adapted form as Graetz, Phys. Med. Biol. 2021 [45]

in the style of the approaches by Cho et al. [20] and Strubel et al. [177] (who worked with fully known structures) in order to then obtain simpler relations between those points in the projection image and the geometry parameters. A general methodology for the assessment of uniqueness and stability of calibration problems by means of analyzing the propagation of random errors through the respective forward model has been discussed by Ma et al. [104].

Smekal et al. [172] were, to the author's knowledge, the first to explicitly address the case of complete auto-calibration (up to an unknown object scale, yet including detector tilt) of cone beam tomography systems based on multiple rotating markers at unknown positions *and distances*. The latter were either required or assumed known in the methods discussed so far. They choose a different parametrization for the analysis of the projected circles more directly related to the forward model than the otherwise often used ellipse equation and are able to find relations of those observable parameters to all geometric parameters. In contrast to the previous literature, Smekal et al. conclude that one marker is, in principle, sufficient for all parameters but tilt (and absolute scale). In accordance with previous literature they find that at least two projected trajectories (yet without knowledge of the marker's distance) are required to infer tilt provided that the detector is also slanted about the rotational axis. They do not further investigate the case of zero slant. In their experiments, they use between eight and twelve markers and average the obtained geometry parameters.

The more recent publications by Gross et al. [52], Sawall et al. [157] and Li et al. [94] also consider the problem of complete auto-calibration (up to an unknown scale) without reverting to known sample properties, although all, in contrast to Smekal, require global optimization techniques.

Gross et al. [52] formulate the problem in terms of a homography transform parametrized by the sought-for system properties relating the observable ellipses to a canonical representation of circular trajectories. They were thereby able to eliminate the trajectory parameters from the optimization problem, reducing it to 6 degrees of freedom describing the projection geometry (in comparison, Robert et al. [153] previously reported a reduction of the optimization problem relating ellipse parameters and geometry parameters to 3 dimensions for the case of known trajectory parameters). As has been the case also with previous techniques based on ellipse analysis [130, 20, 177, 206, 153, 198, 203], the evaluated ellipses are expected to be non-degenerate in order to successfully reconstruct the projection geometry. In their experiments, they use between three and twelve markers and generally recommend the use of more than four non-degenerate ellipses for their method.

Sawall et al. [157] apply a genetic optimization algorithm to a straight-forward objective function penalizing the least squares errors between forward model and observations. Rather than using multiple rotating markers within one tomographic scan, they use a single marker scanned at multiple different geometric configurations of the employed tomography setup. As discussed earlier [9, 187], this provides enough information to simultaneously determine each scan geometry. Sawall et al. were the only ones to actually work with the absolute minimum of one marker, although simultaneous calibration of multiple systems or multiple configurations of the same system has been addressed before [9, 187, 78].

Li et al. [94] likewise use global optimization to relate the forward model to observed marker projections, yet specifically design the cost function to exploit known consistency constraints of two-view geometries. Namely, the lines between focal spot, marker and the marker's projection on the detector for two views of the same marker must obviously intersect, and do so at the location of the marker. The complete elimination of degrees of freedom to be optimized, as previously shown by Gross et al. [52], could thereby not be achieved.

In the following, an analytically motivated approach to reference-free calibration will be presented that, in contrast to the ones by Gross et al. [52], Sawall et al. [157] and Li et al. [94], does not require the use of generic non-convex optimization techniques, and thus in particular does not require initial estimates for any of the parameters. It is in this respect most similar to the method described by Smekal et al. [172]. Other than in [172] and other previous approaches, the problem will be parametrized by projection matrix elements, which has previously only been done in the context of known calibration structures (cf. [154, 126, 173, 177, 69, 96]). This will on the one hand allow a very simple representation of the core calibration problem and on the other hand expose the link between methods solely based on constraints on the detector geometry ([172, 52, 157, 94]) and those based on (partial) prior knowledge on the sample (e.g. [9, 10, 177, 20, 187, 78, 153, 203]).

Chapter 3 is published in adapted form as Graetz, Phys. Med. Biol. 2021 [45]

3.3 Formalization of the calibration task

As has been pointed out previously in Section 1.1.2, perspective projections onto planar detectors can generally be expressed in terms of homogeneous coordinates and projection matrices. The 2D cone beam projection $(h(\phi), v(\phi))$ of a circular trajectory $(r\cos(\phi-\phi_0), r\sin(\phi-\phi_0), z)$ about the z-axis then takes the following form:

$$\begin{bmatrix} h'(\phi) \\ v'(\phi) \\ w'(\phi) \end{bmatrix} = \begin{bmatrix} P_{11} & P_{12} & P_{13} & P_{14} \\ P_{21} & P_{22} & P_{23} & P_{24} \\ P_{31} & P_{32} & P_{33} & P_{34} \end{bmatrix} \begin{bmatrix} r'\cos(\phi-\phi_0) \\ r'\sin(\phi-\phi_0) \\ z' \\ w \end{bmatrix} \tag{3.1}$$

$$h(\phi) = h'(\phi)/w'(\phi) \tag{3.2}$$

$$v(\phi) = v'(\phi)/w'(\phi) \tag{3.3}$$

with

$$r = r'/w$$
$$z = z'/w\,.$$

w and w' are the scaling components of the vector on the right-hand side and its projection on the left-hand side respectively. Although the component w on the right-hand side would, if projections of known points were to be calculated, commonly be defined to equal 1, it will be beneficial for the purposes of the following derivations to actually leave it as an open parameter. P_{mn} represent the components of a 3×4 projection matrix $\boldsymbol{P}$ encoding the projection geometry, i.e. the placement of source and detector in 3D space as well as the detector pixel pitches. The detailed relation between geometry and projection matrix is given in Section 1.1.6.

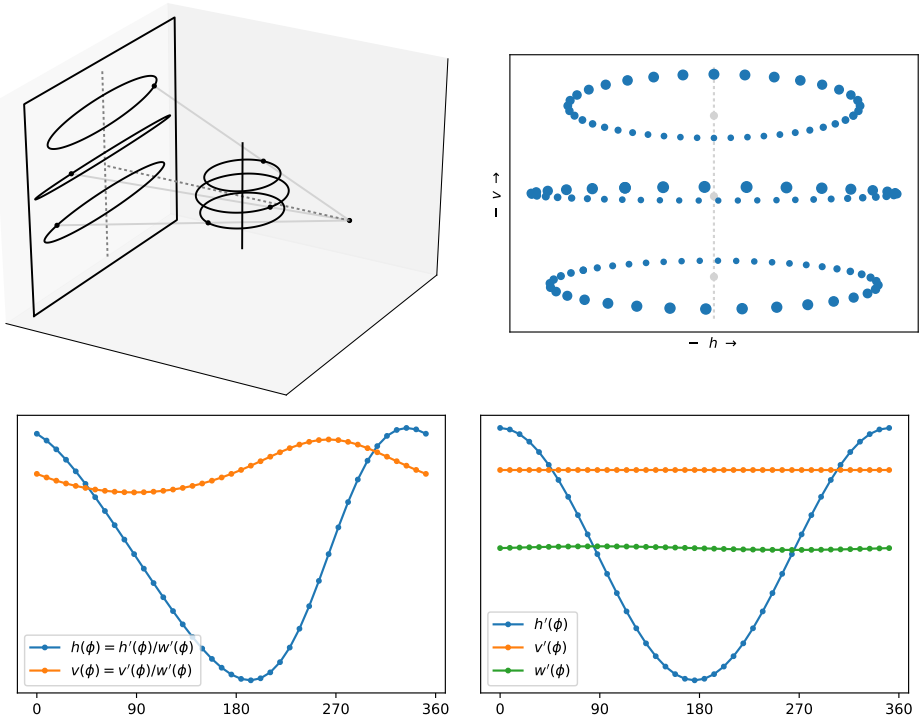

Figure 3.1: *Upper left*: Fiducial markers moving along circular trajectories about the rotational axis (center) of a cone beam computed tomography setup, projected by a point source (right) onto a planar detector (left). *Upper right*: Superposition of respective projection images on the detector. *Lower left*: Horizontal and vertical components of a projected trajectory in dependence of the projection angle ϕ (cf. Eqs. 3.6, 3.7). *Lower right*: Decomposition of the projection components into independent sinusoids describing the orthographic horizontal and vertical projections $h'(\phi)$ and $v'(\phi)$ as well as the perspective scaling component $w'(\phi)$ (cf. Eq. 3.4).

Chapter 3 is published in adapted form as Graetz, Phys. Med. Biol. 2021 [45]

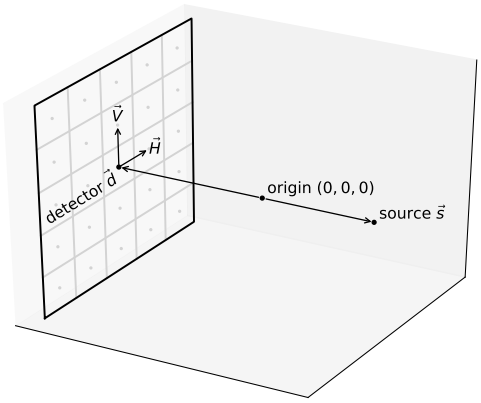

Figure 3.2: Depiction of the real space geometry description used here. The world coordinate origin is centered in the field of view and the positions of source ($\vec{s}$) and detector coordinate origin ($\vec{d}$) are defined relative to that. The row and column vectors $\vec{H}$ and $\vec{V}$ characterize the detector orientation and pixel pitches. $\vec{H}$ and $\vec{V}$ are neither constrained to be orthogonal nor of equal length. The corresponding 3D world coordinates of 2D projection coordinates (h, v) in the projection coordinate system on the detector plane are given by $\vec{d} + h\vec{H} + v\vec{V}$. The relation to projection matrices is described in Section 1.1.2, Eq. 1.7.

Evaluating the above matrix-vector product and applying trigonometric identities yields

$$\begin{bmatrix} h'(\phi) \\ v'(\phi) \\ w'(\phi) \end{bmatrix} = \begin{bmatrix} r'(P_{11}\cos(\phi-\phi_0) + P_{12}\sin(\phi-\phi_0)) + P_{13}z' + P_{14}w \\ r'(P_{21}\cos(\phi-\phi_0) + P_{22}\sin(\phi-\phi_0)) + P_{23}z' + P_{24}w \\ r'(P_{31}\cos(\phi-\phi_0) + P_{32}\sin(\phi-\phi_0)) + P_{33}z' + P_{34}w \end{bmatrix} \tag{3.4}$$

$$= \begin{bmatrix} r'P_{1\mathrm{a}}\sin(\phi-\phi_0-\phi_\mathrm{h}) + P_{13}z' + P_{14}w \\ r'P_{2\mathrm{a}}\sin(\phi-\phi_0-\phi_\mathrm{v}) + P_{23}z' + P_{24}w \\ r'P_{3\mathrm{a}}\sin(\phi-\phi_0-\phi_\mathrm{w}) + P_{33}z' + P_{34}w \end{bmatrix} \tag{3.5}$$

with

$$\begin{aligned} P_{m\mathrm{a}} &= \sqrt{P_{m1}^2 + P_{m2}^2} \\ \phi_\mathrm{h} &= \arctan2(-P_{11}, P_{12}) \\ \phi_\mathrm{v} &= \arctan2(-P_{21}, P_{22}) \\ \phi_\mathrm{w} &= \arctan2(-P_{31}, P_{32}) \\ &\Updownarrow \\ P_{m1} &= -P_{1\mathrm{a}}\sin(\phi_m) \\ P_{m2} &= \;\; P_{1\mathrm{a}}\cos(\phi_m)\,, \end{aligned}$$

where m equally enumerates both the rows (1, 2 and 3) of $\boldsymbol{P}$ as well the associated subscript labels h, v and w, which have been chosen to clearly indicate the relation of the rows or their respective parameters to the three components of the left-hand side homogeneous vector.

The h and v projection coordinates on the detection plane are thus finally given by:

$$h(\phi) = \frac{r'P_{1\mathrm{a}}\sin(\phi-\phi_0-\phi_\mathrm{h}) + P_{13}z' + P_{14}w}{r'P_{3\mathrm{a}}\sin(\phi-\phi_0-\phi_\mathrm{w}) + P_{33}z' + P_{34}w} \tag{3.6}$$

$$v(\phi) = \frac{r'P_{2\mathrm{a}}\sin(\phi-\phi_0-\phi_\mathrm{v}) + P_{23}z' + P_{24}w}{r'P_{3\mathrm{a}}\sin(\phi-\phi_0-\phi_\mathrm{w}) + P_{33}z' + P_{34}w} \quad . \tag{3.7}$$

The numerators in these expressions correspond to the orthographic ("parallel beam") projection, while the common denominator describes the distance dependent perspective scaling. See Figure 3.1 for an example.

As in the context of self consistent calibration neither P_{mn} nor r', z', ϕ_0 and w are known, the above equations may as well be expressed in terms of the independent sinusoid parameters $a_{i\mathrm{h}}$,

Chapter 3 is published in adapted form as Graetz, Phys. Med. Biol. 2021 [45]

$a_{i\mathrm{v}}$, $a_{i\mathrm{w}}$, $\phi_{i0\mathrm{h}}$, $\phi_{i0\mathrm{v}}$, $\phi_{i0\mathrm{w}}$, $o_{i\mathrm{h}}$ and $o_{i\mathrm{v}}$ representing amplitudes, phases and offsets respectively and including an additional index i for the enumeration of multiple projected trajectories:

$$h_i(\phi) = \frac{a_{i\mathrm{h}} \sin(\phi - \phi_{i0\mathrm{h}}) + o_{i\mathrm{h}}}{a_{i\mathrm{w}} \sin(\phi - \phi_{i0\mathrm{w}}) + 1} \tag{3.8}$$

$$v_i(\phi) = \frac{a_{i\mathrm{v}} \sin(\phi - \phi_{i0\mathrm{v}}) + o_{i\mathrm{v}}}{a_{i\mathrm{w}} \sin(\phi - \phi_{i0\mathrm{w}}) + 1} \quad . \tag{3.9}$$

The determination of these 8 sinusoid parameters from projection data $(h_i(\phi), v_i(\phi))$ for each projected trajectory i is detailed in Section 3.7.2 (Eqs. 3.28–3.38 and Alg. 3.2). In the following, the parameters $a_{i\mathrm{h}}$, $a_{i\mathrm{v}}$, $a_{i\mathrm{w}}$, $\phi_{i0\mathrm{h}}$, $\phi_{i0\mathrm{v}}$, $\phi_{i0\mathrm{w}}$, $o_{i\mathrm{h}}$ and $o_{i\mathrm{v}}$ can thus be considered known.

The calibration problem, i.e. the simultaneous reconstruction of both the unknown projection matrix $\boldsymbol{P}$ and the unknown fiducial marker orbits from given projections $(h_i(\phi), v_i(\phi))$, can now be identified as the solution of the following linear system of equations relating the observable sinusoid parameters of the projected trajectories to the unknown projection matrix and orbit parameters for all imaged trajectories i:

$$r_i' P_{1\mathrm{a}} = a_{i\mathrm{h}} \tag{3.10}$$
$$r_i' P_{2\mathrm{a}} = a_{i\mathrm{v}} \tag{3.11}$$
$$r_i' P_{3\mathrm{a}} = a_{i\mathrm{w}} \tag{3.12}$$

$$P_{13} z_i' + P_{14} w_i = o_{i\mathrm{h}} \tag{3.13}$$
$$P_{23} z_i' + P_{24} w_i = o_{i\mathrm{v}} \tag{3.14}$$
$$P_{33} z_i' + P_{34} w_i = o_{i\mathrm{w}} = 1 \tag{3.15}$$

$$\phi_{\mathrm{h}} = 0 \tag{3.16}$$
$$\phi_{\mathrm{v}} = \phi_{i0\mathrm{v}} - \phi_{i0\mathrm{h}} \tag{3.17}$$
$$\phi_{\mathrm{w}} = \phi_{i0\mathrm{w}} - \phi_{i0\mathrm{h}} \tag{3.18}$$

where ϕ_{h} is defined to be 0, exploiting the freedom of choice of the projection angle for a rotationally symmetric imaging configuration (or equivalently the freedom of choice of the initial phase of a periodic trajectory). Further, the fixed parameter $o_{i\mathrm{w}} = 1$ has been introduced in order to maintain a uniform representation of the equations. For the same reason, the subscripts "h", "v" and "w" will in the following as well be represented by the projection matrix' row index m, i.e. $\mathrm{h} \mathrel{\widehat{=}} 1, \mathrm{v} \mathrel{\widehat{=}} 2, \mathrm{w} \mathrel{\widehat{=}} 3$. A practical method for the solution of the above calibration equations is described in Section 3.7.1.

3.4 Projective ambiguities

The given equations further reveal that the first two and last two columns of $\boldsymbol{P}$ are independent, i.e. there are no equations interrelating these parts of the projection matrix (Eqs. 3.10–3.12 are independent from Eqs. 3.13–3.15). Similarly, the relation between z_i' and w_i and consequently the third and fourth column of $\boldsymbol{P}$ is not unique (cf. Eqs. 3.13–3.15). Together with the ambiguities expected by design, i.e., arbitrary choice of length units, object scale and related source–object distance, definition of the $\phi = 0°$ orientation within the x-y plane and the choice of origin on the z-axis, these ambiguities are a special case of general projective ambiguities of the form

$$\boldsymbol{P}\vec{x} = \boldsymbol{P}\boldsymbol{H}^{-1}\boldsymbol{H}\vec{x} = (\boldsymbol{P}\boldsymbol{H}^{-1})(\boldsymbol{H}\vec{x}) = \tilde{\boldsymbol{P}}\tilde{\vec{x}}\,, \tag{3.19}$$

with the homography $\boldsymbol{H}$ being composed of the following transformations in the present case:

$$\begin{aligned} \boldsymbol{H} &= \boldsymbol{R}_z(\omega)\, \boldsymbol{T}_z(\Delta z)\, \boldsymbol{S}(s_{\mathrm{d}}, s_{\mathrm{o}})\, \boldsymbol{D}(\delta, \gamma) \\ \boldsymbol{H}^{-1} &= \boldsymbol{D}^{-1}(\delta, \gamma)\, \boldsymbol{S}(s_{\mathrm{d}}^{-1}, s_{\mathrm{o}}^{-1})\, \boldsymbol{T}_z(-\Delta z)\, \boldsymbol{R}_z(-\omega)\,, \end{aligned} \tag{3.20}$$

Chapter 3 is published in adapted form as Graetz, Phys. Med. Biol. 2021 [45]

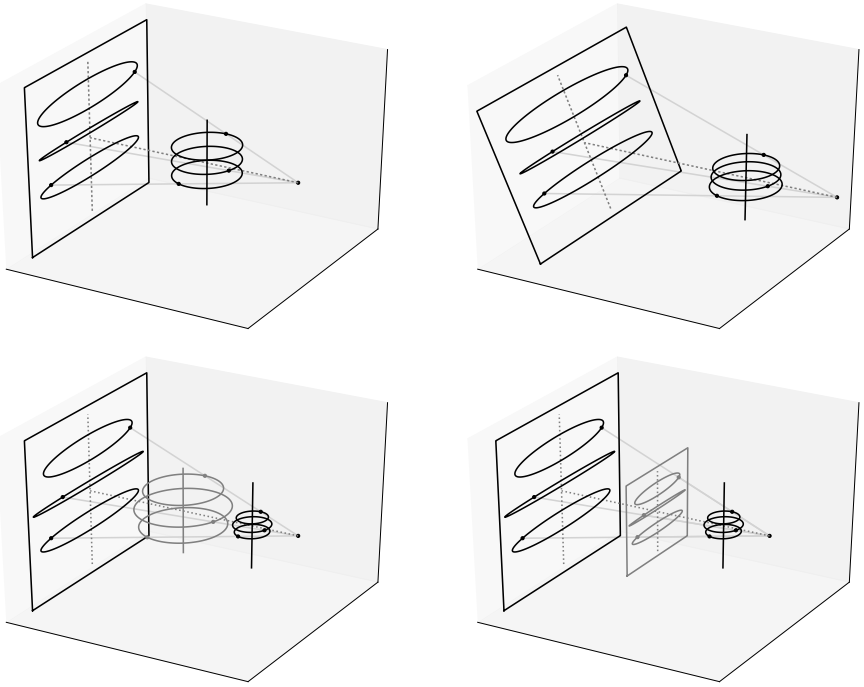

Figure 3.3: Examples of projective ambiguity: the same projections $(h(\phi), v(\phi))$ may originate from different combinations of imaging configuration and marker locations. The top row illustrates the effect of $\boldsymbol{D}(\delta = 1, \gamma \neq 0)$, while the bottom row shows examples of $\boldsymbol{S}$ with the effects of the parameters s_o (bottom left) and s_d (bottom right) respectively (cf. Eqs. 3.19–3.23). The latter case corresponds to the general scaling degree of freedom of homogeneous projection matrices.

with

$$\boldsymbol{R}_z(\omega) = \begin{bmatrix} \cos(\omega) & -\sin(\omega) & 0 & 0 \\ \sin(\omega) & \cos(\omega) & 0 & 0 \\ 0 & 0 & 1 & 0 \\ 0 & 0 & 0 & 1 \end{bmatrix} \qquad \boldsymbol{T}_z(\Delta z) = \begin{bmatrix} 1 & 0 & 0 & 0 \\ 0 & 1 & 0 & 0 \\ 0 & 0 & 1 & \Delta z \\ 0 & 0 & 0 & 1 \end{bmatrix} \tag{3.21}$$

$$\boldsymbol{S}(s_\mathrm{d}, s_\mathrm{o}) = s_\mathrm{d} \begin{bmatrix} 1 & 0 & 0 & 0 \\ 0 & 1 & 0 & 0 \\ 0 & 0 & 1 & 0 \\ 0 & 0 & 0 & s_\mathrm{o} \end{bmatrix} \tag{3.22}$$

$$\boldsymbol{D}(\delta, \gamma) = \begin{bmatrix} 1 & 0 & 0 & 0 \\ 0 & 1 & 0 & 0 \\ 0 & 0 & 1/\delta & 0 \\ 0 & 0 & \gamma & 1 \end{bmatrix} \qquad \boldsymbol{D}^{-1}(\delta, \gamma) = \begin{bmatrix} 1 & 0 & 0 & 0 \\ 0 & 1 & 0 & 0 \\ 0 & 0 & \delta & 0 \\ 0 & 0 & -\delta\gamma & 1 \end{bmatrix}. \tag{3.23}$$

Rotation $\boldsymbol{R}_z(\omega)$, z-translation $\boldsymbol{T}_z(\Delta z)$ and gobal scale s_d correspond to a choice of reference frame and length unit that can be made at the users convenience. The object scale s_o affects both the object size and the relation between source–axis and detector–axis distance accordingly and can only be determined based on prior knowledge on the sample and will therefore be arbitrarily fixed to $s_\mathrm{o} = 1$ here. $\boldsymbol{D}(\delta, \gamma)$ describes the initially mentioned independence of Eqs. 3.10–3.12 and Eqs. 3.13–3.15 and affects the object and detector geometry respectively and is therefore of particular interest here. Examples of the ambiguities described by $\boldsymbol{D}$ and $\boldsymbol{S}$ are depicted in Figure 3.3.

In contrast to the other transformations, $\boldsymbol{D}(\delta, \gamma)$ can be constrained by drawing upon further knowledge on the imaging system, whose pixel aspect ratio as well as the angle between detector rows and columns is commonly known. Anticipating the following subsections, it can be summarized that with $\gamma = 0$, δ may be chosen according to Equation 3.24. Otherwise, γ and δ can be simultaneously

Chapter 3 is published in adapted form as Graetz, Phys. Med. Biol. 2021 [45]

determined by optimization of an objective function as defined by Equation 3.25. In the case of zero detector slant about the rotational axis, Equation 3.25 has no unique minimum and therefore many solutions for γ and δ.

Equivalently, knowledge on the sample such as relative distances between markers could be used as well in order to determine the two parameters defining $\boldsymbol{D}$. This however shall not be further considered here given the specific focus on calibration based on unknown marker locations.

3.4.1 Detector pixel aspect ratio

When considering the relations $r'_i P_{m\mathrm{a}} = a_{im}$ (Eqs. 3.10–3.12) and assuming some consistent solutions for r'_i and $P_{m\mathrm{a}}$ have already been found, it is easy to see that these solutions may be scaled by an arbitrary factor $\alpha \neq 0$:

$$r'_i P_{m\mathrm{a}} = r'_i \frac{\alpha}{\alpha} P_{m\mathrm{a}} = (\alpha r'_i)(\frac{1}{\alpha} P_{m\mathrm{a}}) = \tilde{r}'_i \tilde{P}_{m\mathrm{a}} = a_{im} \quad .$$

The same is true for z'_i and P_{m3} (Eqs. 3.13–3.15):

$$z'_i P_{m3} = z'_i \frac{\beta}{\beta} P_{m3} = (\beta z'_i)(\frac{1}{\beta} P_{m3}) = \tilde{z}'_i \tilde{P}_{m3} = o_{im}$$

with an independent scaling parameter $\beta \neq 0$. While the freedom to choose an arbitrary overall scale corresponds to the unknown absolute size of the imaged phantom, the freedom to choose *independent* scales for the x-y and the z dimensions or equivalently for r'_i and z'_i or $P_{m\mathrm{a}}$ and P_{m3} corresponds to the disregarded pixel pitches of the detector, i.e. the calibration equations can equally be satisfied by a detector with asymmetric pixels and a correspondingly squeezed or stretched object.

Conversely, this ambiguity corresponding to the homography parameter δ (cf. Eq. 3.23) can be resolved by choosing the relative scale $\alpha/\beta = \delta_\varepsilon$ such that the detector encoded in $\boldsymbol{P}$ actually features the correct pixel aspect ratio (denoted by ε) for the given hardware. As derived in Section 1.1.6, the vector products $(P_{11}, P_{12}, P_{13}) \times (P_{31}, P_{32}, P_{33})$ and $(P_{21}, P_{22}, P_{23}) \times (P_{31}, P_{32}, P_{33})$ are proportional to the detector row and column vectors $\vec{H}$ and $\vec{V}$ (Fig. 3.2, Eq. 1.17). Given a known pixel aspect ratio $\varepsilon \stackrel{!}{=} \|\vec{H}\| / \|\vec{V}\|$, δ_ε may therefore be defined as the solution to

$$\begin{gathered} \varepsilon \|\vec{V}(\delta_\varepsilon)\| \stackrel{!}{=} \|\vec{H}(\delta_\varepsilon)\| \\ \varepsilon \,\|(P_{11}, P_{12}, \delta_\varepsilon P_{13}) \times (P_{31}, P_{32}, \delta_\varepsilon P_{33})\| = \|(P_{21}, P_{22}, \delta_\varepsilon P_{23}) \times (P_{31}, P_{32}, \delta_\varepsilon P_{33})\| \quad , \end{gathered}$$

i.e.

$$\begin{aligned} \delta_\epsilon &= \sqrt{\frac{(P_{21}P_{32} - P_{22}P_{31})^2 - \varepsilon^2 (P_{11}P_{32} - P_{12}P_{31})^2}{\varepsilon^2 (P_{12}P_{33} - P_{13}P_{32})^2 + \varepsilon^2 (P_{13}P_{31} - P_{11}P_{33})^2 \\ \qquad - (P_{22}P_{33} - P_{23}P_{32})^2 - (P_{23}P_{31} - P_{21}P_{33})^2}} \\ &= \sqrt{\frac{H_z^2 - \varepsilon^2 V_z^2}{\varepsilon^2 (V_x^2 + V_y^2) - (H_x^2 + H_y^2)}} \quad , \end{aligned} \tag{3.24}$$

where the H_x, H_y, H_z and V_x, V_y, V_z components refer here to those prior to the correction by the derived scaling factor δ_ε. The above derivations assumed that the remaining homography parameter γ is zero.

Chapter 3 is published in adapted form as Graetz, Phys. Med. Biol. 2021 [45]

3.4.2 Detector tilt and shear

Also the relations $P_{m3}z'_i + P_{m4}w_i = o_{im}$ (Eqs. 3.13–3.15) may similarly be satisfied by transformed $\tilde{P}_{m3}$, $\tilde{z}'_i$ and $\tilde{w}_i$, now including also γ:

$$P_{m3}z'_i + P_{m4}w_i = \delta(P_{m3} - \gamma P_{m4})(\frac{1}{\delta}z'_i) + P_{m4}(w_i + \gamma z'_i) = \tilde{P}_{m3}\tilde{z}'_i + P_{m4}\tilde{w}_i = o_{im} \quad .$$

By relating w_i and P_{m3}, γ will affect the detector tilt and shear as will be explained in the following.

Equation 3.15 ($P_{33}z'_i + P_{34}w_i = o_{iw} = 1$) concerning the mean $o_{iw} = 1$ of the projection equations' denominators (cf. Eqs. 3.8 and 3.9) reveals that for $w_i = \text{const.}$, P_{33} must equal 0. Vice versa, w_i varying among several imaged trajectories i (i.e. being z'_i-dependent) implies $P_{33} \neq 0$. Given $\tilde{w}_i = w_i + \gamma z'_i$ and $\tilde{P}_{33} = P_{33} - \gamma P_{34}$, it can therefore be concluded that both the relevance of the homogeneous coordinates' scaling components w_i and the role of the homography parameter γ are directly related to the P_{33} component of the projection matrix. Eq 1.7 (Section 1.1.2) shows that the vector (P_{31}, P_{32}, P_{33}) in the last row of $\boldsymbol{P}$ corresponds to the cross product $\vec{H} \times \vec{V}$ of the detector row and column orientations and is therefore normal to the detector plane. The z component P_{33} is thus directly related to the detector tilt towards the rotational axis, which was defined to coincide with the z-axis. In consequence, γ controls the detector tilt encoded in $\tilde{\boldsymbol{P}}$. As changes to P_{m3} have more general implications on the cross products of $(\vec{d} - \vec{s})$, $\vec{H}$ and $\vec{V}$ encoded in the first three columns of $\boldsymbol{P}$, γ will also influence the angle between $\vec{H}$ and $\vec{V}$. As this is commonly a known property of the detector (typically, $\vec{H} \cdot \vec{V} = 0$), it can be used to constrain γ and consequently to determine the detector tilt towards the z-axis. As γ will as well affect the norms of $\vec{H}$ and $\vec{V}$, i.e. the pixel aspect ratio, γ usually needs to be determined simultaneously with δ using a suiting objective function constraining both the pixel aspect ratio and orthogonality:

$$\gamma, \delta_\varepsilon = \underset{\gamma,\delta}{\operatorname{argmin}} \left(\left(\frac{\left\|\vec{H}(\gamma,\delta)\right\|}{\varepsilon\left\|\vec{V}(\gamma,\delta)\right\|} - \frac{\varepsilon\left\|\vec{V}(\gamma,\delta)\right\|}{\left\|\vec{H}(\gamma,\delta)\right\|} \right)^2 + \left(\frac{\vec{H}(\gamma,\delta) \cdot \vec{V}(\gamma,\delta)}{\left\|\vec{H}(\gamma,\delta)\right\| \left\|\vec{V}(\gamma,\delta)\right\|} \right)^2 \right) \tag{3.25}$$

with ε denoting the pixel aspect ratio and assuming that the detector rows and columns are expected to be orthogonal. In case of actually non-orthogonal detectors such as hexagonal pixel arrangements, the objective function may be adjusted accordingly to favor the respective expected shear angle.

The detector tilt has been identified by many authors to have the smallest influence on the observable projections and therefore can, in the presence of noise, only be determined with very little precision. In particular in the context of calibration based on unknown phantoms, the detector is therefore often fixed to be parallel to the rotational axis. Within the present approach, this is equivalent to fixing w_i to 1 and consequently P_{33} to 0, as has been done within the present solution strategy for the reconstruction of $\boldsymbol{P}$ (cf. Algorithm 3.1, Section 3.7.1). Actual detector tilts will then manifest themselves in a slight amount of artificial shear (slightly non-orthogonal detector rows and columns) in the determined projection geometry. As this corresponds to a valid projective homography, resulting tomographic reconstructions using so constrained geometries will be transformed by the corresponding inverse homography. In contrast to the case of both constrained tilt *and* pixel geometry, actual artifacts due to geometric inconsistencies are avoided.

In accordance with the findings by Smekal et al. [172], the tilt cannot be uniquely determined when the detector is not slanted about the rotational axis. This remaining ambiguity manifests itself in a non-unique minimum of the objective function in Eq. 3.25 in the case of zero detector slant.

Chapter 3 is published in adapted form as Graetz, Phys. Med. Biol. 2021 [45]

3.5 Simulation Study

The calibration procedure has been tested on simulations of a large set of randomly generated imaging configurations and fiducial marker positions in order to obtain information on the average precision independent of the particular projection geometry or calibration phantom. The random samples are generated from both a mean imaging configuration and mean phantom shape with broad variances on the actual positions and orientations. In units of detector pixels, detectors with roughly 1500 to 3000 pixels width and 1000 to 2000 pixels height at a source–detector distance of 10000 times the detector pixel size are modeled, yielding cone angles in the range of about $(12 \pm 5)°$. With the rotational axis virtually placed at the location of the detector, also the sample units can be meaningfully measured in units of detector pixels. Fiducial markers are, on average, distributed equidistantly along the z-direction between -650 and $+650$ pixels at a mean distance of 800 pixels from the z-axis (i.e., the rotational axis). Apart from the source–detector distance, all parameters including detector shifts and tilts are varied randomly. The marker vertical positions and lateral distances (i.e., radii) are varied based on a a normal distribution of 150 and 250 pixels standard deviation respectively. The projection parameters are varied with uniform distributions. The considered ranges are ± 250 and ± 500 pixels for the horizontal and vertical offsets of the detector center from the optical axis respectively and $\pm 5°$ for detector tilt, slant and rotation. In order to avoid the unresolvable projective ambiguity in the case of zero slant of the detector about the rotational axis, the interval of $[-0.2°, +0.2°]$ has been excluded here. For each configuration, 120 projections in 3° increments about the rotational axis have been calculated and Gaussian noise with a variance of half a pixel was added to the marker projections to account for imprecisions usually occurring when evaluating actual projection data of opaque markers. Figure 3.4 shows examples of respective simulated projection data.

Calibration was performed based on the solution strategy for Eqs. 3.12–3.18 derived in Section 3.7. More specifically, each projected trajectory is first reduced to its sinusoid parameters by means of Algorithm 3.2. Based on these observables, a self consistent solution for markers and projection matrix is found by means of Algorithm 3.1. The projective ambiguities are resolved by means of Eq. 3.19, 3.23 and 3.25 constraining the detector rows and columns to be orthogonal and the pixel aspect ratio to be 1. The resulting projection matrix is transformed into real space geometry vectors describing relative source and detector position as well as row and column orientation by means of Algorithm 1.1 and the known detector pixel pitch. In order to compare this result to the original (randomly generated) imaging geometry, the reconstructed geometry is finally rotated and shifted about and along the z axis respectively such that the source comes to line on the y axis.

Figure 3.5 shows the distribution of errors found for 10^6 random realizations of the just described experiment. Table 3.1 summarizes the error ranges corresponding to a 98% confidence interval, i.e. in 98% of the cases, the true values will lie within the listed intervals about the reconstructed values.

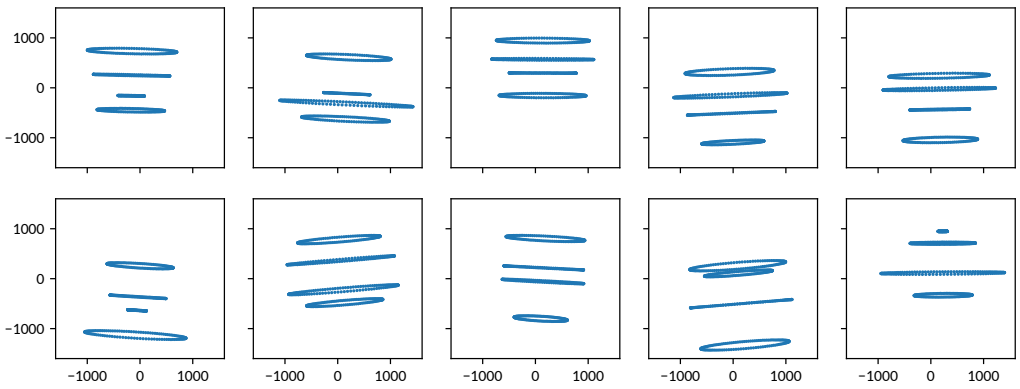

Figure 3.4: Examples of simulated projections of rotating fiducial markers as used to quantify the auto calibration precision. Both the projection geometry and the marker placement are randomly generated. Positions are given in units of detector pixels, with the origin defined in the detector's center. Auto calibration is performed both from all shown trajectories (4 markers) as well as from only the top and bottom ones (2 markers). Cf. Fig. 3.5.

Chapter 3 is published in adapted form as Graetz, Phys. Med. Biol. 2021 [45]

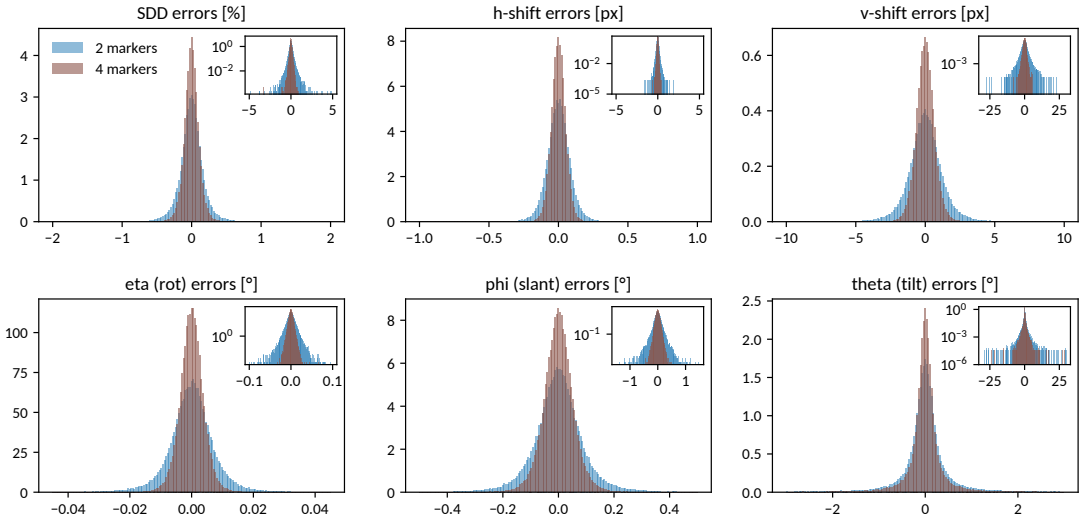

Figure 3.5: Normalized histograms (probability densities) showing calibration variances in terms of classic geometry parameters found for projection geometries reconstructed from noisy projections of circular trajectories. (examples given in Fig. 3.4). Actual projection geometries and trajectories are generated randomly. The reconstructions have been performed using either four (purple) or only two (blue) of the projected trajectories. The inset graphs visualize the tails of the respective distributions using a logarithmic scale. Table 3.1 summarizes the error ranges for a 98% confidence interval. The respective reprojection errors between the reconstructed projections and the input data are found to reproduce the modeled noise of 0.5px standard deviation within a standard error of 0.05px, which appears consistent with the number of simulated projections.

	source–detector distance	horizontal detector shift	vertical detector shift	detector slant (φ)	detector rotation (η)	detector tilt (θ)
4 markers	$\pm 0.3\%$	± 0.13px	± 1.7px	$\pm 0.14°$	$\pm 0.01°$	$\pm 1.6°$
2 markers	$\pm 0.5\%$	± 0.22px	± 3.6px	$\pm 0.27°$	$\pm 0.02°$	$\pm 2.3°$

Table 3.1: Geometry reconstruction errors within a 98% confidence interval for reconstructions based on two and four projected marker trajectories respectively. The differing orders of magnitude of uncertainty associated with different geometry parameters reflect their differing impact on actual projection errors. Rotation η and horizontal shift h (cf. Fig. 3.6) have the most direct relation to projections and are therefore recovered most precisely.

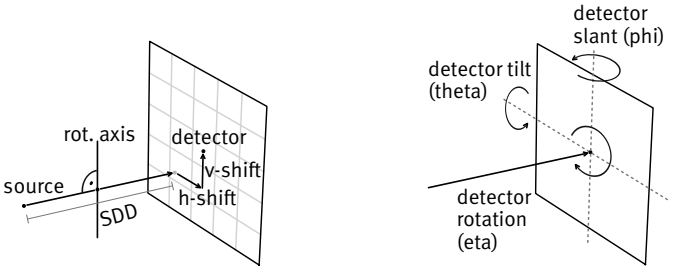

Figure 3.6: Sketches depicting the employed geometry parametrization. The source–detector distance SDD is measured parallel to the source position vector $\vec{s}$, horizontal (h) and vectical (v) detector shifts are measured in units of the row and column vectors $\vec{H}$ and $\vec{V}$. The detector orientation is characterized by the angles φ and θ describing the orientation of its normal with respect to the source orientation $\vec{s}$ as well as the angle η describing the in-plane rotation of the detector about its normal.

Chapter 3 is published in adapted form as Graetz, Phys. Med. Biol. 2021 [45]

Particularly the distribution of errors on the detector tilt towards the rotational axis exhibits long tails including rare (as seldom as one in a million) yet extreme deviations (up to 25°) from the true value. As the detector tilt is part of the projective ambiguity in the solution of Equations 3.10–3.18 as detailed in Section 3.4, it has to be inferred by enforcing a known detector pixel geometry. As the latter is implicitly assumed to be unaffected by noise, any actual noise will translate onto the remaining parameters of the imaging geometry, causing large uncertainties on the inferred tilt. Further, as the determined homography inversely applies to the reconstructed sample, errors on the detector tilt will come along with errors on the z scale and consequently on the aspect ratio of the reconstructed samples.

3.6 Discussion

An auto-calibration method for cone beam tomography systems has been derived from the projection matrix formulation of the perspective projection of rotating fiducial markers. The representation in cylinder coordinates directly reveals both a fractions-of-sinusoids model describing the observable projections as well as linear relations of this model's parameters to both the unknown projection matrix and the parameters of the circular marker trajectories. (In the case of known trajectory parameters, the system of equations could at this point be directly solved for the unknown projection matrix analog to other projection matrix calibration methods based on known objects [154, 173, 96].) An iterative scheme is proposed that alternatingly solves the linear system of equations with respect to the projection matrix and the trajectories until a self consistent solution is obtained, starting with initial approximations for the trajectory parameters. A simple weighting heuristic accounts for the adequate consideration of redundant equations. The ambiguities in the self consistent solution are formalized to a sparse homography matrix, which is then constrained based on knowledge of the detector pixel geometry. Finally, a transformation of projection matrices into real space vectors describing source and detector position as well as detector row and column orientations is given. Other geometry descriptions can be derived from either the projection matrices or the real space vectors using common techniques that have not been further detailed here.

The forward model reveals that the projected circular trajectories are completely described by a total of 8 parameters (which can be identified with those that were previously also used by Smekal et al. [172]). In contrast to the ellipse description of projected circles (generally using 5 parameters) that has been used by many authors [130, 20, 177, 206, 78, 153, 198, 52, 203], not only the shape, but also the projection angle (ϕ) dependence is captured in this description. This assumably is the underlying reason why degeneracy of ellipses, which is a major issue for the respective methods based on ellipse parameters, is not a particularly special case in this representation – all 8 parameters are still defined also in the case of an edge-on projection within the plane of rotation of a circular orbit. The forward model itself almost directly exposes the solution to the calibration problem in form of the system of equations relating the sinusoid parameters to the contained system parameters. The employed forward model is further clearly separated into orthographic projections (numerators) and perspective scaling (denominator), allowing for direct interpretations of the parameters. The denominator or perspective scaling component is associated with the third row of the projection matrix (cf. Eqs. 3.4–3.7), which in turn describes, as is explicitly shown in Eq. 1.7, the detector normal and focal distance. This clearly highlights that the ability to determine the orientation of the detector normal (i.e., to determine detector slant and tilt) without knowledge of the sample dimensions is ultimately founded in the specific perspective scaling effects associated with the detector orientation. Conversely, this ability becomes restricted in the case of ambiguous scaling effects: in the case of zero detector slant (i.e., the rotational axis intersects the orthogonal connecting line between detector and source), scaling effects due to a potentially tilted detector become indiscernible from an actually distorted sample, and, as has been reported previously by several authors [152, 9, 187, 157], additional knowledge or assumptions will thus be required (usually, the assumption of zero detector tilt will be adequate given its typically small effect [130, 172, 206]). In the present method, this ambiguity manifests itself in a degenerate minimum of the objective function used to determine the homography parameters as discussed in Section 3.4.

Regarding the positioning or selection of fiducial markers within the field of view, although no explicit analyses have been shown, several general arguments can be made. First of all, markers

Chapter 3 is published in adapted form as Graetz, Phys. Med. Biol. 2021 [45]

obviously must not be located on the rotational axis, i.e., the radius of its circular trajectory must not be zero. The larger the radius relative to the detector grid, the smaller the relative errors in the determination of the projected positions. Larger radii further imply larger covered cone angles and thus more pronounced perspective scaling effects, which have been identified to be essential to auto-calibration from unknown samples. Analogously, although edge-on projections are not a fundamental issue here, trajectories further away from the cone center plane will exhibit stronger perspective effects and are therefore expected to be favorable. This is also consistent with the observations by Bequé et al. [10] in context of their least squares optimization approach. Also, placement of markers only within one half of the cone does not constitute a special case, in contrast to ellipse based methods as introduced by Noo et al. [130]. In order to account for the original assumption of the present work that markers are apriori unknown, the presented simulation study intentionally addresses a wide range of imaginable marker placements and projection geometries, without explicitly investigating potentially favorable configurations.

One reason for the simplicity of the present calibration approach lies in the additional degree of freedom of oblique detector grids that is implicit in the projection matrix formalism. The relation between detector tilt and detector grid geometry through the homography parameters γ and δ (cf. Section 3.4) on the one hand allows to shift the determination of tilt into a downstream postprocessing procedure, and on the other hand provides another view on the previously reported imprecision immanent to the determination of detector tilt [172, 52], which could also be observed in the present results. The imprecision in the determination of tilt is in fact an imprecision in the determination of the correct homography transformation (affecting both the projection matrix and the object coordinate system) based on constraints on the detector geometry instead of constraints on the sample geometry. As even considerable tilts in the range of degrees translate to rather moderate amounts of detector non-orthogonality, the noise susceptibility for the converse inference of tilt by means of constraining detector shear is very high. In particular the long tails of the error distribution found in the present simulations (cf. Fig. 3.5 and Table 3.1) evidence a very high uncertainty in the determination of tilt that often ranges within the order of magnitude of its actual value. The plain assumption of zero tilt is thus, as has been concluded by others previously [172, 52], often well within the error margin. In contrast to previous work though, which by design also constrained the detector geometry, consistency won't be affected here, as actual effects due to tilt will still be accounted for by means of an artificially oblique detector geometry.

The remaining homography parameters regarding the choice of origin and scale of the coordinate system have not been explicitly treated. They are straight-forwardly chosen based on the real space geometry description extracted from the reconstructed projection matrix (cf. Section 1.1.2) in order to e.g. align the source position or the detector normal with the x-z or y-z plane and scale and shift source and detector within the available degrees of freedom such that a user defined tomographic reconstruction field of view optimally fits the projection cone.

Chapter 3 is published in adapted form as Graetz, Phys. Med. Biol. 2021 [45]

3.7 Appendix: Implementation

3.7.1 Iterative projection matrix reconstruction

Now that the calibration problem has been formalized to the solution of a small system of linear equations, an iterative scheme technique shall be proposed for its self consistent solution. The calibration equations (Eqs. 3.10–3.18) may to this end be rearranged for each parameter to be determined, assuming the respective parameters on the right-hand side known (beginning with initial estimates). As there will be multiple analog equations for each parameter relating it to either different rows of the projection matrix or to multiple of the observed projected trajectories, weighted averages will be used to adequately incorporate all available information for each parameter. In order to avoid potential oscillations due to inconsistencies, the iterative updates may be damped by a relaxation factor $\lambda \in [0;1]$ scaling between no update ($\lambda = 0$) and no damping ($\lambda = 1$).

Without specifying the averaging weights yet, the described scheme results in:

$$
\begin{aligned}
w_i &:= 1 \\
r_i'^{(k+1)} &= (1-\lambda) r_i'^{(k)} + \lambda \left\langle \frac{a_{im}}{P_{m\mathrm{a}}^{(k)}} \right\rangle_m \\
z_i'^{(k+1)} &= (1-\lambda) z_i'^{(k)} + \lambda \left\langle \frac{o_{im} - P_{m4}^{(k)}}{P_{m3}^{(k)}} \right\rangle_m \\
P_{m\mathrm{a}}^{(k+1)} &= (1-\lambda) P_{m\mathrm{a}}^{(k)} + \lambda \left\langle \frac{a_{im}}{r_i'^{(k)}} \right\rangle_i \\
\begin{matrix} P_{m3}^{(k+1)} \\ P_{m4}^{(k+1)} \end{matrix} &= (1-\lambda) \begin{matrix} P_{m3}^{(k)} \\ P_{m4}^{(k)} \end{matrix} + \lambda \underset{P_{m3}^*, P_{m4}^*}{\operatorname{argmin}} \left(P_{m3}^* z_i'^{(k)} + P_{m4}^* - o_{im} \right)^2 \\
\phi_{\mathrm{h}} &:= 0 \\
\phi_{\mathrm{v}} &= \langle \phi_{i0\mathrm{v}} - \phi_{i0\mathrm{h}} \rangle_i \\
\phi_{\mathrm{w}} &= \langle \phi_{i0\mathrm{w}} - \phi_{i0\mathrm{h}} \rangle_i
\end{aligned}
$$

where k is the iteration index, $\langle \cdot \rangle_i$ and $\langle \cdot \rangle_m$ denote (to be further defined) weighted averages over the marker index i and the projection matrix row index m respectively. For uniformity of the representation, the row related "h", "v" and "w" indices of the observable sinusoid parameters are equally enumerated by m in the above averages, i.e. $\mathrm{h} \mathrel{\widehat{=}} 1, \mathrm{v} \mathrel{\widehat{=}} 2, \mathrm{w} \mathrel{\widehat{=}} 3$. Based on the discussion given in Section 3.4.2, w_i has been chosen $w_i = 1$ without loss of generality. The parameters P_{m3}, P_{m4} are determined by means of linear regression. The phases ϕ_{w} and ϕ_{v} can be evaluated independently as a weighted average over the available observations, whereas ϕ_{h} is, without loss of generality, defined 0.

Now that the iterative update scheme has been established, actual averaging weights need to be defined. These weights shall respect the varying certainty or error bar associated with the different available equations for each parameter. It will be argued that the denominators occurring in the right-hand-side expressions are reasonable indicators in this respect and may be used as weighting factors, which in addition avoids potential divisions by zero. This can be easily seen on the example of r_i': the observable amplitudes a_{im} on the right hand side correspond to actual horizontal and vertical ranges covered by the projections observed on a rasterized detector. Given some absolute precision in the determination of the projection's coordinates, the relative uncertainty of some a_{im} will be lower the larger its absolute value. As a_{im} are, given the relation $a_{im} = r_i' P_{m\mathrm{a}}$, proportional to the parameters $P_{m\mathrm{a}}$, the latter may as well be used for the respective importance weighting. This reasoning can analogously be transferred to the remaining parameters as well, finally leading to the explicit alternating update scheme stated in Algorithm 3.1, with the weights being formed as the square of the denominators to ensure positivity. The averages over the differences $\phi_{i0\mathrm{v}} - \phi_{i0\mathrm{h}}$ and $\phi_{i0\mathrm{w}} - \phi_{i0\mathrm{h}}$ are performed (cf. Alg. 3.1) over their complex amplitude representation (with $\boldsymbol{i}$ denoting the imaginary unit). The weighting factors $a_{i\mathrm{h}}^2$, $a_{i\mathrm{v}}^2$ and $a_{i\mathrm{w}}^2$ for the phases $\phi_{i0\mathrm{h}}$, $\phi_{i0\mathrm{v}}$ and $\phi_{i0\mathrm{h}}$ thereby follow the same heuristic as outlined previously.

Chapter 3 is published in adapted form as Graetz, Phys. Med. Biol. 2021 [45]

Algorithm 3.1 Self-consistent reconstruction of projection matrix and marker coordinates from projections of circular marker trajectories (solving Eqs. 3.10–3.18). The homogeneous scaling components w_i are, without loss of generality, constrained to 1 (thereby constraining the detector tilt angle towards the rotational axis to $\theta = 0$). Differing values of tilt and scaling of the marker trajectories can be recovered subsequently based on projective homographies as outlined in Section 3.4.

$$\left.\begin{matrix} a_{i\mathrm{h}} & \phi_{i0\mathrm{h}} & o_{i\mathrm{h}} \\ a_{i\mathrm{v}} & \phi_{i0\mathrm{v}} & o_{i\mathrm{v}} \\ a_{i\mathrm{w}} & \phi_{i0\mathrm{w}} & o_{i\mathrm{w}} \end{matrix}\right\} \leftarrow \text{Algorithm 3.2 } (h_i(\phi), v_i(\phi))\ \forall\, i \qquad \triangleright \text{ Sinusoid parameters extracted from projection data}$$

$r_i'^{(0)} \leftarrow a_{i\mathrm{h}}$ ▷ initialize radii with horizontal trajectory amplitudes

$z_i'^{(0)} \leftarrow o_{i\mathrm{v}}$ ▷ initialize z-coordinates with vertical means

$P_{m\mathrm{a}}^{(0)} \leftarrow \frac{\sum_i r_i'^{(0)} a_{im}}{\sum_i r_i'^{(0)\,2}}$ ▷ initialize with (weighted) mean amplitudes

$P_{m3}^{(0)} \leftarrow \frac{\sum_i (z_i'^{(0)} - \overline{z'}^{(0)})(o_{im} - \overline{o}_m)}{\sum_i (z_i'^{(0)} - \overline{z'}^{(0)})^2}$ ▷ $P_{m3}^{(0)}, P_{m4}^{(0)} = \underset{P_{m3}, P_{m4}}{\operatorname{argmin}} \left(P_{m3}\, z_i'^{(0)} + P_{m4} - o_{im} \right)$

$P_{m4}^{(0)} \leftarrow \overline{o}_m - P_{m3}^{(0)}\, \overline{z'}^{(0)}$ ▷ with $\overline{z'}^{(0)} = \frac{1}{N}\sum_i z_i'^{(0)}; \quad \overline{o}_m = \frac{1}{N}\sum_i o_{im}$

for $k = 0 \,..\, N_{\mathrm{iter}} - 1$ **do** with $\lambda \in]0; 1]$ ▷ iteratively enforce Eqs. 3.10–3.15

$r_i'^{(k+1)} \leftarrow (1-\lambda) r_i'^{(k)} + \lambda \frac{\sum_m P_{m\mathrm{a}}^{(k)} a_{im}}{\sum_m P_{m\mathrm{a}}^{(k)\,2}}$

$z_i'^{(k+1)} \leftarrow (1-\lambda) z_i'^{(k)} + \lambda \frac{\sum_m P_{m3}^{(k)} (o_{im} - P_{m4}^{(k)})}{\sum_m P_{m3}^{(k)\,2}}$

$P_{m\mathrm{a}}^{(k+1)} \leftarrow (1-\lambda) P_{m\mathrm{a}}^{(k)} + \lambda \frac{\sum_i r_i'^{(k)} a_{im}}{\sum_i r_i'^{(k)\,2}}$

$P_{m3}^{(k+1)} \leftarrow (1-\lambda) P_{m3}^{(k)} + \lambda \frac{\sum_i (z_i'^{(k)} - \overline{z'}^{(k)})(o_{im} - \overline{o}_m)}{\sum_i (z_i'^{(k)} - \overline{z'}^{(k)})^2}$ ▷ $\underset{P_{m3}, P_{m4}}{\operatorname{argmin}} \left(P_{m3}\, z_i'^{(k)} + P_{m4} - o_{im} \right)$

$P_{m4}^{(k+1)} \leftarrow (1-\lambda) P_{m4}^{(k)} + \lambda \left(\overline{o}_m - P_{m3}^{(k)}\, \overline{z'}^{(k)} \right)$ ▷ $\overline{z'}^{(k)} = \frac{1}{N}\sum_i z_i'^{(k)};\ \overline{o}_m = \frac{1}{N}\sum_i o_{im}$

end for

$\phi_{\mathrm{h}} \leftarrow 0$

$\phi_{\mathrm{v}} \leftarrow \arg\left(\sum_i (e^{\boldsymbol{i}(\phi_{i0\mathrm{v}} - \phi_{i0\mathrm{h}})} a_{i\mathrm{v}}^2 a_{i\mathrm{h}}^2) \right)$

$\phi_{\mathrm{w}} \leftarrow \arg\left(\sum_i (e^{\boldsymbol{i}(\phi_{i0\mathrm{w}} - \phi_{i0\mathrm{h}})} a_{i\mathrm{w}}^2 a_{i\mathrm{h}}^2) \right)$

$\phi_{i0} \leftarrow \arg\left(\sum_m (e^{\boldsymbol{i}(\phi_{i0m} - \phi_m)} a_{im}^2) \right)$

$$\boldsymbol{P} \leftarrow \begin{bmatrix} -P_{1\mathrm{a}}\sin(\phi_{\mathrm{h}}) & P_{1\mathrm{a}}\cos(\phi_{\mathrm{h}}) & P_{13} & P_{14} \\ -P_{2\mathrm{a}}\sin(\phi_{\mathrm{v}}) & P_{2\mathrm{a}}\cos(\phi_{\mathrm{v}}) & P_{23} & P_{14} \\ -P_{3\mathrm{a}}\sin(\phi_{\mathrm{w}}) & P_{3\mathrm{a}}\cos(\phi_{\mathrm{w}}) & P_{33} & P_{14} \end{bmatrix}; \qquad \boldsymbol{x}_i \leftarrow \begin{bmatrix} r_i'\cos(\phi_{i0}) \\ -r_i'\sin(\phi_{i0}) \\ z_i' \\ 1 \end{bmatrix}$$

$\boldsymbol{P} \leftarrow \boldsymbol{P}\boldsymbol{H}^{-1}; \quad \boldsymbol{x}_i \leftarrow \boldsymbol{H}\boldsymbol{x}_i$ ▷ resolve projective ambiguities with additional contraints, cf. Section 3.4 and especially Eqs. 3.23, 3.24, 3.25

Chapter 3 is published in adapted form as Graetz, Phys. Med. Biol. 2021 [45]

3.7.2 Extraction of the trajectories' sinusoid parameters

As explained previously in Section 3.3, arbitrary cone beam projections of circular trajectories can be represented in the following way:

$$u(\phi) = \frac{a_\mathrm{u} \sin(\phi - \phi_{\mathrm{u}0}) + o_\mathrm{u}}{a_\mathrm{w} \sin(\phi - \phi_{\mathrm{w}0}) + 1} \quad ,$$

with $u(\phi)$ on the left-hand side representing either of the projections' $h(\phi)$ and $v(\phi)$ coordinates on the detection plane and $a_\mathrm{u}, a_\mathrm{w}, \phi_{\mathrm{u}0}, \phi_{\mathrm{w}0}, o_\mathrm{u}$ being the parameters encoding both the location of the projected marker and properties of the projection geometry. While Section 3.3 covered the reconstruction of both the actual trajectories and the projection matrix from these parameters, their extraction from the measured projections $(h(\phi), v(\phi))$ shall be detailed here using an approach inspired by the Fourier decomposition of h and v used by Smekal et al 2004 [172].

The above equation may be rearranged by multiplying with the denominator:

$$u(\phi)\,(a_\mathrm{w} \sin(\phi - \phi_{\mathrm{w}0}) + 1) = a_\mathrm{u} \sin(\phi - \phi_{\mathrm{u}0}) + o_\mathrm{u}$$

and expanding the sine functions $a_\mathrm{u} \sin(\phi - \phi_{\mathrm{u}0})$ into $s_\mathrm{u} \sin(\phi) + c_\mathrm{u} \cos(\phi)$ such that

$$u(\phi)\,(s_\mathrm{w} \sin(\phi) + c_\mathrm{w} \cos(\phi) + 1) = s_\mathrm{u} \sin(\phi) + c_\mathrm{u} \cos(\phi) + o_\mathrm{u} \tag{3.26}$$

with

$$\begin{aligned} a_\mathrm{u} &= \sqrt{s_\mathrm{u}^2 + c_\mathrm{u}^2} \\ \phi_{\mathrm{u}0} &= \operatorname{arctan2}\left(\sin(\phi_{\mathrm{u}0}), \cos(\phi_{\mathrm{u}0})\right) \\ &= \operatorname{arctan2}(-c_\mathrm{u}, s_\mathrm{u}) \,. \end{aligned}$$

Now the above ϕ dependent equation (3.26) relating $u(\phi)$ to the five parameters $s_\mathrm{w}, c_\mathrm{w}$ and $s_\mathrm{u}, c_\mathrm{u}, o_\mathrm{u}$ can be expanded into five ϕ independent equations by considering different integrals of both sides exploiting the orthogonality relations of the sine and cosine functions on the interval $\phi \in [0, 2\pi)$. When considering the right-hand side it is easy to see that integrating with respect to ϕ over multiples of a period will effectively single out o_u, and similarly multiplying the equation by $\sin(\phi)$ or $\cos(\phi)$ prior to integration will "select" parameters s_u or c_u respectively, while at the same time obviously eliminating the ϕ dependence of the equation. Further equations required to determine also s_w and c_w are obtained by considering integrals over $\sin(2\phi)$ and $\cos(2\phi)$ respectively, which is equivalent to regarding higher frequency components of the equations. Applying the aforesaid integrals yields:

$$\begin{array}{llll} s_\mathrm{w} \int_0^{2\pi} \mathrm{d}\phi\, u(\phi) \sin(\phi) & + c_\mathrm{w} \int_0^{2\pi} \mathrm{d}\phi\, u(\phi) \cos(\phi) & + \int_0^{2\pi} \mathrm{d}\phi\, u(\phi) & = 2\pi o_\mathrm{u} \\ s_\mathrm{w} \int_0^{2\pi} \mathrm{d}\phi\, u(\phi) \sin^2(\phi) & + c_\mathrm{w} \int_0^{2\pi} \mathrm{d}\phi\, u(\phi) \sin(\phi) \cos(\phi) & + \int_0^{2\pi} \mathrm{d}\phi\, u(\phi) \sin(\phi) & = \pi s_\mathrm{u} \\ s_\mathrm{w} \int_0^{2\pi} \mathrm{d}\phi\, u(\phi) \sin(\phi) \cos(\phi) & + c_\mathrm{w} \int_0^{2\pi} \mathrm{d}\phi\, u(\phi) \cos^2(\phi) & + \int_0^{2\pi} \mathrm{d}\phi\, u(\phi) \cos(\phi) & = \pi c_\mathrm{u} \\ s_\mathrm{w} \int_0^{2\pi} \mathrm{d}\phi\, u(\phi) \sin(2\phi) \sin(\phi) & + c_\mathrm{w} \int_0^{2\pi} \mathrm{d}\phi\, u(\phi) \sin(2\phi) \cos(\phi) & + \int_0^{2\pi} \mathrm{d}\phi\, u(\phi) \sin(2\phi) & = 0 \\ s_\mathrm{w} \int_0^{2\pi} \mathrm{d}\phi\, u(\phi) \cos(2\phi) \sin(\phi) & + c_\mathrm{w} \int_0^{2\pi} \mathrm{d}\phi\, u(\phi) \cos(2\phi) \cos(\phi) & + \int_0^{2\pi} \mathrm{d}\phi\, u(\phi) \cos(2\phi) & = 0 \quad . \end{array}$$

When dividing by 2π and denoting the different integrals over $u(\phi)$ by $\overline{u}, u_\mathrm{s}, u_\mathrm{c}, u_\mathrm{sc} u_\mathrm{ss}, u_{\mathrm{s}_2\mathrm{c}}$, etc. with indices indicating the accompanying sine and cosine terms (i.e. $u_{\mathrm{s}_2\mathrm{c}} = \frac{1}{2\pi} \int_0^{2\pi} \mathrm{d}\phi\, u(\phi) \sin(2\phi) \cos(\phi)$, $\overline{u} = \frac{1}{2\pi} \int_0^{2\pi} \mathrm{d}\phi\, u(\phi)$), the system of equations simplifies to

$$\begin{aligned} s_\mathrm{w} u_\mathrm{s} + c_\mathrm{w} u_\mathrm{c} + \overline{u} &= o_\mathrm{u} \\ s_\mathrm{w} u_\mathrm{ss} + c_\mathrm{w} u_\mathrm{sc} + u_\mathrm{s} &= \frac{s_\mathrm{u}}{2} \\ s_\mathrm{w} u_\mathrm{sc} + c_\mathrm{w} u_\mathrm{cc} + u_\mathrm{c} &= \frac{c_\mathrm{u}}{2} \\ s_\mathrm{w} u_{\mathrm{s}_2\mathrm{s}} + c_\mathrm{w} u_{\mathrm{s}_2\mathrm{c}} + u_{\mathrm{s}_2} &= 0 \\ s_\mathrm{w} u_{\mathrm{sc}_2} + c_\mathrm{w} u_{\mathrm{cc}_2} + u_{\mathrm{c}_2} &= 0 \quad , \end{aligned} \tag{3.27}$$

Chapter 3 is published in adapted form as Graetz, Phys. Med. Biol. 2021 [45]

with $s_\mathrm{u}, c_\mathrm{u}, o_\mathrm{u}$ and $s_\mathrm{w}, c_\mathrm{w}$ being the sought unknowns. The latter two can be obtained by inverting the last two equations, while the former can then be directly computed using the first three equations:

$$\begin{bmatrix} u_{\mathrm{s_2s}} & u_{\mathrm{s_2c}} \\ u_{\mathrm{sc_2}} & u_{\mathrm{cc_2}} \end{bmatrix} \begin{bmatrix} s_\mathrm{w} \\ c_\mathrm{w} \end{bmatrix} = - \begin{bmatrix} u_{\mathrm{s_2}} \\ u_{\mathrm{c_2}} \end{bmatrix}$$

$$\begin{bmatrix} s_\mathrm{w} \\ c_\mathrm{w} \end{bmatrix} = - \begin{bmatrix} u_{\mathrm{s_2s}} & u_{\mathrm{s_2c}} \\ u_{\mathrm{sc_2}} & u_{\mathrm{cc_2}} \end{bmatrix}^{-1} \begin{bmatrix} u_{\mathrm{s_2}} \\ u_{\mathrm{c_2}} \end{bmatrix}$$

$$\begin{bmatrix} s_\mathrm{w} \\ c_\mathrm{w} \end{bmatrix} = (u_{\mathrm{s_2c}} u_{\mathrm{sc_2}} - u_{\mathrm{s_2s}} u_{\mathrm{cc_2}})^{-1} \begin{bmatrix} u_{\mathrm{cc_2}} & -u_{\mathrm{s_2c}} \\ -u_{\mathrm{sc_2}} & u_{\mathrm{s_2s}} \end{bmatrix} \begin{bmatrix} u_{\mathrm{s_2}} \\ u_{\mathrm{c_2}} \end{bmatrix}$$

i.e.

$$s_{\mathrm{w}(u)} = \frac{u_{\mathrm{cc_2}} u_{\mathrm{s_2}} - u_{\mathrm{s_2c}} u_{\mathrm{c_2}}}{u_{\mathrm{s_2c}} u_{\mathrm{sc_2}} - u_{\mathrm{s_2s}} u_{\mathrm{cc_2}}} \tag{3.28}$$

$$c_{\mathrm{w}(u)} = \frac{u_{\mathrm{s_2s}} u_{\mathrm{c_2}} - u_{\mathrm{sc_2}} u_{\mathrm{s_2}}}{u_{\mathrm{s_2c}} u_{\mathrm{sc_2}} - u_{\mathrm{s_2s}} u_{\mathrm{cc_2}}} \tag{3.29}$$

$$o_\mathrm{u} = \quad s_\mathrm{w} u_\mathrm{s} + c_\mathrm{w} u_\mathrm{c} + \overline{u} \tag{3.30}$$

$$s_\mathrm{u} = 2(s_\mathrm{w} u_\mathrm{ss} + c_\mathrm{w} u_\mathrm{sc} + u_\mathrm{s}) \tag{3.31}$$

$$c_\mathrm{u} = 2(s_\mathrm{w} u_\mathrm{sc} + c_\mathrm{w} u_\mathrm{cc} + u_\mathrm{c}) \tag{3.32}$$

$$a_\mathrm{u} = \sqrt{s_\mathrm{u}^2 + c_\mathrm{u}^2} \tag{3.33}$$

$$a_\mathrm{w} = \sqrt{s_\mathrm{w}^2 + c_\mathrm{w}^2} \tag{3.34}$$

$$\phi_{\mathrm{w}0} = \mathrm{arctan2}(-c_\mathrm{w}, s_\mathrm{w}) \tag{3.35}$$

$$\phi_{\mathrm{u}0} = \mathrm{arctan2}(-c_\mathrm{u}, s_\mathrm{u}) \quad . \tag{3.36}$$

Although all five parameters can be determined independently for both horizontal and vertical projection components $h(\phi)$ and $v(\phi)$ respectively (represented by $u(\phi)$ here), s_w and c_w – or equivalently a_w and $\phi_{\mathrm{w}0}$ – are shared parameters that are expected to be identical for both $h(\phi)$ and $v(\phi)$. It is therefore advisable to use a weighted average of the respective $s_{\mathrm{w}(u)}$ and $c_{\mathrm{w}(u)}$ parameters obtained from the horizontal ($u = \mathrm{h}$) and vertical ($u = \mathrm{v}$) projection components for the computation of the remaining parameters. A sensible choice for the relative importance weights are the respective determinants of both available systems of equations for s_w and c_w, i.e.:

$$s_w = \frac{(h_{\mathrm{s_2c}} h_{\mathrm{sc_2}} - h_{\mathrm{s_2s}} h_{\mathrm{cc_2}})(h_{\mathrm{cc_2}} h_{\mathrm{s_2}} - h_{\mathrm{s_2c}} h_{\mathrm{c_2}}) + (v_{\mathrm{s_2c}} v_{\mathrm{sc_2}} - v_{\mathrm{s_2s}} v_{\mathrm{cc_2}})(v_{\mathrm{cc_2}} v_{\mathrm{s_2}} - v_{\mathrm{s_2c}} v_{\mathrm{c_2}})}{(h_{\mathrm{s_2c}} h_{\mathrm{sc_2}} - h_{\mathrm{s_2s}} h_{\mathrm{cc_2}})^2 + (v_{\mathrm{s_2c}} v_{\mathrm{sc_2}} - v_{\mathrm{s_2s}} v_{\mathrm{cc_2}})^2} \tag{3.37}$$

$$c_w = \frac{(h_{\mathrm{s_2c}} h_{\mathrm{sc_2}} - h_{\mathrm{s_2s}} h_{\mathrm{cc_2}})(h_{\mathrm{s_2s}} h_{\mathrm{c_2}} - h_{\mathrm{sc_2}} h_{\mathrm{s_2}}) + (v_{\mathrm{s_2c}} v_{\mathrm{sc_2}} - v_{\mathrm{s_2s}} v_{\mathrm{cc_2}})(v_{\mathrm{s_2s}} v_{\mathrm{c_2}} - v_{\mathrm{sc_2}} v_{\mathrm{s_2}})}{(h_{\mathrm{s_2c}} h_{\mathrm{sc_2}} - h_{\mathrm{s_2s}} h_{\mathrm{cc_2}})^2 + (v_{\mathrm{s_2c}} v_{\mathrm{sc_2}} - v_{\mathrm{s_2s}} v_{\mathrm{cc_2}})^2} \,. \tag{3.38}$$

The weighting accounts for the generally considerably differing amplitudes of $h(\phi)$ and $v(\phi)$ and the therefore differing relative error within the derived quantities; and in particular also for the singular case of one of the determinants becoming zero. This occurs in the case of a projection view parallel to the circular trajectory when either $h(\phi)$ or $v(\phi)$ become constant (ϕ independent), which commonly is the case for $v(\phi)$ in a perfectly aligned system.

Algorithm 3.2 compiles the above derivations into an explicit procedure for the deduction of the sinusoid parameters $a_{i\mathrm{h}}$, $a_{i\mathrm{v}}$, $a_{i\mathrm{w}}$, $\phi_{i0\mathrm{h}}$, $\phi_{i0\mathrm{v}}$, $\phi_{i0\mathrm{w}}$, $o_{i\mathrm{h}}$ and $o_{i\mathrm{v}}$ fully describing the perspective projections of rotating points (cf. Eqs. 3.8–3.9). The inner products with respect to various trigonometric functions are expressed as explicit sums over equidistantly sampled rotation angles ϕ_j. The nature of trigonometric functions and the periodic form of the considered problem thereby ensures that no discretization errors are introduced, analog to classic Fourier analysis (cf. e.g. the Handbook of Mathematics [14]). Indeed, these sums can, by application of trigonometric identities, also be formulated in terms of standard Fourier coefficients $u_{\mathrm{s}_n} = \frac{1}{N} \sum_{j=0}^{N-1} u_j \sin(n \frac{2\pi}{N} j)$ and $u_{\mathrm{c}_n} = \frac{1}{N} \sum_{j=0}^{N-1} u_j \cos(n \frac{2\pi}{N} j)$, such that e.g. $u_{\mathrm{sc_2}} = \frac{1}{4}(u_{\mathrm{s}_1} + u_{\mathrm{s}_3})$, with $u \in \{h, v\}$.

The latter representation reveals that Fourier components of $u(\phi)$ up to the third harmonic are implicitly used in the above derivations implying that $N \geq 6$ (despite the fact that only 5

Chapter 3 is published in adapted form as Graetz, Phys. Med. Biol. 2021 [45]

parameters are actually to be determined), which is e.g. also consistent with the publication by Noo et al. [130] in context of a completely different method for the actual retrieval of the projection parameters. Fourier coefficients up to the third harmonic of the projected trajectories were also used by Smekal et al. [172] as input to their calibration procedure.

Chapter 3 is published in adapted form as Graetz, Phys. Med. Biol. 2021 [45]

Algorithm 3.2 Extraction of circular trajectories' sinusoid parameters $a_{i\mathrm{h}}$, $a_{i\mathrm{v}}$, $a_{i\mathrm{w}}$, $\phi_{i0\mathrm{h}}$, $\phi_{i0\mathrm{v}}$, $\phi_{i0\mathrm{w}}$, $o_{i\mathrm{h}}$ and $o_{i\mathrm{v}}$ (cf. Eqs. 3.8–3.9) as required for Algorithm 3.1 from perspective projections $(h_i(\phi), v_i(\phi))$, assuming an equidistant sampling of the rotation phase $\phi \in [0, 2\pi[$. The trajectory index i has been omitted for better readability. A detailed derivation is given in Section 3.7.2.

$$
\begin{aligned}
\phi_j &= 2\pi/N\, j \\
h_j &= h(\phi_j) \\
v_j &= v(\phi_j)
\end{aligned}
$$

$$
\begin{aligned}
\overline{h} &= \tfrac{1}{N}\textstyle\sum_{j=0}^{N-1} h_j & \qquad \overline{v} &= \tfrac{1}{N}\textstyle\sum_{j=0}^{N-1} v_j \\
h_{\mathrm{s}} &= \tfrac{1}{N}\textstyle\sum_{j=0}^{N-1} h_j \sin(\phi_j) & \qquad v_{\mathrm{s}} &= \tfrac{1}{N}\textstyle\sum_{j=0}^{N-1} v_j \sin(\phi_j) \\
h_{\mathrm{c}} &= \tfrac{1}{N}\textstyle\sum_{j=0}^{N-1} h_j \cos(\phi_j) & \qquad v_{\mathrm{c}} &= \tfrac{1}{N}\textstyle\sum_{j=0}^{N-1} v_j \cos(\phi_j) \\
h_{\mathrm{ss}} &= \tfrac{1}{N}\textstyle\sum_{j=0}^{N-1} h_j \sin^2(\phi_j) & \qquad v_{\mathrm{ss}} &= \tfrac{1}{N}\textstyle\sum_{j=0}^{N-1} v_j \sin^2(\phi_j) \\
h_{\mathrm{sc}} &= \tfrac{1}{N}\textstyle\sum_{j=0}^{N-1} h_j \sin(\phi_j)\cos(\phi_j) & \qquad v_{\mathrm{sc}} &= \tfrac{1}{N}\textstyle\sum_{j=0}^{N-1} v_j \sin(\phi_j)\cos(\phi_j) \\
h_{\mathrm{cc}} &= \tfrac{1}{N}\textstyle\sum_{j=0}^{N-1} h_j \cos^2(\phi_j) & \qquad v_{\mathrm{cc}} &= \tfrac{1}{N}\textstyle\sum_{j=0}^{N-1} v_j \cos^2(\phi_j) \\
h_{\mathrm{s}_2} &= \tfrac{1}{N}\textstyle\sum_{j=0}^{N-1} h_j \sin(2\phi_j) & \qquad v_{\mathrm{s}_2} &= \tfrac{1}{N}\textstyle\sum_{j=0}^{N-1} v_j \sin(2\phi_j) \\
h_{\mathrm{c}_2} &= \tfrac{1}{N}\textstyle\sum_{j=0}^{N-1} h_j \cos(2\phi_j) & \qquad v_{\mathrm{c}_2} &= \tfrac{1}{N}\textstyle\sum_{j=0}^{N-1} v_j \cos(2\phi_j) \\
h_{\mathrm{s}_2\mathrm{s}} &= \tfrac{1}{N}\textstyle\sum_{j=0}^{N-1} h_j \sin(2\phi_j)\sin(\phi_j) & \qquad v_{\mathrm{s}_2\mathrm{s}} &= \tfrac{1}{N}\textstyle\sum_{j=0}^{N-1} v_j \sin(2\phi_j)\sin(\phi_j) \\
h_{\mathrm{s}_2\mathrm{c}} &= \tfrac{1}{N}\textstyle\sum_{j=0}^{N-1} h_j \sin(2\phi_j)\cos(\phi_j) & \qquad v_{\mathrm{s}_2\mathrm{c}} &= \tfrac{1}{N}\textstyle\sum_{j=0}^{N-1} v_j \sin(2\phi_j)\cos(\phi_j) \\
h_{\mathrm{sc}_2} &= \tfrac{1}{N}\textstyle\sum_{j=0}^{N-1} h_j \sin(\phi_j)\cos(2\phi_j) & \qquad v_{\mathrm{sc}_2} &= \tfrac{1}{N}\textstyle\sum_{j=0}^{N-1} v_j \sin(\phi_j)\cos(2\phi_j) \\
h_{\mathrm{cc}_2} &= \tfrac{1}{N}\textstyle\sum_{j=0}^{N-1} h_j \cos(\phi_j)\cos(2\phi_j) & \qquad v_{\mathrm{cc}_2} &= \tfrac{1}{N}\textstyle\sum_{j=0}^{N-1} v_j \cos(\phi_j)\cos(2\phi_j)
\end{aligned}
$$

$$
\begin{aligned}
s_{\mathrm{w}} &= \frac{(h_{\mathrm{s}_2\mathrm{c}}h_{\mathrm{sc}_2} - h_{\mathrm{s}_2\mathrm{s}}h_{\mathrm{cc}_2})(h_{\mathrm{cc}_2}h_{\mathrm{s}_2} - h_{\mathrm{s}_2\mathrm{c}}h_{\mathrm{c}_2}) + (v_{\mathrm{s}_2\mathrm{c}}v_{\mathrm{sc}_2} - v_{\mathrm{s}_2\mathrm{s}}v_{\mathrm{cc}_2})(v_{\mathrm{cc}_2}v_{\mathrm{s}_2} - v_{\mathrm{s}_2\mathrm{c}}v_{\mathrm{c}_2})}{(h_{\mathrm{s}_2\mathrm{c}}h_{\mathrm{sc}_2} - h_{\mathrm{s}_2\mathrm{s}}h_{\mathrm{cc}_2})^2 + (v_{\mathrm{s}_2\mathrm{c}}v_{\mathrm{sc}_2} - v_{\mathrm{s}_2\mathrm{s}}v_{\mathrm{cc}_2})^2} \\
c_{\mathrm{w}} &= \frac{(h_{\mathrm{s}_2\mathrm{c}}h_{\mathrm{sc}_2} - h_{\mathrm{s}_2\mathrm{s}}h_{\mathrm{cc}_2})(h_{\mathrm{s}_2\mathrm{s}}h_{\mathrm{c}_2} - h_{\mathrm{sc}_2}h_{\mathrm{s}_2}) + (v_{\mathrm{s}_2\mathrm{c}}v_{\mathrm{sc}_2} - v_{\mathrm{s}_2\mathrm{s}}v_{\mathrm{cc}_2})(v_{\mathrm{s}_2\mathrm{s}}v_{\mathrm{c}_2} - v_{\mathrm{sc}_2}v_{\mathrm{s}_2})}{(h_{\mathrm{s}_2\mathrm{c}}h_{\mathrm{sc}_2} - h_{\mathrm{s}_2\mathrm{s}}h_{\mathrm{cc}_2})^2 + (v_{\mathrm{s}_2\mathrm{c}}v_{\mathrm{sc}_2} - v_{\mathrm{s}_2\mathrm{s}}v_{\mathrm{cc}_2})^2}
\end{aligned}
$$

$$
\begin{aligned}
s_{\mathrm{h}} &= 2(s_{\mathrm{w}}h_{\mathrm{ss}} + c_{\mathrm{w}}h_{\mathrm{sc}} + h_{\mathrm{s}}) & \qquad s_{\mathrm{v}} &= 2(s_{\mathrm{w}}v_{\mathrm{ss}} + c_{\mathrm{w}}v_{\mathrm{sc}} + v_{\mathrm{s}}) \\
c_{\mathrm{h}} &= 2(s_{\mathrm{w}}h_{\mathrm{sc}} + c_{\mathrm{w}}h_{\mathrm{cc}} + h_{\mathrm{c}}) & \qquad c_{\mathrm{v}} &= 2(s_{\mathrm{w}}v_{\mathrm{sc}} + c_{\mathrm{w}}v_{\mathrm{cc}} + v_{\mathrm{c}})
\end{aligned}
$$

$$
\begin{aligned}
o_{\mathrm{h}} &= \quad s_{\mathrm{w}}h_{\mathrm{s}} + c_{\mathrm{w}}h_{\mathrm{c}} + \overline{h} & \qquad o_{\mathrm{v}} &= \quad s_{\mathrm{w}}v_{\mathrm{s}} + c_{\mathrm{w}}v_{\mathrm{c}} + \overline{v} \\
a_{\mathrm{h}} &= \sqrt{s_{\mathrm{h}}^2 + c_{\mathrm{h}}^2} & \qquad a_{\mathrm{v}} &= \sqrt{s_{\mathrm{v}}^2 + c_{\mathrm{v}}^2} \\
\phi_{\mathrm{h}0} &= \operatorname{arctan2}(-c_{\mathrm{h}}, s_{\mathrm{h}}) & \qquad \phi_{\mathrm{v}0} &= \operatorname{arctan2}(-c_{\mathrm{v}}, s_{\mathrm{v}}) \\
& & \qquad o_{\mathrm{w}} &= 1 \\
& & \qquad a_{\mathrm{w}} &= \sqrt{s_{\mathrm{w}}^2 + c_{\mathrm{w}}^2} \\
& & \qquad \phi_{\mathrm{w}0} &= \operatorname{arctan2}(-c_{\mathrm{w}}, s_{\mathrm{w}})
\end{aligned}
$$

Chapter 3 is published in adapted form as Graetz, Phys. Med. Biol. 2021 [45]

Chapter 4

Talbot-Lau Imaging

The anisotropic diffractive dark-field contrast obtained by means of Talbot or Talbot-Lau imaging provides the central ingredient for X-ray tensor tomography. Talbot interferometry as a means of multi modal X-ray imaging has been initially developed at coherent synchrotron light sources in the first decade of this century and successively transferred to and optimized at laboratory systems throughout the past decade. Due to its central role with regard to X-ray tensor tomography, both the technical aspects regarding data analysis (Sections 4.2–4.3) and the physical aspects of quantitative signal interpretation in radiography, tomography and anisotropic dark-field imaging (Sections 4.4–4.6) will be investigated at greatest detail in the following. Previous literature is to this end brought into a joint context and complemented with original derivations, analyses and methods with regard to quantitative applications, resulting in a comprehensive and consistent picture of isotropic and anisotropic X-ray dark-field imaging. Large parts of the present chapter have been published in [29] (robust signal extraction) and [47] (quantitative signal interpretation).

4.1 Grating Interferometer

A Talbot(-Lau) grating interferometer is a specific realization of a shearing interferometer based on the Talbot-effect. It can be implemented for the X-ray spectrum and, in addition to classic attenuation contrast, further gives access to diffraction contrasts in the form of differential phase shift information and ultra small angle X-ray scattering contrast (cf. [21, 22, 120, 191, 139]). The latter is commonly referred to as "dark-field contrast" in analogy to the respective scattering contrasts in other fields of imaging, and will be the focus of the following chapters due to its sensitivity to the unresolved substructure of the sample. The unique advantages of the grating interferometer with respect to other diffractive X-ray imaging techniques, such as the crystal analyzer based "diffraction enhanced imaging" or "multiple image radiography" methods (cf. [216, 133, 135, 196]), are its ability to directly capture planar images (in contrast to pixel or line scanning methods), its sensitivity to micrometer scaled diffractive effects within centimeter sized fields of view, and finally its tolerance to non-monochromatic X-rays and its practical feasibility also in laboratory environments (as opposed to synchrotron facilities). Other related approaches that will not be further discussed here are single grating approaches based on larger grating periods (Wen et. al [195, 194]) or microscopic detectors (Balles et. al [3]), edge illumination approaches (Olivo et. al [132], Endrizzi et al. [36, 37]), phase grating Moiré approaches (Miao et al. [114]), and speckle-based imaging techniques applicable in microscopic X-ray imaging (cf. e.g. the recent review by Zdora [212]).

Generally, an X-ray Talbot-Lau interferometer consists of three micrometer-pitched gratings, of which the first is placed close to the X-ray source, shaping it into multiple small slit sources in order to increase coherence of the emitted radiation. It can be omitted for sufficiently coherent sources such as synchrotron radiation or microfocus X-ray tubes (Talbot interferometer, cf. Fig. 4.1). The second grating imposes a periodic phase or amplitude modulation. Although the coherent wavefront is subject to interference while propagating, its periodic intensity modulation is restored at specific distances characteristic to the grating pitch and X-ray energy (Talbot effect). At these distances, it can be analyzed by means of a third grating with matching periodicity in combination with an

Section 4.1 is published in adapted form as part of Graetz et al. 2020 [47]

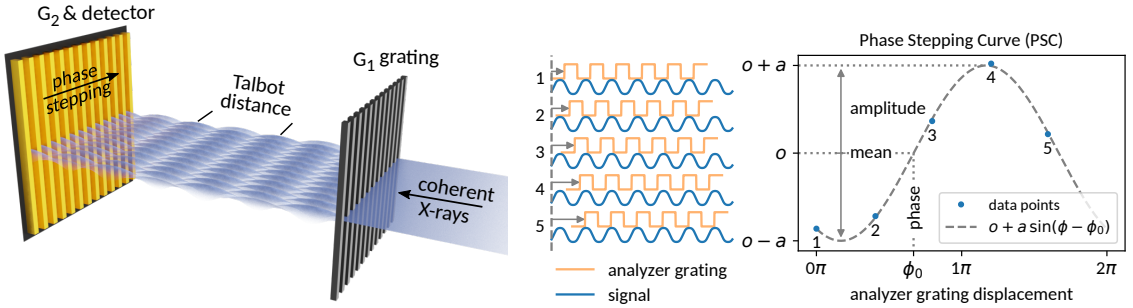

Figure 4.1: Sketch of a Talbot-interferometer (left). Coherent X-rays are modulated by a periodic, phase-shifting or absorbing grating G_1. Coherent diffraction within the Fresnel-regime leads to a periodic reproduction (in intervals of the Talbot distance) of the periodic amplitude modulation induced by the G_1 grating (Talbot-effect). The original wavefront is reproduced in multiples of the Talbot-distance. The patterned beam can be analyzed by means of a period-matched absorption grating G_2 in front of an integrating detector. The detector pixel size is typically at least one order of magnitude larger than the grating period. By moving the analyzer grating G_2 in front of the detector about one period in multiple steps, a phase stepping curve can be acquired (cf. right panel. Stepping of G_1 will have an equivalent effect). Wavefront changes due to a sample will result in attenuation, deflection or blurring of the G_1-induced beam modulation and result in corresponding changes of the phase stepping curve that finally constitute the contrast modalities of a grating interferometer. Samples may be placed between G_1 and G_2 or in front of G_1. Experimental realizations often use an additional absorption grating G_0 upstream of G_1, structuring common laboratory X-ray sources into multiple narrow slit sources of sufficient coherence (Talbot-Lau interferometer).

X-ray detector placed behind it (having a pixel size considerably larger than the grating period). When the structured beam is perturbed by a sample, three effects can be observed: As for classic X-ray imaging, the intensity may be diminished due to absorption. Moreover, the periodic pattern may be reduced in contrast (visibility) due to scattering, and shifted in phase due to refraction. The effects of a sample can be analyzed by comparison of the phase stepping curves (Fig. 4.1, right) for the perturbed (by the sample) and unperturbed beam.

The additional contrast modalities have enabled new applications. In particular the dark-field contrast promises to provide new complementary information both in non-destructive testing and life sciences due to its sensitivity to sub-resolution structures such as micro cracks and porous or fibrous matter. The initial interest arose from early synchrotron experiments on mammography with monochromatic radiation [77] and crystal analyzers [19]. With the introduction of Talbot-Lau imaging to the laboratory by Pfeiffer et al. [139, 138], many more examples have been shown. Applications of X-ray dark-field imaging besides the characterization of micro-calcifications in mammography [115, 48] include imaging of lungs [208, 184, 51, 102], characterization of bone and dentin [141, 121, 81, 80, 70] as well as the analysis of general porous and fibrous materials or microscopic defects in the field of non destructive testing [148, 76, 50]. Other applications that have been shown include water transport in cement [142, 205] or the monitoring of germinating seeds [129]. Due to its origin in the ultra small angle scattering properties of a given sample, dark-field contrast also reflects anisotropies in scattering and thereby allows to detect local orientations within fibrous materials (cf. [74, 75, 141, 6, 150, 160, 60]). Grating interferometric dark-field imaging has further been realized analogously for neutrons [176, 53, 175, 147, 166, 156, 86], with unique applications e.g. in imaging of magnetic fields [92, 62, 127].

With respect to quantitative interpretations of the obtained images, a solid understanding of the underlying contrast mechanisms is of great importance, particularly in the light of long processing chains beginning with phase stepping analysis (cf. Section 4.2) and ending in tensor valued volume reconstructions of anisotropically scattering materials (cf. Chapter 5). The aim of the present Chapter is to provide a unified view on the numerous explanations on dark-field signal origination that have been given in previous literature, and to provide experimental support for the central results. The existing theories will further be extended to cone beam geometries using the Fresnel scaling relation. Moreover, in preparation of Chapter 5, a model for the description of generally oriented anisotropic scatterers will be derived based on the concepts presented by Yashiro et al. [211] and Lynch et al. [103]. Experimental support will be given likewise.

Section 4.1 is published in adapted form as part of Graetz et al. 2020 [47]

4.2 Image Extraction from Phase Stepping Series

By continuously shifting the analyzer grating with respect to the structured beam (commonly referred to as "phase stepping"), local convolutions of beam and grating profile are acquired at each detector pixel. The pixels themselves act, by means of their large extent with respect to the grating pitch, as integrator. The convolution of two period-matched functions is again periodic, and provided that one of them is constant (the analyzer grating profile), all changes in mean, phase and amplitude of the convolution can be directly attributed to respective properties of the sought signal (i.e., sample-induced alterations of the structured beam profile).

These detectable changes constitute the three contrast modalities (attenuation, refraction, ultra small angle scattering) of a Talbot-Lau interferometer, and their reliable extraction from phase stepping series is thus a key aspect of Talbot imaging. Several approaches may be used to this end. The most straight forward techniques are Fourier analysis [22, 120, 139] or direct matrix inversion (used e.g. in [183, 165] as part of a more complex method). Other approaches derive from Taylor expansion (as opposed to Fourier analysis) [137] or perform explicit deconvolution (Lucy-Richardson) of phase stepping curves [118]. All mentioned techniques require that the stepping process can be assumed perfectly stable and precise.

The assumption of perfect mechanical stability of the instrumentation turns out to be a common cause of image artifacts in practice though, wherefore optimization techniques have been proposed for the evaluation of stepping series accounting also for imperfect stepping motions. The approaches vary both in their respective objective function to be optimized as well as the particular optimization algorithm used: The objective function may either be derived from a signal and noise model (cf. e.g. [183, 165, 29]), or rather penalize artifact models (cf. e.g. [82, 65]). The optimization strategies may be either generic ones (compromising on efficiency and possibly stability) or specifically designed to the given purpose (compromising on flexibility). Further approaches combine non-iterative signal analysis with artifact reducing post-processing strategies [83, 109, 56]. Most recently, a new optimization approach based on mathematical modeling of the artifact patterns generated by variations both in phase stepping and illumination has been proposed by [64]. By compromising on spatial resolution, the challenges of mechanical phase stepping can alternatively be avoided by means of Moiré imaging: the respective variation in phase otherwise generated in the time domain by sequential stepping is thereby realized in the spatial domain by slightly mismatched grating periods [195, 8, 164]. Further techniques avoiding stepping of gratings are based on moving the source spot [113] or the sample [88] in order to realize alternative phase stepping approaches.

Each approach to the processing of phase stepping series (or Moiré images) represents a certain trade-off between algorithm complexity, stability, resulting image quality, computational effort and the assumptions required with respect to the input data. Here, the focus is put on maximizing the final signal quality while maintaining robust convergence in constant time at minimal computational overhead and complexity. After the introduction of the basic linear techniques in the following subsection, an efficient optimization scheme accounting also for variances in the phase steps will be given.

4.2.1 Sinusoid Fitting and Fourier Analysis

The periodic phase stepping curve (PSC) found for each detector pixel as the convolution between the Talbot self-image of the modulating grating and the profile of the analyzer grating may generally be characterized by a sinusoid of matching frequency reproducing its mean, amplitude and phase (cf. Fig. 4.1). As various experimental factors tend to suppress higher frequency features, the sinusoid is usually not only approximation, but indeed a reasonable description.

With ϕ denoting the experimentally controlled phase of the shifted grating, i.e., its lateral position in terms of radians with respect to its period, a sinusoid phase stepping curve $\mathrm{PSC}(\phi)$ can be defined as

$$\mathrm{PSC}(\phi) = o + a\sin(\phi - \phi_0)\,,$$

with o, a and ϕ_0 denoting the mean intensity, amplitude and phase shift respectively.

Section 4.2 presents concepts published in Dittmann et al., J. Imaging 2018 [29]

By means of the auxiliary amplitudes a_s and a_c

$$\begin{aligned} a_\mathrm{s} &= \quad \cos(\phi_0) \\ a_\mathrm{c} &= -\sin(\phi_0) \\ a &= \sqrt{a_\mathrm{s}^2 + a_\mathrm{c}^2}\,, \end{aligned}$$

this definition can further be transcribed in a linear fashion:

$$\begin{aligned} \mathrm{PSC}(\phi) &= o + a_\mathrm{s}\sin\phi + a_\mathrm{c}\cos\phi \\ &= \begin{bmatrix} 1 \\ \sin(\phi) \\ \cos(\phi) \end{bmatrix} \begin{bmatrix} o \\ a_\mathrm{s} \\ a_\mathrm{c} \end{bmatrix}, \end{aligned}$$

i.e., as a Fourier series.

In a discrete form with $\mathrm{PSC}(\phi_i) = \tilde{y}_i$ at defined phases ϕ_i, the following linear system of equation emerges:

$$\underbrace{\begin{bmatrix} \tilde{y}_1 \\ \vdots \\ \tilde{y}_N \end{bmatrix}}_{\boldsymbol{y}} = \underbrace{\begin{bmatrix} 1 & \sin(\phi_1) & \cos(\phi_1) \\ \vdots & \vdots & \vdots \\ 1 & \sin(\phi_N) & \cos(\phi_N) \end{bmatrix}}_{\boldsymbol{B}} \underbrace{\begin{bmatrix} o \\ a_\mathrm{s} \\ a_\mathrm{c} \end{bmatrix}}_{\boldsymbol{x}}$$

$$\boldsymbol{y} = \boldsymbol{B}\boldsymbol{x}\,,$$

with generally non-square $\boldsymbol{B}$, i.e., $N > 3$. The above system can be identified as a generalized linear least squares problem, which can be solved in a least squares sense by first multiplying by $\boldsymbol{B}^T$(cf. e.g. [145]):

$$\begin{aligned} \boldsymbol{B}^T\boldsymbol{y} &= \boldsymbol{B}^T\boldsymbol{B}\boldsymbol{x} \\ \boldsymbol{x} &= \left[\boldsymbol{B}^T\boldsymbol{B}\right]^{-1}\boldsymbol{B}^T\boldsymbol{y}\,, \end{aligned}$$

with $\boldsymbol{B}^T\boldsymbol{B}$ being a square matrix. In their most general form (not shown), least squares solutions can also account for varying noise variances for different components i by means of a covariance matrix (cf. e.g. [189]). In the context of phase stepping curve analysis with moderate a/o ratios, i.e., moderate intensity variations, the noise variance is approximated to be the same for all i.

For the case of $\phi_i = i2\pi/N$ (and homogeneous noise variance), classic Fourier analysis is reproduced:

$$\left[\boldsymbol{B}^T\boldsymbol{B}\right]^{-1} = \begin{bmatrix} \frac{1}{N} & 0 & 0 \\ 0 & \frac{2}{N} & 0 \\ 0 & 0 & \frac{2}{N} \end{bmatrix} \quad \text{for } \phi_i = i\frac{2\pi}{N}\,,$$

such that

$$\begin{aligned} o &= \frac{1}{N}\sum_i y_i \\ a_\mathrm{s} &= \frac{2}{N}\sum_i y_i \sin(\phi_i) \\ a_\mathrm{c} &= \frac{2}{N}\sum_i y_i \cos(\phi_i)\,. \end{aligned} \tag{4.1}$$

The linear least squares problem $\boldsymbol{y} = \boldsymbol{B}\boldsymbol{x}$ may also be solved iteratively by means of the

Section 4.2 presents concepts published in Dittmann et al., J. Imaging 2018 [29]

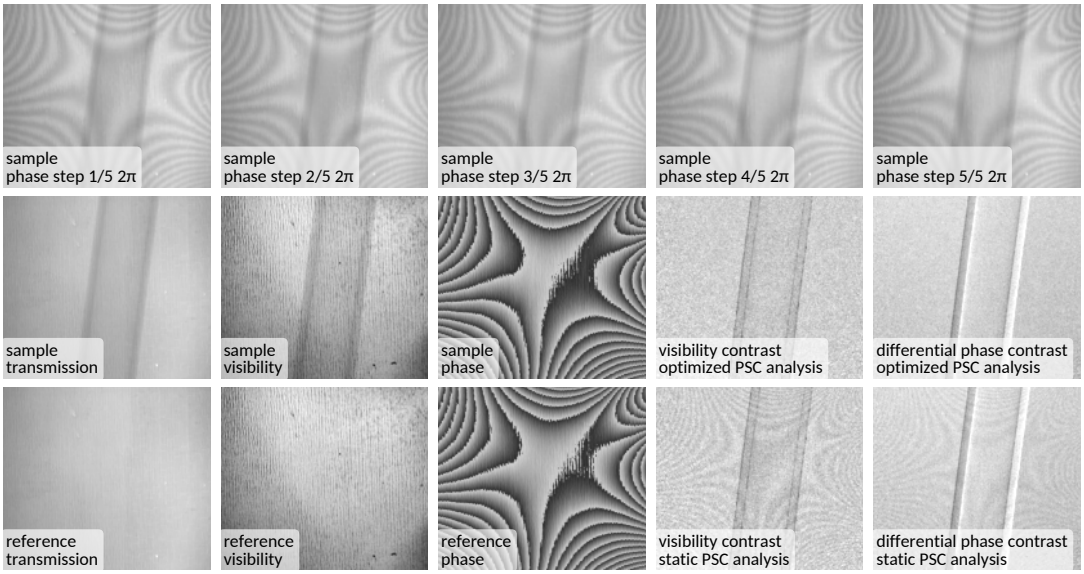

Figure 4.2: Example experimental data from a Talbot-Lau interferometer with notably mismatched gratings, causing a pronounced Moiré pattern. The top row shows a phase stepping image series acquired with a sample (a plastic hose of about 2 cm diameter) in the beam. The collection of 2×3 images on the lower left show the results after pixelwise evaluation of the phase stepping curves (PSC), depicting the transmission, amplitude visibility and phase of the respective scans with and without sample. The group of 2×2 images on the lower right shows the final, normalized visibility and differential phase contrast images (omitting transmission images). The Moiré pattern visibly translates to the final results in the presence of unaccounted stepping motion imprecisions when using static Fourier analysis as shown on the bottom right (cf. Eqs. 4.1, 4.3). Above, respective results obtained using Algorithm 4.1 are shown, which simultaneously also reconstructs the actual grating motions. A more detailed analysis of this example has been published in [29].

following gradient descent scheme minimizing the square error $\left\|\boldsymbol{y} - \boldsymbol{B}\boldsymbol{x}\right\|^2$

$$\begin{aligned} o^{(0)}, a_\mathrm{s}^{(0)}, a_\mathrm{c}^{(0)} &= 0, 0, 0 \\ \tilde{y}_i^{(k)} &= o^{(k)} + a_\mathrm{s}^{(k)} \sin(\phi_i) + a_\mathrm{c}^{(k)} \cos(\phi_i) \\ o^{(k+1)} &= o^{(k)} + \frac{1}{N} \sum_i (y_i - \tilde{y}_i^{(k)}) \\ a_\mathrm{s}^{(k+1)} &= a_\mathrm{s}^{(k)} + \frac{2}{N} \sum_i (y_i - \tilde{y}_i^{(k)}) \sin(\phi_i) \\ a_\mathrm{c}^{(k+1)} &= a_\mathrm{c}^{(k)} + \frac{2}{N} \sum_i (y_i - \tilde{y}_i^{(k)}) \cos(\phi_i) \,, \end{aligned} \tag{4.2}$$

with (ϕ_i, y_i) denoting the data samples to be fitted, N the amount of samples, k the iteration index and $y_i - \tilde{y}_i^{(k)}$ the residuals at iteration k. The scheme reduces to classic Fourier analysis for $\phi_i = i2\pi/N$ as well. As the iterative updates to the sinusoid parameters $o^{(k)}$, $a_\mathrm{s}^{(k)}$ and $a_\mathrm{c}^{(k)}$ are proportional to the respective gradients of the square error $\sum_i (y_i - \tilde{y}_i)^2$, the fixpoint of the iterative scheme will be the least squares fit also in all other cases. In practice, 10 to 20 iterations are usually found to be sufficient (cf. Dittmann et al. 2018 [29]). A practical advantage of the iterative approach lies in its algorithmic simplicity, which is a favorable property for massively parallel computations on graphics processing units.

The original sinusoid parameters o, a and ϕ_0 are retrieved by

$$\begin{aligned} o &= o \\ a &= \sqrt{a_\mathrm{s}^2 + a_\mathrm{c}^2} \\ \phi_0 &= \operatorname{arctan2}(-a_\mathrm{c}, a_\mathrm{s}) \end{aligned} \tag{4.3}$$

Section 4.2 presents concepts published in Dittmann et al., J. Imaging 2018 [29]

4.2.2 Phase stepping analysis in the presence of motion imprecisions

The just presented linear least squares techniques (iterative, non-iterative or Fourier analysis) formally solve the optimization problem

$$o_j, a_j, \phi_{0,j} = \underset{o_j, a_j, \phi_{0,j}}{\operatorname{argmin}} \sum_i \left(o_j + a_j \sin(\phi_i - \phi_{0,j}) - y_{ij}\right)^2 \tag{4.4}$$

for each detector pixel j and require the sampling phases ϕ_i to be known (y_{ij} denotes the detector readings at pixel j and phase step i). As outlined previously, any unaccounted variances on ϕ_i (due to mechanical imprecisions on the sub-micrometer scale within the phase stepping procedure) will translate to non-negligible errors on the derived quantities o_j, a_j and $\phi_{0,j}$, typically causing Moiré artifacts in the final 2D dark-field and differential phase images (see Fig. 4.2 (lower right) and the derivations in [66]). These characteristic artifacts correspond to crosstalk among $\phi_{0,j}$, o_j and a_j in the presence of noise or systematic errors on ϕ_i.

Mechanical variations in the stepping motion of a grating do however affect all detector pixels simultaneously, with the number of pixels (i.e., the number of individual phase stepping curves) usually outnumbering the degrees of freedom of the individual optimization problems by several orders of magnitude. Due to this correlation among many PSCs, the shared stepping phases may thus be treated as optimization variables as well (assuming local optimization about their intended values):

$$o_j, a_j, \phi_{0,j}, \phi_i(j) = \underset{o_j, a_j, \phi_{0,j}, \phi_i(j)}{\operatorname{argmin}} \sum_{i,j} \left(o_j + a_j \sin(\phi_i(j) - \phi_{0,j}) - y_{ij}\right)^2 . \tag{4.5}$$

$\phi_i(j)$ generally are slowly varying polynomials over the two dimensional imaging plane (as detailed by the author in [29]), here formally parametrized by the sequential pixel index j, although the assumption of constant (w.r.t. j) stepping phases is usually found to be sufficient.

In contrast to the initial problem of sinusoid fitting based on known ϕ_i, this problem is not linear anymore. The nonlinear aspect, i.e., the local optimization of $\phi_i(j)$, may however be separated into an isolated optimization problem to be solved alternatingly with the remaining linear problem in an iterative manner:

$$\begin{aligned} o_j^{(k)}, a_j^{(k)}, \phi_{0,j}^{(k)} &= \underset{o_j, a_j, \phi_{0,j}}{\operatorname{argmin}} \sum_i \left(o_j + a_j \sin(\phi_i^{(k)}(j) - \phi_{0,j}) - y_{ij}\right)^2 \\ \Delta\phi_i^{(k)}(j) &= \underset{\Delta\phi_i(j)}{\operatorname{argmin}} \sum_j \left(o_j^{(k)} + a_j^{(k)} \sin(\phi_i^{(k)}(j) + \Delta\phi_i(j) - \phi_{0,j}^{(k)}) - y_{ij}\right)^2 , \\ \text{with} \quad \phi_i^{(k)}(j) &= \phi_i + \sum_{k'=0}^{k-1} \Delta\phi_i^{(k')}(j) \end{aligned} \tag{4.6}$$

and ϕ_i being the originally intended (i.e., known) stepping phases. The large parameter space of Eq. 4.6, defined by the number of phase steps multiplied by the number of polynomial coefficients in $\Delta\phi_i(j)$, still makes the use of general purpose non-linear optimizers such as the widely used BFGS algorithm unattractive. Instead, the deviations $\Delta\phi_i^{(k)}(j)$ may rather be determined by means of the following surrogate linear least squares optimization problem based on noisy, pixel wise estimations $\Delta\phi_{ij}^{(k)}$ for $\Delta\phi_i^{(k)}(j)$ to be detailed afterwards:

$$\begin{aligned} \Delta\phi_i^{(k)}(j) &= \underset{\Delta\phi_i(j)}{\operatorname{argmin}} \sum_j \sigma_{ij}^{-2} \left(\Delta\phi_i(j) - \Delta\phi_{ij}^{(k)}\right)^2 , \\ \text{with } \Delta\phi_i(h(j), v(j)) &= \Delta\phi_i + \nabla_{\mathrm{h}}\phi_i\, h + \nabla_{\mathrm{v}}\phi_i\, v + \nabla_{\mathrm{hv}}\phi_i\, h\, v + \nabla_{\mathrm{h}^2}\phi_i\, h^2 \\ h(j), v(j): &\quad \text{2D coordinates on the detector plane} \\ &\quad \text{perpendicular } (h) \text{ and parallel } (v) \text{ to the grating bars} \\ \Delta\phi_i, \nabla_{\mathrm{h}}\phi_i, \nabla_{\mathrm{v}}\phi_i, \nabla_{\mathrm{hv}}\phi_i, \nabla_{\mathrm{h}^2}\phi_i: &\quad \text{polynomial coefficients .} \end{aligned}$$

A term quadratic in v has no physical correspondence in the considered problem and is thus omitted. The inverse variances σ_{ij}^{-2} describe the expected certainty of the respective estimates. The following

Section 4.2 presents concepts published in Dittmann et al., J. Imaging 2018 [29]

definitions have been derived by the author in [29] by means of locally linear approximations of the objective function 4.6:

$$\begin{aligned}
\Delta\phi_{ij}^{(k)} &= \operatorname{limit}\Bigg(\cos(\phi_{ij}^{(k)} - \phi_{0,j}^{(k)})\left(a_j^{(k)}(y_{ij}^{(k)} - o_j^{(k)}) - a_j^{(k)\,2}\sin(\phi_{ij}^{(k)} - \phi_{0,j}^{(k)})\right), \\
&\qquad \frac{1}{2}a_j^{(k)\,2}\cos^4(\phi_{ij}^{(k)} - \phi_{0,j}^{(k)})\Bigg) \\
\sigma_{ij}^{-2} &\propto a_j^{(k)\,2}\cos^2(\phi_{ij}^{(k)} - \phi_{0,j}^{(k)}) \\
\operatorname{limit}(\Delta\phi, m \geq 0) &= \begin{cases} 0 & m = 0 \\ m\tanh\left(\frac{\Delta\phi}{m}\right) & \text{else} \end{cases}.
\end{aligned}$$

The $\operatorname{limit}(\cdot,\cdot)$ function (and the weights σ_{ij}^{-2}) ensure (and weight) compliance with the validity ranges of the involved approximations. The absolute scale of σ_{ij}^{-2} is thereby irrelevant to the optimization.

Finally, the following iterative algorithm based on an alternation of linear least squares problems can be stated, which for practical examples (Fig 4.2) has been demonstrated to converge within as few as one to five iterations:

Algorithm 4.1 Iterative reconstruction of phase stepping curves' parameters and the actual phase steps, with ϕ_i and y_{ij} being the input data and $\Delta\phi_i^{(k)}(j)$ a polynomial model of the physically expected sampling phase deviations as detailed by the author in [29]. All argmin operations are in the form of efficiently solvable linear least squares problems.

$$\begin{aligned}
\phi_{ij}^{(0)} &= \phi_i \\
o_j^{(0)}, a_j^{(0)}, \phi_{0,j}^{(0)} &= \underset{o_j, a_j, \phi_{0,j}}{\operatorname{argmin}} \sum_i \left(o_j + a_j\sin(\phi_{ij}^{(0)} - \phi_{0,j}) - y_{ij}\right)^2 \\
\Delta\phi_{ij}^{(k)} &= \operatorname{limit}\Bigg(\cos(\phi_{ij}^{(k)} - \phi_{0,j}^{(k)})\left(a_j^{(k)}(y_{ij}^{(k)} - o_j^{(k)}) - a_j^{(k)\,2}\sin(\phi_{ij}^{(k)} - \phi_{0,j}^{(k)})\right), \\
&\qquad \frac{1}{2}a_j^{(k)\,2}\cos^4(\phi_{ij}^{(k)} - \phi_{0,j}^{(k)})\Bigg) \\
\Delta\phi_i^{(k)}(j) &= \underset{\Delta\phi_i(j)}{\operatorname{argmin}} \sum_j \underbrace{\left(a_j^{(k)\,2}\cos^2(\phi_{ij}^{(k)} - \phi_{0,j}^{(k)})\right)}_{\text{weighting factor } \sigma_{ij}^{-2}} \Big(\underbrace{\Delta\phi_i(j)}_{\substack{\text{2D polynomial} \\ \text{up to } 2^{\text{nd}} \text{ order}}} - \Delta\phi_{ij}^{(k)}\Big)^2, \\
\phi_{ij}^{(k+1)} &= \phi_{ij}^{(k)} + \Delta\phi_i^{(k)}(j) \\
o_j^{(k+1)}, a_j^{(k+1)}, \phi_{0,j}^{(k+1)} &= \underset{o_j, a_j, \phi_{0,j}}{\operatorname{argmin}} \left(o_j + a_j\sin(\phi_{ij}^{(k)} - \phi_{0,j}) - y_{ij}\right)^2
\end{aligned}$$

Conclusion With respect to the direct, non-linear optimization of Eq. 4.5 or Eq. 4.6, two considerable simplifications have been achieved: Foremost, the optimization of the deviations $\Delta\phi_i^{(k)}(j)$ has been separated into individually solvable problems for each step i. Moreover, the individual problems for each phase step have been reduced to a common 2D polynomial regression problem, allowing to easily account for non-constant $\Delta\phi_i(j)$. The approach is therefore well applicable to use cases with a large number of phase steps and can easily handle as many as 10^2 optimization variables within the unknown deviations $\Delta\phi_i(j)$. Due to the very large number of phase stepping curves (detector pixels), typically in the order of magnitude of 10^6, considerable noise levels on the estimations $\Delta\phi_{ij}$ are tolerated, in particular if only the dominating constant term of $\Delta\phi_i(j)$ is to be determined.

Section 4.2 presents concepts published in Dittmann et al., J. Imaging 2018 [29]

4.3 Noise properties of grating interferometric images

With regard to derived applications of Talbot-Lau imaging such as dark-field computed tomography (cf. Sections 4.5 and 5), the noise properties of the respective contrast modalities are of particular interest. As will be shown in the following, the signal to noise ratio of dark-field contrast is generally substantially lower than that of absorption contrast, and diminishes even faster in the limit of thick samples (cf. Figure 4.3). Respective quantitative insights do provide important guidance for the planning and evaluation of experiments.

Noise on the recorded intensity values y_i at each phase step i (the detector pixel index j is omitted here for brevity) emerges both from statistical photon noise and additional detector readout noise. The resulting noise characteristics of the derived contrast modalities shall be analyzed in the following by means of linear error propagation, which approximates the relation between the variances $\sigma^2_{y_i}$ of the measured intensities y_i and the variance σ^2_f of a derived quantity $f(y_1, y_2, ...)$ by means of its local partial derivatives:

$$\sigma^2_f(y_1, ..., y_i, ...) \approx \sum_i \left(\frac{\partial}{\partial y_i} f(y_{i=1}, y_{i=2}, ...) \Big|_{y_i} \sigma_{y_i} \right)^2 , \tag{4.7}$$

assuming uncorrelated zero-mean Gaussian random noise on the input variables y_i. While particular focus will be put on the dark-field signal, first the propagation of $\sigma^2_{y_i}$ onto the sinusoid parameters of the phase stepping analysis needs to be considered.

4.3.1 Noise variance of the stepping curve's sinusoid parameters

In the ideal case of a sinusoid phase stepping curve sampled at equidistantly distributed phase steps ϕ_i over multiples of 2π (such that mean, sine and cosine form an orthogonal basis), further assuming a homogeneous noise variance $\sigma^2_y = \sigma^2_{y_i}$, the following relations for the variances σ^2_o, σ^2_a and $\sigma^2_{\phi_0}$ of the sinusoid parameters a (amplitude), o (mean) and ϕ_0 (phase) result from Equations 4.1 and 4.7:

$$\sigma^2_o = \frac{1}{N}\sigma^2_y \qquad \sigma^2_a = \sigma^2_{a_\mathrm{s}} = \sigma^2_{a_\mathrm{c}} = \frac{2}{N}\sigma^2_y = 2\sigma^2_o \qquad \sigma^2_{\phi_0} = \frac{2}{N}\frac{\sigma^2_y}{a} = \frac{\sigma^2_a}{a^2} = 2\frac{\sigma^2_o}{a^2} ,$$

with N denoting the total number of phase steps, i.e., the total number of input data values y_i. Due to the orthogonality of the Fourier basis and the assumption of uncorrelated zero-mean random noise, the random errors on o, a and ϕ_0 (or o, a_s and a_c) remain statistically independent. Eq. 4.1 therefore remains applicable to quantities derived from these parameters. For completeness, it shall be pointed out that $\sigma^2_{\phi_0}$ is, due to the periodic nature of the sinusoid, bounded at $\pi/\sqrt{3}$ in the limit of $\sigma^2_y \to \infty$, corresponding to a uniform distribution on the circle (cf. [189]).

The above relations hold, for a sinusoid signal, also under consideration of the following i-dependent Poisson noise model:

$$\sigma^2_{y_i} = \sigma^2_0 + \alpha y_i \tag{4.8}$$

with σ_0 characterizing the constant signal read out noise and αy_i the intensity-proportional variance. After substitution of $\sigma^2_{y_i} = \sigma^2_0 + \alpha y_i$ into Eqs. 4.1 and 4.7, the initially assumed mean variance σ^2_y can be explicitly identified as the average of $\sigma^2_{y_i}$:

$$\sigma^2_y = \sigma^2_0 + \alpha o = \frac{1}{N}\sum_i \sigma^2_{y_i} ,$$

corresponding to the expected variance at the mean intensity $y_i = o$.

4.3.2 Noise variance of the dark-field image

The dark-field contrast μ_{DF} is obtained from the negative logarithm of the visibility ratio of perturbed beam (by the sample) and empty beam:

$$\begin{aligned}\mu_{\mathrm{DF}} &= -\ln(\frac{v_{\mathrm{smp}}}{v_{\mathrm{ref}}}) = -\ln(\frac{a_{\mathrm{smp}}/o_{\mathrm{smp}}}{a_{\mathrm{ref}}/o_{\mathrm{ref}}}) \\ &= \ln(a_{\mathrm{ref}}) - \ln(a_{\mathrm{smp}}) + \ln(o_{\mathrm{smp}}) - \ln(o_{\mathrm{ref}})\,,\end{aligned}$$

with the subscripts "smp" and "ref" indicating the sinusoid parameters o (mean) and a (amplitude) for the phase stepping curves acquired with and without sample respectively. By application of Eq. 4.7, the variance is given by

$$\sigma^2_{\mathrm{DF}} = \underbrace{\frac{\sigma^2_{o_{\mathrm{smp}}}}{o^2_{\mathrm{smp}}} + \frac{\sigma^2_{o_{\mathrm{ref}}}}{o^2_{\mathrm{ref}}}}_{=\sigma^2_\mu} + \frac{\sigma^2_{a_{\mathrm{smp}}}}{a^2_{\mathrm{smp}}} + \frac{\sigma^2_{a_{\mathrm{ref}}}}{a^2_{\mathrm{ref}}}\,, \tag{4.9}$$

with the first terms corresponding to the variance σ^2_μ of the absorption contrast

$$\mu = -\ln(o_{\mathrm{smp}}/o_{\mathrm{ref}}) = \ln(o_{\mathrm{ref}}) - \ln(o_{\mathrm{smp}})\,.$$

Given a homogeneous sample of some scattering material, the observed dark-field signal will be proportional to the sample thickness and therefore also to its absorption μ. The phase stepping curve's mean o and visibility $v = a/o$ may thus, for the purpose of noise analysis, be modeled using the following relations:

$$\begin{aligned}o_{\mathrm{smp}} &= o_{\mathrm{ref}} e^{-\mu} \\ v_{\mathrm{smp}} &= v_{\mathrm{ref}} e^{-c\mu}\,,\end{aligned} \tag{4.10}$$

with c denoting the proportionality factor between μ and μ_{DF}. Analyzing the dark-field contrast in terms of the accompanying attenuation signal will provide an intuitive understanding of its noise characteristics in relation to classic X-ray imaging, and will in particular directly exhibit its limits in terms of resolution and sample size as compared to common attenuation imaging.

Substitution of Eq. 4.10 into Eq. 4.9 yields:

$$\begin{aligned}\sigma^2_{\mathrm{DF}} &= \sigma^2_\mu + \frac{\sigma^2_{a_{\mathrm{smp}}}}{a^2_{\mathrm{smp}}} + \frac{\sigma^2_{a_{\mathrm{ref}}}}{a^2_{\mathrm{ref}}} = \sigma^2_\mu + \frac{2}{v^2_{\mathrm{smp}}}\frac{\sigma^2_{o_{\mathrm{smp}}}}{o^2_{\mathrm{smp}}} + \frac{2}{v^2_{\mathrm{ref}}}\frac{\sigma^2_{o_{\mathrm{ref}}}}{o^2_{\mathrm{ref}}} \\ &= \sigma^2_\mu + 2\frac{1}{v^2_{\mathrm{ref}} o^2_{\mathrm{ref}}}\left[e^{2c\mu+2\mu}\sigma^2_{o_{\mathrm{smp}}} + \sigma^2_{o_{\mathrm{ref}}}\right] \qquad (4.11) \\ \sigma^2_\mu &= \frac{1}{o^2_{\mathrm{ref}}}\left[e^{2\mu}\sigma^2_{o_{\mathrm{smp}}} + \sigma^2_{o_{\mathrm{ref}}}\right]\,. \qquad (4.12)\end{aligned}$$

By further substituting a Poisson noise model $\sigma^2_o = \bar{\sigma}^2_0 + \alpha o$ (analog to Eq. 4.8) and the resulting relation $\sigma^2_{o_{\mathrm{smp}}} = \bar{\sigma}^2_0 + e^{-\mu}(\sigma^2_{o_{\mathrm{ref}}} - \bar{\sigma}^2_0) = \bar{\sigma}^2_0(1-e^{-\mu}) + \sigma^2_{o_{\mathrm{ref}}} e^{-\mu}$ into Eqs. 4.11 and 4.12, the variances σ^2_{DF} and σ^2_μ can be expressed in terms of the reference noise and intensity values ($\sigma_{o_{\mathrm{ref}}}$ and o_{ref}) and the absorption and dark-field signals μ and $c\mu$:

$$\sigma^2_{\mathrm{DF}} = \sigma^2_\mu + 2\frac{1}{v^2_{\mathrm{ref}} o^2_{\mathrm{ref}}}\left[e^{2c\mu}e^{\mu}\left(\bar{\sigma}^2_0(e^\mu - 1) + \sigma^2_{o_{\mathrm{ref}}}\right) + \sigma^2_{o_{\mathrm{ref}}}\right] \tag{4.13}$$

$$\sigma^2_\mu = \frac{1}{o^2_{\mathrm{ref}}}\left[e^{\mu}\left(\bar{\sigma}^2_0(e^\mu - 1) + \sigma^2_{o_{\mathrm{ref}}}\right) + \sigma^2_{o_{\mathrm{ref}}}\right]\,, \tag{4.14}$$

where $\bar{\sigma}_0$ is the constant noise component of the mean intensity o as opposed to the respective constant component σ_0 of individual data points y_i as used in Eq. 4.8. Typically, $\bar{\sigma}_0 = \sigma_0/\sqrt{N}$.

Figure 4.3 gives some practical examples of the above results. In order to provide more qualitative insights, the asymptotic behaviour of Eqs. 4.11 and 4.13 shall be considered in the following.

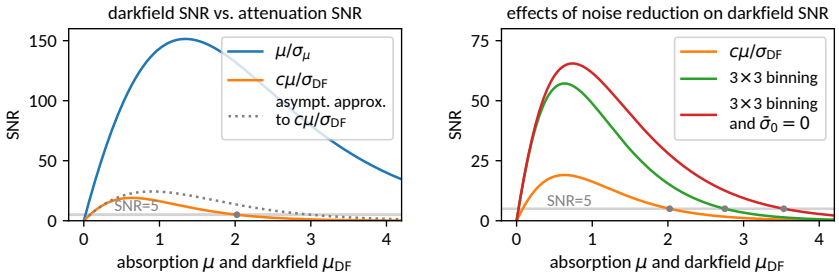

Figure 4.3: Example material thickness dependent signal-to-noise ratio for attenuation and dark-field contrast based on Eqs. 4.13–4.14 using a set of experimental parameters ($o_{\mathrm{ref}} = 5000$, $v_{\mathrm{ref}} = 0.4$, $\bar{\sigma}_0 = 9$, $\sigma_{o_{\mathrm{ref}}} = 15$) observed in the synchrotron experiments shown in Section 5.4. The model proportionality factor c between attenuation μ and dark-field μ_{DF} has been chosen $c = 1$ (as a mean order of magnitude, cf. Fig. 5.7). On the left hand side, the considerable difference in SNR for μ and μ_{DF} becomes apparent. In addition, the asymptotic approximation to the dark-field SNR based on Eq. 4.15 is shown. On the right hand side, the effects of noise reduction by means of pixel binning (reducing $\bar{\sigma}_0$ and $\sigma_{o_{\mathrm{ref}}}$) and by elimination of readout noise (i.e., $\bar{\sigma}_0 = 0$) are demonstrated. Gray markers indicate when the SNR drops below 5, which can be considered a required minimum.

4.3.3 Asymptotic properties of dark-field noise variance

The dark-field noise variance σ^2_{DF} as described by Eq. 4.11 can be, both in the limit of $c\mu \to 0$ and in the limit of $e^{2c\mu+2\mu}\sigma^2_{o_{\mathrm{smp}}} \gg \sigma^2_{o_{\mathrm{ref}}}$, expressed in terms of σ^2_μ:

$$\sigma^2_{\mathrm{DF}} \approx \sigma^2_\mu\left(1 + \frac{2}{v^2_{\mathrm{ref}}}e^{2c\mu}\right) \approx 2\frac{e^{2c\mu}}{v^2_{\mathrm{ref}}}\sigma^2_\mu \,,$$

which has further been simplified using the approximation $\frac{2}{v^2_{\mathrm{ref}}} \gg 1$ based on the fact that $v_{\mathrm{ref}} \in]0;1]$ usually ranges below 0.5 for most systems (in particular for polychromatic laboratory setups). I.e.:

$$\sigma_{\mathrm{DF}} \approx \sqrt{2}\frac{e^{c\mu}}{v_{\mathrm{ref}}}\sigma_\mu = \frac{\sqrt{2}}{v_{\mathrm{smp}}}\sigma_\mu \quad \text{for } c\mu \to 0 \text{ and } c\mu \to \infty \,. \tag{4.15}$$

See Fig. 4.3 for an example. Eq. 4.15 directly reveals that the signal to noise ratio of the dark-field signal is generally considerably lower than that of the absorption contrast and in particular degrades much faster as the sample thickness increases due to the additional exponential factor $e^{c\mu} = e^{\mu_{\mathrm{DF}}}$ with respect to σ_μ.

In the thick sample limit, $\sigma^2_{o_{\mathrm{ref}}}$ becomes negligible, such that Eqs. 4.13–4.14 reduce to:

$$\lim_{\mu\to\infty}(\sigma^2_\mu) = \frac{e^{2\mu}}{o^2_{\mathrm{ref}}}\bar{\sigma}^2_0 = \frac{1}{o^2_{\mathrm{smp}}}\bar{\sigma}^2_0$$
$$\lim_{\mu\to\infty}(\sigma^2_{\mathrm{DF}}) = 2\frac{e^{2\mu}}{o^2_{\mathrm{ref}}}\frac{e^{2c\mu}}{v^2_{\mathrm{ref}}}\bar{\sigma}^2_0 = 2\frac{1}{o^2_{\mathrm{smp}}v^2_{\mathrm{smp}}}\bar{\sigma}^2_0 \,,$$

and the detector readout noise variance σ^2_0 becomes the limiting factor. The impact of $\bar{\sigma}_0$ is also demonstrated in Fig. 4.3. For the case of $\sigma^2_0 = \bar{\sigma}^2_0 = 0$, as in the case of photon counting detectors, the following limits for Eqs. 4.13–4.14 result in contrast:

$$\lim_{\substack{\mu\to\infty \\ \sigma^2_0\to 0}}(\sigma^2_\mu) = \frac{e^{\mu}}{o^2_{\mathrm{ref}}}\sigma^2_{o_{\mathrm{ref}}} = \frac{1}{o_{\mathrm{ref}}o_{\mathrm{smp}}}\sigma^2_{o_{\mathrm{ref}}}$$
$$\lim_{\substack{\mu\to\infty \\ \sigma^2_0\to 0}}(\sigma^2_{\mathrm{DF}}) = 2\frac{e^{\mu}}{o^2_{\mathrm{ref}}}\frac{e^{2c\mu}}{v^2_{\mathrm{ref}}}\sigma^2_{o_{\mathrm{ref}}} = \frac{1}{o_{\mathrm{ref}}o_{\mathrm{smp}}v^2_{\mathrm{smp}}}\sigma^2_{o_{\mathrm{ref}}} \,.$$

4.3.4 Systematic errors in phase stepping analysis

Bias errors in interferometric imaging have been discussed e.g. by Chabior et al. [18] and Kaeppler et al. [82], based on previous literature on the analysis of quadrature signals. Bias refers to systematic erroneous offsets often smaller than the random errors, yet persistent after reducing the statistical variance of noisy signals by temporal or spatial averaging. Given the outlined noise characteristics of the dark-field signal, averaging (pixel binning) is regularly required, making the discussion of bias obligatory. While [18, 82] specifically focused on the visibility contrast (as opposed to its negative logarithm or the entire phase stepping curve) and respective technical details, the following discussion shall give a more general understanding of bias applicable also to other contrast modalities.

Bias effects can generally emerge after signal transformations despite the original signal noise being zero-mean, i.e., unbiased. This can be easily seen for general magnitudes (e.g., amplitude or contrast visibility of the phase stepping curve), which are by definition always positive irrespective of the underlying quantity and respective noise. This is particularly important to realize as such induced bias effects are obviously specific to the particular transformation (e.g., absolute magnitude) as opposed to the original signal. When recalling the estimation of error propagation based on local series expansions (cf. Eq. 4.7), bias errors can be attributed to even-ordered (and thus axial symmetric) polynomial expansion terms of the particular transformation considered. This further implies that corrections for bias cannot be generally applied as an intermediate step within a longer processing chain, but should typically be applied last based on the integral higher-order error propagation properties of the entire processing chain. Given the previous discussions by Chabior et al. [18] and Kaeppler et al. [82] regarding bias within the visibility signal $v = \exp(-\mu_{\mathrm{DF}})$, and given further that the present work focuses on the analysis of dark-field signals $-\ln(v) = \mu_{\mathrm{DF}}$, it shall be explicitly pointed out here that bias corrections with respect to v as stated in [18, 82] are only advisable when actually working or performing averages (e.g., detector binning) in the visibility domain. The amplification of bias errors as compared to random noise can – as done in the present work – otherwise be avoided by averaging (binning) in the original image domain (or any *odd* function thereof) exhibiting zero-mean noise, prior to the evaluation of visibility and dark-field signals (i.e., prior to the application of nonlinear transforms).

4.4 Dark-field Contrast Interpretation

The origination of X-ray dark-field contrast has been discussed from different points of view and varying levels of mathematical rigor in previous literature. As the underlying physical relations are essential with respect to quantitative interpretations of X-ray dark-field images, the following Sections will review common approaches to the interpretation of dark-field contrast and demonstrate their interrelations. Respective approaches range from heuristic characterizations of point spread over analogies to classic small angle scattering up to ab-initio derivations based on wave optics. It will be shown that all presented ideas can be understood as approximations of the latter. The link to wave optics further allows to introduce Fresnel scaling to explain the changed propagation distance dependence of dark-field contrast in cone beam laboratory setups as compared to parallel beam configurations at synchrotron beamlines. Experimental evidence for the presented relations will be shown in Sections 4.4.5, 4.5.1, 4.5.2 and 4.6.4.

4.4.1 Visibility reduction by Gaussian point spread

Analog to the characterization of the modulation transfer properties of an optical system, visibility or contrast reduction of the structured beam (i.e., the reduction of the first harmonic Fourier component normalized to the zeroth as e.g. defined by [138]) can generally be modeled as Gaussian blurring of the reference sinusoid profile. The underlying conception is a convolution of the incident intensity distribution with an effective point spread function or scattering profile of a sample. Normalizing the Gaussian to the ratio of transmitted intensity $t \in [0, 1]$ (i.e., also accounting for attenuation or general reduction of intensity), the following convolution kernel can be stated:

$$\frac{t}{\sqrt{2\pi}\sigma_\phi} e^{-\frac{1}{2}\frac{\Delta\phi^2}{\sigma_\phi^2}} ,$$

with σ_ϕ being its standard deviation in units of radians and $\Delta\phi$ the phase with respect to the periodic irradiation profile (not to be confused with a scattering angle). The width σ_ϕ will later be expressed in terms of geometric parameters based on absolute scales of the instrument. Yet to begin with, the present formulation will be convenient.

By explicitly solving the convolution integral over a generic sinusoid reference profile $o_\mathrm{ref} + a_\mathrm{ref}\cos(\phi)$:

$$\frac{t}{\sqrt{2\pi}\sigma_\phi} \int_{-\infty}^{+\infty} \mathrm{d}\Delta\phi \left(o_\mathrm{ref} + a_\mathrm{ref}\cos(\Delta\phi - \phi)\right) e^{-\frac{1}{2}\frac{\Delta\phi^2}{\sigma_\phi^2}} = \underbrace{t\, o_\mathrm{ref}}_{=o_\mathrm{smp}} + \underbrace{t\, a_\mathrm{ref}\, e^{-\frac{\sigma_\phi^2}{2}}}_{=a_\mathrm{smp}}\cos(\phi)$$

and identifying the changed mean intensity and amplitude parameters o_smp and a_smp on the right hand side, the sample-induced visibility reduction v, defined as $v = v_\mathrm{smp}/v_\mathrm{ref} = \frac{a_\mathrm{smp}/o_\mathrm{smp}}{a_\mathrm{ref}/o_\mathrm{ref}}$, can be directly identified:

$$v = e^{-\frac{\sigma_\phi^2}{2}} . \tag{4.16}$$

Due to the orthogonality of the Fourier basis, this result also applies to non-sinusoidal phase stepping curves and generally describes the contrast visibility of a particular harmonic of the periodic pattern implicitly selected by the respective definition of ϕ with respect to spatial dimensions, which will be concretized in the following Section.

Although visibility is, by virtue of describing a normalized amplitude, an inherently positive quantity, it can in the context of grating based phase contrast imaging (which will not be further considered in the present work) be meaningful to explicitly define negative visibilities as well. Due to the ambiguity $a\cos(\phi) = -a\cos(\phi \pm \pi)$, the sign of a sinusoid's amplitude may generally be flipped when simultaneously accounting for a phase shift of 180°. Whenever the phase shift is explicitly constrained by suiting prior knowledge, negative amplitudes and visibilities can therefore result, as is e.g. the case in [210]. A physical interpretation of this mathematical peculiarity can be found in the relation between the complex amplitude and the observable intensity of light waves.

Sections 4.4–4.6 are published in adapted form in Graetz et al., Phys. Med. Biol. 2020 [47]

4.4.2 Linear diffusion interpretation

Given the period T_{G2} of the Talbot interferometer's analyzer grating, the sample induced blurring width σ_ϕ of the first harmonic can be expressed in spatial units (indicated by the subscript x):

$$\sigma_x = \frac{T_{\mathrm{G2}}}{2\pi}\sigma_\phi \,.$$

When further arguing that the specific width σ_x at the location of the analyzer grating arises due to a beam divergence caused by the sample at distance d, the respective divergence may as well be characterized by an angular standard deviation σ_θ. Using the small-angle approximation $\Delta\theta \approx \tan\Delta\theta = \frac{\Delta x}{d}$ for $d \gg \Delta x$, we find:

$$\begin{aligned}\sigma_\theta &= \frac{\sigma_x}{d} = \frac{T_{\mathrm{G2}}}{d}\frac{\sigma_\phi}{2\pi} \\ &= \frac{T_{\mathrm{G2}}}{2\pi\, d}\sqrt{-2\ln(v)}\,. \end{aligned} \tag{4.17}$$

Within the model of angular beam diffusion and geometric propagation onto the analyzer grating, σ_θ represents an invariant property of the sample (at a given X-ray energy), while v, σ_ϕ and σ_x include properties of the instrument.

This geometric interpretation has e.g. been given by Wang et al. (2009 [188]) to describe the origination of dark-field contrast, and Bech and Grünzweig et al. (2010/2013 [7, 53]) introduced this concept as "linear diffusion coefficient"

$$\epsilon = \frac{\sigma_\theta^2}{\Delta z} = -\frac{1}{\Delta z}\frac{T_{\mathrm{G2}}^2}{2\pi^2 d^2}\ln(v)\,, \tag{4.18}$$

further normalizing σ_θ^2 to the sample thickness Δz in order to obtain a thickness independent material constant analog to the classic "linear absorption coefficient" μ, such that:

$$-\ln\left(v(x,y)\right) \propto \int \mathrm{d}z\, \epsilon(x,y,z)\,,$$

with z denoting the optical axis and x, y being the planar projection image coordinates.

Anticipating the following Sections, it shall be noted here that the linear diffusion interpretation only holds in a parallel beam geometry and in the limit of sufficiently large and smooth scattering structures. The critical length scale depends on the interferometer parameters, as will be explained in the following (cf. Sections 4.4.3 and 4.4.4). Additional geometric scaling effects beyond the trigonometric relation $\sigma_x \approx d\sigma_\theta$ need to be explicitly accounted for in the case of a Talbot interferometer in cone beam geometry, i.e., in the typical laboratory use case (cf. Secion 4.4.5).

4.4.3 Ab initio derivation of visibility reduction

Yashiro et al. and Lynch et al. (2010–2011 [211, 103]) derive the origination of dark-field contrast (or visibility reduction) starting from a first principles approach, explicitly modeling spatially varying refractive indices of grating and sample. By coherent propagation of the complex wavefront to the location of the analyzer grating within the optical Fresnel regime and subsequent Fourier analysis (analog to the effect of the analyzer grating), a complete model of the Talbot imaging process in a parallel beam geometry is obtained. While Yashiro et al. considered the sample to be placed in front of the Talbot interferometer, Lynch et al. considered the case of the sample placed between the modulator and analyzer grating. Both arrive at the same conclusions employing a statistic model of the sample's refractive properties on the scale below the system's spatial resolution. More specifically, the sample is characterized by its total phase shift Φ along the optical axis (its absorbing properties are treated separately), which varies in the perpendicular x, y plane (the imaging plane), i.e., $\Phi = \Phi(x, y)$. Decomposing $\Phi(x, y)$ into low- and high-frequency (smooth and fine) components $\Phi_{\mathrm{s}}(x, y)$ and $\Phi_{\mathrm{f}}(x, y)$, the dark-field contrast can be attributed to the high frequency component Φ_{f}. High frequency variations in absorption are neglected. The lower cutoff frequency of Φ_{f} is determined by the spatial resolution of the imaging system, i.e., by its effective point spread width.

Sections 4.4–4.6 are published in adapted form in Graetz et al., Phys. Med. Biol. 2020 [47]

The final result given by both Yashiro and Lynch (although using different notations) relates the visibility v to the autocorrelation of the high frequency part Φ_f of the sample's phase shifting properties Φ:

$$v = e^{-\sigma^2_{\Phi_\mathrm{f}}(1-\gamma(\xi))}, \tag{4.19}$$

with $\gamma(\xi)$ being the normalized autocorrelation function (i.e., $\gamma(0) = 1$), $\sigma^2_{\Phi_\mathrm{f}}$ the variance of Φ_f and ξ the correlation distance. $\gamma(\xi)$ and $\sigma^2_{\Phi_\mathrm{f}}$ are to be understood as respective mean properties of Φ_f on the spatial scale of the imaging system's point spread width at a given location (x, y). The explicit x, y dependence has been omitted here for improved readability. $\sigma^2_{\Phi_\mathrm{f}}$ has, within an analogy to general scattering theory by Strobl and Prade et al. [174, 143], been identified with a scattering cross section (cf. Section 4.4.6). The one dimensional autocorrelation parametrized by ξ is performed along the interferometer's sensitivity direction, i.e., perpendicular to the interferometer grating bars. This for most setups is the horizontal or x direction.

The correlation distance ξ is determined by the X-ray wavelength λ, the analyzer grating period T_{G2} and the distance d between sample and analyzer grating [211, 103]:

$$\xi = \frac{\lambda}{T_{\mathrm{G2}}} d\,. \tag{4.20}$$

This relation has been consistently given also in the context of other derivations, e.g. [195, 174]. The correlation distance can thus be easily tuned by varying d, i.e., by moving the sample closer to or further from the analyzer grating. The system constants λ and T_{G2} (and the maximum possible distance d) determine the accessible order of magnitude of ξ, which typically ranges at the micrometer level for most X-ray Talbot interferometers.

Although Yashiro and Lynch did not explicitly consider the case of d being larger than the G_1–G_2 distance (i.e., the sample was assumed to be either directly in front of G_1, or between G_1 and G_2), experiments indicate that this situation is not fundamentally different (cf. Fig. 4.4.5)

The distinction between effective cross section $\sigma^2_{\Phi_\mathrm{f}}$ and autocorrelation $\gamma(\xi)$ can also be interpreted as a representation of orthogonal sample properties. While $\gamma(\xi)$ is characteristic to the structure perpendicular to the optical axis, $\sigma^2_{\Phi_\mathrm{f}}$ characterizes the sample along the optical axis. In particular, $\sigma^2_{\Phi_\mathrm{f}}$ will scale with sample thickness, while $\gamma(\xi)$ depends on the sample's characteristic structure.

4.4.4 Relation to the linear diffusion interpretation

The geometric beam diffusion interpretation given by Wang, Bech and Grünzweig et al. (2009–2013 [188, 7, 53]) can be found as a special case of the more general result $v = \exp(-\sigma^2_{\Phi_\mathrm{f}}(1-\gamma(\xi))$ given by Yashiro and Lynch when considering the limit of smooth convex (spheroid) scattering structures of diameter $D \gg \xi$. The autocorrelation function γ can then be approximated by $\exp(-\frac{1}{2}\frac{\xi^2}{(D/3)^2})$ (cf. [143] and references therein):

$$\begin{aligned} \gamma_D(\xi) &\approx e^{-\frac{1}{2}\frac{\xi^2}{(D/3)^2}} \\ \text{(parabolic approx.)} &\approx 1 - \frac{1}{2}\frac{\xi^2}{(D/3)^2} \quad \text{for } D \gg \xi\,, \end{aligned} \tag{4.21}$$

such that

$$v \approx \exp\left(-\frac{1}{2}\frac{\sigma^2_{\Phi_\mathrm{f}}\xi^2}{(D/3)^2}\right) = \exp\Bigg(-\frac{1}{2}\underbrace{\left(\frac{\sigma_{\Phi_\mathrm{f}}}{D/3}\right)^2\left(\frac{\lambda}{T_{\mathrm{G2}}}\right)^2 d^2}_{=\sigma^2_\phi}\Bigg)\,. \tag{4.22}$$

In this limit, the linear distance dependence of the blurring width σ_ϕ on the sample distance d as assumed in the angular diffusion interpretation is reproduced. By substitution of Eq. 4.22 into Eq. 4.18, the following identity results:

$$\epsilon \approx \frac{1}{\Delta z}\left(\frac{\lambda}{2\pi}\frac{\sigma_{\Phi_\mathrm{f}}}{D/3}\right)^2\,. \tag{4.23}$$

Sections 4.4–4.6 are published in adapted form in Graetz et al., Phys. Med. Biol. 2020 [47]

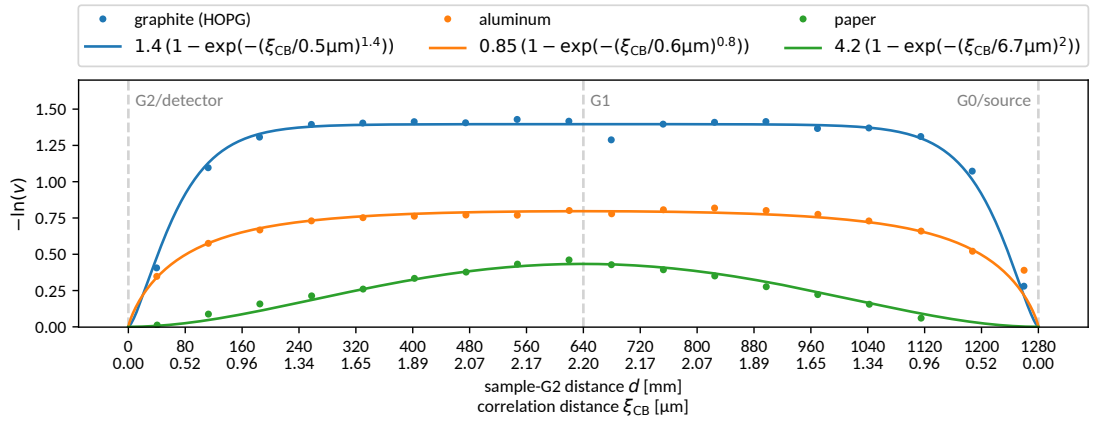

Figure 4.4: Comparison of experimental data acquired in cone beam geometry by M. Chabior [17] with the Yashiro-Lynch model (Eq. 4.19) under consideration of Fresnel scaling (cf. Eq. 4.26) and a generic exponential autocorrelation model (cf. Eq. 4.27).

The linear diffusion model becomes inaccurate as soon as γ deviates from a parabolic approximation, which either is the case for too large values of ξ/D (i.e., for too small diameters D), or when γ actually is not parabolic even for small ξ/D. The former case applies for too small scattering particles, while the latter case applies for non-smooth shaped structures.

While the geometric beam diffusion interpretation was originally proposed independent of the particular imaging geometry (parallel beam versus cone beam), it's relation to the more rigorous Yashiro-Lynch theory suggests that additional geometric scaling effects as predicted by coherent optics need to be taken into account when considering laboratory instruments operating in cone beam geometry.

4.4.5 Magnification and Fresnel scaling in cone beam geometry

The derivations by Yashiro and Lynch, as well as the numeric simulations by Malecki et al. [107] confirming their results, were explicitly performed in a planar illumination context, which in experimental terms is commonly given only at synchrotron facilities. Laboratory setups operate at moderate distances from an X-ray point source as compared to the extent of the illuminated field of view and therefore exhibit non-negligible changes in geometric magnification for different positions along the optical axis. However, by means of the Fresnel scaling theorem, all results obtained for plane wave illumination within the Fresnel approximation can be directly transferred to a cone beam or point source illumination scenario by geometric scaling of all dimensions, i.e. [134]:

$$I^{(\mathrm{SOD})}(x, y, d) = M^{-2} I^{(\infty)}\left(\frac{x}{M}, \frac{y}{M}, \frac{d}{M}\right) \tag{4.24}$$

$$M = \frac{\mathrm{SDD}}{\mathrm{SOD}} = \frac{\mathrm{SDD}}{\mathrm{SDD} - d}\,, \tag{4.25}$$

with M being the geometric magnification factor defined by the ratio of source–detector distance SDD (assumed to be equivalent to the source–G_2 distance) and source–object distance SOD. The optical axis is oriented along the z-axis, x and y are the orthogonal image plane coordinates. $I^{(\mathrm{SOD})}$ is the intensity distribution at the detector (placed directly behind the analyzer grating G_2 at distance d from the sample) in the case of a source placed at distance SOD. $I^{(\infty)}$ is the intensity pattern for the case of an infinitely distant source (i.e., the case of plane wave illumination). The Fresnel scaling theorem essentially states that classic geometric magnification based on the intercept theorem applies also to coherent wave propagation within the Fresnel regime, affecting both the plane perpendicular to the optical axis as well as propagation distances along the optical axis.

While this scaling relation is taken into account in the design of laboratory type Talbot-Lau interferometers by scaling the position and period of the modulating G_1 grating appropriately with

Sections 4.4–4.6 are published in adapted form in Graetz et al., Phys. Med. Biol. 2020 [47]

respect to the analyzer grating G_2 [191, 190, 33], it has, to the author's knowledge, not yet been regarded in models of the distance dependence of the visibility or dark-field contrast.

When consequently applying the above scaling relation to the correlation distance ξ (cf. Eq. 4.20), the effective correlation distance in terms of the actual sample dimensions becomes, for a cone beam (CB) geometry,

$$\xi_{\mathrm{CB}} = \xi/M = \underbrace{\frac{\lambda}{T_{\mathrm{G2}}} d}_{\xi} \underbrace{(1 - \frac{d}{\mathrm{SDD}})}_{=1/M(d)} . \tag{4.26}$$

This result can be either interpreted as a consequence of scaled sampling from the sample's phase $\Phi(x, y)$ according to the Fresnel scaling theorem, or, more intuitively, as the consequence of the geometric magnification of the sample at the location of the analyzer grating, which serves as the reference scale for all other (downscaled) planes along the optical axis (cf. the definition of M, Eq. 4.25). Consequences of the specific form of ξ_{CB} are its symmetry about $d = \mathrm{SDD}/2$ and its maximum at $d = \mathrm{SDD}/2$:

$$\xi_{\mathrm{CB,max}} = \frac{\lambda}{T_{\mathrm{G2}}} \frac{\mathrm{SDD}}{4} .$$

Within the Fresnel approximation, the spatial order of optical elements along the optical axis is related to their respective propagation distances. As Eqs. 4.19–4.20, which have been derived from a wave optical approach, are independent of the position of G_1, so is the scaled version 4.26. In contrast to the geometric optics reasoning given by Donath et al. [33] in the context of differential phase contrast imaging, which was transferred by several authors to dark-field imaging, the symmetry of Eq. 4.26 emerges from the specific relation between physical distance, geometric magnification and resulting effective propagation distance of the sample with respect to the detector (cf. Eq. 4.26), and is thus in particular expected to be independent of the position of G_1.

This also has implications on the angular beam diffusion model (cf. Sections 4.4.2 and 4.4.4) for the origination of dark-field contrast. By its conception of diffused incident beams, geometric scaling was assumed to arise, independent of the actual system geometry, only due to the trigonometric relation between diffusion angle σ_θ and sample–detector distance d. When considering the beam diffusion model as an approximation of the Yashiro-Lynch theory in the case of large sample structures in relation to ξ, as was discussed in Section 4.4.4, the following modified relation is found though:

$$v \approx \exp\left(-\frac{1}{2}\frac{\sigma_{\Phi_\mathrm{f}}^2 \xi_{\mathrm{CB}}^2}{(D/3)^2}\right) = \exp\Bigg(-\frac{1}{2}\underbrace{\left(\frac{\sigma_{\Phi_\mathrm{f}}}{D/3}\right)^2 \left(\frac{\lambda}{T_{\mathrm{G2}}}\right)^2 \left(\frac{d}{M(d)}\right)^2}_{=\sigma_\phi^2}\Bigg) ,$$

i.e., $\sigma_\theta \propto \frac{d}{M(d)}$ rather than $\propto d$.

Experimental evidence can be found e.g. in the Thesis of M. Chabior [17] (cf. data reproduced in Fig. 4.4), who indeed finds, for a paper sample in a cone beam setup, a deviation from the quadratic distance dependence of $\ln(v)$ as expected by the classic linear diffusion model (cf. Section 4.4.2). The severe deviations found in the same work for aluminum and graphite samples can on the other hand be explained by an additional violation of the implicit $D \ll \xi$ assumption (cf. Section 4.4.4). Eq. 4.26 further reproduces the symmetry in the distance dependence about the midpoint between source and G_2 that was experimentally shown e.g. by Chabior [17] and Prade et al. [143]. This symmetry has previously been associated with the geometric optics argument given by Donath et al. [33] (expecting the maximal propagation distance to be explicitly related to the position of G_1), which was transferred e.g. by Strobl [174] to the context of dark-field imaging.

Figure 4.4 reproduces the data published by Chabior [17] (using an interferometer designed to 45keV with an analyzer grating period T_{G2} of 4µm, i.e., $\lambda/T_{\mathrm{G2}} \approx 6.89 \times 10^{-6}$) and compares it to the Yashiro-Lynch model under consideration of Fresnel scaling (cf. Eq. 4.26) and the generic autocorrelation model

$$\gamma(\xi_{\mathrm{CB}}) = e^{-(\xi_{\mathrm{CB}}/L)^{2H}} \tag{4.27}$$

also used in [211], with L being a characteristic correlation length and the Hurst exponent H characterizing the shape of the autocorrelation function and in particular allowing for both sharp and smooth autocorrelation profiles. The results shown in Fig. 4.4 are perfectly consistent with the

Sections 4.4–4.6 are published in adapted form in Graetz et al., Phys. Med. Biol. 2020 [47]

expectations of Eq. 4.26, although the particular experiment does not allow to explicitly confirm the independence of the observed symmetry from the actual placement of G_1.

Besides the correlation distance ξ, also the effective integration area of a detector pixel with respect to the sample dimensions is subject to geometric scaling. As the autocorrelation function $\gamma(\xi_{\mathrm{CB}})$ represents the mean statistical properties of the sample's phase shifting properties below the imaging resolution (cf. Section 4.4.3), γ itself will be subject to change whenever the the imaging resolution (i.e., the pixel integration area) crosses characteristic lengths scales of the sample's structure. This effect was experimentally observed by Koenig et al. [87], who further consistently find a dependence also on the X-ray focal spot size, which likewise affects the imaging resolution.

4.4.6 Relation to Small Angle Scattering

Small angle scattering (SAS) techniques, or more specifically, small angle X-ray scattering (SAXS), sense a sample's differential scattering cross section (its scattering angle distribution) usually by means of illuminating it with a collimated X-ray pencil beam. A planar detector array placed behind the sample at a sufficient distance captures the scattered radiation. By application of fundamental principles from optics and Fourier analysis, the observable two-dimensional diffraction pattern is commonly shown to correspond to the Fourier transform of the auto correlation function of the sample's scattering length density (cf. e.g. the textbook by da Sivia [171]). As the latter is, on a larger scale, related to the sample's mass density, the observed pattern can be, more qualitatively, understood as the Fourier transform of the autocorrelation function of a sample's micro- or mesoscopic structure. The resolution and range of sampled correlation distances depends on the sensed angular range, with smaller scattering angles corresponding to larger correlation distances, i.e., to larger structure scales.

While SAXS commonly addresses length scales in the 10^1 to 10^2 nanometer range, the signal captured by X-ray Talbot interferometers corresponds to ultra small angle X-ray scattering (USAXS) typically related to lengths scales on the micrometer scale (cf. Eqs. 4.19 and 4.20). An important practical difference between SAXS and USAXS with respect to data analysis and interpretation emerges from the relation to the incident radiation: while the larger scattering angles in SAXS generate signals well separated from the incident radiation, USAXS analyses require explicit consideration of contributions of the original beam.

Following the convolution concept of dark-field contrast origination, Modregger et al. infer the effective point spread function (PSF) of a sample by means of actual deconvolution of the phase stepping curves (PSC) acquired with and without sample [118]. The result is directly interpreted, in analogy to classic SAXS, as differential scattering cross section and Fourier transform of the sample's autocorrelation function [117, 116]. Implicit to this reasoning is the assumption that the incident radiation entirely participates in the scattering process described by the inferred PSF.

Another analogy between small angle scattering theory and dark-field imaging was drawn by Strobl [174] and Prade et al. [143], who model an incoherent superposition of scattered and unscattered fractions of the incident radiation in order to arrive at an expression equivalent to the wave optical results by Yashiro and Lynch (cf. Eq. 4.19) in parallel beam geometry. The factor $\sigma^2_{\Phi_\mathrm{f}}$ (cf. Eq. 4.19) is thereby identified as the scattering cross section defining the ratio of scattered radiation. An experimental comparison of the latter model (and consequently also of the Yashiro-Lynch model) to SAXS is given by Gkoumas et al. [43], who investigate contributions of the structure factor to the autocorrelation function – as expected in classic scattering experiments – for dense sphere suspensions in a parallel beam synchrotron setting.

The PSF deconvolution approach is, in terms of Fourier analysis, equivalent to the evaluation of higher order Fourier components of the PSCs, of which commonly only the zeroth (mean attenuation) and the first (mean attenuation and visibility reduction) are evaluated. I.e., when directly interpreting the point spread function (or convolution kernel) as a SAXS pattern, the respective Fourier coefficients q_m of the phase stepping curves with and without sample are expected to be related by an autocorrelation function $\gamma'(m\xi)$:

$$|q_m^{(\mathrm{PSC_{sample}})}| \propto \gamma'(m\xi)\, |q_m^{(\mathrm{PSC_{reference}})}|$$

with m enumerating the harmonics. The prime explicitly distinguishes it from the autocorrelation function γ as defined by Yashiro and Lynch (and Strobl and Prade), although γ and γ' are expected

Sections 4.4–4.6 are published in adapted form in Graetz et al., Phys. Med. Biol. 2020 [47]

to be closely related. When directly comparing γ' with the Yashiro-Lynch theory for a thin sample and $m = 1$, we find (assuming $1 \gg \sigma^2_{\Phi_\mathrm{f}}(1 - \gamma(m\xi)) \geq 0$):

$$\begin{aligned}\gamma'(\xi) \hat{=} e^{-\sigma^2_{\Phi_\mathrm{f}}(1-\gamma(\xi))} &\approx 1 - \sigma^2_{\Phi_\mathrm{f}}(1 - \gamma(\xi)) \\ &\hat{\approx} \sigma^2_{\Phi_\mathrm{f}}\gamma(\xi) + (1 - \sigma^2_{\Phi_\mathrm{f}}) \,,\end{aligned}$$

i.e., the Yashiro-Lynch theory is qualitatively consistent with the expectations from classic scattering theory, yet differs in detail. First, SAXS theory is inherently founded on a single scattering assumption, i.e., a thin sample assumption. This gives rise to the linear vs. exponential relation with the autocorrelation function. The constant offset $(1 - \sigma^2_{\Phi_\mathrm{f}})$ corresponds, within the model employed by Strobl and Prade et al. [174, 143], to the unscattered fraction of the incident radiation, which was not explicitly modeled in the SAXS analogy by Modregger et al. [118, 117, 116].

4.4.7 Superposition of dark-field signals

With respect to tomographic imaging, linearity of the given contrast modality is a necessary prerequisite. I.e., the signal generated by a stack of samples must equal the sum of their isolated signals. Analogously, the signal response is required to be proportional to the thickness of a homogeneous sample. In classic X-ray computed tomography, this is provided by the well known Lambert-Beer law of intensity attenuation.

An equivalent relation is also found for the dark-field contrast modality: most directly, it can be inferred from the Gaussian convolution model given previously in Section 4.4. Under the assumption that multiple samples (sections of a larger sample), characterized by their effective point spread widths $\sigma_{\phi,i}$, don't interact, their combined effect will be a series of convolutions (as direct consequence of their individual effects). As convolutions of Gaussian kernels correspond to a summation over their variances, the combined signal is then, with Eq. 4.16, given by the product of their individual visibilities:

$$v = e^{-\frac{1}{2}\sum_i \sigma^2_{\phi,i}} = \prod_i e^{-\frac{\sigma^2_{\phi,i}}{2}} = \prod_i v_i \,. \tag{4.28}$$

This argument has been employed e.g. by Wang et al. [188] (in analogy to Khelashvili et al. [85]) and Bech et al. [7] to derive the feasibility of dark-field tomography. The relation can further be generalized to non-Gaussian convolution kernels by means of the convolution theorem, as has been done by Modregger et al. [117, 116]:

$$\begin{aligned} g(\Delta\phi) &= g_1(\Delta\phi) \circledast g_2(\Delta\phi) \circledast \cdots \\ v'(q) = \mathcal{F}(g(\Delta\phi)) &= \prod_i \mathcal{F}(g_i(\Delta\phi)) \\ &= \exp\left(\sum_i \ln \mathcal{F}(g_i)\right) \end{aligned}$$

with $\circledast$ denoting the convolution operation and $\mathcal{F}$ the Fourier transformation. q is the conjugate variable to $\Delta\phi$ after transformation. $g(\Delta\phi)$ is the effective point spread kernel found for a sample, with $g_i(\Delta\phi)$ being individual contributions. The prime on $v'(q)$ indicates the missing normalization to $v'(0)$. The Gaussian convolution model is in fact a special case of this more general formulation. The frequency (q) dependence of v is usually not explicitly addressed in the majority of articles on the subject, as v is commonly explicitly defined as the visibility of the first harmonic of the grating period, i.e., $v = v'(q_1)/v'(q_0)$ (cf. Pfeiffer et al. (2008) [138]).

The linear superposition of exponential arguments is, independent of the above considerations, also found by Yashiro et al. [211] and Lynch et al. [103] within their wave optical derivations of dark-field contrast origination (cf. Section 4.4.3).

With respect to tomographic applications, for which the Lambert-Beer relation is generally exploited, it shall be already noted here that the positional dependence of the dark-field contrast needs to be considered as well, as will be done in the following Section 4.6.

Sections 4.4–4.6 are published in adapted form in Graetz et al., Phys. Med. Biol. 2020 [47]

4.5 Dark-field tomography

4.5.1 Experimental verification of distance and structure size effects

While the dependence of the system's correlation length ξ on the distance d between sample and analyzer grating G_2 is beneficial with respect to quantitative material characterization analog to other scattering techniques, the resulting distance dependence of the dark-field signal is an undesired perturbation in the context of tomographic dark-field imaging. For centimeter scaled samples, the sample extent is typically not negligible anymore with respect to its mean distance d_0 from the analyzer grating, wherefore the distance dependence has been explicitly examined using a rotating circular arrangement of differently sized spherules and compared to the theoretical expectations discussed in Sections 4.4.2–4.4.4. Figure 4.5 shows a sketch of the experimental setup and a summary of the respective results.

The distance and sphere diameter dependent signals (Fig. 4.5 left) extracted from projections of the rotating sample cylinder shall be in particular compared to the explicit expressions for μ_{DF} and the autocorrelation function $\gamma_D(\xi)$ for spherical particles of diameter D given by Lynch et al. [103] and Yashiro et al. [209] respectively:

$$\mu_{\mathrm{DF}}(D,\xi) = \Delta z \frac{3\pi^2}{\lambda^2} f \left|\Delta\chi\right|^2 D \begin{cases} 1 - \sqrt{1-\frac{\xi^2}{D^2}}\left(1+\frac{1}{2}\frac{\xi^2}{D^2}\right) & \\ \quad + \left(\frac{\xi^2}{D^2} - \frac{1}{4}\frac{\xi^4}{D^4}\right)\ln\left(\frac{1+\sqrt{1-\xi^2/D^2}}{1-\sqrt{1-\xi^2/D^2}}\right) & \text{for } D > \xi \\ 1 & \text{for } D \leq \xi \end{cases} \tag{4.29}$$

$$\gamma_D(\xi) = \left(1+\frac{1}{2}\frac{\xi^2}{D^2}\right)\sqrt{1-\frac{\xi^2}{D^2}} + \left(2\frac{\xi^2}{D^2} + \frac{1}{4}\frac{\xi^4}{D^4}\right)\ln\left(\frac{\xi/D}{1+\sqrt{1-\xi^2/D^2}}\right) \quad \text{for } D \geq \xi \tag{4.30}$$

$$\xi = \frac{\lambda}{T_{\mathrm{G2}}} d \quad \text{(cf. Eq. 4.20)}\,.$$

Constants of the material and experiment will be specified later. Beforehand, the specific methodology of the present data analysis shall be further outlined: By Eq. 4.22, the dark-field signal is expected to be approximately quadratic in d. The data is thus, after subtraction of the background dark-field signal caused by the sample container (cf. Fig. 4.5, upper left), considered in the square root domain, i.e. transformed to $\sigma_\phi = \sqrt{2\mu_{\mathrm{DF}}} = \sqrt{-2\ln(v)}$. It is then fitted to the first order Taylor expansion

$$\sigma_\phi(D,d) \approx \sigma_\phi(D,d_0)\,(1 + \alpha_D \underbrace{r\sin(\omega-\omega_0)}_{\Delta d(\omega)}) \tag{4.31}$$

of the unknown actual function $\sigma_\phi(D,d)$ about the mean sample-G_2-distance d_0, with

$$\alpha_D = \frac{1}{\sigma_\phi(D,d_0)} \left.\frac{\partial}{\partial d}\sigma_\phi(D,d)\right|_{d=d_0}\,. \tag{4.32}$$

The parameters r and $\omega-\omega_0$ denote the distance and rotation phase of the considered sample capillary with respect to the rotational axis, and $d_0 + \Delta d(\omega)$ describes the resulting orientation dependent sample-G_2-distance d. Deviations from $\alpha_D = 1/d_0$ correspond to deviations from the assumptions of the linear diffusion model (Eqs. 4.17, 4.18 and 4.22), as can be easily verified by comparison of Eq. 4.31 with the Taylor expansion of the respective model $\sigma_\phi(D,d) \propto d\,\sigma_\theta(D)$.

While the mean dark-field signal $\mu_{\mathrm{DF}}(D,d_0) = \frac{1}{2}\sigma_\phi(D,d_0)^2$ contained in Eq. 4.31 can now be directly compared to Eq. 4.29 given an estimate of the involved material constants (which will be provided later), further transformations are required for a comparison of α_D with the $d(\omega)$-dependent autocorrelation function $\gamma_D(\xi(d))$ (Eq. 4.30). By substituting the relations

$$\sigma_\phi = \sqrt{2\mu_{\mathrm{DF}}} = \sqrt{2\,\sigma^2_{\Phi_{\mathrm{f}}}(D)\,(1-\gamma(\xi(d)))}$$

$$\text{and} \quad \frac{\partial}{\partial d}\gamma(\xi(d)) = \frac{\partial}{\partial\xi}\gamma(\xi)\frac{\partial\xi}{\partial d} = \frac{\partial}{\partial\xi}\gamma(\xi)\frac{\xi}{d}$$

Sections 4.4–4.6 are published in adapted form in Graetz et al., Phys. Med. Biol. 2020 [47]

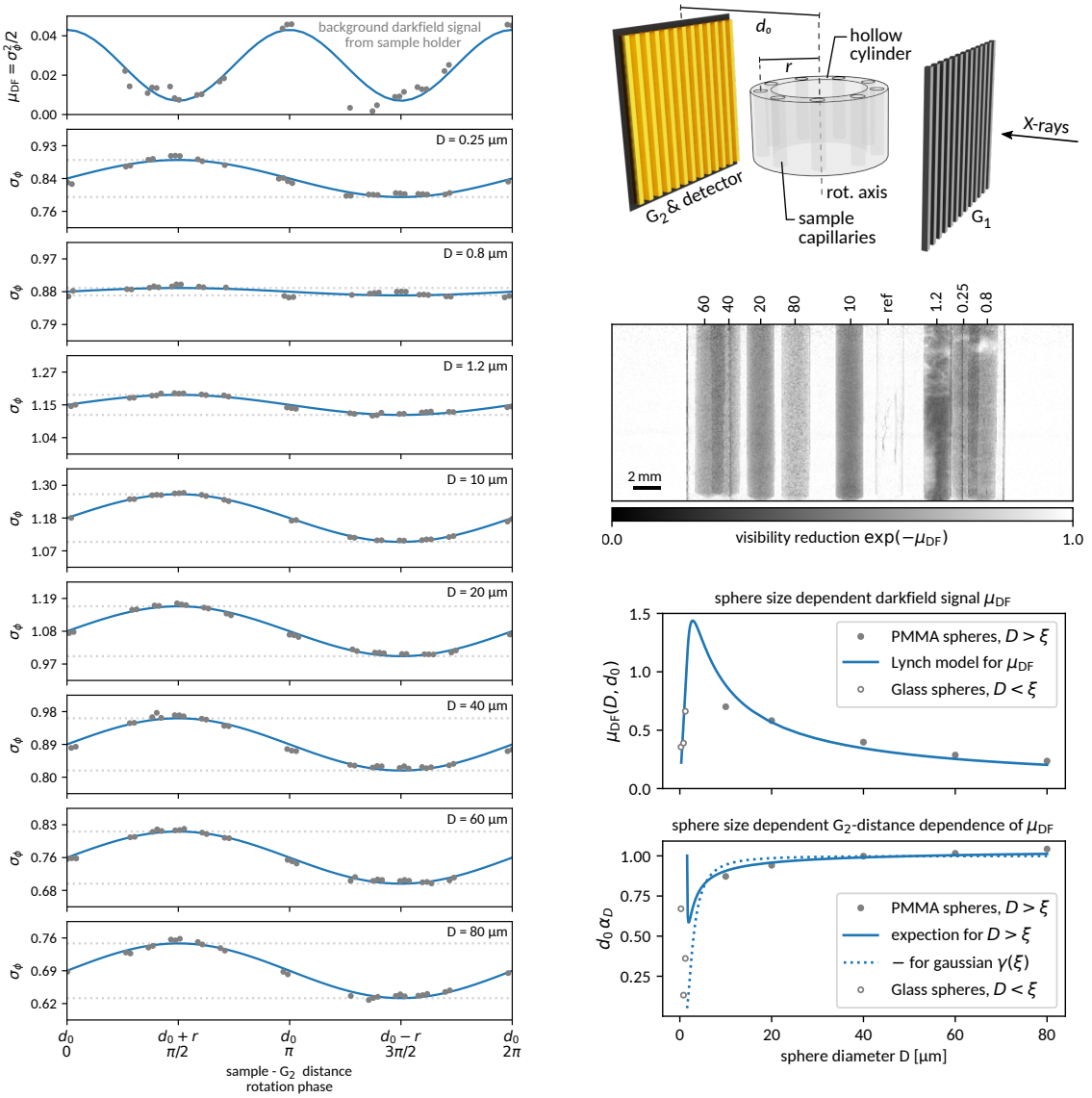

Figure 4.5: Experimental data (left) on the dependence of dark-field contrast both on the distance d between sample and analyzer grating G_2 and on the structure size. Sinusoidal distance variations for multiple samples were realized by rotating a cylindrical container of radius $r \approx 1\,\mathrm{cm}$ comprising nine capillary tubes arranged equidistantly along the perimeter, eight of which are filled with spherules of diameters D ranging between 0.25 µm to 80 µm (cf. sketch on the upper right). The ninth empty one serves as reference for the background signal generated by the sample container, which is approximated using a $\cos^2$ function due to the expected 180° symmetry. Dark-field signals are evaluated for all viewing angles which allow for unobstructed views on individual capillaries (hence the uneven sampling pattern), and the background signal is subtracted prior to further processing. An example projection image is shown on the right. As the distance dependence is expected to be linearly approximable for $\sigma_\phi = \sqrt{2\mu_{\mathrm{DF}}}$ (cf. Eqs. 4.16 and 4.22), the signals are evaluated accordingly and approximated by a sinusoid corresponding to the variation in sample-G_2 distance. Quantitative comparisons of both the spherule size dependence and the distance dependence of the dark-field signal with the respective models given in Eqs. 4.29, 4.33 (with Eq. 4.30) and 4.35 are shown on the lower right. Deviations of $\mu_{\mathrm{DF}}(D, d_0)$ from the expected model (in particular at $D = 10\,\mu\mathrm{m}$) can be related to unaccounted variations in the volume fraction of spheres, cf. Figures 4.6–4.7. The d-dependence in cases of $D < \xi$ (particularly pronounced for $D = 0.25\,\mu\mathrm{m}$) can be attributed to the non-vanishing autocorrelation function of the sphere arrangement rather than the spheres themselves.

Sections 4.4–4.6 are published in adapted form in Graetz et al., Phys. Med. Biol. 2020 [47]

into Eq. 4.32, the following correspondence results at $d = d_0$:

$$\alpha_D = -\frac{1}{2}\frac{\xi_0}{d_0}\frac{\frac{\partial}{\partial\xi}\gamma(\xi)|_{\xi=\xi_0}}{1-\gamma(\xi_0)} \tag{4.33}$$

$$\text{with} \quad \xi_0 = \frac{\lambda}{T_{\mathrm{G2}}} d_0 \,, \tag{4.34}$$

which can be compared to the observed values of α_D determined using Eq. 4.31. The above expression may either be evaluated using Eq. 4.30, or may further be approximated using the Gaussian autocorrelation model given in Eqs. 4.21–4.22. Eq. 4.33 then simplifies to

$$\alpha_D \approx \frac{1}{2}\frac{1}{d_0}\frac{\xi_0^2}{(D/3)^2}\left(e^{\frac{1}{2}\frac{\xi_0^2}{(D/3)^2}} - 1\right)^{-1} . \tag{4.35}$$

In the limit of large spheres, i.e., $D \to \infty$, the following limit as expected by the linear diffusion model is approached both for Eq. 4.33 with Eq. 4.30 as well as its approximation in Eq. 4.35:

$$\lim_{D\to\infty} \alpha_D = \frac{1}{d_0} \,. \tag{4.36}$$

A comparison of the experimental data (Fig. 4.5 left) with Eqs. 4.29, 4.33 (using Eq. 4.30) and 4.35 is shown on the bottom right of Fig. 4.5. In contrast to Eq. 4.29, Eqs. 4.33–4.35 do have only one single free parameter, d_0. A least squares fit yields

$$d_0 \approx 10.7\,\mathrm{cm} \tag{4.37}$$

$$\text{and thus } \xi_0 \approx 1.5\,\mu\mathrm{m} \tag{4.38}$$

which is in excellent agreement with the actual experimental configuration of $d_0 = (0.1 \pm 0.01)\,\mathrm{m}$.

Note that the autocorrelation of a given finite shape (as the spheres) inherently becomes zero for correlation distances larger than the extent (diameter) of that shape, wherefore the submicrometer sized glass spherules are not described by Eqs. 4.30 and 4.33. That they nevertheless exhibit a distance dependence (cf. Fig. 4.5) can rather be attributed to the fact that the dense packing of spheres of 0.25 to 1.2 µm diameter implies that the autocorrelation of the sphere arrangement, i.e., the structure factor (see also Section 4.4.6 and reference [43]), becomes non-negligible at the given mean correlation distance ξ_0 of 1.5 µm

Finally, with respect to the quantitative comparison of the actual dark-field signals $\mu_{\mathrm{DF}}(D)$ at d_0 to the theoretic prediction as given by Eq. 4.29, the following constants are used:

$$\begin{aligned} \lambda &= 35.54 \times 10^{-12}\,\mathrm{m} & f &\approx 0.74 \\ T_{\mathrm{G2}} &= 2.4\,\mu\mathrm{m} & \Delta z &\approx 10^{-3}\,\mathrm{m} \\ d = d_0 &\approx 10^{-1}\,\mathrm{m} & r_e\rho_{e,\mathrm{PMMA}} &\approx 10^{15}\,\mathrm{m}^{-2} \\ \Delta\chi &\approx -\frac{\lambda^2}{2\pi} r_e\rho_e & \text{such that } \Delta z \frac{3\pi^2}{\lambda^2} f\left|\Delta\chi\right|^2 &\approx 0.7\,\mu\mathrm{m}^{-1} \,, \end{aligned}$$

with λ being the X-ray wavelength (corresponding to 35keV), T_{G2} the analyzer grating period, d the sample-G_2 distance, f the volume fill factor (assuming dense sphere packing), Δz the average sample thickness and $r_e\rho_{e,\mathrm{PMMA}}$ the scattering length density for PMMA.[1] $\Delta\chi$ is the refractive index, whose imaginary part is, in the present case, negligible with respect to its absolute magnitude. Note the difference in notation with respect to [103] regarding μ_{DF} which here for consistency refers to the actual dark-field signal as opposed to a thickness normalized dark-field coefficient. Thickness is here explicitly accounted for by Δz.

[1] estimated for $C_5H_8O_2$ with density of 1.2g/cm^3 from information provided by NIST for Cu and Mo K_α lines at `https://www.ncnr.nist.gov/resources/activation/`

Sections 4.4–4.6 are published in adapted form in Graetz et al., Phys. Med. Biol. 2020 [47]

4.5.2 Quantitative dark-field tomography despite distance dependence

Tomographic reconstruction, i.e., the transformation of projections of an object to a volume representation of that object, generally presumes that all projections correspond to linear combinations of a static set of scalar volume elements (voxels), which are to be reconstructed. For samples rotating about an axis parallel to the interferometer's gratings, as required for tomographic imaging, the distance dependence of the dark-field contrast inevitably also leads to an apparent orientation dependence of the signal originating from isotropic scatteres away from the rotational axis. As has been shown previously, this distance dependence is not generally negligible and further not independent of the actual sample properties, which are inherently unknown prior to reconstruction. Explicit modeling of this dependence in the context of general iterative tomographic reconstruction methods would therefore be a non-trivial option. The effects of distance dependence can however be eliminated to a large degree by symmetric acquisition of projections from opposing directions, by means of performing full 360° scans:

Due to the linearity – and thus additivity – of the dark-field contrast, individual volume elements (voxels) may be analyzed isolated without loss of generality. When considering an individual voxel at a distance Δd from the rotational axis (at distance d_0) with respect to the optical path, the respective signals from opposing object orientations are expected to exhibit the following relations (to first order in $\sigma_\phi(d)$):

$$\begin{aligned}\mu_{\mathrm{DF}}(d(\omega\quad)) &\approx \frac{1}{2}\left[\sigma_\phi(d_0)\,(1+\alpha\,\Delta d_\omega)\right]^2 = \mu_{\mathrm{DF}}(d_0)\,(1+2\alpha\Delta d_\omega+\alpha^2\Delta d_\omega^2)\\ \mu_{\mathrm{DF}}(d(\omega+\pi)) &\approx \frac{1}{2}\left[\sigma_\phi(d_0)\,(1-\alpha\,\Delta d_\omega)\right]^2 = \mu_{\mathrm{DF}}(d_0)\,(1-2\alpha\Delta d_\omega+\alpha^2\Delta d_\omega^2)\,,\end{aligned}$$

with α characterizing the distance dependence as discussed in the previous Section. The mean signal from opposing orientations is thuscu

$$\frac{1}{2}\left(\mu_{\mathrm{DF}}(d(\omega))+\mu_{\mathrm{DF}}(d(\omega+\pi))\right) = \mu_{\mathrm{DF}}(d_0)\,(1+\underbrace{\alpha^2\Delta d_\omega^2}_{\leq \Delta d_\omega^2/d_0^2})\,,$$

with $\alpha^2\Delta d_\omega^2$ representing the relative error with respect to $\mu_{\mathrm{DF}}(d_0)$. Given that $\alpha \leq d_0^{-1}$ is expected (cf. Eq. 4.36 and Fig. 4.5, lower right), that error is not larger than $\Delta d_\omega^2/d_0^2$, which can be realistically kept below 5% even for sample diameters (and thus values of Δd) of almost up to $d_0/2$.

Figure 4.6 shows tomographic reconstructions of the data previously presented in Figure 4.5. The effects of dark-field distance dependence on tomographic reconstructions are illustrated by means of reconstructions from two complementary sets of projections covering an angular range of only 180° each.

A quantitative analysis of the respective gray values is given in Figure 4.7. By considering the absorption normalized dark-field signal μ_{DF}/μ, effects of varying packing density are eliminated, so that variations in dark-field contrast can be expected to solely arise from differences in material (Glass vs. PMMA) and structure size (spherule diameter). The data for PMMA is compared to Eq. 4.29 (normalized by the absorption coefficient for PMMA at 35keV) at the correlation distance $\xi_0 \approx 1.5\mu\mathrm{m}$ corresponding to the mean sample–G_2 distance $d_0 \approx 10.7\,\mathrm{cm}$ as found previously (Eq. 4.37), i.e., the distance between the axis of rotation and the analyzer grating G_2:

$$\frac{\mu_{\mathrm{DF}}^{(\mathrm{PMMA})}(D)}{\mu_{\mathrm{PMMA}}^{(35\mathrm{keV})}} = c_{\mathrm{fit}}\,D\left(1-\sqrt{1-\frac{\xi_0^2}{D^2}}\left(1+\frac{1}{2}\frac{\xi_0^2}{D^2}\right)+\left(\frac{\xi_0^2}{D^2}-\frac{1}{4}\frac{\xi_0^4}{D^4}\right)\ln\left(\frac{1+\sqrt{1-\xi_0^2/D^2}}{1-\sqrt{1-\xi_0^2/D^2}}\right)\right), \tag{4.39}$$

where the proportionality constant fitting the experimental data is found to be

$$c_{\mathrm{fit}} \approx 23\,\mu\mathrm{m}^{-1}\,.$$

The theoretical expectation (cf. Eqs. 4.29 and 4.39) evaluates to

$$\frac{\Delta z}{\mu_{\mathrm{PMMA}}^{(35\mathrm{keV})}}\frac{3\pi^2}{\lambda^2}\left|\Delta\chi\right|^2 = c_{\mathrm{theo}} \approx 30\,\mu\mathrm{m}^{-1}$$

Sections 4.4–4.6 are published in adapted form in Graetz et al., Phys. Med. Biol. 2020 [47]

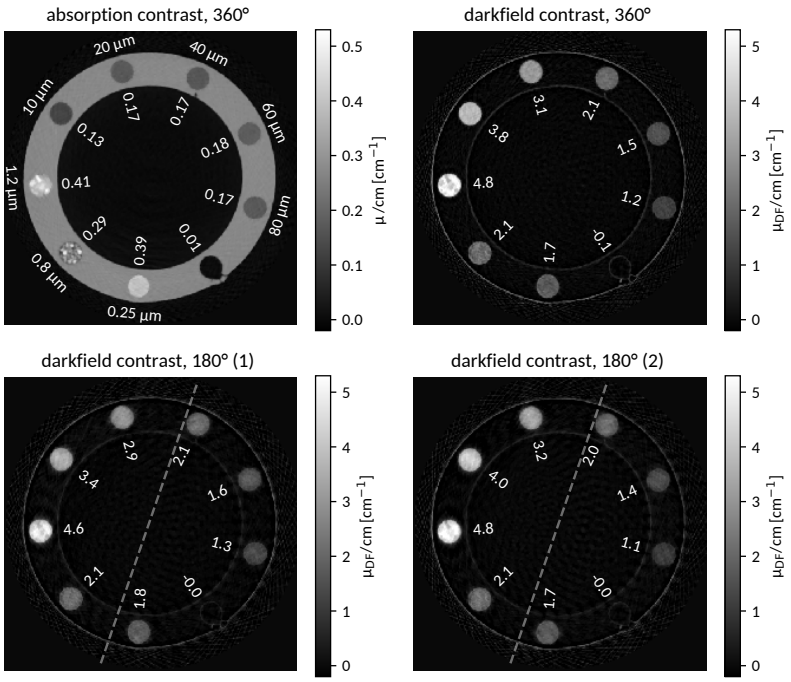

Figure 4.6: Tomographic reconstructions of a cylindrical sample container comprising nine capillaries filled with spherules of varying diameter between 0.25µm and 80µm (cf. Fig. 4.5) from absorption and dark-field projections acquired in parallel beam geometry. The reconstruction voxel size is 61.6µm, i.e., spherules are not resolved individually. The respective spherule diameters are indicated along the outer perimeter, the mean gray values are indicated along the inner perimeter. Spherules smaller than 5µm are made of glass, while the larger ones consist of PMMA. Variations in absorption (upper left) within each material class indicate variations in packing density. The dark-field signal (upper right and lower row) is further dependent on the size of the spherules. The sample container itself exhibits dark-field contrast only at edges. The distance dependence of the dark-field signal is mostly canceled when reconstructing from the full set of projections (upper right). It has a significant effect though when reconstructing from 180° subsets (bottom row). Dashed lines indicate the boundary between over- and underestimations of the dark-field signal in these cases.

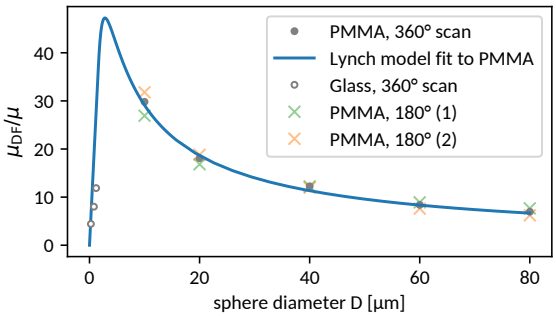

Figure 4.7: Evaluation of the dark-field contrast after tomographic reconstruction (Fig. 4.6). In order to eliminate the volume fractions f, the ratio μ_{DF}/μ (dark-field over absorption) is considered. For a given material, variations in μ_{DF}/μ are now expected to arise solely due to variations in the sphere diameter D. The respective model according to Lynch (cf. Eqs. 4.29, 4.39) is compared to the data, assuming $d_0 = 10.7\mathrm{cm}$ as found previously (Eq. 4.37). The absolute scale is fitted to the data. The good agreement of theory and experiment support the validity of the Yashiro-Lynch model of dark-field contrast origination with respect to the predicted structure size dependence. Further, the quantitative effects of dark-field distance dependence on short-scan tomographies are shown as well (see also Fig. 4.6).

Sections 4.4–4.6 are published in adapted form in Graetz et al., Phys. Med. Biol. 2020 [47]

based on the constants provided in the previous section and $\frac{\mu_{\mathrm{PMMA}}^{(35\mathrm{keV})}}{\Delta z} = 0.31\,\mathrm{cm}^{-1}$, as found in the NIST Xcom database assuming a mass density of $1.2\frac{\mathrm{g}}{\mathrm{cm}^3}$ for PMMA.

I.e., in addition to the distance dependence discussed previously, also the size dependence is perfectly consistent with the models given by Yashiro and Lynch, and can further be verified within tomographic reconstructions. The absolute quantitative scale found in the experiment agrees with the theoretic model within a margin of 25%.

Sections 4.4–4.6 are published in adapted form in Graetz et al., Phys. Med. Biol. 2020 [47]

4.6 Anisotropic Dark-field Contrast

The dark-field contrast is an oriented effect. As has been described in the previous sections, it arises from refractive effects below the spatial resolution of the imaging system and can be understood in terms of the scattering cross section and autocorrelation function of the sample's substructure. So far, the actual direction of autocorrelation was not explicitly discussed and rather implicitly determined by the orientation of the interferometer gratings. In fact, the scalar visibility contrast found in a particular experiment is to be understood as a projection of a higher dimensional property, which may or may not be isotropic. Here, a well motivated model of this anisotropy shall be derived as required for the validation of tensor tomography in Chapter 5.

4.6.1 Literature review

Dark-field anisotropy has been experimentally demonstrated e.g. by Wen et al. [193], Jensen et al. [74, 75], Revol et al. [149], Potdevin et al. [141] and Schaff et al. [160], who considered planar samples exhibiting highly ordered fibrous structures perpendicular to the optical axis, such as carbon fibers, wood fibers, dentinal tubules or trabecular bone. Technically, these cases all address distinctive variations of the autocorrelation width of long fibers with respect to their orientation. Yashiro et al. [209] considered the case of moderately anisotropic structures within an extended sample and investigated the individual effects of autocorrelation width, scattering cross section and autocorrelation shape (by both rotating the sample and sampling multiple correlation lengths, cf. Sections 4.4.3 and 4.4.6). A systematic observation of dark-field signal variation in dependence of the 3D orientation – i.e., also considering inclinations with respect to the optical axis – of highly oriented fibers was presented by Bayer et al. [6].

The theoretic modeling of these anisotropy effects has been treated phenomenologically using sinusoids reproducing the periodicity, phase and an assessment of the degree of anisotropy of the signal in dependence of a single orientation angle. This representation straight forwardly enables planar vector radiographs, augmenting 2D X-ray images with directional information on the unresolved substructure in the detection plane. Mathematically, it is equivalent to a linear approximation of the directional dependencies (as has also been pointed out by Jensen et al. [75]). Malecki et al. [105] further investigated the sinusoid approximation in numerical simulations of fibrous structures parallel to the detection plane. Current approaches extending the concept of directional imaging to tomography on volumetric samples (cf. Chapter 5) derive from these planar signal models and thus implicitly presume that the autocorrelation width perpendicular to the optical axis is the principal origin of orientation dependency of the dark-field signal. A first heuristic model of dark-field anisotropy extending beyond autocorrelation effects and also accounting for variations in scattering cross section has recently been presented parallel to the present work by Felsner et al. [39].

In the following, a model of general dark-field anisotropy for arbitrarily oriented scatterers shall be derived based on the wave optical considerations given by Yashiro and Lynch, thereby implicitly accounting both for autocorrelation and scattering cross section dependencies.

4.6.2 Gaussian ellipsoid model of anisotropic scatterers

In preparation of the following Chapter 5 on tensor tomography, the anisotropy properties with respect to general sample orientations shall be reviewed based on dark-field signal origination discussed previously in Section 4.4.3.

The anisotropy of arbitrary elongated structures shall be modeled by means of an anisotropic Gaussian mass (or electron) density distribution

$$\rho(\vec{r}) = \rho_0 e^{-\frac{1}{2}\vec{r}\boldsymbol{T}\vec{r}} \tag{4.40}$$

with $\vec{r}$ denoting a point in three dimensional space and

$$\boldsymbol{T} = \begin{bmatrix} T_{\mathrm{xx}} & T_{\mathrm{xy}} & T_{\mathrm{xz}} \\ T_{\mathrm{xy}} & T_{\mathrm{yy}} & T_{\mathrm{yz}} \\ T_{\mathrm{xz}} & T_{\mathrm{yz}} & T_{\mathrm{zz}} \end{bmatrix} = \boldsymbol{R} \begin{bmatrix} \sigma_1^{-2} & 0 & 0 \\ 0 & \sigma_2^{-2} & 0 \\ 0 & 0 & \sigma_3^{-2} \end{bmatrix} \boldsymbol{R}^T \tag{4.41}$$

Sections 4.4–4.6 are published in adapted form in Graetz et al., Phys. Med. Biol. 2020 [47]

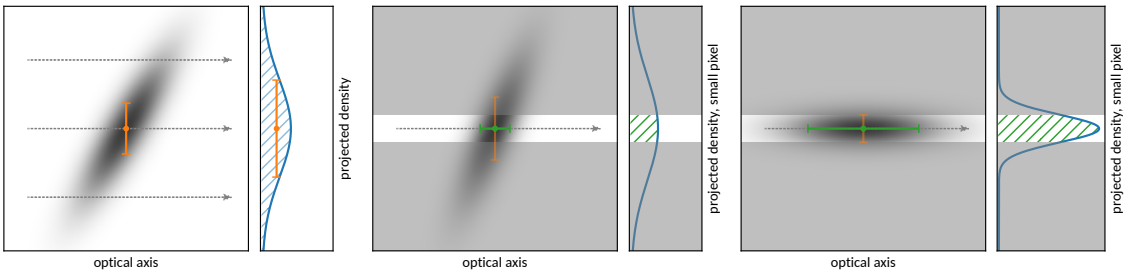

Figure 4.8: Illustration of the projection of a Gaussian mass density distribution along the optical axis (*left*). The standard deviation of the projection will typically be larger than the distribution's standard deviation parallel to the projection plane (both marked in orange for comparison, cf. Eqs. 4.42–4.43). When considering the case of pixels smaller than an elongated object (with regions outside that pixel shaded in gray), the projected volume contributing to an individual pixel will be confined by the pixel itself (*center and right*). Variations in the total projection (hatched) affecting the scattering cross section captured by that pixel are then dominated by the extent of the mass distribution along the optical axis (indicated in green). Cf. Eq. 4.48.

being a symmetric, positive definite tensor characterized by positive eigenvalues $(\sigma_1^{-2}, \sigma_2^{-2}, \sigma_3^{-2}$, representing the inverse variances of $\rho(\vec{r})$) and a unitary rotation matrix $\boldsymbol{R}$ (with the supscript T denoting the transpose operation). $\boldsymbol{R}$ defines the orientation of the Gaussian ellipsoid object characterized by three orthogonal standard deviations σ_1, σ_2 and σ_3. The Gaussian mass density $\rho(\vec{r})$ may be interpreted as description of a stochastic ensemble of smaller structures, or, more abstractly, as a generating structure to approximate the phase shifting properties along the optical axis (Eqs. 4.42–4.43) and resulting autocorrelation function (Eq. 4.49) of convex anisotropic structures irrespective of the precise microscopic material distribution (e.g., a cylindrical fiber). It may in this respect also be interpreted as a generalization of the Gaussian approximation of the autocorrelation properties of spherical objects (cf. Section 4.4.4).

4.6.2.1 Scattering cross section

The scattering cross section, as has been discussed in Section 4.4.3, is governed by the variance of phase front fluctuations $\sigma^2_{\Phi_\mathrm{f}}$ below the scale of the imaging system's spatial resolution. The total phase shift $\Phi(x, y)$ along the optical axis (here: z) caused by the presumed Gaussian density distribution is given by:

$$\begin{aligned}\Phi(x,y) &= \Phi_0 \int_{-\infty}^{\infty} e^{-\frac{1}{2}\vec{r}\boldsymbol{T}\vec{r}}\mathrm{d}z \\ &= \Phi_0 \sqrt{\frac{2\pi}{T_{zz}}} e^{-\frac{1}{2}\vec{r}\boldsymbol{T}_\Phi\vec{r}}\end{aligned} \tag{4.42}$$

with

$$\boldsymbol{T}_\Phi = \begin{bmatrix} T_{xx} - \frac{T_{xz}^2}{T_{zz}} & T_{xy} - \frac{T_{xz}T_{yz}}{T_{zz}} & 0 \\ T_{xy} - \frac{T_{xz}T_{yz}}{T_{zz}} & T_{yy} - \frac{T_{yz}^2}{T_{zz}} & 0 \\ 0 & 0 & 0 \end{bmatrix} \tag{4.43}$$

and Φ_0 being a constant factor resulting from the Gaussian density distribution's maximum value ρ_0 and the material's refractive index for the considered wavelength. The difference between T_{xx} and $T_{xx} - \frac{T_{xz}^2}{T_{zz}}$ is illustrated in Figure 4.8 (left).

When defining the local mean variance used by Yashiro and Lynch et al. [211, 103] within the discussion of dark-field origination (cf. Section 4.4.3)

$$\sigma^2_{\Phi_\mathrm{f}} = \overline{(\Phi_\mathrm{f}(x,y) - \overline{\Phi_\mathrm{f}(x,y)})^2} \tag{4.44}$$

by means of a Gaussian weighting kernel accounting for the imaging point spread function's width σ_PSF and assuming this point spread to be larger than the considered structure sizes σ_i, i.e.,

Sections 4.4–4.6 are published in adapted form in Graetz et al., Phys. Med. Biol. 2020 [47]

$\sigma_{\mathrm{PSF}}/\sigma_i \gg 1$, we find:

$$\sigma^2_{\Phi_\mathrm{f}} \approx \frac{1}{2\pi\sigma^2_{\mathrm{PSF}}} \int_{-\infty}^{\infty} e^{-\frac{1}{2}\frac{x^2+y^2}{\sigma^2_{\mathrm{PSF}}}} \left(\Phi(x,y) - \frac{1}{2\pi\sigma^2_{\mathrm{PSF}}} \int_{-\infty}^{\infty} e^{-\frac{1}{2}\frac{x^2+y^2}{\sigma^2_{\mathrm{PSF}}}} \Phi(x,y)\,\mathrm{d}x\,\mathrm{d}y\right)^2 \mathrm{d}x\,\mathrm{d}y \tag{4.45}$$

$$\begin{aligned}
&\approx \frac{1}{2\pi\sigma^2_{\mathrm{PSF}}} \int_{-\infty}^{\infty} e^{-\frac{1}{2}\frac{x^2+y^2}{\sigma^2_{\mathrm{PSF}}}} \left(\Phi(x,y) - \frac{1}{2\pi\sigma^2_{\mathrm{PSF}}} \int_{-\infty}^{\infty} \Phi(x,y)\,\mathrm{d}x\,\mathrm{d}y\right)^2 \mathrm{d}x\,\mathrm{d}y \\
&\approx \frac{\Phi_0^2\pi}{\sigma_{\mathrm{PSF}}\sqrt{\det(\boldsymbol{T})}} \left(\frac{1}{\sigma_{\mathrm{PSF}}\sqrt{T_{\mathrm{zz}}}} - \frac{2}{\sigma^3_{\mathrm{PSF}}\sqrt{\det(\boldsymbol{T})}}\right) \\
&\approx \frac{\Phi_0^2\pi}{\sigma^2_{\mathrm{PSF}}\sqrt{\det(\boldsymbol{T})}} \frac{1}{\sqrt{T_{\mathrm{zz}}}}\,,
\end{aligned} \tag{4.46}$$

and can thus finally state:

$$\sigma^2_{\Phi_\mathrm{f}} \approx \frac{1}{\sqrt{\hat{n}\boldsymbol{T}\hat{n}}} \overbrace{\left(\frac{\Phi_0^2\pi}{\sigma^2_{\mathrm{PSF}}\sqrt{\det(\boldsymbol{T})}}\right)}^{\text{orientation independent}} \quad \text{for objects smaller than the pixel size.} \tag{4.47}$$

$\sqrt{T_{\mathrm{zz}}}^{-1}$ was identified here as the standard deviation along the optical axis and is therefore in more general terms described by $\sqrt{\hat{n}\boldsymbol{T}\hat{n}}^{-1}$ for arbitrary orientations $\hat{n}$ of the optical axis ($\left\|\hat{n}\right\| = 1$). The determinant $\det(\boldsymbol{T}) = (\sigma_1\sigma_2\sigma_3)^{-2}$ is invariant under rotations $\boldsymbol{R}$ and therefore, as Φ_0, an invariant factor with respect to the orientation dependence of $\sigma^2_{\Phi_\mathrm{f}}$ (provided the density distribution fits into the considered integration range defined by σ_{PSF}).

The following conclusions can be drawn from these results on $\sigma^2_{\Phi_\mathrm{f}}$. It is proportional to the extent $\sqrt{\hat{n}\boldsymbol{T}\hat{n}}^{-1}$ of the considered structure along the optical axis, and with $\sqrt{\det(\boldsymbol{T})}^{-1} = \sigma_1\sigma_2\sigma_3$ further proportional to its volume. In the eigenbasis of $\boldsymbol{T}$, the relation $\sigma^2_{\Phi_\mathrm{f}} \propto \sqrt{\det(\boldsymbol{T})\,\hat{n}\boldsymbol{T}\hat{n}}^{-1}$ simplifies to $\sigma^2_{\Phi_\mathrm{f}} \propto (\sigma_1\sigma_2)\sigma_3^2$: the variance $\sigma^2_{\Phi_\mathrm{f}}$ is directly proportional to the variance σ_3^2 of the underlying density distribution along the optical axis and scales with its cross sectional area, which is proportional to $\sigma_1\sigma_2$.

In the limit of objects extending way beyond the size of a detector pixel (e.g., long fibers), the cross sectional area of the object's projection onto a pixel becomes almost independent of its orientation, as the considered area is rather confined by the detection area of the pixel itself, which is proportional to σ^2_{PSF} (cf. Figure 4.8). In these cases, the orientation dependence of the scattering cross section affecting that pixel is thus, given the previous observations, dominated by the variance of the density distribution along the optical axis, while the cross sectional area is bounded by σ^2_{PSF}, as opposed to the extent of the material distribution:

$$\sigma^2_{\Phi_\mathrm{f}} \propto \frac{1}{\hat{n}\boldsymbol{T}\hat{n}} \overbrace{\left(\frac{\Phi_0^2\pi}{\sigma^2_{\mathrm{PSF}}\sigma^2_{\mathrm{PSF}}}\right)}^{\text{orientation independent}} \quad \text{for objects larger than the pixel size.} \tag{4.48}$$

4.6.2.2 Autocorrelation function

The normalized planar autocorrelation $\gamma_{\mathrm{2D}}(\vec{\xi})$ corresponding to $\Phi(x,y)$ is, based on the additivity of variances for convolutions of Gaussians, given by

$$\gamma_{\mathrm{2D}}(\vec{\xi}) = e^{-\frac{1}{4}\vec{\xi}\boldsymbol{T}_\Phi\vec{\xi}}\,,$$

assuming $\vec{\xi}$ to lie in the x-y plane perpendicular to the optical axis (z). When assuming that all relative rotations of interferometer and object are accounted for in $\boldsymbol{R}$ and thus in $\boldsymbol{T}$ and $\boldsymbol{T}_\Phi$, the autocorrelation direction may without loss of generality be defined parallel to the x axis, i.e., $\vec{\xi} = (\xi, 0, 0)$, such that

$$\gamma(\xi) = e^{-\frac{1}{4}\xi^2\left(T_{\mathrm{xx}} - \frac{T_{\mathrm{xz}}^2}{T_{\mathrm{zz}}}\right)}\,. \tag{4.49}$$

Sections 4.4–4.6 are published in adapted form in Graetz et al., Phys. Med. Biol. 2020 [47]

As the mass density distribution characterized by $\boldsymbol{T}$ by design already represents all structures within the optical path relevant to the considered detector pixel, no further averaging of autocorrelation properties over the pixel area is required. The autocorrelation width moreover is an immanent property of the mass density distribution, and thus in contrast to the scattering cross section not limited by the pixel extent σ_{PSF}.

For isotropic density distributions ($\sigma_i = \sigma$), the off-diagonals of $\boldsymbol{T}$ and $\boldsymbol{T}_\Phi$ will be zero. The autocorrelation then reduces to $\gamma(\xi) = \exp(-\frac{1}{4}\frac{\xi^2}{\sigma^2})$, corresponding directly to the 3D autocorrelation function of an isotropic Gaussian density distribution without explicit averaging over the optical axis. In order to provide further intuition to the modeled Gaussian density distribution, this result may be compared to the approximate autocorrelation function for spheres of diameter D ($\gamma(\xi) \approx \exp(-\frac{1}{2}\frac{\xi^2}{(D/3)^2})$, cf. Eq. 4.21)). I.e., an isotropic Gaussian mass density distribution with standard deviation σ can be interpreted as modeling a sphere of diameter $D \approx 4\sigma$.

4.6.3 Model of dark-field contrast anisotropy

Substituting the above results (Eqs. 4.47–4.49) on scattering cross section and autocorrelation into Eq. 4.19, the fringe contrast visibility is given by:

$$v_{\mathrm{lp}} \approx \exp\left(-\frac{1}{\sqrt{\hat{n}\boldsymbol{T}\hat{n}}}\overbrace{\left(\frac{\Phi_0^2\pi}{\sigma_{\mathrm{PSF}}^2\sqrt{\det(\boldsymbol{T})}}\right)}^{\text{orientation independent}}\left(1-e^{-\frac{1}{4}\vec{\xi}\boldsymbol{T}_\Phi\vec{\xi}}\right)\right) \tag{4.50}$$

which for scatterers, such as long fibers, larger than the typical integration width (e.g., pixel size) characterized by σ_{PSF}, modifies to

$$v_{\mathrm{sp}} \approx \exp\left(-\frac{1}{\hat{n}\boldsymbol{T}\hat{n}}\overbrace{\left(\frac{\Phi_0^2\pi}{\sigma_{\mathrm{PSF}}^4}\right)}^{\text{orientation independent}}\left(1-e^{-\frac{1}{4}\vec{\xi}\boldsymbol{T}_\Phi\vec{\xi}}\right)\right) \tag{4.51}$$

with $\boldsymbol{T}$ characterizing the inverse variances of the considered scatterers' density distribution (Eq. 4.41), $\hat{n}$ the unit vector along the optical path, $\vec{\xi}$ the oriented autocorrelation distance and $\boldsymbol{T}_\Phi$ (Eq. 4.43) describing the inverse variances of the scatterers' total phase shift along the optical axis (Eq. 4.42), based on their density distribution characterized by $\boldsymbol{T}$. The subscripts "sp" and "lp" indicate the "small pixel" and "large pixel" cases as compared to the extent of the considered scatterers characterized by $\boldsymbol{T}$.

When defining, without loss of generality, $\hat{\boldsymbol{n}}$ parallel to the z-axis and $\vec{\xi}$ parallel to the x-axis (assuming all rotations to be considered within $\boldsymbol{T}$, cf. Eq. 4.41), and further using the first order approximation $1-\exp(-u) \approx u$ for small u, then the following simplified proportionality relations for the expected orientation dependence of the dark-field contrast $\mu_{\mathrm{DF}} = -\ln(v)$ for the large pixel (lp) and small pixel (sp) cases respectively:

$$-\ln(v_{\mathrm{lp}}) \overset{\propto}{\approx} \frac{1}{\sqrt{T_{\mathrm{zz}}}}(T_{\mathrm{xx}} - \frac{T_{\mathrm{xz}}^2}{T_{\mathrm{zz}}}) \tag{4.52}$$

$$-\ln(v_{\mathrm{sp}}) \overset{\propto}{\approx} \frac{1}{T_{\mathrm{zz}}}(T_{\mathrm{xx}} - \frac{T_{\mathrm{xz}}^2}{T_{\mathrm{zz}}})\,. \tag{4.53}$$

For the special case of objects oriented perpendicular to the optical axis (here: z), i.e., for $T_{\mathrm{xz}} = 0$ and $T_{\mathrm{zz}} = \text{const.}$, both models reproduce the classic sinusoid signal variations as a function of orientation that have been consistently reported in previous literature. This can be easily seen in the explicit expressions given in Eqs. 4.55–4.56 when considering the case $\omega = 0$.

Sections 4.4–4.6 are published in adapted form in Graetz et al., Phys. Med. Biol. 2020 [47]

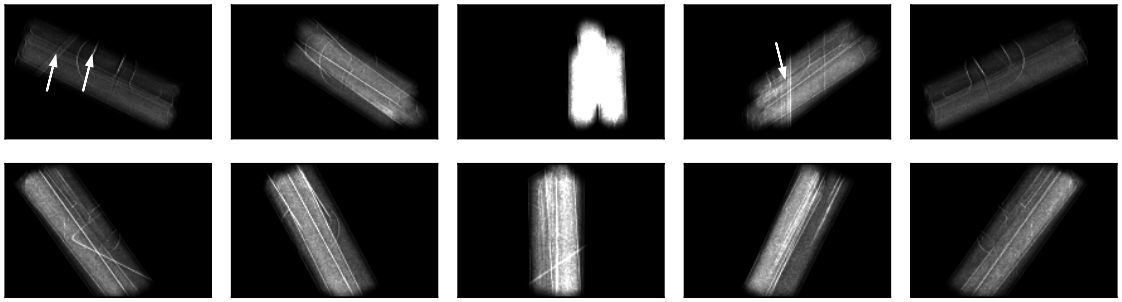

Figure 4.9: Two dark-field image series of a pack of three carbon fiber reinforced rods (of ca. 1cm length) rotating about the vertical image axis over a range of 180° (0°, 45°, 90°, 135°, 180° from left to right). A sketch is depicted in Fig. 4.10. The rods are inclined about 65° (top row) and 36° (bottom row) with respect to the rotational axis. The grating sensitivity is parallel to the horizontal image axis. The color scale ranges from 0 (black) to 0.7 (white). White arrows indicate examples of dark-field signals originating from the sample support structure, which has been masked outside of the sample silhouette. The center column and the outermost columns show the isolated effects of varying scattering cross section (center) and varying autocorrelation width (left and right) respectively. Quantitative results are shown in Figure 4.10.

4.6.4 Experimental confirmation

In order to verify the expected orientation dependence of the dark-field contrast, a sample consisting of long carbon fibers has been imaged at various orientations in analogy to the experiment performed by Bayer et al. [6]. In contrast to the latter experiment, the sample is explicitly chosen smaller than the field of view. The carbon fibers are contained in three plastic rods of about 1cm length and 2mm diameter, and extend over the full length of the rods. The fiber sample is attached to a polyhedral sample cage (made of UV resin, see also Figure 5.5) by means of an acrylic stand and hot glue. The cage allows to easily vary the inclination of the carbon fibers with respect to the rotational axis of a tomography setup, while the acrylic stand centers the sample in the polyhedral cage. Although the support structures are made of non-scattering materials, a small contribution to the dark-field contrast is generated by their edges. Figure 4.9 shows selected examples. In order to keep their impact on the following analyses minimal, the signal of the sample support structures has been masked where possible (i.e., outside of the sample's silhouette).

The acquired images can be analyzed in two ways: most obviously, the average dark-field signal per detector pixel over the area of the sample silhouette may be considered, yielding a signal corresponding to fibers much longer than the pixel size. In order to reproduce the case of fibers fully contained within a single integrating pixel, the phase stepping curves' complex amplitudes as well as their mean transmission are averaged over the full detector area prior to the evaluation of visibility and its negative logarithm (the dark-field signal). The result is then equivalent to that of a larger integrating detector.

For the comparison of the rotation series acquired at varying fiber inclinations to the anisotropy model derived in Section 4.6.3, a Gaussian mass distribution model of the rotating fibers is used according to Eqs. 4.40–4.41:

$$\begin{aligned} \rho(\vec{r}) &= \rho_0 e^{-\frac{1}{2}\vec{r}\boldsymbol{T}\vec{r}} \\ \boldsymbol{T}(\omega,\theta) &= \boldsymbol{R}(\omega,\theta) \begin{bmatrix} \sigma_D^{-2} & 0 & 0 \\ 0 & \sigma_L^{-2} & 0 \\ 0 & 0 & \sigma_D^{-2} \end{bmatrix} \boldsymbol{R}^T(\omega,\theta) \\ \boldsymbol{R}(\omega,\theta) &= \begin{bmatrix} \cos\omega & 0 & \sin\omega \\ 0 & 1 & 0 \\ -\sin\omega & 0 & \cos\omega \end{bmatrix} \begin{bmatrix} \cos\theta & -\sin\theta & 0 \\ \sin\theta & \cos\theta & 0 \\ 0 & 0 & 1 \end{bmatrix} \end{aligned} \tag{4.54}$$

with σ_D and σ_L denoting standard deviations characterizing an effective diameter and length of the fiber bundle and ω and θ describing its orientation in terms of rotation and inclination as sketched in Figure 4.10.

Sections 4.4–4.6 are published in adapted form in Graetz et al., Phys. Med. Biol. 2020 [47]

For the first case considering small detector pixels (indicated by the subscript "sp"), the following is expected from the previous theoretic derivations (cf. Eq. 4.53):

$$-\ln(v_{\mathrm{sp}}) \overset{\propto}{\approx} \frac{1}{T_{\mathrm{zz}}}(T_{\mathrm{xx}} - \frac{T_{\mathrm{xz}}^2}{T_{\mathrm{zz}}}) \propto \frac{\cos^2\theta + \frac{\sigma_D^2}{\sigma_L^2}\sin^2\theta}{(\cos^2\omega + (\cos^2\theta + \frac{\sigma_D^2}{\sigma_L^2}\sin^2\theta)\sin^2\omega)^2}\,. \tag{4.55}$$

For the case of a single large detector ("lp") integrating over the full extent of all fibers,

$$-\ln(v_{\mathrm{lp}}) \overset{\propto}{\approx} \frac{1}{\sqrt{T_{\mathrm{zz}}}}(T_{\mathrm{xx}} - \frac{T_{\mathrm{xz}}^2}{T_{\mathrm{zz}}}) \propto \frac{1}{\sigma_D}\frac{\cos^2\theta + \frac{\sigma_D^2}{\sigma_L^2}\sin^2\theta}{(\cos^2\omega + (\cos^2\theta + \frac{\sigma_D^2}{\sigma_L^2}\sin^2\theta)\sin^2\omega)^{3/2}} \tag{4.56}$$

is expected in contrast (cf. Eq. 4.52).

Figure 4.10 shows a respective comparison of experimental data and theoretic model. While the individual carbon fibers contained in the considered sample are expected to have an aspect ratio of about 10^3 (ca. 10^{-2}m length at ca. 10^{-5}m diameter), the observed signal is best reproduced (in a least squares sense) with aspect ratios σ_L/σ_D of 3.5 and 1.7 in the small and large pixel case respectively. The general discrepancy between the extreme aspect ratio of individual fibers and the deduced aspect ratios of the fiber ensemble is expected to arise from a finite distribution width of fiber orientations. Such variations in orientation are generated whenever fibers are bent or not perfectly aligned parallel, which is especially expected among the three separate rods constituting the sample. Similarly, the reduced aspect ratio found for the case of the integrating detector (as compared to the small pixel case) might be attributed to the larger ensemble of fibers considered simultaneously in that case.

While the present data doesn't allow further microscopic analyses of the observed aspect ratios, the observed orientation dependence with respect to rotations and inclinations is in good agreement with the theoretic expectation despite the considerable number of first order approximations that have been made towards the derivation of Eqs. 4.55–4.56. First of all, both the dependence on changes in scattering cross section and in autocorrelation width are reproduced, although the integrating pixel case appears to be more susceptible to imperfections of the sample. The scattering cross section dependence is found to be – as expected by Eq. 4.55 – considerably more pronounced in the case of objects exceeding the pixels' integration area. Moreover, the narrowly peaked rotation angle dependence for strongly inclined fibers is reproduced, which can be attributed to the influence of the off-diagonal term $T_{\mathrm{xz}}^2/T_{\mathrm{zz}}$ originating from inclinations of the anisotropic mass distribution with respect to the optical axis (cf. Figure 4.8 left).

Figure 4.11 further displays the θ-dependence in the case of $\sin\omega = 0$, i.e., for fibers within the plane perpendicular to the optical axis. In this case, Eqs. 4.55–4.56 reproduce the typical sinusoidal signal variation that has been consistently documented in previous literature, whereat the respective model parameters are identical with those describing the ω-dependence in Fig. 4.10.

Sections 4.4–4.6 are published in adapted form in Graetz et al., Phys. Med. Biol. 2020 [47]

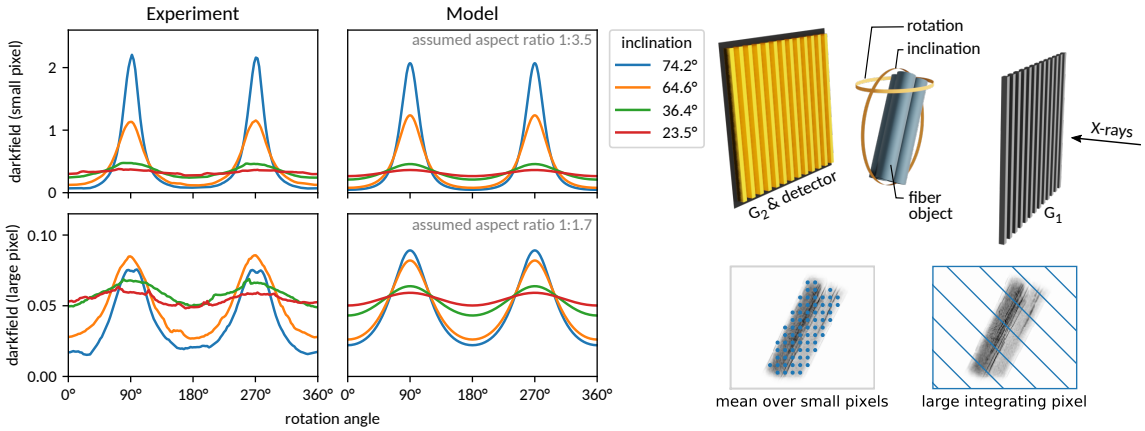

Figure 4.10: Dark-field signals (negative logarithm of visibility) for different fiber orientations in the large pixel and small pixel cases. In the former case, the fibers are always fully contained within the integration area. Four inclination angles of the fibers with respect to the rotational axis are considered (cf. legend), and a full rotation over 360° is performed at each inclination. Experimental data and theoretical model are shown in the left and right column respectively. Diameter/length aspect ratios $\sigma_D : \sigma_L$ of $1:3.5$ and $1:1.7$ have been determined for the model data (cf. Eqs. 4.54–4.56) shown on the right hand side for the small and large pixel case respectively in order to approximate the experimental observations on the left hand side.

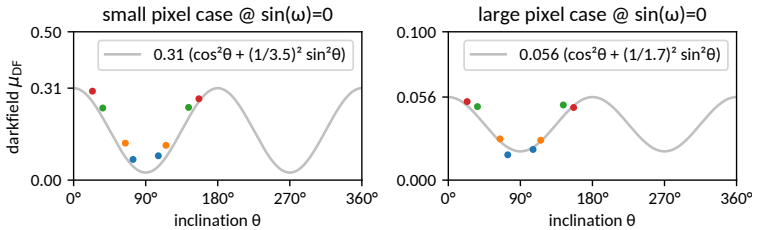

Figure 4.11: Comparison of model and data for the classic case of fibers perpendicular to the optical axis, which is here given for $\omega \in \{0°, 180°\}$. Colors and model parameters correspond to Fig. 4.10. Data points have been mapped to the range $\theta \in [0°, 180°]$ for better visualization.

Sections 4.4–4.6 are published in adapted form in Graetz et al., Phys. Med. Biol. 2020 [47]

Chapter 5

X-Ray Dark-Field Tensor Tomography

Tensor tomography is the final objective of the present dissertation. It refers to the volume reconstruction of non-scalar quantities arising from anisotropic physical effects in the context of a given tomographic imaging modality. The name derives from the use of tensors for the modeling of the particular anisotropic effect (A prominent example is the reconstruction of diffusion tensors in the field of magnetic resonance tomography). In the context of X-ray tomography, anisotropic, i.e., direction-dependent signals, are found in the ultra-small angle scattering signal (dark-field contrast) obtained with Talbot-Lau grating interferometry (cf. Section 4.4).

As the scattering properties of a given structure are related to its shape, dark-field imaging provides a way to characterize structural anisotropy below the actual imaging resolution. Tensor tomography aims at extending directional dark-field imaging techniques for planar samples to both volumetric samples and arbitrary orientations of the substructure within such samples. An important use case are fibrous materials, for which the local fiber orientation can thus be determined without the necessity of actually directly resolving the individual fibers in the imaging process. This ability allows to considerably increase the accessible field of view, i.e., the accessible sample size, by about one to two orders of magnitude.

The contribution of the following work is threefold: A reconstruction methodology is motivated, based on the foundations developed in Chapters 1 and 2, from mathematical-technical aspects of tomography and explicitly discussed and evaluated with respect to the physical insights on dark-field anisotropy obtained in Section 4.6. Likewise, the particular experimental design is explicitly motivated from the preceding conclusions of Sections 4.5–4.6. Finally, the proposed methodologies are applied to experimental data acquired to this end at the ID19 imaging beamline of the European Synchrotron Radiation Facility, yielding tensor valued volume reconstructions with a field of view of 3 to 4 cm at a spatial resolution of 0.1mm. The results are quantitatively compared to classic micro-CT based fiber orientation analysis.

5.1 Literature reviewr

The first examples of X-ray scattering tensor tomography based on the dark-field contrast modality – following the suggestion by Jensen at al. [75] in 2010 – have been demonstrated by Malecki et al. [106] in 2014, using an auxiliary non-orthogonal vector basis for the description of voxel anisotropy within the actual reconstruction process before fitting an ellipsoid model – parametrized by a tensor – to each voxel. Vogel et al. [185] presented an alternative iterative reconstruction technique as compared to the one employed by Malecki in order to compensate for reported instabilities in the tensor fitting process. Bayer et al. [5] proposed a sinusoid model for the description of anisotropy solely within a predefined plane determined by the tomographic scan trajectory. Wieczorek et al. [197] introduced the use of spherical harmonics as a more general orthogonal basis for the description of scattering functions in the context of anisotropic dark-field tomography with the prospect of distinguishing more complex superpositions of scatterers. Spherical harmonics were also

Sections 5.1–5.3 extend on presentations in Dittmann et al. 2017 [31] and Graetz, Sci. Rep. 2021 [45]

employed by Liebi et al. [97] in the context of anisotropic scanning SAXS tomography. The present work will be based on the reconstruction approach first presented by the author in [31], which discusses the nested nature of the tensor recovery problem within the volume tomography problem and proposes a straight forward reconstruction approach for generic linear anisotropy models such as the scattering tensor (or expansion bases such as spherical harmonics). Further work by Schaff et al. [161] and Sharma et al. [168, 167] considered alternative projection acquisition schemes. Sayyedi et al. [158] reported on total variation regularization within tensor tomographic reconstruction.

Despite the differences in detail, all current approaches to anisotropic X-ray dark-field tomography implicitly or explicitly share the central assumption that the anisotropic dark-field signal can be understood in terms of a scalar function defined on the unit sphere. The sphere itself is identified with the set of orientations of the sensitivity axis of the grating interferometer with respect to the sample, in analogy to the initial works on planar anisotropic dark-field imaging (cf. Section 4.6.1). Immanent to this model is the assumption that the signal anisotropy solely arises from the anisotropy of the sample's autocorrelation function, implying the scattering cross section to be generally isotropic. Given the results of Section 4.6, this assumption remains to be justified. Due to the dependencies between signal model and tomographic reconstruction, the latter shall be introduced first in the following section prior to continuing the discussion on a suited signal model in Section 5.3.

5.2 Nested iterative tomographic reconstruction

The concept of nested tomography as proposed by the author in Dittmann et al. 2017 [31] arises from the observation that the reconstruction of an individual non-scalar volume element (e.g., a tensor voxel) from multiple observations can be considered a small tomography problem in its own right. The tomographic reconstruction of non-scalar-valued volumes may thus be addressed by nesting iterative reconstruction schemes for volume and voxel respectively. By defining, complementary to a given anisotropic signal model mapping higher dimensional voxels to scalar observables, a suiting backprojection operation mapping updates to these observables back onto the underlying parameters characterizing individual voxels, classic iterative forward-backprojection schemes for volume reconstruction (cf. Section 1.2.3) can be formally extended to arbitrary voxel and signal models by chaining respective forward- and backprojection operations (putting aside for now the questions of uniqueness or required input data). An illustration is given in Figure 5.1. After formalizing the idea in the following, basic constraints on respective signal models become apparent.

Using, following Section 1.2.3, the notation

$$\boldsymbol{A}\boldsymbol{f} = \boldsymbol{g}$$
$$\sum_j A_{ij} f_j = g_i$$

for the discretized tomography problem, with the system matrix $\boldsymbol{A}$ describing line integrals through a set of voxels $\boldsymbol{f}$, and $\boldsymbol{g}$ holding the respective projection sums, an additional embedded transformation $t_i : \boldsymbol{f}_j \to f_{ij}$ allows for a straight forward extension to non-scalar voxels:

$$\sum_j A_{ij} \overbrace{t_i(\underbrace{\boldsymbol{f}_j}_{\text{nonscalar voxel}})}^{\text{scalar projection}} = g_i \,.$$

Bold symbols indicate non-scalar quantities, while i and j index observations and voxels respectively. The transformation $t_i(\boldsymbol{f}_j)$ maps non-scalar voxels $\boldsymbol{f}_j$ to scalar observables f_{ij} depending on i. Whenever $t_i(\cdot)$ is invariant with respect to i, the quantity described by $\boldsymbol{f}_j$ is actually isotropic with respect to the relative orientations of system and sample covered by the set of measurements acquired within a given experiment modeled by $\boldsymbol{A}$ and t.

Iterative volume reconstruction algorithms for scalar voxels f_j commonly adhere to the following general scheme:

$$f_j^{(k+1)} = f_j^{(k)} + \lambda_{ijk} \sum_{i \in S_k} B_{ji} \left[g_i - \sum_{j'} A_{ij'} f_{j'}^{(k)} \right] ,$$

with B_{ji} characterizing the backprojection operation. In the case of SART (cf. Section 1.2.3) as used here, it will be evaluated on the fly and represents blockwise approximate pseudo-inverses to the forward model A_{ij} such that

$$\sum_j A_{ij} \sum_{i \in S_k} B_{ji} x_i \approx x_i \quad \forall i \in S_k, x_i \in \mathbb{R} \,.$$

The superscript index k denotes iterations, and S_k is the set of row indices i considered within the respective iteration k. $\lambda_{ijk} \in [0,1]$ is a relaxation factor commonly introduced to stabilize convergence by means of damping it, particularly in the presence of inconsistencies between the imaging model $\boldsymbol{A}$ and the observed data $\boldsymbol{g}$. It is often chosen constant, i.e., $\lambda_{ijk} = \lambda$, and typically ranges within 0.1 to 0.5.

By analogously defining a pseudo-inverse $t_i^+ : f_{ij} \to \boldsymbol{f}_j$ to the voxel transformation $t_i(\cdot)$ with

$$t_i(t_i^+(f_{ij})) = f_{ij} \,,$$

the iterative volume reconstruction scheme can be directly extended to non-scalar voxels $\boldsymbol{f}_j$:

$$\boldsymbol{f}_j^{(k+1)} = \underbrace{t_i^+}_{\substack{\text{backproj. of scalar} \\ \text{into nonscalar voxel}}} \left(t_i(\boldsymbol{f}_j^{(k)}) + \lambda_{ijk} \underbrace{\sum_{i \in S_k} B_{ji} \left[\overbrace{g_i}^{\text{data}} - \overbrace{\sum_{j'} A_{ij'} t_i(\boldsymbol{f}_{j'}^{(k)})}^{\text{forward model}} \right]}_{\text{scalar backprojection}} \right) . \tag{5.1}$$

Analog to the reasoning of classic tomographic reconstruction, the sum of projections of sub volumes is expected to be equivalent to the projection of the entire volume, i.e.

$$\sum_j A_{ij} t_i(\boldsymbol{f}_j^{(k)}) \stackrel{!}{=} t_i \left(\sum_j A_{ij} \boldsymbol{f}_j^{(k)} \right) ,$$

which implies that the transformation $t_i(\cdot)$ is expected to be linear. The required commutability of $t_i(\cdot)$ and A_{ij} also implies that whenever the transform $t_i(\cdot)$ is actually constant with respect to i, the problems of volume reconstruction and the reconstruction of the non-scalar voxels $\boldsymbol{f}_j$ become independent, i.e., may be solved sequentially. This will become more obvious once concrete choices for $t_i(\cdot)$ and $\boldsymbol{f}_j$ are made, which will be the subject of the following section. Algorithm 5.1 provides a more explicit formulation of Eq. 5.1 using the tensor voxel model presented in the following.

5.3 Tensor as linear anisotropy model

Following up on the previous introduction of nesting voxel-level anisotropy reconstruction into classic volume reconstruction schemes, an anisotropic dark-field model suited in this context remains to be defined. While the model of dark-field anisotropy derived in Section 4.6 is well motivated, it is however not linear in its underlying mass distribution tensor. In order to ensure stable convergence of the iterative nested tomographic reconstruction scheme, surrogate linear tensor models shall thus be defined and validated in the following.

A natural choice for a minimal linear anisotropic model is a symmetric 3×3 tensor in analogy to many other fields of physics, with diffusion tensor tomography probably being the most related example. Using the indices $m, n \in \{1,2,3\}$, a normalized sensing orientation $\hat{\boldsymbol{u}}_i \in \mathbb{R}^3$ with $\left\|\hat{\boldsymbol{u}}_i\right\| = 1$ and the tensor elements f_{jmn}, the following transformations shall be defined:

$$\begin{aligned} \boldsymbol{f}_j &:= f_{jmn} = f_{jnm} \\ t_i(\boldsymbol{f}_j) &:= \hat{\boldsymbol{u}}_i \boldsymbol{f}_j \hat{\boldsymbol{u}}_i = \sum_{m,n} \hat{u}_{im} f_{jmn} \hat{u}_{in} \\ t_i^+(s \in \mathbb{R}) &:= s\, \hat{u}_{im} \hat{u}_{in} \\ \text{with} \quad t_i(t_i^+(s)) &= \sum_{m,n} \hat{u}_{im} (\hat{u}_{im} s\, \hat{u}_{in}) \hat{u}_{in} = s \end{aligned}$$

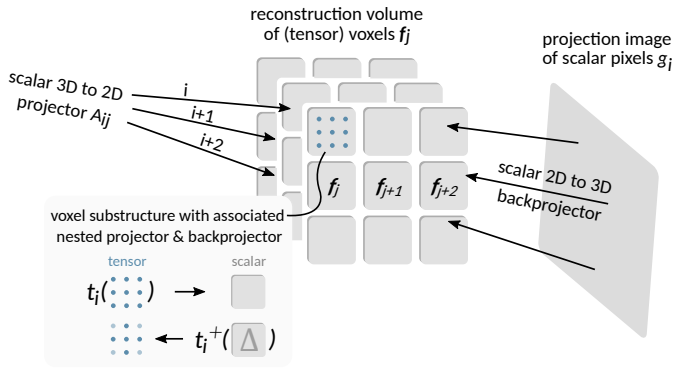

Figure 5.1: Illustration of nesting additional projection (from tensor to scalar) and backprojection (from scalar to tensor) operations at the voxel level. This allows for a transparent extension of iterative reconstruction techniques for scalar tomography to tensor tomography (see Alg. 5.1).

Algorithm 5.1 Tensor-SART for the iterative reconstruction of tensor valued volumes from scalar projections. Following the "nested tomography" conception outlined in Section 5.2 and Fig. 5.1, the simulatenous algebraic reconstruction technique SART (cf. Algorithm 1.3) has been augmented with additional forward- and backprojection operations transforming between tensor voxels and their scalar observables based on sensing orientations $\hat{\boldsymbol{u}}_\omega$. ω enumerates projection views characterized by $\vec{s}_\omega$, $\vec{d}_\omega, \vec{H}_\omega, \vec{V}_\omega$ (cf. Secion 1.1) and sensing orientation $\hat{\boldsymbol{u}}_\omega$ (cf. Section 5.3).

cone beam projection data: $g(\omega, v, h)$: line integrals at orientation ω and detector pixel (h, v)

projection geometries defining $\boldsymbol{A}$: $\vec{s}_\omega, \vec{d}_\omega, \vec{H}_\omega, \vec{V}_\omega, \hat{\boldsymbol{u}}_\omega$

sets of row indices i of $\boldsymbol{A}$ to be considered in iteration k: P_k : each set characterizes a 2D image at ω_k

initial (tensor valued) volume: $f^{(0)}_{jmn} = 0$

relaxation factor(s) weighting individual update steps: $\lambda_k \in]0, 1]$; typically $\lambda_k = \lambda \lesssim 0.5$

for $k = 0..N_{\text{iter}} - 1$ **do** :

forward projection using Algorithm 2.1 and reduction of tensor voxels:
$$\tilde{g}^{(k)}_i = \hat{\boldsymbol{u}}_{\omega_k} \boldsymbol{A}_i \boldsymbol{f}^{(k)} \hat{\boldsymbol{u}}_{\omega_k} \quad \forall\, i \in P_k$$

corresponding ray lengths:
$$l(\omega_k, v_i, h_i) = \left\| \boldsymbol{A}_i \right\|_1 \qquad \forall\, i \in P_k$$

2D residual projection image at $\omega_k = \omega_i\ \forall\, i \in P_k$:
$$\Delta g^{(k)}(\omega_k, v_i, h_i) = g(\omega_k, v_i, h_i) - \tilde{g}^{(k)}_i \quad \forall\, i \in P_k$$

grid projection onto detector (Eq. 1.5):
$$\begin{aligned} v(\vec{p}_j, \omega) &= -[\vec{H}_\omega \times (\vec{d}_\omega - \vec{s}_\omega)] \cdot (\vec{p}_j - \vec{s}_\omega) \,/\, [\vec{H}_\omega \times \vec{V}_\omega] \cdot (\vec{p} - \vec{s}_\omega) \\ h(\vec{p}_j, \omega) &= [\vec{V}_\omega \times (\vec{d}_\omega - \vec{s}_\omega)] \cdot (\vec{p}_j - \vec{s}_\omega) \,/\, [\vec{H}_\omega \times \vec{V}_\omega] \cdot (\vec{p} - \vec{s}_\omega) \end{aligned}$$

backprojection of residuals into tensor volume space:
$$f^{(k+1)}_{jmn} = f^{(k)}_{jmn} + \lambda_k \underbrace{u_{\omega,m} u_{\omega,n}}_{\substack{\text{tensor} \\ \text{backproj.} \\ \text{within voxel}}} \underbrace{\frac{\Delta g^{(k)}\Big(\omega_k, v(\vec{p}_j, \omega_k), h(\vec{p}_j, \omega_k)\Big)}{l\Big(\omega_k, v(\vec{p}_j, \omega_k), h(\vec{p}_j, \omega_k)\Big)}}_{\substack{\text{scalar backprojection of} \\ \text{residuals to voxel } j \text{ at } \vec{p}_j}}$$

end for.

The sensing orientation $\hat{\boldsymbol{u}}_i$ may vary with the particular view i considered. $t_i(\boldsymbol{f}_j)$ can be understood as probing the value of the tensor for a specific direction $\hat{\boldsymbol{u}}_i$, while $t_i^+(s)$ will conversely generate a second order tensor of rank one mapping a scalar value s to the sensing orientation $\hat{\boldsymbol{u}}_i$. The transformation $t_i(\cdot)$ is obviously invariant with respect to the sign of $\hat{\boldsymbol{u}}_i$ in accordance with the 180° symmetry of dark-field anisotropy. The symmetric 3×3 tensors $\boldsymbol{f}_j$ are fully characterized by three eigenvalues and respective eigenvectors, which directly provide an intuitive geometric interpretation.

Two meaningful options for the concretization of $\hat{\boldsymbol{u}}_i$ can be named in the context of dark-field tomography: The sensitivity orientation $\hat{\boldsymbol{e}}$ of the Talbot grating interferometer, and the optical path $\hat{\boldsymbol{n}}$ (i.e., the direction of integration) perpendicular to $\hat{\boldsymbol{e}}$. The former choice is consistent with previous approaches to anisotropic dark-field modeling both in planar and tomographic (cf. [106, 5, 197]) scenarios and is able to represent variations in autocorrelation width when rotating a sample about the optical axis. The latter choice ($\hat{\boldsymbol{n}}$) has not been regarded previously and is in contrast able to represent variations in scattering cross section when rotating the sample about the sensitivity axis of the interferometer – a situation that has no relevance in the context of projection imaging of planar samples yet occurs in the case of anisotropic tomographic imaging (see Figures 4.9 and 4.10 in Section 4.6). Either choice will leave the respective other effect unconsidered. I.e., when modeling anisotropy based on the direction of grating sensitivity, variations in the scattering cross section will be averaged. Conversely, when modeling anisotropy with respect to the optical path, variations in auto correlation width occurring when rotating the sample (or grating) about the optical path will be averaged.

Both approaches represent considerable approximations with regard to the actual orientation dependence shown in Sections 4.6.3–4.6.4 and shall therefore be first explicitly discussed for the basic scenario of individual volume elements. To this end, the models $\hat{\boldsymbol{n}}\boldsymbol{T}_{(\boldsymbol{n})}\hat{\boldsymbol{n}}$ and $\hat{\boldsymbol{e}}\boldsymbol{T}_{(\boldsymbol{e})}\hat{\boldsymbol{e}}$ will be fitted (by means of iterative forward-backprojection as discussed previously) to both actual and simulated anisotropic dark-field signals, providing both an exhaustive coverage of feasible situations as well as selective experimental examples.

Figures 5.2 and 5.3 visualize actual dark-field signals of the fiber object discussed in Section 4.6 with respect to the directions $\hat{\boldsymbol{n}}_i$ or $\hat{\boldsymbol{e}}_i$ of the acquisition geometry along with corresponding second order tensor approximations. The effect of averaging over one of two orientation dependencies is here well observable along the x-axis. Conversely, a lack of redundant observations (redundant with respect to one of $\hat{\boldsymbol{n}}_i$ or $\hat{\boldsymbol{e}}_i$) to be averaged over can cause crosstalk between the effects of autocorrelation width and scattering cross section. This has, for the tensors shown in Figs. 5.2–5.3, been avoided by exploiting the rotational symmetry of the given experiment about the fiber orientation, assuming that the same data has likewise been acquired along equivalent trajectories rotated by 90° about the fiber axis. The eigensystems of the reconstructed tensors $\boldsymbol{T}_{(\boldsymbol{e})}$ and $\boldsymbol{T}_{(\boldsymbol{n})}$ are found to be well aligned with the known fiber orientation. For $\boldsymbol{T}_{(\boldsymbol{e})}$, modeling the anisotropic autocorrelation length of the sample, the fiber orientation is indicated by the eigenvector corresponding to the smallest eigenvalue, as the dark-field signal scales inversely with structure size (cf. Fig. 5.3). For $\boldsymbol{T}_{(\boldsymbol{n})}$, modeling the anisotropic scattering cross section of the sample, the fiber orientation is in contrast expected to correlate with the largest eigenvalue, as dark-field contrast scales with the amount of scattering material along the optical axis. This is reproduced in Fig. 5.2.

Figure 5.4 provides, in addition to the illustrative experimental examples, systematic evaluations of the proposed models' relations to the signal generating mass distribution tensor based on the dark-field signal model derived in Section 4.6.3. With synthesized anisotropic dark-field signals of 120000 different Gaussian mass distributions using the acquisition scheme outlined in Section 5.4 and Figure 5.5, direct correspondences between the respective eigenvalues and eigenvectors of the physical and linearized tensor models can be drawn. Despite the expectedly large root mean square errors between the simplified reconstruction models and the simulated anisotropic dark-field signals, the intrinsic imprecision in the recovery of the dominant orientation ranges, with 0.33° and 1° respectively, well below expected noise levels in the case of actual experimental data. Given that the eigenvalues of both reconstruction models are found to be approximately linear in the (normalized) inverse variances of the mass distribution (Fig. 5.4, bottom row), it may be conjectured that the variations in auto-correlation width (perpendicular to the optical axis $\hat{\boldsymbol{n}}$) are the dominating orientation dependence. This is consistent with the observation that reconstructions based on the $\hat{\boldsymbol{e}}\boldsymbol{T}_{(\boldsymbol{e})}\hat{\boldsymbol{e}}$ model (as opposed to $\hat{\boldsymbol{n}}\boldsymbol{T}_{(\boldsymbol{n})}\hat{\boldsymbol{n}}$) yield slightly reduced root mean square errors and an improved recovery of principal orientations (see Fig. 5.4, top row).

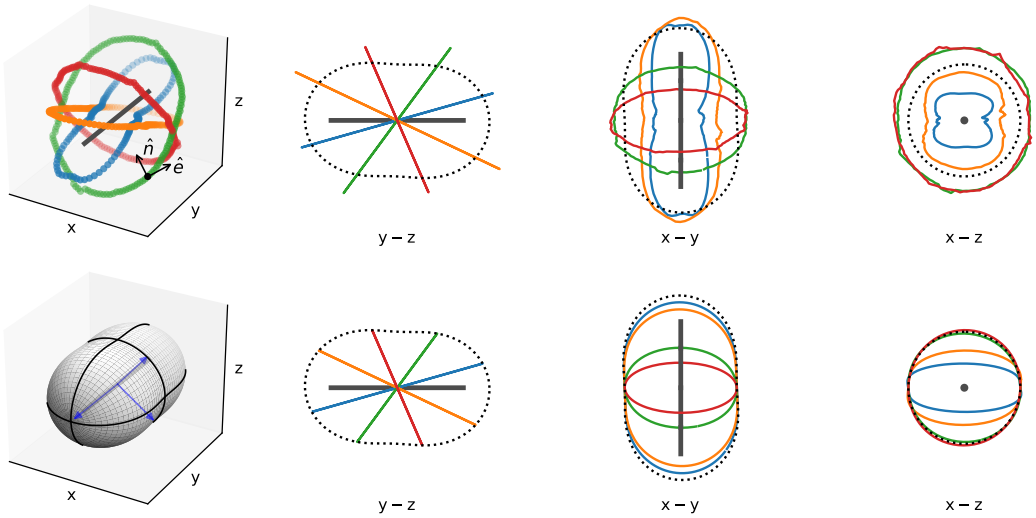

Figure 5.2: Spatial representation of the anisotropic dark-field signal of a fiber object (top row) and a respective tensor model fit (bottom row). The experimental data (cf. Section 4.6.4, Fig. 4.10, large pixel case) is here represented on a unit sphere defined by the optical paths or grating normals $\hat{\boldsymbol{n}}_i$. Signal intensity is represented by the distance from the origin. The respective grating sensitivity orientations $\hat{\boldsymbol{e}}_i$ are, due to the particular experimental configuration, always tangential to the circular scanning trajectories. The bottom row shows the corresponding approximation by the model $\hat{\boldsymbol{n}}\boldsymbol{T}_{(n)}\hat{\boldsymbol{n}}$. Black lines represent the model values within the y-z, x-y and x-z planes respectively. They are shown in both rows for comparison. Signal variations along the x-axis caused by varying $\hat{\boldsymbol{e}}$ at constant $\hat{\boldsymbol{n}}$ cannot be captured by the model (cf. x-y and x-z projections). Blue arrows (bottom left) represent the eigenvectors and -values of $\boldsymbol{T}_{(n)}$.

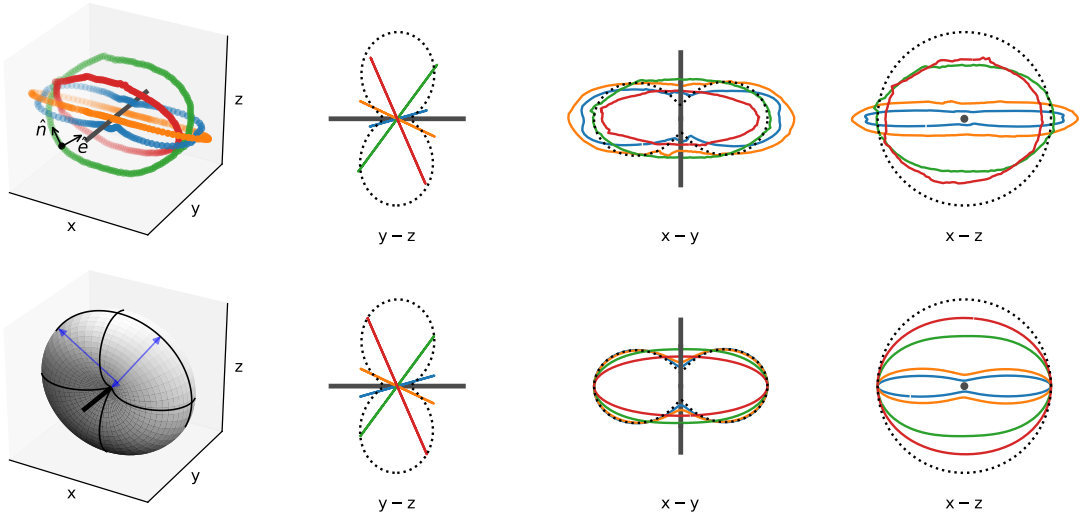

Figure 5.3: Spatial representation of the anisotropic dark-field signal of a fiber object (top row) and a respective tensor model fit (bottom row) analog to Fig. 5.2. The data is here represented on a unit sphere defined by the grating sensitivity orientations $\hat{\boldsymbol{e}}_i$, with signal intensity being represented by the distance from the origin. The optical paths or grating normals $\hat{\boldsymbol{n}}_i$ are always perpendicular to $\hat{\boldsymbol{e}}_i$. The bottom row shows the corresponding approximation by the model $\hat{\boldsymbol{e}}\boldsymbol{T}_{(e)}\hat{\boldsymbol{e}}$. Black lines represent the model values within the y-z, x-y and x-z planes respectively and are shown in both rows for comparison. Signal variations along the x-axis caused by varying $\hat{\boldsymbol{n}}$ at constant $\hat{\boldsymbol{e}}$ cannot be captured by the model (cf. x-y and x-z projections). Blue arrows (bottom left) represent the eigenvectors and -values of $\boldsymbol{T}_{(e)}$.

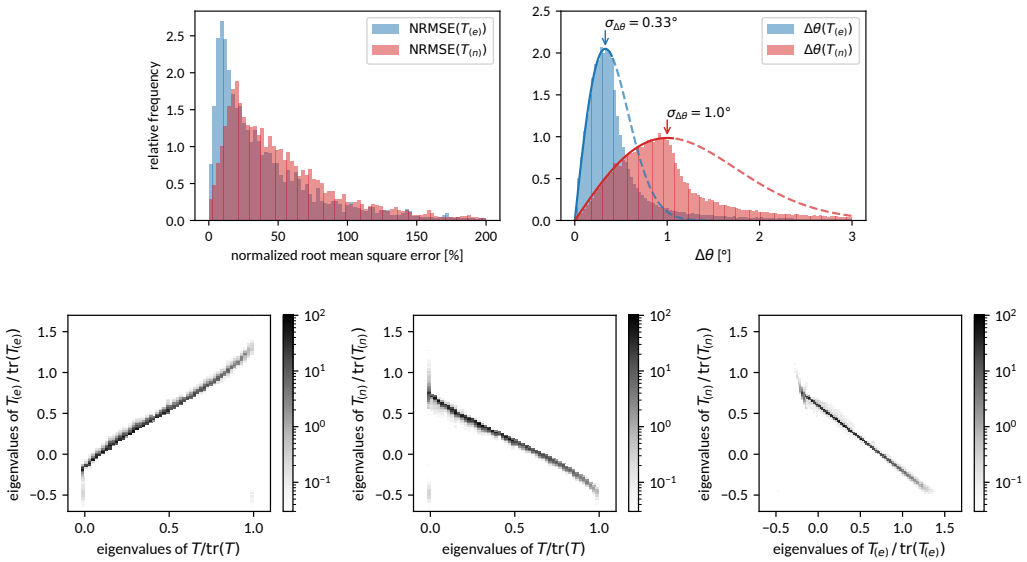

Figure 5.4: Systematic comparison of approximative dark-field models $\hat{\boldsymbol{n}}\boldsymbol{T}_{(\boldsymbol{n})}\hat{\boldsymbol{n}}$ and $\hat{\boldsymbol{e}}\boldsymbol{T}_{(\boldsymbol{e})}\hat{\boldsymbol{e}}$ to the physical model $\mu_{\mathrm{DF}}(\boldsymbol{T}, \hat{\boldsymbol{n}}, \hat{\boldsymbol{e}})$ (Eq. 4.52) and its Gaussian mass distribution tensor $\boldsymbol{T}$ (Eq. 4.41) in analogy to the selective experiments shown in Figs. 5.2–5.3, using the acquisition scheme shown in Fig. 5.5. Different histograms show the normalized root mean square errors of the simplified signal models (upper left), angular deviations of their smallest or largest eigenvectors (upper right) and the relations of their eigenvalues (bottom row). The simulations cover the full range of feasible eigenvalues (i.e., anisotropies) of $\boldsymbol{T}$ as well as a large set of random orientations. The angular deviations are compared to (unnormalized) Gaussian distributions of inclination angles integrated over the azimuthal degree of freedom (Eq. 5.4). The (normalized) eigenvalues of both linear tensor models are found to be approximately linear in those of $\boldsymbol{T}$. A more detailed description is published in [46].

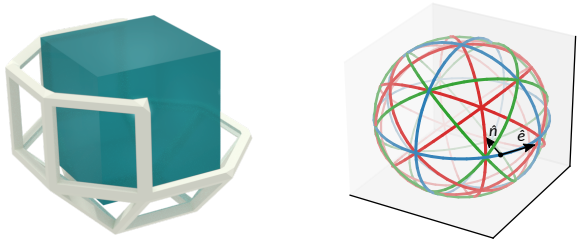

Figure 5.5: Illustration of a 13-faced polyhedral sample cage for anisotropic X-ray dark-field tensor tomography with an example cubic sample (left) and the resulting feasible scanning trajectories about the sample (right). Each face normal of the cage constitutes a possible axis of rotation. All coordinate axes and their diagonals are considered. Redundant, opposing faces are omitted. The cage is realized as a frame structure both to minimize the amount of material within the field of view and to provide a simple means of fixating the cage on a base plate with matching structures accommodating both the quadratic and triangular faces. The effective scanning trajectories with respect to the sample coordinate system, shown on the right, are visually grouped into orthogonal trajectories about the coordinate axes (blue), space diagonals corresponding to triangular faces on the sample cage (green) and the remaining diagonals corresponding to oblique quadratic faces adjacent to triangular ones (red). Given that the orientation of the interferometer gratings is fixed with respect to the rotational axis, $\hat{\boldsymbol{e}}$ is always tangential to the scanning trajectories. Trajectory intersections represent points of constant projection direction $\hat{\boldsymbol{n}}$ at varying grating orientation $\hat{\boldsymbol{e}}$ (cf. Section 5.3).

Figures 5.4 and 5.5 are published in Graetz, Sci. Rep. 2021 [46]

5.4 Experiment

Given the insights into the properties of dark-field contrast discussed so far, a practical data acquisition protocol remains to be defined with respect to the final objective of performing tensor valued volume tomography based on anisotropic dark-field signals. A number of constraints can be summarized:

- First, in order to compensate for the dependence of dark-field signals from individual volume elements from their particular distance to the interferometer's analyzer grating, symmetric projections from opposing orientations are generally advisable with respect to tomographic imaging of extended samples (cf. Section 4.5).
- Secondly, the dependence of dark-field anisotropy on two orientations demands a much more comprehensive sampling of combinations of viewing angles and grating orientations as would be expected for a tensor model as defined for the purpose of reconstruction in Section 5.3.
- Finally, existing instrumentation generally provides circular scanning trajectories by means of a rotating sample stage, with the grating orientation typically being fixed.

As a direct consequence of the first requirement, 360° scans are generally necessary with the direction of interferometer sensitivity being oriented either perpendicular or parallel to the rotational axis in order to ensure 180° symmetry. A fixed relation between rotational axis and interferometer further implies that the trajectories at oblique angles (as shown e.g. in Figure 5.2) must be realized by repositioning the sample (as opposed to inclining the entire rotation stage the sample is mounted on, e.g. using an euler cradle). Most importantly, the instrumentation used to implement the required orientational degrees of freedom must never block the optical path.

All of the above constraints are here satisfied by means of a polyhedral sample cage that allows positioning the sample on a rotary stage at defined orientations while keeping the relation between rotational axis and grating interferometer unchanged. By choice of a low absorbing material with negligible dark-field contrast, such a positioning device ensures minimal interference with any projection view of the sample. The feasible trajectories are determined by the number and orientation of faces of the polyhedral cage. An illustration is given in Figure 5.5.

Although the relative positions of each scanning trajectory are, in principle, defined by the polyhedral cage and its corresponding support on the rotational stage, practical limitations in mechanical precision typically demand a retrospective registration of all scan trajectories in a common coordinate system. This can be realized by first reconstructing volume images from each circular trajectory individually based on the isotropic absorption contrast. This results in thirteen volume images of the sample at different orientations in the coordinate system of the rotary stage. Volume image registration then allows to find the relative coordinate transformations between all scans. The respective transformations can now be inversely applied to the original scan trajectories (which are defined relative to the rotary stage) in order to finally define them within the sample coordinate system (cf. Figure 5.6). Once all trajectories have been defined within the sample coordinate system, the process of iterative tensor tomographic reconstruction can be started (cf. Sections 5.2–5.3 and 1.2.3), incorporating the complete set of anisotropic dark-field projections.

The described methodology has been implemented at the ID19 X-ray imaging beamline of the European Synchrotron Radiation Facility (ESRF, Grenoble, France), using the grating interferometer setup described in [192] (operating at 35keV and a correlation distance of $\xi \approx 1.5\mu m$ in the present configuration as discussed in Section 4.5.1, Eq. 4.38) and an additively manufactured sample cage (based on UV resin) as depicted in 5.5. The acquisition and processing chain is outlined in Figure 5.6. Along each of the 13 circular scan trajectories determined by the sample cage, 149 projection views have been acquired. Reference images for transmission, differential phase and visibility have been acquired every 20 projection angles by temporarily moving the sample out of the beam. Gliding averages of respective reference images have been used for the normalization of the sample projections. Each projection image triplet is computed from seven phase stepping images (cf. Section 4.2), and vertical stitching was required in order to compensate for the asymmetric beam geometry at the synchrotron beamline. I.e., a total of about 4×10^4 raw images are processed to 2×1937 X-ray and dark-field projections (cf. Fig. 5.7 for examples). The original detector sampling of 30.8 µm has been binned to a resolution of 92.4 µm in order to increase the SNR (cf. Figure 4.3). The reduced spatial resolution will be compensated for by the tensor valued statistical representation of the unresolved substructure that will finally be reconstructed. Registration of the

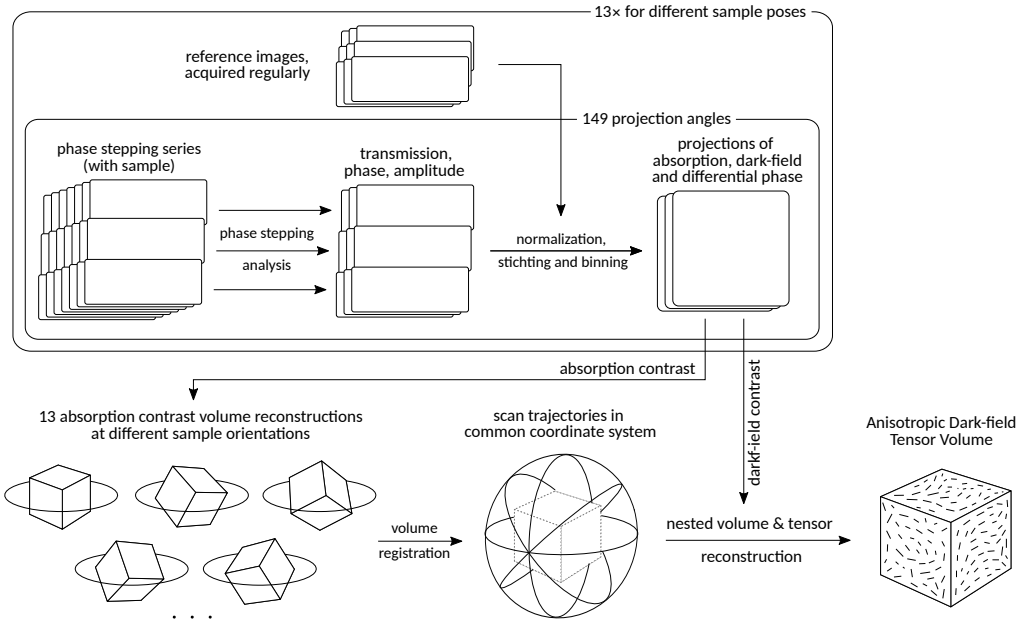

Figure 5.6: Diagrammatic representation of the acquisition and processing workflow for the generation of tensor valued volume reconstructions of anisotropic dark-field signals. Key aspect is the acquisition of multiple tomographic scans at different sample orientations, and their registration based on the isotropic absorption contrast. Due to the large number of scans, each individual scan only comprises a reduced set of 149 projection angles. Once all scan trajectories are registered into the sample's coordinate system based on preliminary reconstructions of the isotropic absorption signal, final reconstructions from all projections can be performed, for each contrast modality respectively. Binning improves the dark-field contrast's signal to noise ratio (cf. Section 4.3 and Fig. 4.3). The corresponding reduction of spatial resolution is generally desired, as the sample's fine structure is captured in the dark-field signal. Here, 13×149 projections (each comprising three phase stepping series of seven images) have been acquired with a final pixel size (after binning) of 0.1mm and a field of view of about 4cm. Stitching is required to obtain a symmetric field of view from the given X-ray beam profile.

scan trajectories within the sample coordinate system is realized by minimizing the sum of absolute differences among volume reconstructions of the absorption contrast modality, whereat rotational and translational degrees of freedom are considered. A tensor valued volume reconstruction of the anisotropic dark-field contrast is finally obtained by five iterations of Algorithm 5.1 using a small relaxation factor $\lambda = 0.1$ in order to damp negative effects of the known inconsistencies of the tensor model with respect to the actual dark-field anisotropy properties (cf. Section 5.3).

5.5 Discussion of Results

Two samples with non-trivial shape and a size fully exploiting the interferometer's field of view have been chosen for the experiments (illustrations are given in Figure 5.8). The contained fibers feature diameters on the 1 to 10 µm scale, which is well detectable (cf. Fig. 4.7) by the given interferometer setup. After reconstruction, eigenvectors and eigenvalues are computed for each voxel. As the rich information contained within tensor tomographic volumes does not have a unique graphic representation, it generally demands for task-specific illustration approaches, which have here been realized by combinations of customized processing and subsequent visualization using ParaView.

The planar structure of the plastic clips (Fig. 5.8, right) makes them well suited for 2D visualization. Figures 5.9–5.10 show, for a selected slice of the tomographic volume, the actually reconstructed tensor components, the deduced fiber orientation and density, as well as a micro CT image for comparison.

The second sample (Fig. 5.8, left) is in contrast markedly three dimensional, and thus represents a prime use case for X-ray tensor tomography as opposed to planar anisotropic dark-field imaging. The reconstruction results are discussed and compared to a micro CT reference in Figures 5.11–5.14.

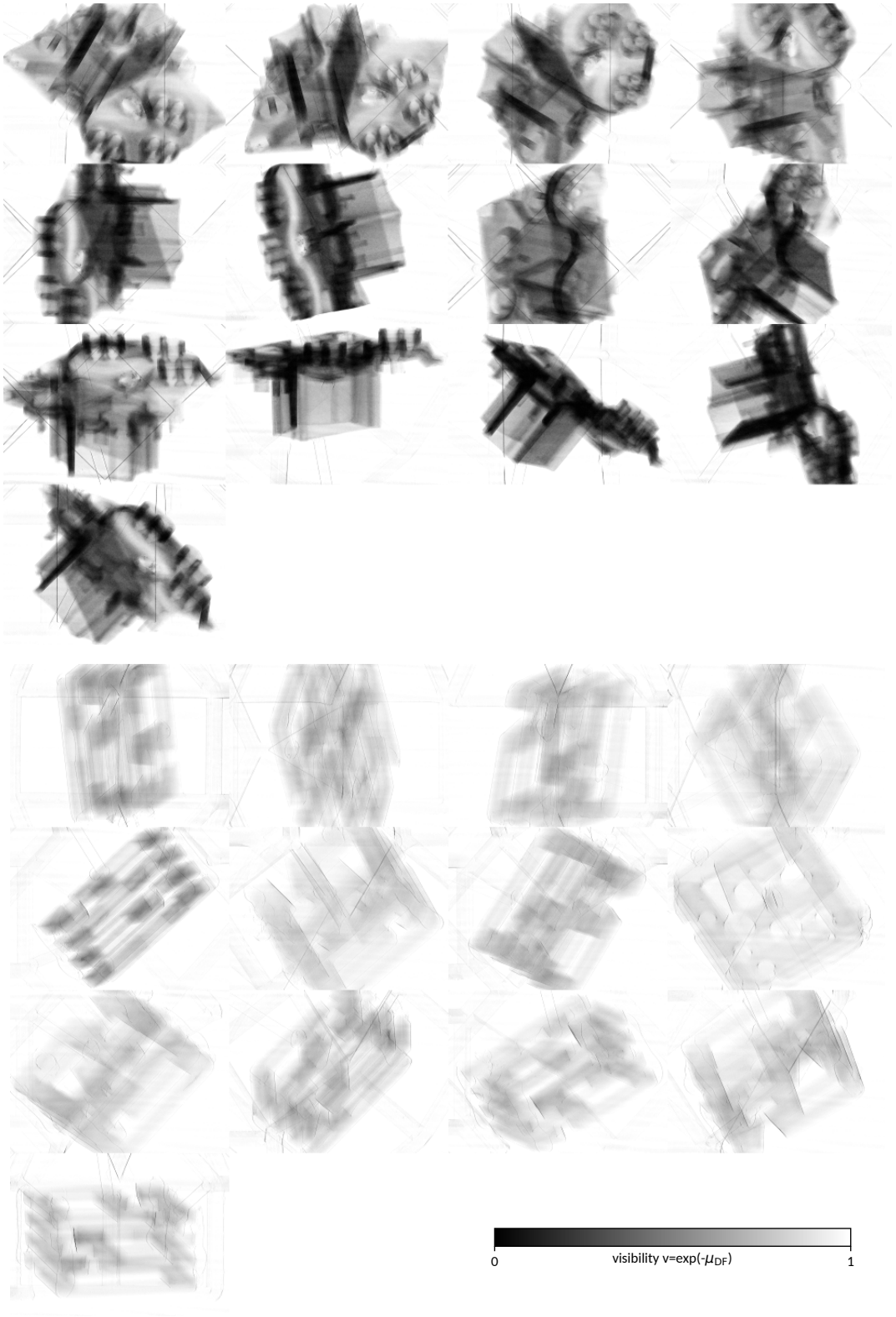

Figure 5.7: Example projection images for each orientation of the rotational axis for both considered samples (cf. Fig. 5.8). For practical purposes of visualization, the visibility contrast $v = e^{-\mu_{\mathrm{DF}}}$ is shown. The ratio $c = \mu_{\mathrm{DF}}/\mu$ between dark-field contrast μ_{DF} and attenuation μ as used to discuss the signal to noise ratio (cf. Section 4.3) is here found to range, on average, around 2 for the glass fiber reinforced sample (top) and 1/2 for the cellulose fiber reinforce sample (bottom). Thin lines overlaying the images originate from edges of the sample cage (cf. Fig. 5.5).

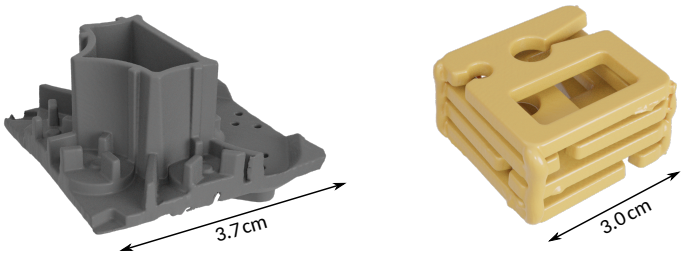

Figure 5.8: Injection molded fiber reinforced plastic samples considered here for X-ray dark-field tensor tomography. On the left, a short glass fiber reinforced part cut from a typical industrially produced housing component is shown. On the right, a stack of four clips made of cellulose fiber reinforced plastic (Fraunhofer WKI, Braunschweig) is shown. The samples have been chosen for their complex shape (left) and their small and low contrast fibers (right).

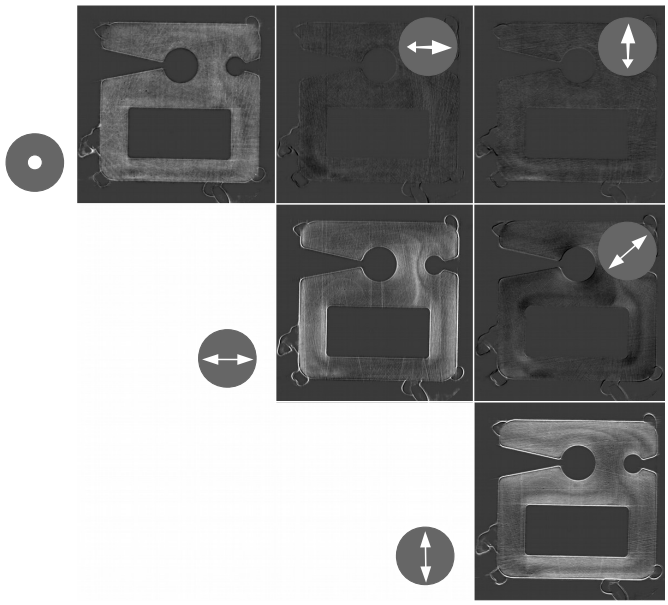

Figure 5.9: Depiction of the reconstructed dark-field tensor components for a single slice (using model $\hat{e}\boldsymbol{T}_{(e)}\hat{e}$, cf. Fig. 5.3, i.e., signals are expected perpendicular to the fiber orientation). As the tensor is symmetric, only the upper triangle is shown. Due to the alignment of the sample in the reconstruction coordinate system, most contributions are found on the diagonal. Arrows indicate the spatial orientation associated with each tensor component. See Figure 5.10 for derived results.

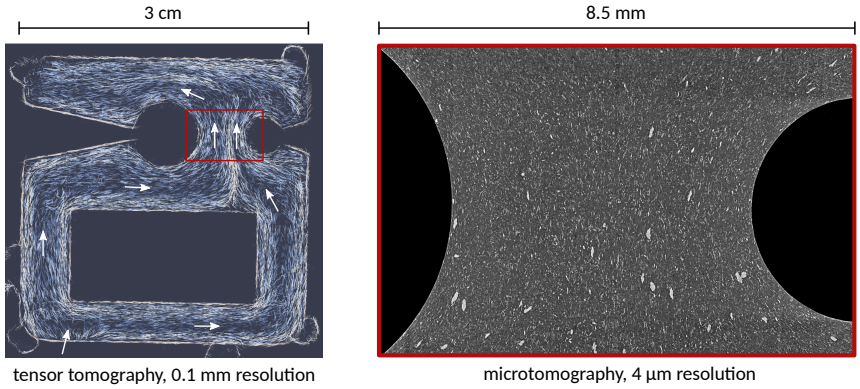

Figure 5.10: Tensor tomography of an injection molded cellulose fiber reinforced sample. On the left, dominant fiber orientations (line glyphs) and fiber densities (brightness) for a representative center slice through one of the four plastic clips (Fig. 5.8, right) are illustrated. The paths of material flow can be visually recognized and are indicated with arrows. On the right, a high resolution micro CT scan of the subsection indicated in red is shown.

Figure 5.9 gives a plain depiction of the reconstructed tensor components. Some qualitative aspects can be readily deduced from this raw representation: The first diagonal component (upper left) encoding signals perpendicular to the image plane shows little variation, corresponding to little variation in the signal-generating fibers along this axis. This in consequence implies that they are mostly oriented parallel to the image plane. In contrast, notable and complementary signal variations within the remaining diagonal components indicate varying in-plane orientations of the fibers. The off-diagonal elements relate to the details of orientation and anisotropy, yet are less intuitive and shall thus not be further elaborated on here.

Figure 5.10 (left) instead provides a visualization of the orientation vector field obtained after eigenanalysis of the tensors. Assuming a single type of scatterer producing some typical amount of total signal per instance, the absolute signal intensity (i.e., the mean eigenvalue or normalized tensor trace) observed at each voxel is interpreted as an indicator of local fiber density. It is here graphically represented as brightness modulation of the visualized vector field. Whenever the projected length of the depicted vectors within the image plane reduces markedly, they actually point in the perpendicular direction as can be observed at the upper left end of the shown sample slice. Analog to the salient in-plane alignments of fibers, this change in orientation plausibly relates to the production process of the sample, with the flow of molten (fiber reinforced) plastic hitting a wall of the injection mold and aligning to it. The prominent "fibers" framing the sample can in contrast be attributed to strong dark-field signals caused by the material-air interfaces at the sample boundaries, as is also visible in the raw tensor data (Fig. 5.9).

Figure 5.10 (right) shows, to give an intuition for the structures contrasted by means of dark-field imaging, a micro CT image of a subsection for comparison. The high resolution required to directly resolve the thin cellulose fibers strongly limits the accessible field of view.

Figure 5.11 illustrates the properties of the second sample using a different visualization approach and further comparing two different reconstructions based on alternative forward models as discussed in Section 5.3. Instead of a planar slice, rather an inner surface of the complex shaped sample is shown. The orientation vector fields are colored to highlight planar vs. vertical orientation, while a graphic representation of the signal strength is given separately. A visual comparison of the vector fields obtained from two alternative reconstruction approaches (Fig. 5.11, left column) confirms a good degree of consistency, giving a further indication for the fitness of the employed signal models discussed previously.

An additional representation of the tensors' degree of anisotropy indicates where the deduced orientation vector field is expected to be well or ill defined respectively, using the definition of "fractional anisotropy" proposed for positive symmetric 3×3 tensors in the context of diffusion tensor imaging [4, 218]:

$$\mathrm{FA}(\boldsymbol{T}) = \sqrt{\frac{1}{2}\left(3 - \frac{\mathrm{trace}(\boldsymbol{T})^2}{\mathrm{trace}(\boldsymbol{T}^2)}\right)}\,. \tag{5.2}$$

FA ranges from 0 for the case of three identical eigenvalues to 1 for the case of a single non-zero eigenvalue. While low degrees of anisotropy ($\mathrm{FA} \to 0$) correspond to randomly oriented fiber ensembles, high degrees ($\mathrm{FA} \to 1$) indicate unique fiber orientations. For $\boldsymbol{T_{(e)}}$ (cf. Figs. 5.3 and 5.11 top), FA is expected to not notably exceed 0.7 (as opposed to 1 for $\boldsymbol{T_{(n)}}$), as it yields two dominant eigenvalues (as opposed to one) in the case of perfectly oriented scatterers. This is indeed confirmed by the experimental findings shown in Fig. 5.11.

Strong orientation can e.g. be observed in the extended vertical sample regions allowing unperturbed material flow during the molding process, while confined and complex shaped or terminal regions typically associated with non-laminar flow tend to feature a wider distribution of fiber orientations, yielding smaller anisotropy values.

With regard to further quantitative comparisons, a high resolution micro CT reference scan of a subsection of the sample has been acquired, allowing for direct analysis of local orientation tensors using classic image based fiber analysis [140]. The scan is precisely aligned relative to the dark-field tensor tomography, and the fiber orientation information from the high resolution scan is reduced to orientation tensors characterizing the statistic orientation distribution within regions spanning, for technical reasons, exactly $2 \times 2 \times 2$ voxels of the tensor tomography. The µCT fiber analysis was kindly provided by Dr. P. Pinter. Direct voxelwise comparisons of the respective tensors obtained with different methodologies are now feasible.

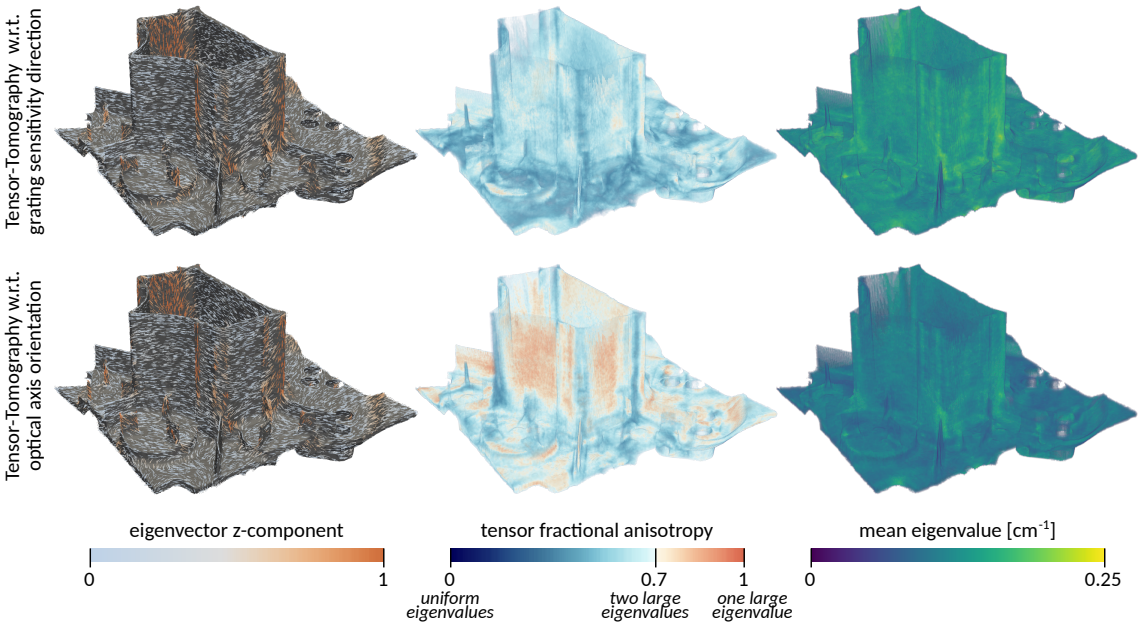

Figure 5.11: Illustrations of dominant fiber orientation, tensor anisotropy and mean eigenvalue for two different tensor tomographic reconstructions of a short glass fiber reinforced sample. In order to show the bulk properties within the sample, a layer of about 0.5 mm thickness has been artificially removed from all surfaces for visualization. In the top row, the reconstruction is based on signal variations perpendicular to the optical axis (related to the structure's autocorrelation width), while in the bottom row it is based on signal variations along the optical axis (related to the structure's scattering cross section). See Section 5.3 and Figs. 5.2–5.3 for more detailed information. Both methods yield largely consistent reconstructions of the predominant fiber orientation (given by the eigenvectors corresponding to the smallest or largest eigenvalue respectively), yet visibly differ in the degree of tensor anisotropy (Eq. 5.2) and mean eigenvalue. Tensor anisotropy is indeed expected to differ due to the differing relations between the reconstructed dark-field tensor and the underlying mass distribution (see Section 5.3, Figs. 5.2–5.3). Unidirectional fiber orientation corresponds to limits of 0.7 (top row) and 1 (bottom).

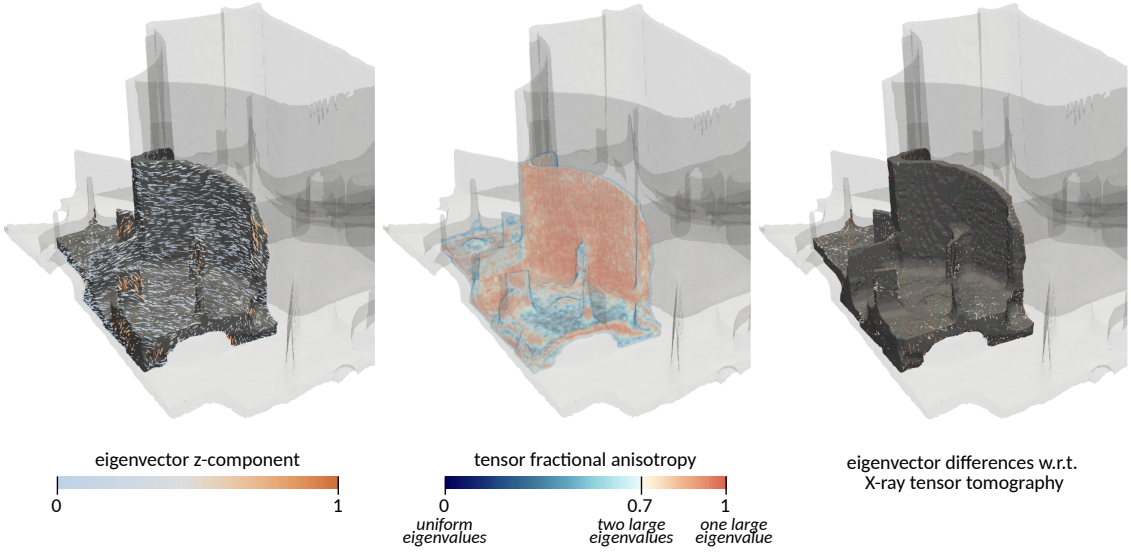

Figure 5.12: Results from classic fiber orientation tensor analysis based on micro CT images resolving the actual fibers (µCT tensor analysis kindly performed by Dr. P. Pinter). The accessible field of view is restricted to a subsection of the sample. Dominant fiber orientation and tensor anisotropy are depicted analog to Fig. 5.11. Anisotropy values of 1 correspond to unidirectional fiber orientation, 0 to isotropic fiber distributions. On the right, the (mostly minor) differences between dominant orientation vectors obtained from micro CT analysis and X-ray tensor tomography respectively (data from Fig. 5.11, top row) are depicted. Quantitative comparisons are given in Figs. 5.13–5.14.

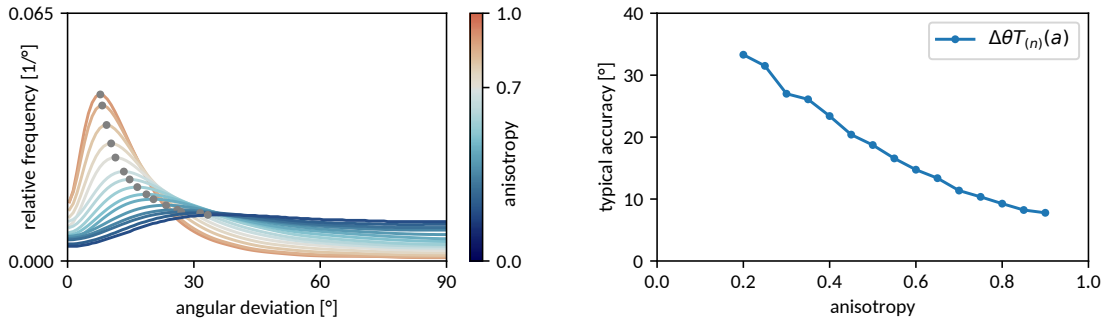

Figure 5.13: Angular deviations between tensor tomography w.r.t. optical axis ($\boldsymbol{T}_{(\boldsymbol{n})}$, Fig. 5.11 bottom) and micro CT reference (cf. Fig. 5.12). On the left, respective statistical distributions over the available reference volume are shown for varying degrees of orientation tensor anisotropy (Fig. 5.12, center). Under the approximative assumption of normally distributed angles (as introduced in Fig. 5.4 and Eq. 5.4), the distributions' maxima correspond to standard deviations and are summarized as a function of anisotropy on the right.

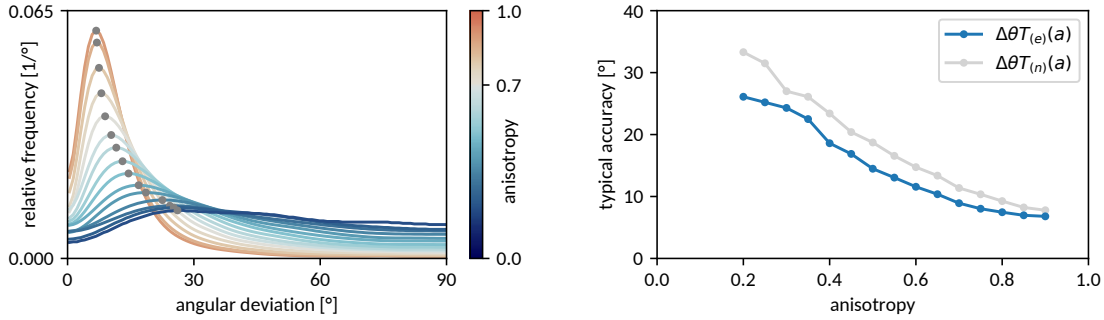

Figure 5.14: Angular deviations between tensor tomography w.r.t. grating sensitivity orientation ($\boldsymbol{T}_{(\boldsymbol{e})}$, Fig. 5.11 top) and micro CT reference analog to Fig. 5.13. The typical angular accuracy (right, blue) is compared to the preceding findings (right, gray). Note that the statistical variance of the reference analysis, likewise contributing to the relative deviations, is unknown.

Figure 5.12 gives an illustration of the resulting orientation vector field and tensor anisotropy analog to the previous tensor tomography results. A depiction of the differences between the respective vector fields provides a first visual impression of the relation between both datasets.

Quantitative analyses are given in Figures 5.13–5.14 showing statistical distributions of relative inclination angles

$$\Delta\theta = \arccos(|\hat{v}_{\mathrm{ref}} \cdot \hat{v}|) \tag{5.3}$$

between normalized orientation vectors of the micro CT reference and either of the two dark-field tensor tomography reconstructions respectively. The data is partitioned into different sets according to the respective degree of orientation tensor anisotropy. The expected correlation between tensor anisotropy and precision of the deduced orientation is clearly visible. The respective error distributions found for the dark-field tensor reconstruction with respect to the optical axis (signal model $\hat{\boldsymbol{n}}\boldsymbol{T}_{(\boldsymbol{n})}\hat{\boldsymbol{n}}$) are, in accordance with the respective simulation results results (Fig. 5.4), found to be slightly wider as compared to dark-field tensor reconstruction with respect to the grating sensitivity axis (signal model $\hat{\boldsymbol{e}}\boldsymbol{T}_{(\boldsymbol{e})}\hat{\boldsymbol{e}}$).

With regard to a more compact quantification of the observed statistics, the distributions are, analog to Fig. 5.4, compared to a Gaussian distribution of relative inclination angles $\Delta\theta$, which, when integrated over the azimuthal degree of freedom, becomes

$$\mathrm{PDF}(\Delta\theta, \sigma_{\Delta\theta}) \propto \sin(\Delta\theta) e^{-\frac{1}{2}\frac{\Delta\theta^2}{\sigma_{\Delta\theta}}} \approx \Delta\theta e^{-\frac{1}{2}\frac{\Delta\theta^2}{\sigma^2_{\Delta\theta}}}, \tag{5.4}$$

exhibiting its maximum right at its standard deviation $\sigma_{\Delta\theta}$.

In the limit of maximally orientated regions (i.e., high anisotropy), the typical statistical deviation from the reference data is here found to range at 7° or 8° respectively (Figs 5.13–5.14), and surpasses 15° and 20° for anisotropy values below 0.5. Already for values of anisotropy below 0.7, the distributions become markedly wider-tailed, whereat deviations ranging up to 90° can be understood in terms of close eigenvalues (related to orthogonal eigenvectors respectively), whose order and the associated identification of dominant orientation is easily affected by noise.

A comparison of statistical deviations from the micro CT based fiber analysis for both tensor tomography reconstructions given in Fig. 5.14 (right) shows, in accordance with Fig. 5.4, a systematic advantage of model $\hat{\boldsymbol{e}}\boldsymbol{T}_{(\boldsymbol{e})}\hat{\boldsymbol{e}}$ over $\hat{\boldsymbol{n}}\boldsymbol{T}_{(\boldsymbol{n})}\hat{\boldsymbol{n}}$, although both models nevertheless reproduce orientations correctly on average. Due to the unknown noise statistics of the reference orientation tensors, no absolute conclusions on precision can be given though. The apparent – and unexpected, given Fig. 5.4 – convergence of the statistical deviations of both dark-field tensor reconstructions in the limit of high anisotropies however gives reason to hypothesize that the remaining statistical uncertainty on the order of magnitude of 5° is also inherently contained in the reference data set.

Conclusion

X-Ray Dark-Field Tensor Tomography is, with regard to its actual realization, a multi-faceted problem at the intersection of applied mathematics, physics and computer science. The final reconstruction and visualization of tensor valued volumes from experimental data thereby represents only the smallest aspect of the problem, which is rather characterized by a multitude of individual methodological aspects at all levels of the required processing chain, which are typically excluded in mathematical considerations of tensor tomography. Three general dimensions of the problem can be identified: quantitative understanding of the available contrast mechanism (dark-field) and its relation to the requirements of tensor tomography, development of flexible and robust image and volume reconstruction algorithms allowing for ubiquitous deviations from ideal acquisition schemes, and finally, actual implementations of these techniques able to handle large amounts of data up to the 100 gigabyte scale.

Chapters 1, 2 and 3 developed modern formulations of iterative and non-iterative tomographic volume reconstruction algorithms for arbitrary X-ray imaging geometries starting from a general vectorial description of perspective projections, including a well motivated and highly efficient discrete X-ray imaging model and a likewise well supported approach to the precise determination of the actual imaging geometry. These essential basics, targeting implementations on recent massively parallel general purpose graphics processors, form the sound basis for the subsequent extension of iterative tomographic reconstruction techniques to tensor-valued volumes. Chapter 4 introduced, developed and validated all methods and relations required towards the efficient computation and quantitative interpretation of (anisotropic) dark-field images from phase stepping series acquired with Talbot or Talbot-Lau interferometers, also addressing practical aspects of experimental imprecisions, noise, and position dependence. Chapter 5 finally derives, building on these fundamentals, both a suited image acquisition scheme and an efficient reconstruction technique for tensor valued volumes, also validating the required approximations in dark-field anisotropy modeling.

The entire processing chain is finally successfully applied to actual experimental data of fiber reinforced samples explicitly acquired for this purpose. The observed results and especially the qualitative differences among the different signal models considered are found to be consistent with the preceding theoretical analyses. An explicit comparison to an established fiber orientation analysis approach based on processing high resolution micro CT images provides further empirical validation of the deduced vector fields and confirms that local orientations can be practically reconstructed, within larger tomographic volumes on the scale of 300^3 to 500^3 tensor voxels, to a typical precision of 5° to 10° for reasonably anisotropic fiber ensembles also in notably non-uniform and large samples (note that this includes also the statistical noise inherent to small ensembles), i.e., in use cases which truly benefit from fully three dimensional information and can not be easily addressed with alternative planar imaging approaches.

Publications

First author publications directly related to this dissertation

- **J. Graetz**: „Simulation study towards quantitative X-ray and neutron tensor tomography regarding the validity of linear approximations of dark-field anisotropy“ Scientific Reports (2021). doi:10.1038/s41598-021-97389-y [1]
- **J. Graetz**: „Auto-calibration of cone beam geometries from arbitrary rotating markers using a vector geometry formulation of projection matrices“ Physics in Medicine and Biology (2021). doi:10.1088/1361-6560/abe75f [2]
- **J. Graetz**, A. Balles, R. Hanke, S. Zabler: „Review and experimental verification of x-ray dark-field signal interpretations with respect to quantitative isotropic and anisotropic dark-field computed tomography“ Physics in Medicine and Biology (2020). doi:10.1088/1361-6560/abb7c6 [3]
- **J. Dittmann**, A. Balles, S. Zabler: „Optimization Based Evaluation of Grating Interferometric Phase Stepping Series and Analysis of Mechanical Setup Instabilities“, Journal of Imaging 4(6) (2018). doi:10.3390/jimaging4060077 [4]
- **J. Dittmann**, R. Hanke: „Simple and efficient raycasting on modern GPU's read-and-write memory for fast forward projections in iterative CBCT reconstruction“, Proc. Fully3D (2017). doi:10.12059/Fully3D.2017-11-3203040 [5]

[1] Contains Figs. 5.4–5.5, published under CC BY 4.0.

[2] Presents the contents of Chapter 3 and Sections 1.1.1–1.1.2. Published under CC BY 4.0.

[3] Presents the contents of Sections 4.4–4.6. Published under CC BY 4.0. Authors contributions: J.G. conceived and performed the study, did the literature research, worked out the theory, wrote the image processing software, performed the data analysis and visualization and wrote the manuscript. J.G., A.B. and S.Z conceived, prepared and performed the experiments (with support by M.O., A.R., D.M, M.U., M.S.) and reviewed the manuscript. R.H. supervises the PhD project of J.G., secured funding and reviewed the manuscript. J.G. updated the manuscript based on reviews of the co-authors and anonymous referees.

[4] Presents the basis of Section 4.2. Published under CC BY 4.0. Authors' contributions: Conceptualization, J.D., A.B. and S.Z.; Methodology, J.D.; Software, J.D.; Validation, J.D.; Formal Analysis, J.D.; Investigation, J.D. and A.B.; Resources, S.Z. and A.B.; Data Curation, J.D.; Writing—Original Draft Preparation, J.D.; Writing—Review and Editing, J.D., A.B. and S.Z.; Visualization, J.D.; Supervision, S.Z.; and Project Administration, S.Z.

[5] Preliminary results of Chapter 2. Authors' contributions: J.D. conceived and performed the work, wrote the manuscript and prepared the figures. R.H. supervises the PhD project of J.D., facilitated the present work and secured funding.

Publications on other topics and co-authored publications

- D. Müller, **J. Graetz**, A. Balles, S. Stier, R. Hanke, C. Fella: „Laboratory Based Nano Computed Tomography and Examples of its Application in the Field of Materials Research“. Crystals 11 (6) (2021). doi:10.3390/cryst11060677
- **J. Graetz**, D. Müller, A. Balles, C. Fella: „Lensless nano-tomography down to 150nm resolution: on the quantification of modulation transfer and focal spot of the lab-based ntCT system“ J. Instrumentation (2021). doi:10.1088/1748-0221/16/01/P01034
- **J. Graetz**, J. Dombrowski, A. Eggert, A. Rack, U. Kulozik, J. Hinrichs, R. Hanke, S. Zabler: „Synchrotron micro-CT for sudying coarsening in milk protein stabilized foams in situ“ Colloids and Surfaces A 601 (2020). doi:10.1016/j.colsurfa.2020.124832
- S. Zabler, K. Schladitz, K. Dremel, **J. Graetz**, D. Dobrovolskij: „Region-of-Interest X-Ray Tomography for the Non-Destructive Characterization of Local Fiber Orientation in Large Fiber Composite Parts“ Key Engineering Materials 809 (2019). doi:10.4028/www.scientific.net/KEM.809.587
- C. Fella, **J. Dittmann**, D. Müller, T. Donath, D. Murer, T. Tuohimaa, A. Sofiienko, S. Zabler, R. Hanke: „Implementation of a Computed Tomography System based on a Laboratory Nanofocus X-Ray Source“ Microscopy and Microanalysis, 24(S2). doi:10.1017/S1431927618013521
- A. Balles, D. Müller, **J. Dittmann**, C. Fella, R. Hanke, S. Zabler: „Computed Tomography from a Single Grating X-Ray Interferometer at a Laboratory Liquid-Metal-jet Source“ Microscopy and Microanalysis, 24(S2). doi:10.1017/S1431927618013156
- A. Balles, **J. Dittmann**, C. Fella, R. Hanke, S. Zabler: „Quantitative phase contrast and X-ray scattering micro-tomography with the 9.2keV liquid metal jet anode: applications on materials and life science“. Proc SPIE 10391 (2017). doi:10.1117/12.2275889
- P. Stahlhut, K. Dremel, **J. Dittmann**, J. Engel, S. Zabler, A. Hoelzing, R. Hanke: „First results on laboratory nano-CT with a needle reflection target and an adapted toolchain“, Proc. SPIE 9967 (2016). doi:10.1117/12.2240561
- K. Blum, W. Wiest, C. Fella, A. Balles, **J. Dittmann**, A. Rack, D. Maier, R. Thomann, B. Spies, R. Kohal, S. Zabler, K. Nelson: „Fatigue induced changes in conical implant-abutment connections“, Dental Materials 31 (11) (2016). doi:10.1016/j.dental.2015.09.004
- **J. Dittmann**, A. Eggert, M. Lambertus, J. Dombrowski, A. Rack. S. Zabler: „Finding robust descriptive features for the characterization of the coarsening dynamics of three dimensional whey protein foams“, Journal of Colloid and Interface Science 467 (2016). doi:10.1016/j.jcis.2015.12.055
- A. Balles, C. Fella, **J. Dittmann**, W. Wiest, S. Zabler, R. Hanke: “X-ray grating interferometry for 9.25 keV design energy at a liquid-metal-jet source“, AIP Conf. Proc. 1696, (2016). doi:10.1063/1.4937537
- T. Fuchs, T. Schön, **J. Dittmann**, F. Sukowski, R. Hanke: „Recent progress in 3-D imaging of sea freight containers“, AIP Conf. Proc. 1650, 556 (2016). doi:10.1063/1.4914653

Acknowledgements

- Prof. Dr. Randolf Hanke for ensuring funding and the freedom to conduct this manifold work
- PD Dr. Simon Zabler for proposing and supporting the topic of Dark-Field Tensor Tomography, his essential initiatives towards actual experiments and is trust and patience while working on this dissertation
- Dr. Christian Fella for his work on X-ray microscopy instrumentation and his trust and patience while finishing this dissertation
- Britta Dorsch, Alison Haydock and Markus Kiunke for their administrative support and the friendly atmosphere at the chair
- Dr. Andreas Balles for his experimental work on grating based imaging and X-ray microscopy and the enjoyable times in the office
- Dominik Müller for his work on X-ray microscopy instrumentation and his passion for applications and well designed images
- Dr. Benedikt Sochor, Dr. Bernhard Schummer and Dr. Stefan Gerth for discussions on SAXS
- Dr. Kilian Dremel, Dominik Müller, Philipp Stahlhut, Daniel Althoff, Dr. Jens Engel, Dr. Astrid Hölzing for their work on X-ray microscopy instrumentation
- The European Synchrotron Radiation Facility for granting beamtime, Dr. Alexander Rack and Dr. Margie Olbinado for user support, and Dr. Andreas Balles, Dominik Müller, Dr. Maximilian Ullherr and Dr. Simon Zabler for supporting the experiments
- Dr. Vincent Revol, Dr. Rolf Kaufmann, Dr. Marian Willner for sharing dark-field data in the early stages of this work
- Dr. Khanlian Chung for a memorable conference-trip to China and discussions on CBCT
- Dr. Florian Bittner and Oliver Focke for sharing fiber reinforced samples
- Dr. Pascal Pinter for performing the fiber analysis on the µCT reference scan used in Section 5.5

Bibliography

[1] J. Amanatides and A. Woo. A fast voxel traversal algorithm for ray tracing. *Eurographics*, 87(3):10, 1987. URL: http://www.cse.chalmers.se/edu/year/2015/course/TDA361/grid.pdf.

[2] A. H. Andersen and A. C. Kak. Simultaneous algebraic reconstruction technique (sart): A superior implementation of the art algorithm. *Ultrasonic Imaging*, 6:81–94, 1984. doi:10.1016/0161-7346(84)90008-7.

[3] A. Balles, D. Müller, J. Dittmann, C. Fella, R. Hanke, and S. Zabler. Computed tomography from a single grating x-ray interferometer at a laboratory liquid-metal-jet source. *Microsc. Microanal.*, 24(2):152–153, 2018. doi:10.1017/S1431927618013156.

[4] P. J. Basser and C. Pierpaoli. Microstructural and physiological features of tissues elucidated by quantitative-diffusion-tensor MRI. *J. Magn. Reson. Ser. B*, 111:209–219, 1996. doi:10.1016/j.jmr.2011.09.022.

[5] F. Bayer, S. Hu, A. Maier, T. Weber, G. Anton, T. Michel, and C. Riess. Reconstruction of scalar and vectorial components in x-ray dark-field tomography. *PNAS*, 111(35):12699–12704, 2014. doi:10.1073/pnas.1321080111.

[6] F. Bayer, S. Zabler, C. Brendel, G. Pelzer, J. Rieger, A. Ritter, T. Weber, T. Michel, and G. Anton. Projection angle dependence in garting-based x-ray dark-field imaging of ordered structures. *Opt. Express*, 21(17):19922–19933, 2013.

[7] M. Bech, O. Bunk, T. Donath, R. Feidenhans'l, C. David, and F. Pfeiffer. Quantitative x-ray dark-field computed tomography. *Phys. Med. Biol.*, 55(18):5529–5539, 2010. doi:10.1088/0031-9155/55/18/017.

[8] E. E. Bennet, R. Kopace, A. F. Stein, and H. Wen. A grating-based single-shot x-ray phase contrast and diffraction method for in vivo imaging. *Med. Phys.*, 37(11):6047–6054, 2010. doi:10.1118/1.3501311.

[9] D. Bequé, J. Nuyts, G. Bormans, P. Suetens, and P. Dupont. Characterization of pinhole spect acquisition geometry. *IEEE Trans. Med. Imaging*, 22(5):599–612, 2003. doi:10.1109/TMI.2003.812258.

[10] D. Bequé, J. Nuyts, P. Suetens, and G. Bormans. Optimization of geometrical calibration in pinhole spect. *IEEE Trans. Med. Imaging*, 24(2):180–190, 2005. doi:10.1109/TMI.2004.839367.

[11] J. Beyer, M. Hadwiger, and H. Pfister. A survey of gpu-based large-scale volume visualization. *Eurographics Conference on Visualization*, 2014. doi:10.2312/eurovisstar.20141175.

[12] R. Bippus, T. Köhler, F. Bergner, B. Brendel, E. Hansis, and R. Proksa. Projector and backprojector for iterative ct reconstruction with blobs using cuda. *11th International Meeting on Fully Three-Dimensional Image Reconstruction in Radiology and Nuclear Medicine*, 2011.

[13] J. Brokish, D. Keesing, and Y. Bresler. Iterative circular conebeam ct reconstruction using fast hierarchical backprojection/reprojection operators. *Proc. SPIE 7622, Medical Imaging*, page 76221R, 2010. doi:10.1117/12.844026.

[14] I. N Bronstein, K. A. Semendjajew, G. Musiol, and H. Mühlig. *Taschenbuch der Mathematik, 5. überarbeitete und erweiterte Auflage*. Verlag Harri Deutsch, 2001. URL: http://d-nb.info/959260714.

[15] T. M. Buzug. *Einführung in die Computertomographie: mathematisch-physikalische Grundlagen der Bildrekonstruktion*. Springer-Verlag, 2011. doi:10.1007/978-3-642-18593-9.

[16] G. G. Cameron and P. E. Undrill. Rendering volumetric medical image data on a simd-architecture computer. *Proceedings of the Third Eurographics Workshop on Rendering*, page 135–145, May 1992.

[17] M. Chabior. *Contributions to the characterization of grating-based x-ray phase-contrast imaging*. PhD thesis, 2011. URL: https://nbn-resolving.org/urn:nbn:de:bsz:14-qucosa-81705.

[18] M. Chabior, T. Donath, C. David, M. Schuster, C. Schroer, and F. Pfeiffer. Signal-to-noise ratio in x ray dark-field imaging using a grating interferometer. *J. Appl. Phys.*, 110(5):053105, 2011. doi:10.1063/1.3630051.

[19] D. Chapman, W. Thomlinson, R. E. Johnston, D. Washburn, E. Pisano, N. Gmür, Z. Zhong, R. Menk, F. Arfelli, and D. Sayers. Diffraction enhanced x-ray imaging. *Phys. Med. Biol.*, 42(11):2015–2025, 1997. doi:10.1088/0031-9155/42/11/001.

[20] Y. Cho, D. J. Moseley, J. H. Siewerdsen, and D. A. Jaffray. Accurate technqiue for complete geometric calibration of cone-beam computed tomography systems. *Med. Phys.*, 32(4):968–983, 2005. doi:10.1118/1.1869652.

[21] P. Cloetens, J. P. Guigay, C. De Martino, J. Baruchel, and M. Schlenker. Fractional talbot imaging of phase gratings with hard x rays. *Opt. Lett.*, 22(14):1095–1061, 1997. doi:10.1364/OL.22.001059.

[22] C. David, B. Nöhammer, H. H. Solak, and E. Ziegler. Differential x-ray phase contrast imaging using a shearing interferometer. *Appl. Phys. Lett.*, 81(17):3287–3289, 2002. doi:10.1063/1.1516611.

[23] M. de Greef, J. Crezee, J. C. van Eijk, R. Pool, and A. Bel. Accelerated ray tracing for radiotherapy dose calculations on a gpu. *Med. Phys.*, 36(9):4095–4102, 2009. doi:10.1118/1.3190156.

[24] Bruno De Man and Samit Basu. Distance-driven projection and backprojection in three dimensions. *Phys. Med. Biol.*, 49(11):2463–2475, 2004. doi:10.1088/0031-9155/49/11/024.

[25] M. Defrise, C. Vanhove, and J. Nuyts. Perturbative refinement of the geometric calibration in pinhole spect. *IEEE Trans. Med. Imaging*, 27(2):204–214, 2008. doi:10.1109/TMI.2007.904687.

[26] D. DeMenthon and L. S. Davis. Model-based object pose in 25 lines of code. *Int. J. Comput. Vision*, 15(1-2):123–141, 1995. doi:10.1007/BF01450852.

[27] P. Després and X. Jia. A review of gpu-based medical image reconstruction. *Physica Medica*, 42, 2017. doi:10.1016/j.ejmp.2017.07.024.

[28] J. Dittmann. Tomographische rekonstruktion aus wenigen röntgenprojektionen auf grundlage der compressed sensing theorie. Master's thesis, JMU Würzburg, 2013.

[29] J. Dittmann, A. Balles, and S. Zabler. Optimization based evaluation of grating interferometric phase stepping series and analysis of mechanical setup instabilities. *J. Imaging*, 4(6):77, 2018. doi:10.3390/jimaging4060077.

[30] J. Dittmann and R. Hanke. Simple and efficient raycasting on modern gpu's read-and-write memory for fast forward projections in iterative cbct reconstruction. *Proc. Fully3D*, page 781–784, 2017. doi:10.12059/Fully3D.2017-11-3203040.

[31] J. Dittmann, S. Zabler, and R. Hanke. Nested tomography: Application to direct ellipsoid reconstruction in anisotropic darkfield tomography. *Conf. XNPIG 2017*, page 49–50, 9 2017. URL: https://www.psi.ch/xnpig2017.

[32] J. Dittmann (Graetz). Efficient ray tracing on 3d regular grids for fast generation of digitally reconstructed radiographs in iterative tomographic reconstruction techniques. *arXiv:1609.00958*, 2016. doi:10.48550/arXiv.1609.00958.

[33] T. Donath, M. Chabior, F. Pfeiffer, O. Bunk, E. Reznikova, J. Mohr, E. Hempel, S. Popescu, M. Hoheisel, M. Schuster, J. Baumann, and C. David. Inverse geometry for grating-based x-ray phase-contrast imaging. *J. Appl. Phys.*, 106(5):054703, 2009. doi:10.1063/1.3208052.

[34] K. Dremel. *Modellbildung des Messprozesses und Umsetzung eines modellbasierten iterativen Lösungsverfahrens der Schnittbild-Rekonstruktion für die Röntgen-Computertomographe*. PhD thesis, JMU Würzburg, 2017. URL: https://nbn-resolving.org/urn:nbn:de:bvb:20-opus-157917.

[35] Robert Endl and Manfred Sommer. Classification of ray-generators in uniform subdivisions and octrees for ray tracing. *Computer Graphics Forum*, 13(1):3–19, 1994. doi:10.1111/1467-8659.1310003.

[36] M. Endrizzi, P. C. Diemoz, T. P. Millard, J. L. Jones, R. D. Speller, I. K. Robinson, and A. Olivo. Hard x-ray dark-field imaging with incoherent sample illumination. *Appl. Phys. Lett.*, 104:024106, 2014. doi:10.1063/1.4861855.

[37] M. Endrizzi, F. A. Vittoria, L. Rigon, D. Dreossi, F. Iacoviello, P. R. Shearing, and A. Olivo. X-ray phase-contrast radiography and tomography with a multiaperture analyzer. *Phys. Rev. Lett.*, 118(24):243902, 2017. doi:10.1103/PhysRevLett.118.243902.

[38] L. Feldkamp, L. Davis, and J. Kress. Practical cone-beam algorithm. *J. Opt. Soc. Am. A*, 1(6):612–619, 1984. doi:10.1364/JOSAA.1.000612.

[39] L. Felsner, S. Hu, A. Maier, J. Bopp, V. Ludwig, G. Anton, and C. Riess. A 3-d projection model for x-ray dark-field imaging. *Sci. Rep.*, 9:9216, 2019. doi:10.1038/s41598-019-45708-9.

[40] J. C. Ford, D. Zhen, and J. F. Williamson. Estimation of ct cone-beam geometry using a novel method insensitive to phantom fabrication inaccuracy: Implications for isocenter localization accuracy. *Med. Phys.*, 38(6):2829–2840, 2011. doi:10.1118/1.3589130.

[41] Akira Fujimoto, Takayuki Tanaka, and Kansei Iwata. Arts: Accelerated ray-tracing system. *Computer Graphics and Applications, IEEE*, 6(4):16–26, 1986. doi:10.1109/MCG.1986.276715.

[42] H. Gao. Fast parallel algorithms for the x-ray transform and its adjoint. *Med. Phys.*, 39(11):7110–7120, 2012. doi:10.1118/1.4761867.

[43] S. Gkoumas, P. Villanueva-Perez, Z. Wang, L. Romano, M. Abis, and M. Stampanoni. A generalized quantitative interpretation of dark-field contrast for highly concentramicrosphere suspensions. *Sci. Rep.*, 6:35259, 2016. doi:10.1038/srep35259.

[44] R. Gordon, R. Bender, and G. T. Herman. Algebraic reconstruction techniques (art) for three-dimensional electron microscopy and x-ray photography. *J. Theor. Biol.*, 29(3):471–476, 1970. doi:10.1016/0022-5193(70)90109-8.

[45] J. Graetz. Auto-calibration of cone beam geometries from arbitrary rotating markers using a vector geometry formulation of projection matrices. *Phys. Med. Biol.*, 66(7):075013, 2021. doi:10.1088/1361-6560/abe75f.

[46] J. Graetz. Simulation study towards quantitative x-ray and neutron tensor tomography regarding the validity of linear approximations of dark-field anisotropy. *Sci. Rep.*, 11:18477, 2021. doi:10.1038/s41598-021-97389-y.

[47] J. Graetz, A. Balles, R. Hanke, and S. Zabler. Review and experimental verification of x-ray dark-field signal interpretations with respect to quantitative isotropic and anisotropic dark-field computed tomography. *Phys. Med. Biol.*, 65(23):235017, 2020. doi:10.1088/1361-6560/abb7c6.

[48] S. Grandl, K. Scherer, A. Sztrókay-Gaul, L. Birnbacher, K. Willer, M. Chabior, J. Herzen, D. Mayr, S. Auweter, F. Pfeiffer, F. Bamberg, and K. Hellerhoff. Improved visualization of breast cancer features in multifocal carcinoma using phase-contrast and dark-field mammography: an ex vivo study. *Eur. Radiol.*, 25:3659–3668, 2015. doi:10.1007/s00330-015-3773-5.

[49] J. Gregson, M. Krimerman, M. Hullin, and W. Heidrich. Stochastic tomography and its applications in 3d imaging of mixing fluids. *ACM Trans. Graph.*, 31(4):Article 52, 2012. doi:10.1145/2185520.2185548.

[50] M. Gresil, V. Revol, K. Kitsianos, G. Kanderakis, I. Koulalis, M. Sauer, H. Trétout, and A. Madrigal. Evita project: Comparison between traditional non-destructive techniques and phase contrast x-ray imaging applied to aerospace carbon fibre reinforced polymer. *Appl. Compos. Mater.*, 24:513–524, 2017. doi:10.1007/s10443-016-9540-1.

[51] L. B. Gromann, F. De Marco, K. Willer, P. B. Noël, K. Scherer, B. Renger, B. Gleich, K. Achterhold, A. A. Fingerle, D. Muenzel, S. Auweter, K. Hellbach, M. Reiser, A. Baehr, M. Dmochewitz, T. J. Schroeter, F. J. Koch, P. Meyer, D. Kunka, J. Mohr, A. Yaroshenko, H. Maack, T. Pralow, H. van der Heijden, R. Proksa, T. Koehler, N. Wieberneit, K. Rindt, E. J. Rummeny, F. Pfeiffer, and J. Herzen. In-vivo x-ray dark-field chest radiography of a pig. *Sci. Rep.*, 7(1):4807, 2017. doi:10.1038/s41598-017-05101-w.

[52] D. Gross, U. Heil, R. Schulze, E. Schoemer, and U. Schwanecke. Auto calibration of a cone-beam-ct. *Med. Phys.*, 39(10):5959–5970, 2012. doi:10.1118/1.4739247.

[53] C. Grünzweig, J. Kopecek, B. Betz, A. Kaestner, K. Jefimovs, J. Kohlbrecher, U. Gasser, O. Bunk, C. David, E. Lehmann, T. Donath, and F. Peiffer. Quantification of the neutron dark-field imaging signal in grating interferometry. *Phys. Rev. B*, 88(12):125104, 2013. doi:10.1103/PhysRevB.88.125104.

[54] H. Guan and R. Gordon. A projection access order for speedy convergence of art (algebraic reconstruction technique): a multilevel scheme for computed tomography. *Phys. Med. Biol.*, 39(11):2005–2022, 1994. doi:10.1088/0031-9155/39/11/013.

[55] G. T. Gullberg, B. M. W. Tsui, C. R. Crawford, J. G. Ballard, and J. T. Hagius. Estimation of geometrical parameters and collimator evaluation for cone beam tomography. *Med. Phys.*, 17(2):264–272, 1990. doi:10.1118/1.596505.

[56] C. Gusenbauer, M. Reiter, B. Plank, D. Salaberger, S. Senck, and J. Kastner. Porosity determination of carbon and glass fibre reinforced polymers using phase-contrast imaging. *J. Nondestruct. Eval.*, 38(1), 2019. doi:10.1007/s10921-018-0529-6.

[57] S. Ha, A. Kumar, and K. Mueller. A study of volume integration models for iterative cone-beam computed tomography. *Proceedings of the 13th Meeting on Fully 3D Image Reconstruction*, 2015.

[58] S. Ha, H. Li, and K. Mueller. Efficient area-based ray integration using summed area tables and regression models. *Proceedings of the 4th International Meeting on image formation in X-ray CT*, page 507–510, 2016.

[59] K. Hahn, H. Schöndube, K. Stiersdorfer, J. Hornegger, and F. Noo. A comparison of linear interpolating models for iterative ct reconstruction. *Med. Phys.*, 43(12):6455–6473, 2016. doi:10.1118/1.4966134.

[60] C. Hannesschläger, V. Revol, B. Plank, D. Salaberger, and J. Kastner. Fibre structure characterisation of injection moulded short fibre-reinforced polymers by x-ray scatter dark field tomography. *Case Stud. Nondestruct. Test. Evaluation*, 3:34–41, 2015. doi:10.1016/j.csndt.2015.04.001.

[61] K. M. Hanson and G. W. Wecksung. Local basis-function approach to computed tomography. *Applied Optics*, 24(23):4028–4039, 1985. doi:10.1364/AO.24.004028.

[62] R. P. Harti, M. Strobl, R. Schäfer, N. Kardjilov, A. S. Temsin, and C. Grünzweig. Dynamic volume magnetic domain wall imaging in grain oriented electrical steel at power frequencies with accumulative high-frame rate neutron dark-field imaging. *Sci. Rep.*, 8:15754, 2018. doi:10.1038/s41598-018-33835-8.

[63] R. Hartley and A. Zisserman. *Multiple View Geometry in computer vision*. Cambridge university press, 2004. doi:10.1017/CBO9780511811685.

[64] K. Hashimoto, H. Takano, and A. Momose. Improved reconstruction method for phase stepping data with stepping errors and dose fluctuations. *Opt. Express*, 28(11):16363–16384, 2020. doi:10.1364/OE.385236.

[65] C. Hauke, G. Anton, K. Hellbach, M. Leghissa, F. G. Meinel, T. Mertelmeier, T. Michel, M. Radicke, S. Sutter, T. Weber, and L. Ritschl. Enhanced reconstruction algorithm for moiré artifact suppression in talbot-lau x-ray imaging. *Phys. Med. Biol.*, 63(13):1425–1440, 2018. doi:10.1088/1361-6560/aacb07.

[66] C. Hauke, M. Leghissa, G. Pelzer, M. Radicke, T. Weber, T. Mertelmeier, G. Anton, and L. Ritschl. Analytical and simulative investigations of moiré artefacts in talbot-lau x-ray imaging. *Opt. Express*, 25(26):32897–32909, 2017. doi:10.1364/OE.25.032897.

[67] G. T. Herman and L. B. Meyer. Algebraic reconstruction technique can be made computationally efficient. *IEEE Trans. Med. Imaging*, 12(3):600–609, 1993. doi:10.1109/42.241889.

[68] C. Hofmann, M. Knaup, and M. Kachelrieß. Effects of ray profile modeling on resolution recovery in clinical CT. *Med. Phys.*, 41(2):021907–1–14, 2014. doi:10.1118/1.4862510.

[69] S. Hoppe, F. Noo, F. Dennerlein, G. Lauritsch, and J. Hornegger. Geometric calibration of the circle-plus-arc trajectory. *Phys. Med. Biol.*, 52(23):6943–6960, 2007. doi:10.1088/0031-9155/52/23/012.

[70] F. Horn, K. Gelse, S. Jabari, C. Hauke, S. Kaeppler, V. Ludwig, P. Meyer, T. Michel, J. Mohr, G. Pelzer, J. Rieger, C. Riess, M. Seifert, and G. Anton. High-energy x-ray talbot–lau radiography of a human knee. *Phys. Med. Biol.*, 62(16):6729–6745, 2017. doi:10.1088/1361-6560/aa772.

[71] G. N. Hounsfield. A method and an apparatus for examination of a body by radiation such as x or gamma radiation. *Patent Specification 1283915, London, England*, 1972.

[72] I. Ihrke and M. Magnor. Adaptive grid optical tomography. *Graphical Models*, 68(5):484–495, 2006. doi:10.1016/j.gmod.2006.08.001.

[73] F. Jacobs, E. Sundermann, B. De Sutter, M. Christiaens, and I. Lemahieu. A fast algorithm to calculate the exact radiological path through a pixel or voxel space. *Journal of computing and information technology*, 6(1):89–94, 1998. URL: http://hdl.handle.net/1854/LU-281913.

[74] T. H. Jensen, M. Bech, O. Bunk, T. Donath, C. David, R. Feidenhans'l, and F. Pfeiffer. Directional x-ray dark-field imaging. *Phys. Med. Biol.*, 55(12):3317–323, 2010. doi:10.1088/0031-9155/55/12/004.

[75] T. H. Jensen, M. Bech, I. Zanette, T. Weitkamp, C. David, H. Deyhle, S. Rutishauser, E. Reznikova, J. Mohr, R. Feidenhans'l, and F. Pfeiffer. Directional x-ray dark-field imaging of strongly ordered systems. *Phys. Rev. B*, 82(21), 2010. doi:10.1103/PhysRevB.82.214103.

[76] I. Jerjen, V. Revol, A. J. Brunner, P. Schuetz, C. Kottler, R. Kaufmann, T. Luethi, G. Nicoletti, C. Urban, and U. Sennhauser. Detection of stress whitening in plastics with the help of x-ray dark field imaging. *Polymer Testing*, 32:1094–1098, 2013. doi:10.1016/j.polymertesting.2013.06.008.

[77] R. E. Johnston, D. Washburn, E. Pisano, C. Burns, W. C. Thomlinson, L. D. Chapman, F. Arfelli, N. F. Gmur, Z. Zhong, and D. Sayers. Mammographic phantom studies with synchrotron radiation. *Radiology*, 200(3):659–663, 1996. doi:10.1148/radiology.200.3.8756911.

[78] S. M. Johnston, G. A. Johnson, and C. T. Badea. Geometric calibration for a dual tube/detector micro-ct system. *Med. Phys.*, 35(5):1820–1829, 2008. doi:10.1118/1.2900000.

[79] P. M. Joseph. An improved algorithms for reprojecting rays through pixel images. *IEEE Trans. Med. Imaging*, MI-1(3):192–196, 1982. doi:10.1109/TMI.1982.4307572.

[80] C. Jud, E. Braig, M. Dierolf, E. Eggl, B. Günther, K. Achterhold, B. Gleich, E. Rummeny, P. Noël, F. Pfeiffer, and D. Muenzel. Trabecular bone anisotropy imaging with a compact laser-undulator synchrotron x-ray source. *Sci. Rep.*, 7(14477):1–6, 2017. doi:10.1038/s41598-017-14830-x.

[81] C. Jud, F. Schaff, I. Zanette, J. Wolf, A. Fehringer, and F. Pfeiffer. Dentinal tubules revealed with x-ray tensor tomography. *Dental Materials*, 32(9):1189–1195, 2016. doi:10.1016/j.dental.2016.06.021.

[82] S. Kaeppler, J. Rieger, G. Pelzer, F. Horn, T. Michel, A. Maier, G. Anton, and C. Riess. Improved reconstruction of phase-stepping data for talbot-lau x-ray imaging. *J. Med. Imag.*, 4(3):034005, 2017. doi:10.1117/1.JMI.4.3.034005.

[83] S. Kaeppler, M. Seifert, F. Horn, G. Pelzer, J. Rieger, T. Michel, A. Maier, G. Anton, and C. Riess. Talbot-lau x-ray phase contrast for tiling-based acquisitions without reference scanning. *Med. Phys.*, 44(5):1886–1898, 2017. doi:10.1002/mp.12200.

[84] A. C. Kak and M. Slaney. *Principles of Computerized Tomographic Imaging*. IEEE Press, 1987.

[85] G. Khelashvili, J. G. Brankov, D. Chapman, M. A. Anastasio, Y. Yang, Z. Zhong, and M. N. Wernick. A physical model of multiple-image radiography. *Phys. Med. Biol.*, 51(2):221–236, 2006. doi:10.1088/0031-9155/51/2/003.

[86] Y. Kim, J. Valsecchi, J. Kim, S. W. Lee, and M. Strobl. Symmetric talbot-lau neutron grating interferometry and incoherent scattering correction for quantitative dark-field imaging. *Sci. Rep.*, 9:18973, 2019. doi:10.1038/s41598-019-55420-3.

[87] T. Koenig, M. Zuber, B. Trimborn, T. Farago, P. Meyer, D. Kunka, F. Albrecht, S. Kreuer, T. Volk, M. Fiederle, and T. Baumbach. On the origin and nature of the grating interferometric dark-field contrast obtained with low-brilliance x-ray sources. *Phys. Med. Biol.*, 61(9):3427–3442, 2016. doi:10.1088/0031-9155/61/9/3427.

[88] C. Kottler, F. Pfeiffer, O. Bunk, C. Grünzweig, and C. David. Grating interferometer based scanning setup for hard x-ray phase contrast imaging. *Rev. Sci. Instrum.*, 78(4):043710, 2007. doi:10.1063/1.2723064.

[89] T. Köhler. A projection access scheme for iterative reconstruction based on the golden section. *IEEE. Nucl. Sci. Conf. R.*, 6:3961–3965, 2004. doi:10.1109/NSSMIC.2004.1466745.

[90] T. Köhler, H. Turbell, and M. Grass. Efficient forward projection through discrete data sets using tri-linear interpolation. *IEEE Nuclear Science Symposium. Conference Record (Cat. No.00CH37149)*, 2:15/113–15/115, 2000. doi:10.1109/NSSMIC.2000.950067.

[91] Philippe Lacroute and Marc Levoy. Fast volume rendering using a shear-warp factorization of the viewing transformation. In Dino Schweitzer, Andrew Glassner, and Mike Keeler, editors, *SIGGRAPH '94*, page 451–458. ACM, 1994. doi:10.1145/192161.192283.

[92] S. W. Lee, K. Kim, O. Y. Kwon, N. Kardjilov, M. Dawson, A. Hilger, and I. Manke. Observation of magnetic domains in insulation-coated electrical steelsby neutron dark-field imaging. *Appl. Phys. Express*, 3:106602, 2010. doi:10.1143/APEX.3.106602.

[93] R. M. Lewitt. Alternatives to voxels for image representation in iterative roconstruction algorithms. *Phys. Med. Biol.*, 37(3):705–716, 1992. doi:10.1088/0031-9155/37/3/015.

[94] G. Li, S. Luo, C. You, M. Getzin, L. Zheng, G. Wang, and N. Gu. A novel calibration method incorporating nonlinear optimization and ball-bearing markers for cone-beam ct with a parametrized trajectory. *Med. Phys.*, 46(1):152–164, 2019. doi:10.1002/mp.13278.

[95] J. Li, R. Jaszczak, H. Wang, K. L. Greer, and R. E. Coleman. Determination of both mechanical and electronic shifts in cone beam spect. *Phys. Med. Biol.*, 38(6):743–754, 1993. doi:10.1088/0031-9155/38/6/008.

[96] X. Li, D. Zhang, and B. Liu. A generic geometric calibration method for tomographic imaging systems with flat panel detectors—a detailed implementation guide. *Med. Phys.*, 37(7):3844–3854, 2010. doi:10.1118/1.3431996.

[97] M. Liebi, M. Georgiadis, A. Menzel, P. Schneider, J. Kohlbrecher, O. Bunk, and M. Guizar-Sicairos. Nanostructure surveys of macroscopic specimens by small-angle scattering tensor tomography. *Nat. Phys.*, 257:349–353, 2015. doi:10.1038/nature16056.

[98] R. Liu, L. Fu, B. De Man, and H. Yu. Gpu-based branchless distance-driven projection and backprojection. *IEEE Trans. Comput. Imag.*, 3(4):617–632, 2017. doi:10.1109/TCI.2017.2675705.

[99] Y. K. Liu and B. Žalik. A general multi-step algorithm for voxel traversing along a line. *Computer Graphics Forum*, 27(1):73–80, 2008. doi:10.1111/j.1467-8659.2007.01097.x.

[100] S. B. Lo. Strip and line path integrals with a square pixel matrix: A unified theory for computational ct projections. *IEEE Trans. Med. Imaging*, 7(4):355–363, 1988. doi:10.1109/42.14519.

[101] Y. Long, A. Fessler, and J. Balter. 3d forward and back-projection for x-ray ct using seperable footprints. *IEEE Trans. Med. Imaging*, 29(11):1839–1850, 2010. doi:10.1109/TMI.2010.2050898.

[102] V. Ludwig, M. Seifert, C. Hauke, K. Hellbach, F. Horn, G. Pelzer, M. Radicke, J. Rieger, S. Sutter, T. Michel, and G. Anton. Exploration of different x-ray talbot–lau setups for dark-field lung imaging examined in a porcine lung. *Phys. Med. Biol.*, 64(6):065013, 2019. doi:10.1088/1361-6560/ab051c.

[103] S. K. Lynch, V. Pai, J. Auxier, A. F. Stein, E. E. Bennet, C. K. Kemble, X. Xiao, W. Lee, N. Y. Morgan, and H. Wen. Interpretation of dark-field contrast and particle-size selectivity in grating interferometers. *Appl. Opt.*, 50(22):4310–4319, 2011. doi:10.1364/AO.50.004310.

[104] T. Ma, R. Yao, and Y. Shao. A svg-based method to assess the uniqueness and accuracy of spect geometrical calibration. *IEEE Trans. Med. Imag.*, 28(12):1929–1939, 2009. doi:10.1109/TMI.2009.2025696.

[105] A. Malecki, G. Potdevin, T. Biernath, E. Eggl, E. Grande Garcia, T. Baum, P. B. Noël, J. S. Sauer, and F. Pfeiffer. Coherent superposition in grating-based directional dark-field imaging. *PLoS ONE*, 8(4):e61268, 2013. doi:10.1371/journal.pone.0061268.

[106] A. Malecki, G. Potdevin, T. Biernath, E. Eggl, K. Willer, T. Lasser, J. Maisenbacher, J. Gibmeier, A. Wanner, and F. Pfeiffer. X-ray tensor tomography. *EPL*, 105:38002, 2014. doi:10.1209/0295-5075/105/38002.

[107] A. Malecki, G. Potdevin, and F. Pfeiffer. Quantitative wave-optical numerical analysis of the dark-field signal in grating-based x-ray interferometry. *EPL*, 99(4):48001, 2012. doi:10.1209/0295-5075/99/48001.

[108] W. Mao, L. Lee, and L. Xing. Development of a qa phantom and automated analysis tool for geometric quality assurance of on-board mv and kv x-ray imaging systems. *Med. Phys.*, 35(4):1497–1506, 2008. doi:10.1118/1.2885719.

[109] F. De Marco, M. Marschner, L. Birnbacher, P. Noël, J. Herzen, and F. Pfeiffer. Analysis and correction of bias induced by phase stepping jitter in grating-based x-ray phase-contrast imaging. *Opt. Express*, 26(10):12707–12722, 2018. doi:10.1364/OE.26.012707.

[110] S. Matej, J. Fessler, and I. Kazantsev. Iterative tomographic image reconstruction using fourier-based forward and back-projectors. *IEEE Trans. Med. Imaging*, 23(4):401–412, 2004. doi:10.1109/TMI.2004.824233.

[111] S. Matej and R. M. Lewitt. Practical considerations for 3-d image reconstruction using spherically symmetric volume elements. *IEEE Trans. Med. Imaging*. doi:10.1109/42.481442.

[112] C. Mennessier, R. Clackdoyle, and F. Noo. Direct determination of geometric alignment parameters for cone-beam scanners. *Phys. Med. Biol.*, 54(6):1633–1660, 2009. doi:10.1088/0031-9155/54/6/016.

[113] H. Miao, L. Chen, E. Bennet, N. Adamo, A. Gomella, A. DeLuca, A. Patel, N. Morgan, and H. Wen. Motionless phase stepping in x-ray phase contrast imaging with a compact source. *PNAS*, 110(48):19268–19272, 2013. doi:10.1073/pnas.1311053110.

[114] H. Miao, A. Panna, A. A. Gomella, E. E. Bennet, S. Znati, L. Chen, and H. Wen. A universal moiré effect and application in x-ray phase-contrast imaging. *Nature Physics Letters*, 12:830–834, 2016. doi:10.1038/NPHYS3734.

[115] T. Michel, J. Rieger, G. Anton, F. Bayer, M. Beckmann, J. Durst, P. Fasching, W. Haas, A. Hartmann, G. Pelzer, M. Radicke, C. Rauh, A. Ritter, P. Sievers, R. Schulz-Wendtland, M. Uder, D. Wachter, T. Weber, E. Wenkel, and A. Zang. On a dark-field signal generated by micrometer-sized calcifications in phase-contrast mammography. *Phys. Med. Biol.*, 58(8):2713–2732, 2013. doi:10.1088/0031-9155/58/8/2713.

[116] P. Modregger, M. Kagias, S. C. Irvine, R. Brönnigmann, K. Jefimovs, M. Endrizzi, and A. Olivo. Interpretation and utility of the moments of small-angle x-ray scattering distributions. *Phys. Rev. Lett.*, 118(26):265501, 2017. doi:10.1103/PhysRevLett.118.265501.

[117] P. Modregger, M. Kagias, S. Peter, M. Abis, V. A. Guzenko, C. David, and M. Stampanoni. Multiple scattering tomography. *Phys. Rev. Lett.*, 113(2):020801, 2014. doi:10.1103/PhysRevLett.113.020801.

[118] P. Modregger, F. Scattarella, B. R. Pinzer, C. David, R. Bellotti, and M. Stampanoni. Imaging the ultrasmall-angle x-ray scattering distribution with grating interferometry. *Phys. Rev. Lett.*, 108(4):048101, 2012. doi:10.1103/PhysRevLett.108.048101.

[119] F. Momey, L. Denis, C. Burnier, É. Thiébaut, J. Becker, and L. Desbat. Spline driven: High accuracy projectors for tomographic reconstruction from few projections. *IEEE. Trans. Imag. Process.*, 24(12):4715–4725, 2015. doi:10.1109/TIP.2015.2466083.

[120] A. Momose, S. Kawamoto, I. Koyama, Y. Hamaishi, K. Takai, and Y. Suzuki. Demonstration of x-ray talbot interferometry. *Jpn. J. Appl. Phys.*, 42(7B):L866–L868, 2003. doi:10.1143/JJAP.42.L866.

[121] A. Momose, W. Yashiro, K. Kido, J. Kiyohara, C. Makifuchi, T. Ito, S. Nagatsuka, C. Honda, D. Noda, T. Hattori, T. Endo, M. Nagashima, and J. Tanaka. X-ray phase imaging: from synchrotron to hospital. *Phil. Trans. R. Soc. A*, 372:20130023, 2014. doi:10.1098/rsta.2013.0023.

[122] A. Momose, W. Yashiro, Y. Takeda, Y. Suzuki, and T. Hattori. Phase tomography by x-ray talbot interferometry for biological imaging. *Jpn. J. Appl. Phys.*, 45(6A):5254–5262, 2006. doi:10.1143/JJAP.45.5254.

[123] K. Mueller, F. Xu, and N. Neophytou. Why do commodity graphics hardware boards (gpus) work so well for acceleration of computed tomography? *Proc. SPIE 6498, Computational Imaging V*, page 64980N, 2007. doi:10.1117/12.716797.

[124] K. Mueller and R. Yagel. Fast perspective volume rendering with splatting by utilizing a ray-driven approach. *Proceedings of the 7th Conference on Visualization '96*, page 65–72, 1996. doi:10.1109/VISUAL.1996.567608.

[125] K. Mueller, R. Yagel, and F. Cornhill. The weighted distance scheme: A globally optimizing projection ordering method for art. *IEEE Trans. Med. Imaging*, 16(2):223–230, 1997. doi:10.1109/42.563668.

[126] N. Navab, A. Bani-Hashemi, M. Mitschke, D. W. Holdsworth, R. Fahrig, A. J. Fox, and R. Graumann. Dynamic geometrical calibration for 3-d cerebral angiography. *Proc. SPIE 2708 Med. Imaging*, page 361–371, 1996. doi:10.1117/12.237798.

[127] T. Neuwirth, A. Backs, A. Gustschin, S. Vogt, F. Pfeiffer, P. Böni, and M. Schulz. A high visibility talbot-lau neutron grating interferometer to investigate stress-induced magnetic degradation in electrical steel. *Sci. Rep.*, 10:1764, 2020. doi:10.1038/s41598-020-58504-7.

[128] V. Nguyen and S. Lee. Graphics processing unit-accelerated iterative tomographic reconstruction with strip-integral system model. *Optical Engineering*, 51(9):093203–1–11, 2012. doi:10.1117/1.OE.51.9.093203.

[129] M. S. Nielsen, K. B. Damkjær, and R. Feidenhans'l. Quantitative in-situ monitoring of germinating barley seeds using x-ray dark-field radiography. *J. Food Eng.*, 198:98–104, 2017. doi:10.1016/j.jfoodeng.2016.11.011.

[130] F. Noo, R. Clackdoyle, C. Mennessier, T. A. White, and T. J. Roney. Analytic method based on identification of ellipse parameters for scanner calibration in cone-beam tomography. *Phys. Med. Biol.*, 45(11):3489–3508, 2000. doi:10.1088/0031-9155/45/11/327.

[131] J. Nuyts, B. De Man, J. Fessler, W. Zbijewski, and F. Beekman. Modelling the physics in the iterative reconstruction for transmission computed tomography. *Phys. Med. Biol.*, 58(12):R63–R96, 2013. doi:10.1088/0031-9155/58/12/R63.

[132] A. Olivo, F. Arfelli, G. Cantatore, R. Longo, R. H. Menk, S. Pani, M. Prest, P. Poropat, L. Rigon, G. Tromba, E. Vallazza, and E. Castelli. An innovative digital imaging set-up allowing a low-dose approach to phase contrast applications in the medical field. *Med. Phys.*, 28(8):1610–1619, 2001. doi:10.1118/1.1388219.

[133] A. Olivo, F. Arfelli, D. Dreossi, R. Longo, R. H. Menk, S. Pani, P. Poropat, L. Rigon, F. Zanconati, and E. Castelli. Preliminary study on extremely small angle x-ray scatter imaging with synchrotron radiation. *Phys. Med. Biol.*, 47(3):469–480, 2002. doi:10.1088/0031-9155/47/3/308.

[134] D. M. Paganin. *Coherent X-Ray Optics*. Oxford University Press, 2006.

[135] E. Pagot, P. Cloetens, S. Fiedler, A. Bravin, P. Coan, J. Baruchel, J. Härtwig, and W. Thomlinson. A method to extract quantitative information in analyzer-based x-ray phase contrast imaging. *Appl. Phys. Lett.*, 82(20):3421–3423, 2003. doi:10.1063/1.1575508.

[136] X. Pan, E. Sidky, and M. Vannier. Why do commercial ct scanners still employ traditional, filtered back-projection for image reconstruction? *Inverse Probl.*, 25(12):123009, 2009. doi:10.1088/0266-5611/25/12/123009.

[137] D. Pelliccia, L. Rigon, F. Arfelli, R. Menk, I. Bukreeva, and A. Cedola. A three-image algorithm for hard x-ray grating interferometry. *Opt. Express*, 21(16):19401–19411, 2013. doi:10.1364/OE.21.019401.

[138] F. Pfeiffer, M. Bech, O. Bunk, P. Kraft, E. F. Eikenberry, C. Brönnimann, C. Grünzweig, and C. David. Hard-x-ray dark-field imaging using a grating interferometer. *Nat. Mater.*, 7:134–137, 2008. doi:10.1038/nmat2096.

[139] F. Pfeiffer, T. Weitkamp, O. Bunk, and C. David. Phase retrieval and differential phase-contrast imaging with low-brilliance x-ray source. *Nat. Phys.*, 2(4):258–261, 2006. doi:10.1038/nphys265.

[140] P. Pinter. *Microstructure Characterization of Continuous-Discontinuous Fibre Reinforced Polymers based on Volumetric Images*. PhD thesis, KIT, 2018. doi:10.5445/IR/1000084499.

[141] G. Potdevin, A. Malecki, T. Biernath, M. Bech, T. Jensen, R. Feidenhans'l, I. Zanette, T. Weitkamp, J. Kenntner, J. Mohr, P. Roschger, M. Kerschnitzki, W. Wagermaier, K. Klaushofer, P. Fratzl, and F. Pfeiffer. X-ray vector radiography for bone micro-architecture diagnostics. *Phys. Med. Biol.*, 57(11):3451–3461, 2012. doi:10.1088/0031-9155/57/11/3451.

[142] F. Prade, K. Fischer, D. Heinz, P. Meyer, J. Mohr, and F. Pfeiffer. Time resolved x-ray dark-field tomography revealing water transport in a fresh cement sample. *Sci. Rep.*, 6(29108), 2016. doi:10.1038/srep29108.

[143] F. Prade, A. Yaroshenko, J. Herzen, and F. Pfeiffer. Short-range order in mesoscale systems probed by x-ray grating interferometry. *EPL*, 112(6):68002, 2015. doi:10.1209/0295-5075/112/68002.

[144] G. Pratx and L. Xing. Gpu computing in medical physics: A review. *Med. Phys.*, 38(5):2685–2697, 2011. doi:10.1118/1.3578605.

[145] W. H. Press, S. A. Teukolsky, W. T. Vetterling, and B. P. Flannery. *Numerical Recipes – The Art of Scientific Computing, Third Edition*. Cambridge University Press, 2007.

[146] G. N. Ramachandran and A. V. Lakshminarayanan. Three-dimensional reconstruction from radiographs and electron micrographs: Application of convolutions instead of fourier transform. *PNAS*, 68(9):2236–2240, 1971. doi:10.1073/pnas.68.9.2236.

[147] R. Reimann, S. Mühlbauer, M. Horisberger, B. Betz, P. Böni, and M. Schulz. The new neutron grating interferometer at the antares beamline: design, principles and applications. *J. Appl. Chryst.*, 49:1488–1500, 2016. doi:10.1107/S1600576716011080.

[148] V. Revol, I. Jerjen, C. Kottler, P. Schütz, R. Kaufmann, T. Lüthi, U. Sennhauser, U. Straumann, and C. Urban. Sub-pixel porosity revealed by x-ray scatter dark field imaging. *J. Appl. Phys.*, 110(4):044912, 2011. doi:10.1063/1.3624592.

[149] V. Revol, C. Kottler, R. Kaufmann, A. Neels, and A. Dommann. Orientation-selective x-ray dark field imaging of ordered systems. *J. Appl. Phys.*, 112(11):114903, 2012. doi:10.1063/1.4768525.

[150] V. Revol, B. Plank, R. Kaufmann, J. Kastner, C. Kottler, and A. Neels. Laminate fibre structure characterisation of carbon fibre-reinforced polymers by x-ray scatter dark field imaging with a grating interferometer. *NDT&E International*, 58:64–71, 2013. doi:10.1016/j.ndteint.2013.04.012.

[151] S. Rit, M. Oliva, S. Brousmiche, R. Labarbe, D. Sarrut, and G. Sharp. The reconstruction toolkit (rtk), an open-source cone-beam ct reconstruction toolkit based on the insight toolkit (itk). *J. Phys.: Conf. Ser*, 489:012079, 2014. doi:10.1088/1742-6596/489/1/012079.

[152] Ph. Rizo, P. Grangeat, and R. Guillemaud. Geometric calibration method for multiple-head cone-beam spect system. *IEEE Trans. Nuc. Sci.*, 41(6):2748–2757, 1994. doi:10.1109/23.340643.

[153] N. Robert, K. N. Watt, X. Wang, and J. G. Mainprize. The geometric calibration of cone-beam systems with arbitrary geometry. *Phys. Med. Biol.*, 54(24):7239–7261, 2009. doi:10.1088/0031-9155/54/24/001.

[154] A. Rougée, C. Picard, C. Ponchut, and Y. Trousset. Geometrical calibration of x-ray imaging chains for three-dimensional reconstruction. *Comp. Med. Imag. Grap.*, 17(4/5):295–300, 1993. doi:10.1016/0895-6111(93)90020-N.

[155] R. Sampson, M. McGaffin, T. Wenisch, and J. Fessler. Investigating multi-threaded simd for helical ct reconstruction on a cpu. *Proceedings of the 4th International Meeting on image formation in X-ray CT*, page 275–278, 2016.

[156] D. Sarenac, D. A. Pushin, M. G. Huber, D. S. Hussey, H. Miao, M. Arif, D. G. Cory, A. D. Cronin, B. Heacock, D. L. Jacobsen, J. M. LaManna, and H. Wen. Three phase-grating moiré neutron interferometer for large interferometer area applications. *Phys. Rev. Lett.*, 120(11):113201, 2018. doi:10.1103/PhysRevLett.120.113201.

[157] S. Sawall, M. Knaup, and M. Kachelrieß. A robust geometry estimation method for spiral, sequential and circular cone-beam micro-ct. *Med. Phys.*, 39(9):5384–5292, 2012. doi:10.1118/1.4739506.

[158] S. Sayyedi, M. Wieczorek, F. Pfeiffer, and T. Lasser. Incorporating a noise reduction technique into x-ray tensor tomography. *IEEE Trans. Computational Imaging*, 4(1):137–146, 2018. doi:10.1109/TCI.2018.2794740.

[159] M. Schabel. 3d shepp logan phantom. *https://de.mathworks.com/matlabcentral/fileexchange/9416-3d-shepp-logan-phantom*, 2006.

[160] F. Schaff, A. Malecki, G. Potdevin, E. Eggl, P. B. Noël, T. Baum, E. Grande Garcia, J. S. Bauer, and F. Pfeiffer. Correlation of x-ray vector radiography to bone micro-architecture. *Sci. Rep.*, 4:3695, 2014. doi:10.1038/srep03695.

[161] F. Schaff, F. Prade, Y. Sharma, M. Bech, and F. Pfeiffer. Non-iterative directional dark-field tomography. *Sci. Rep.*, 7:3307, 2017. doi:10.1038/s41598-017-03307-6.

[162] J. Scheins, K. Vahedipour, U. Pietrzyk, and N. Shah. High performance volume-of-intersection projectors for 3d-pet image reconstruction based on polar symmetries and simd vectorisation. *Phys. Med. Biol.*, 60(24):9349–9375, 2015. doi:10.1088/0031-9155/60/24/9349.

[163] C. Schretter. A fast tube-of-response raytracer. *Med. Phys.*, 33(12):4744–4748, 2006. doi:10.1118/1.2369467.

[164] M. Seifert, M. Gallersdörfer, V. Ludwig, M. Schuster, F. Horn, G. Pelzer, J. Rieger, T. Michel, and G. Anton. Improved reconstruction technique for moiré imaging using an x-ray phase-contrast talbot–lau interferometer. *J. Imaging*, 4(5):62, 2018. doi:10.3390/jimaging4050062.

[165] M. Seifert, S. Kaeppler, C. Hauke, F. Horn, G. Pelzer, J. Rieger, T. Michel, C. Riess, and G. Anton. Optimisation of image reconstruction for phase-contrast x-ray talbot–lau imaging with regard to mechanical robustness. *Phys. Med. Biol.*, 61(17):6441–6464, 2016. doi:10.1088/0031-9155/61/17/6441.

[166] Y. Seki, T. Shinohara, J. D. Parker, W. Yashiro, A. Momose, K. Kato, H. Kato, M. Sadeghilaridjani, Y. Otake, and Y. Kianagi. Development of multi-colored neutron talbot–lau interferometerwith absorption grating fabricated by imprinting method of metallic glass. *J. Phys. Soc. Jap.*, 86:044001, 2017. doi:10.7566/JPSJ.86.044001.

[167] Y. Sharma, F. Schaff, M. Wieczorek, F. Pfeiffer, and T. Lasser. Design of acquisition schemes and setup geometry for anisotropic x-ray dark-field tomography (axdt). *Sci. Rep.*, 7:3195, 2017. doi:10.1038/s41598-017-03329-0.

[168] Y. Sharma, M. Wieczorek, F. Schaff, S. Seyyedi, F. Prade, and F. Pfeiffer. Six dimensional x-ray tensor tomography with a compact laboratory setup. *Appl. Phys. Lett.*, 109(13):134102, 2016. doi:10.1063/1.4963649.

[169] Robert L Siddon. Fast calculation of the exact radiological path for a three-dimensional ct array. *Med. Phys.*, 12(2):252–255, 1985. doi:10.1118/1.595715.

[170] A. Sitek, R. H. Huesman, and G. T. Gullberg. Tomographic reconstruction using an adaptive tetrahedral mesh defined by a point cloud. *IEEE Trans. Med. Imaging*, 25(9):1172–1179, 2006. doi:10.1109/TMI.2006.879319.

[171] D. S. Sivia. *Elementary Scattering Theory for X-ray and neutron users.* Oxford University Press, 2011.

[172] L. Smekal, M. Kachelrieß, E. Stepina, and W. A. Kalender. Geometric misalignment and calibration in cone-beam tomography. *Med. Phys.*, 31(12):3242–3266, 2004. doi:10.1118/1.1803792.

[173] N. K. Strobel, B. Heigl, T. M. Brunner, O. Schuetz, M. Mitschke, K. Wiesent, and T. Mertelmeier. Improving 3d image quality of x-ray c-arm imaging systems by using properly designed pose determination systems for calibrating the projection geometry. *Proc. SPIE 5030 Med. Imaging*, page 943–954, 2003. doi:10.1117/12.479945.

[174] M. Strobl. General solution for quantitative dark-field contrast imaging with grating interferometers. *Sci. Rep.*, 4:7243, 2014. doi:10.1038/srep07243.

[175] M. Strobl, B. Betz, R. P. Harti, A. Hilger, N. Kardjilov, I. Manke, and C. Gruenzweig. Wavelength-dispersive dark-field contrast: micrometre structure resolution in neutron imaging with gratings. *J. Appl. Chryst.*, 49(2):569–573, 2016. doi:10.1107/S1600576716002922.

[176] M. Strobl, C. Grünzweig, A. Hilger, I. Manke, N. Kardjilov, C. David, and F. Pfeiffer. Neutron dark-field tomography. *Phys. Rev. Lett.*, 101(12):123902, 2008. doi:10.1103/PhysRevLett.101.123902.

[177] G. Strubel, R. Clackdoyle, C. Mennessier, and F. Noo. Analytic calibration of cone-beam scanners. *IEEE Nucl. Sci. Symp. Conf. Rec.*, 5:2731–2735, 2005. doi:10.1109/NSSMIC.2005.1596901.

[178] J. Sunnegårdh and P. Danielsson. A new anti-aliased projection operator for iterative ct reconstruction. 2007.

[179] W. Thompson and W. Lionheart. Gpu accelerated structure-exploiting matched forward and back projection for algebraic iterative cone beam ct reconstruction. *The Third International Conference on Image Formation in X-Ray Computed Tomography*, 2014.

[180] H. Turbell. *Cone-Beam Reconstruction Using Filtered Backprojection.* PhD thesis, 2001.

[181] W. van Aarle, W. Palenstijn, J. Cant, E. Janssens, F. Bleichrodt, A. Dabravolski, J. De Beenhouwer, K. J. Batenburg, and J. Sijbers. Fast and flexible x-ray tomography using the astra toolbox. *Optics Express*, 24(22):25129–25147, 2016.

[182] T. van Leeuwen and K. Batenburg. Adaptive grid refinement for discrete tomography. *Discrete Geometry for Computer Imagery. DGCI 2014. Lecture Notes in Computer Science*, 8668, 2014. doi:10.1007/978-3-319-09955-2_25.

[183] J. Vargas, C. O. S. Sorzano, J. C. Estrada, and J. M. Carazo. Generalization of the principal component analysis algorithm for interferometry. *Opt. Comm.*, 286:130–134, 2013. doi:10.1016/j.optcom.2012.09.017.

[184] A. Velroyen, A. Yaroshenko, D. Hahn, A. Fehringer, A. Tapfer, M. Müller, P. Noël, B. Pauwels, A. Sasov, A. Yildirim, O. Eickelberg, K. Hellbach, S. Auweter, F. Meinel, M. Reiser, M. Bech, and F. Pfeiffer. Grating-based x-ray dark-field computed tomography of living mice. *EBioMedicine*, 2:1500–1506, 2015. doi:10.1016/j.ebiom.2015.08.014.

[185] J. Vogel, F. Schaff, A. Fehringer, C. Jud, M. Wieczorek, F. Pfeiffer, and T. Lasser. Constrained x-ray tensor tomography reconstruction. *Opt. Express*, 23(12):15134–15151, 2015. doi:10.1364/OE.23.015134.

[186] G. Wang, T. Lin, P. Cheng, and D. Shinozaki. A general cone-beam reconstruction algorithm. *IEEE Trans. Med. Imaging*, 12(3):486–496, 1993. doi:10.1109/42.241876.

[187] Y. Wang and B. M. W. Tsui. Pinhole spect with different data acquisition geometries: Usefulness of unified projection operators in homogeneous coordinates. *IEEE Trans. Med. Imaging*, 26(3):298–308, 2007. doi:10.1109/TMI.2006.887372.

[188] Z. Wang, K. Kang, Z. Huang, and Z. Chen. Quantitative grating-based x-ray dark-field computed tomography. *Appl. Phys. Lett.*, 95(9):094105, 2009. doi:10.1063/1.3213557.

[189] T. Weber, P. Bartl, F. Bayer, J. Durst, W. Haas, T. Michel, A. Ritter, and G. Anton. Noise in x-ray grating-based phase-contrast imaging. *Med. Phys.*, 38(7):4133–4140, 2011. doi:10.1118/1.3592935.

[190] T. Weitkamp, C. David, C. Kottler, O. Bunk, and F. Pfeiffer. Tomography with grating interferometers at low-brilliance sources. *Proc. SPIE*, 6318:63180S, 2006. doi:10.1117/12.683851.

[191] T. Weitkamp, A. Diaz, C. David, F. Pfeiffer, M. Stampanoni, P. Cloetens, and E. Ziegler. X-ray phase imaging with a grating interferometer. *Opt. Express*, 13(16):6296–6304, 2005. doi:10.1364/OPEX.13.006296.

[192] T. Weitkamp, I. Zanette, C. David, J. Baruchel, M. Bech, P. Bernard, H. Deyhle, T. Donath, J. Kenntner, S. Lang, J. Mohr, B. Müller, F. Pfeiffer, E. Reznikova, S. Rutishauser, G. Schulz, A. Tapfer, and J. Valade. Recent developments in x-ray talbot interferometry at esrf-id19. *Proc. SPIE*, 7804:780406, 2010. doi:10.1117/12.860203.

[193] H. Wen, E. Bennet, M. Hegedus, and S. Rapacchi. Fourier x-ray scattering radiography yields bone structural information. *Radiology*, 251(3):910–918, 2009. doi:10.1148/radiol.2521081903.

[194] H. Wen, E. Bennet, A. F. Stein, and V. Pai. Single-shot x-ray differential phase-contrast and diffraction imaging using two-dimensional transmission gratings. *Opt. Lett.*, 35(2):1932–1934, 2010. doi:10.1364/OL.35.001932.

[195] H. Wen, E. E. Bennet, M. M. Hegedus, and S. C. Carroll. Spatial harmonic imaging of x-ray scattering—initial results. *IEEE Trans. Med. Imaging*, 27(8):997–1002, 2008. doi:10.1109/TMI.2007.912393.

[196] M. N. Wernick, O. Wirjadi, D. Chapman, Z. Zhong, N. Galatsanos, Y. Yang, J. G. Brankov, O. Oltulu, M. A. Anastasio, and C. Muehleman. Multiple-image radiography. *Phys. Med. Biol.*, 48(23):3875–3895, 2003. doi:10.1088/0031-9155/48/23/006.

[197] M. Wieczorek, F. Schaff, F. Pfeiffer, and T. Lasser. Anisotropic x-ray dark-field tomography: A continuous model and its discretization. *Phys. Rev. Lett.*, 117(15):158101, 2016. doi:10.1103/PhysRevLett.117.158101.

[198] D. Wu, L. Li, L. Zhang, Y. Xing, Z. Chen, and Y. Xiao. Geometric calibration of cone-beam ct with a flat-panel detector. *IEEE Nucl. Sci. Conf. R.*, page 2952–2955, 2011. doi:10.1109/NSSMIC.2011.6152527.

[199] M. Wu and J. Fessler. Gpu acceleration of 3d forward and backward projection using separable footprints for x-ray ct image reconstruction. *Proceedings of the International Meeting on Fully 3D Image Reconstruction in Radiology and Nuclear Medicine*, 6:021911, 2011.

[200] K. Xiao, D. Chen, and X. Hu. Efficient implementation of the 3d-dda ray traversal algorithm on gpu and its application in radiation dose calculation. *Med. Phys.*, 39(12):7619–7625, 2012. doi:10.1118/1.4767755.

[201] F. Xu and K. Mueller. Accelerating popular tomographic reconstruction algorithms on commodity pc graphics hardware. *IEEE Trans. Nucl. Sci.*, 52(3):654–663, 2005. doi:10.1109/TNS.2005.851398.

[202] F. Xu and K. Mueller. A comparative study of popular interpolation and integration methods for use in computed tomography. *3rd IEEE International Symposium on Biomedical Imaging: Nano to Macro*, page 1252–1255, 2006. doi:10.1109/ISBI.2006.1625152.

[203] J. Xu and B. Tsui. An analytical geometric calibration method for circular cone-beam geometry. *IEEE Trans. Med. Imaging*, 32(9):1731–1744, 2013. doi:10.1109/TMI.2013.2266638.

[204] M. Xu, C. Zhang, X. Liu, and D. Li. Direct determination of cone-beam geometric parameters using the helical phantom. *Phys. Med. Biol.*, 59(19):5667–5690, 2014. doi:10.1088/0031-9155/59/19/5667.

[205] F. Yang, F. Prade, M. Griffa, R. Kaufmann, J. Herzen, F. Pfeiffer, and P. Lura. X-ray dark-field contrast imaging of water transport during hydration and drying of early-age cement-based materials. *Mater. Charact.*, 142:560–576, 2018. doi:10.1016/j.matchar.2018.06.021.

[206] K. Yang, A. L. C. Kwan, D. F. Miller, and J. M. Boone. A geometric calibration method for cone beam ct systems. *Med. Phys.*, 33(6):1695–1706, 2006. doi:10.1118/1.2198187.

[207] W. Yao and K. Leszczynski. Analytically derived weighting factors for transmission tomography cone beam projections. *Phys. Med. Biol.*, 54(3):13–533, 2009. doi:10.1088/0031-9155/54/3/004.

[208] A. Yaroshenko, K. Hellbach, M. Bech, S. Grandl, M. F. Reiser, F. Pfeiffer, and F. G. Meinel. Grating-based x-ray dark-field imaging: a new paradigm in radiography. *Curr. Radiol. Rep.*, 2(57), 2014. doi:10.1007/s40134-014-0057-9.

[209] W. Yashiro, S. Harasse, K. Kawabata, H. Kuwabara, T. Yamazaki, and A. Momose. Distribution of unresolvable anisotropic microstructures revealed in visibility-contrast images using x-ray talbot interferometry. *Phys. Rev. B*, 84(9):094106, 2011. doi:10.1103/PhysRevB.84.094106.

[210] W. Yashiro, S. Ikeda, Y. Wada, K. Totsu, Y. Suzuki, and A. Takeuchi. Probing surface morphology using x-ray grating interferometry. *Sci. Rep.*, 9:14120, 2019. doi:10.1038/s41598-019-50486-5.

[211] W. Yashiro, Y. Terui, K. Kawabata, and A. Momose. On the origin of visibility contrast in x-ray talbot interferometry. *Opt. Express*, 18(16):16890–16900, 2010. doi:10.1364/OE.18.016890.

[212] M. Zdora. State of the art of x-ray speckle-based phase-contrast and dark-field imaging. *J. Imaging*, 4(5):60, 2018. doi:10.3390/jimaging4050060.

[213] A. Zechner, M. Stock, D. Kellner, I. Ziegler, P. Keuschnigg, P. Huber, U. Mayer, F. Sedlmayer, H. Deutschmann, and P. Steiniger. Development and first use of a novel cylindrical ball bearing phantom for 9-dof geometric calibrations of flat panel imaging devices used in image-guided ion beam therapy. *Phys. Med. Biol.*, 61(22):N592–N605, 2016. doi:10.1088/0031-9155/61/22/N592.

[214] S. Zhang, D. Zhang, H. Gong, O. Ghasemalizadeh, G. Wang, and G. Cao. Fast and accurate computation of system matrix for area integral model-based algebraic reconstruction technique. *Optical Engineering*, 53(11):113101–1–9, 2014. doi:10.1117/1.OE.53.11.113101.

[215] H. Zhao and A. J. Reader. Fast ray-tracing technique to calculate line integral paths in voxel arrays. *Nuclear Science Symposium Conference Record, 2003 IEEE*, 4:2808–2812, 2004. doi:10.1109/NSSMIC.2003.1352469.

[216] Z. Zhong, W. Thomlinson, D. Chapman, and D. Sayers. Implementation of diffraction-enhanced imaging experiments: at the nsls and aps. *Nucl. Instrum. Methods Phys. Res. A*, 450(2–3):556–567, 2000. doi:10.1016/S0168-9002(00)00308-9.

[217] A. Ziegler, T. Köhler, T. Nielsen, and R. Proksa. Efficient projection and backprojection scheme for spherically symmetric basis functions in divergent beam geometry. *Med. Phys.*, 33(12):4653–4663, 2006. doi:10.1118/1.2388570.

[218] E. Özarslan, B. C. Vemuri, and T. H. Mareci. Generalized scalar measures for diffusion MRI using trace, variance, and entropy. *Magn. Reson. Med.*, 53:866–876, 2005. doi:10.1002/mrm.20411.